THESIS

# INTEGRATION, CHARACTERIZATION, AND CALIBRATION OF THE HIGH-FREQUENCY AIRBORNE MICROWAVE AND MILLIMETER-WAVE RADIOMETER (HAMMR) INSTRUMENT

Submitted by

Thaddeus Johnson

Department of Electrical and Computer Engineering

In partial fulfillment of the requirements

For the Degree of Master of Science

Colorado State University

Fort Collins, Colorado

Fall 2014

Master's Committee:

Advisor: Steven C. Reising

Yu Morton
Thomas H. Vonder Haar
Pekka Kangaslahti

# ABSTRACT

## INTEGRATION, CHARACTERIZATION, AND CALIBRATION OF THE HIGH-FREQUENCY AIRBORNE MICROWAVE AND MILLIMETER-WAVE RADIOMETER (HAMMR) INSTRUMENT

Current satellite ocean altimeters include nadir-viewing, co-located 18-34 GHz microwave radiometers to measure wet-tropospheric path delay. Due to the large antenna footprint sizes at these frequencies, the accuracy of wet path retrievals is substantially degraded within 40 km of coastlines, and retrievals are not provided over land. A viable approach to improve their capability is to add wide-band millimeter-wave window channels in the 90-183 GHz band, thereby achieving finer spatial resolution for a fixed antenna size. In this context, the upcoming Surface Water and Ocean Topography (SWOT) mission is in formulation and planned for launch in late 2020 to improve satellite altimetry to meet the science needs of both oceanography and hydrology and to transition satellite altimetry from the open ocean into the coastal zone and over inland water. To address wet-path delay in these regions, the addition of 90-183 GHz millimeter-wave window-channel radiometers to current Jason-class 18-34 GHz radiometers, is expected to improve retrievals of wet-tropospheric delay in coastal areas and to enhance the potential for over-land retrievals.

To this end, an internally-calibrated, wide-band, cross-track scanning airborne microwave and millimeter-wave radiometer is being developed in collaboration between Colorado State University (CSU) and Caltech/NASA's Jet Propulsion Laboratory (JPL). This airborne radiometer includes microwave channels at 18.7, 23.8, and 34.0 GHz at both H and V polarizations; millimeter-wave window channels at 90, 130, 168 GHz; and temperature and water vapor sounding channels adjacent to the 118 and 183 GHz absorption lines, respectively. Since this instrument is demonstrating this technology for the potential use in future Earth science missions, substantial effort has been put into ensuring the instrument has a minimal mass and volume and is robust and well characterized.

To this end the optical alignment has been extensively tested and characterized and a novel blackbody calibration target has been designed and integrated into the system. All supporting sub-systems such as power distribution and data acquisition have been integrated into the chassis allowing the instrument to be easily run by a single operator. Preliminary test flights have been done that demonstrate the reliability and robustness of this instrument as well as demonstrating the increased special resolution of the millimeter-wave window and sounding channels over that of the Jason-class 18-34 GHz radiometers.

# ACKNOWLEDMENTS

I would first like to thank Prof. Steven C. Reising for his support and guidance, not only as my adviser in this research, but also as a role model and mentor for the past six years. I would like to thank Dr. Pekka Kangaslahti, Prof. Branislav Notaros, and Prof. Thomas Vonder Haar for their input on my thesis and for serving on my committee.

I would like to thank the HAMMR IIP-10 team at Caltech/NASA's Jet Propulsion Laboratory for their technical contributions, support, and guidance throughout my thesis. Specifically, I would like to thank Dr. Pekka Kangaslahti, Dr. Alan Tanner, Dr. Sharmila Padmanabhan, Dr. Chaitali Parashare, and Mr. Oliver Montes.

I would like to thank Dr. Javier Bosch-Lluis for his technical contributions, invaluable feedback, and friendship throughout the research completed for this thesis.

Finally, I would like to thank my family, my girlfriend Katie Svoboda, and my roommates Patrick Tangney, Anthony San Lorenzo, and David Ouzts for their unwavering support and patience throughout this project.

# DEDICATION

I would like to dedicate this thesis to my wonderful, supportive family, and to my beloved and cherished girlfriend Katie Svoboda.

TABLE OF CONTENTS

LIST OF TABLES

LIST OF FIGURES

# Chapter I. Introduction

This thesis will discuss the development, fabrication, integration, and characterization of the High-frequency Airborne Microwave and Millimeter-Wave Radiometer (HAMMR) instrument. HAMMR is an airborne cross-track scanning microwave and millimeter-wave radiometer with 25 channels in the frequency range from 18 to 183 GHz. HAMMR was developed under the Instrument Incubator Program (IIP) 2010 project funded by the National Aeronautics and Space Administration (NASA)'s Earth Science Technology Office (ESTO). ESTO is led by Mr. George Komar, and the IIP-10 Program Manager and lead for Advanced Observation Technology is Mr. Parminder Ghuman. The HAMMR IIP-10 program is led by Principal Investigator Prof. Steven C. Reising and is a collaborative effort between the Colorado State University (CSU) Microwave Systems Laboratory (MSL) and the Jet Propulsion Laboratory (JPL), California Institute of Technology (Caltech). The scientific motivation and program objectives for IIP-10 will be discussed and the organization of this thesis will be provided.

## 1.1 Scientific Motivation

The purpose of HAMMR is to measure humidity in the atmosphere. This measurement is useful in weather prediction models and in retrieving wet-tropospheric path delay. Wet-tropospheric path delay is the error that makes a propagating electromagnetic (EM) signal arrive later than expected due to

differences from unity in the refractive index of the atmosphere, which in turn depends upon the amount of water vapor. As the index of refraction of a medium increases, the speed of propagation in the medium decreases. The relationship between the speed of propagation of EM waves and the index of refraction is shown in (I.1).

$$v = \frac{c}{n} = \frac{c}{\sqrt{\varepsilon_r \mu_r}} \tag{I.1}$$

where $v$ is the propagation speed in a medium, $c$ is propagation speed in a vacuum, $n$ is the index of refraction of the medium, $\varepsilon_r$ is the relative permittivity of the medium, and $\mu_r$ is the relative permeability of the medium.

Since their measurements depend upon the arrival time of signals propagating through long atmospheric paths, satellite borne radar altimeters and interferometers are susceptible to wet-tropospheric path delay measurement errors. As the refractive index along the path between the satellite and the surface increases, the speed of propagation of the radar signal decreases, so that the signal is received later, causing the path length to appear longer than it is.

The atmospheric temperature and pressure also affect the atmosphere's refractive index but atmospheric temperature and pressure are easier to estimate with good accuracy, so this project focuses on water vapor as the most important variable.

Precision satellite ocean altimeters such as TOPEX, Jason-1, Jason-2/Ocean Surface Topography Mission (OSTM) and Jason-3 (to be launched in 2015) include co-located 18-37 GHz multichannel microwave radiometers to retrieve wet-

tropospheric path delay (Jet Propulsion Laboratory). At these radiometer's relatively low frequencies, the footprint on Earth is large. So, tropospheric-wet path delay measurements are degraded within 40 km of the coasts. This degradation is called "land contamination", as illustrated in Figure 1.

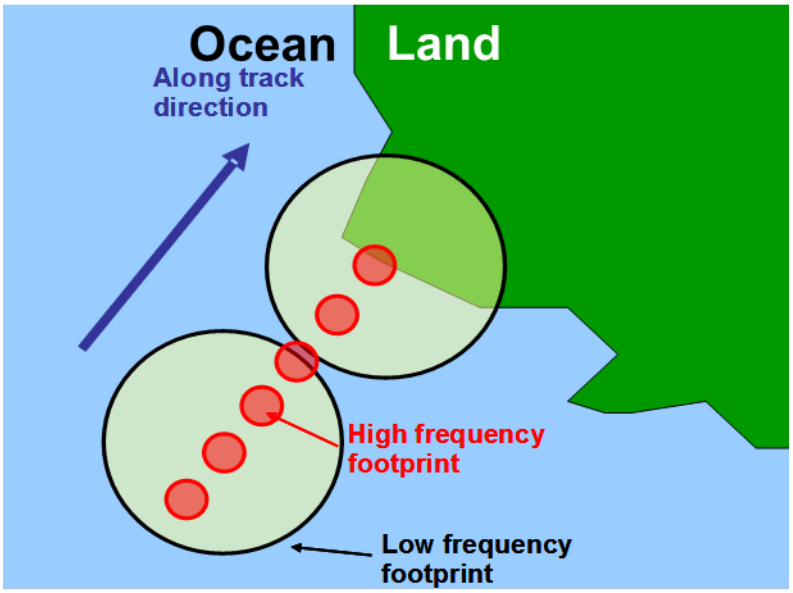


Figure 1: Comparison of footprint sizes for high and low frequency radiometers.

(Reising S. , et al., 2013)

Land contamination is due to the highly variable microwave brightness temperature of land surfaces due to changing temperature and emissivity caused by vegetation, snow, ice, soil moisture, surface temperature, and surface roughness. Adding high frequency channels between 90 and 175 GHz is expected to improve retrievals by reducing the size of the measurement footprint, which is inversely proportional to frequency, so that land contamination does not occur until the beam center is much closer to the coastline.

## 1.2 Instrument Incubator Program (IIP) 10 Objectives

The IIP-10 project led by Professor Steven Reising of CSU will produce an instrument to assess wet-tropospheric path delay variability on 10-km and smaller spatial scales and demonstrate new high-frequency millimeter-wave radiometry technology, including both window and sounding channels (Ghuman, 2010).

NASA ESTO uses a metric called Technology Readiness Levels (TRLs) to describe how close a technology is to being ready to be used in space. NASA ESTO funds programs such as the ACTs and IIPs to increase the TRL of a technologies, as shown in Figure 2 (NASA ESTO, 2014). The TRL scale ranges from 1to 9, with 1 being the lowest level and 9 being the highest level of readiness. During these projects, the components, subsystems, and instruments progress from the early stages of development through space-flight qualified hardware (National Aeronautics and Space Administration (NASA) Earth Science Technology Office (ESTO), 2014).

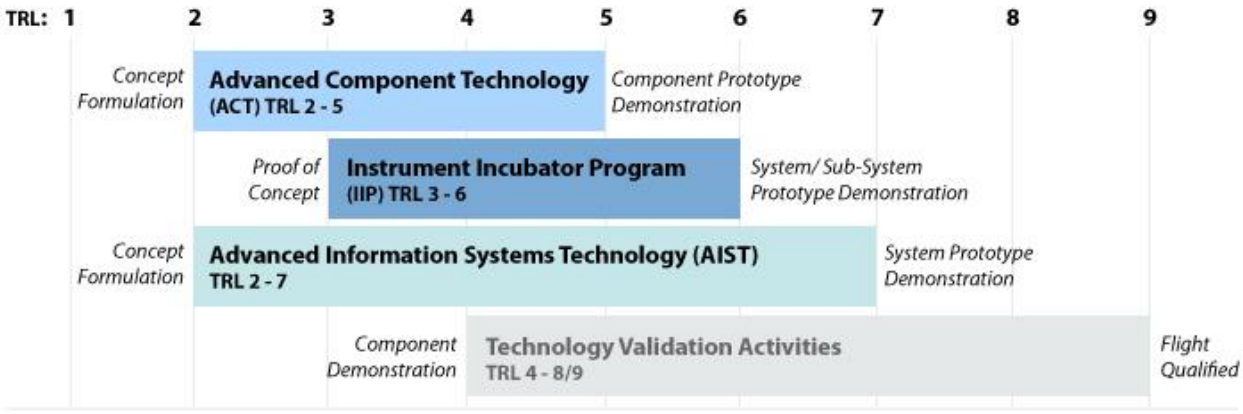


Figure 2: ESTO programs, shown on the TRL scale, by program area (NASA ESTO, 2014).

This IIP-10 project started with three high-frequency millimeter wave radiometer channels developed through a collaboration between JPL, and CSU's Microwave Systems Lab (MSL) under the Advanced Component Technology (ACT-08) project led by Principal Investigator Prof. Steven C. Reising.

The ACT-08 project increased the TRL of these high-frequency millimeter wave radiometers to 4, and the IIP-10 is expected take them to a TRL of 6. In addition to the radiometers developed under the ACT-08 project, new sounding radiometers near the frequencies of 118 and 183 GHz are also being developed under the IIP-10 to enable temperature and humidity sounding as part of the same instrument. Successful airborne demonstration of the HAMMR instrument as a system and measurement of calibrated brightness temperatures will increase the TRL of these technologies to 6.

## 1.3 Thesis Description and Organization

The remainder of this thesis is divided into seven additional chapters. Chapter II discusses the principles of atmospheric microwave radiometry including blackbody radiation, the radiative transfer equation, atmospheric absorption models, noise, radiometer calibration, and two commonly used radiometer architectures. Chapter III presents an overview of the HAMMR mechanical system including the design, integration, and validation of the feed horn antenna placement, the reflector sub-systems, the HAMMR chassis, and the scanning reflector. A description of the supporting sub-systems is also given. The internal blackbody calibration target is discussed in Chapter IV, which primarily focuses on the design and fabrication process. The microwave channels, millimeter-wave window channels and millimeter-wave sounder channels are presented in detail in Chapters V, VI, and VII, respectively. Chapter VIII focuses on the characterization and calibration of the fully integrated HAMMR system including both airborne and ground based tests.

# Chapter II. Radiometry

The fundamental principles of microwave radiometry are covered in this chapter, as well as the basics of radiometer architectures, including calibration methods and radiometer configurations.

## 2.1 Principles of Microwave Radiometry

An overview of the fundamental theory involved in microwave radiometry is presented in this section including blackbody radiation, atmospheric attenuation and the radiative transfer equation.

### 2.1.1 Blackbody Radiation

An ideal blackbody is an object that is a perfect emitter and absorber of EM energy while in thermal equilibrium. The spectral brightness emitted by a blackbody at a physical temperature, *T,* at a frequency, *f,* is given by Planck's Law in (II.1).

$$B_f = \frac{2hf^3}{c^2}\left(e^{\frac{hf}{kT}} - 1\right)^{-1} \qquad \text{(II.1)}$$

where $B_f$ is the spectral brightness of an object in Watts per meter-squared per steradian per Hertz (W/(m$^2$SrHz)), $h$ is Planck's constant in Joule seconds ($J \bullet s$), $f$ is frequency in Hertz (Hz), $k$ is Boltzmann's constant in Joules per Kelvin (J/K), $T$ is absolute physical (thermodynamic) temperature in K, and $c$ is the speed of light in meters per second (m/s) (Ulaby, Moore, & Fung, 1981).

A common approximation of Planck's Law is that in the low-frequency or long-wavelength region, the exponential term in (II.1) becomes close to unity as in (II.2).

$$\frac{hf}{kT} \ll 1 \tag{II.2}$$

Assuming (II.2), the first-order Taylor approximation in (II.3) can be applied.

$$e^{\frac{hf}{kT}} - 1 \cong \frac{hf}{kT} \tag{II.3}$$

Using (II.3), (II.1) can be rewritten as (II.4), known as Rayleigh-Jeans' law for spectral brightness (Ulaby, Moore, & Fung, 1981)

$$B_f = \frac{2kT}{\lambda^2} \tag{II.4}$$

where λ is wavelength in meters. This approximation agrees well with Planck's Law, where the error introduced using Raleigh-Jeans' law instead of Planck's Law at 300 K approximately 0.008% and 2.4% at 1 and 300 GHz respectively. This approximation will be used in the remainder of this thesis.

To measure the radiation of a blackbody, one uses an antenna to convert the EM wave into a usable voltage signal on a transmission line, so the characteristics of the antenna must be taken into account. The power radiated by a blackbody as measured by a lossless antenna is shown in (II.5).

$$P_{bb} = kTB_w \frac{A_r}{\lambda^2} \iint_{4\pi} F_n(\Theta, \Phi) d\Omega \tag{II.5}$$

where $\iint_{4\pi} F_n(\Theta,\Phi)d\Omega$ is the integral of the normalized antenna pattern over the solid angle $d\Omega$, and $B_w$ is the bandwidth of the receiver. The integral is recognized as the solid angle of the antenna pattern as (II.6), assuming that the antenna is surrounded by the blackbody and no radiation sources are present.

$$\iint_{4\pi} F_n(\Theta,\Phi)d\Omega = \Omega_P \tag{II.6}$$

For aperture antennas, $\Omega_P$ is related to the effective aperture, $A_r$ by

$$\Omega_P = \frac{\lambda^2}{A_r} \tag{II.7}$$

allowing simplification of (II.5) as a linear relationship between radiated power and physical temperature shown in (II.8) (Ulaby, Moore, & Fung, 1981).

$$P_{bb} = kTB \tag{II.8}$$

This is the same result as the Johnson-Nyquist noise of a resistor at a physical temperature $T$, also known as thermal noise, shown in (II.9).

$$P = kTB \tag{II.9}$$

This indicates that a lossless antenna observing an ideal blackbody will provide the same available power to the receiver as a matched resistor at a physical temperature equivalent to the temperature of the blackbody being observed (Ulaby, Moore, & Fung, 1981).

The power radiated from a blackbody is usually referred to in terms of brightness temperature instead of Watts. This provides a simple comparison of different systems with different bandwidths.

In practice ideal blackbodies do not exist, a fact that must be taken into account when performing measurements with a radiometer. All matter reflects and transmits a certain amount of energy instead of absorbing it all as a blackbody does. To model emission from matter, a quantity called emissivity, $e$, is introduced. Emissivity defines the relationship between the power radiated by a blackbody and the power radiated by a grey body with the same temperature and using the same measurement bandwidth as

$$e = \frac{P}{kTB}\ ,\ 0 \le e \le 1 \qquad \text{(II.10)}$$

where $P$ is the power radiated by the grey body and $kTB$ is the power radiated by the ideal blackbody. The measured temperature of a grey body can then be shown as

$$T_B = eT \qquad \text{(II.11)}$$

For an ideal blackbody, $e$ is unity and for a perfect reflector $e$ is zero. Measured brightness temperature is used by atmospheric scientists to determine physical characteristics of measured bodies such as the temperature or humidity of the atmosphere. To retrieve these physical characteristics from brightness temperature measurements, retrieval algorithms are used. These algorithms are based on

forward models of the atmosphere using atmospheric absorption coefficients and the radiative transfer equation.

### 2.1.2 Radiative Transfer Equation

When observing the atmosphere, a nadir viewing radiometer, at a distance r from the surface, measures two sources of radiation, as represented in (II.12). The first term, $T_{AP}(0)$, is due to the apparent temperature of the surface measured by the antenna reduced by the atmospheric attenuation, $e^{-\tau(0,r)}$, between the scene and the radiometer. The second term represents upwelling emission of the atmosphere in the direction of the radiometer (Ulaby, Moore, & Fung, 1981).

$$T_{AP}(r) = T_{AP}(0)e^{-\tau(0,r)} + \int_0^r \kappa_a(r')T(r')e^{-\tau(r',r)}dr' \qquad \text{(II.12)}$$

Apparent temperature or $T_{AP}(0)$ is the temperature that the antenna measures due to the scene. This is different from brightness temperature because it takes into account atmospheric attenuation and other contributing factors that are not due to the body of interest. The apparent temperature includes upwelling radiation emitted from the surface, downwelling radiation reflected from the surface, and upwelling radiation emitted from the atmosphere between the antenna and the surface. All of these parameters are reduced by attenuation in the intervening atmosphere, as shown in (II.12) (Ulaby, Moore, & Fung, 1981).

In this thesis we are interested only in the second term. This is why the highly variable emissivity of land contaminates our images, because it is not known and

therefore cannot be removed. In contrast, the emissivities of water vapor and liquid water are known and can be easily removed.

Equation (II.12) is valid only for a scatter free medium, which for our frequency range of interest, 18 to 183 GHz, is a valid assumption under most non-precipitating conditions.

### 2.1.3 Atmospheric Absorption

The amount of attenuation that EM radiation undergoes in the atmosphere varies with frequency. The frequency dependence is due to the resonances of atmospheric constituents such as oxygen and water vapor, as well as from the frequency variation of liquid water, when it is present. At microwave and millimeter-wave frequencies, the major contributors to atmospheric attenuation are oxygen, water vapor and liquid water (Ulaby, Moore, & Fung, 1981). The absorption coefficient with respect to frequency from these three major contributors is shown in Figure 3 as calculated using the Rosenkranz-Liebe model, as explained in (Rosenkranz, Jul.-Aug. 1998).

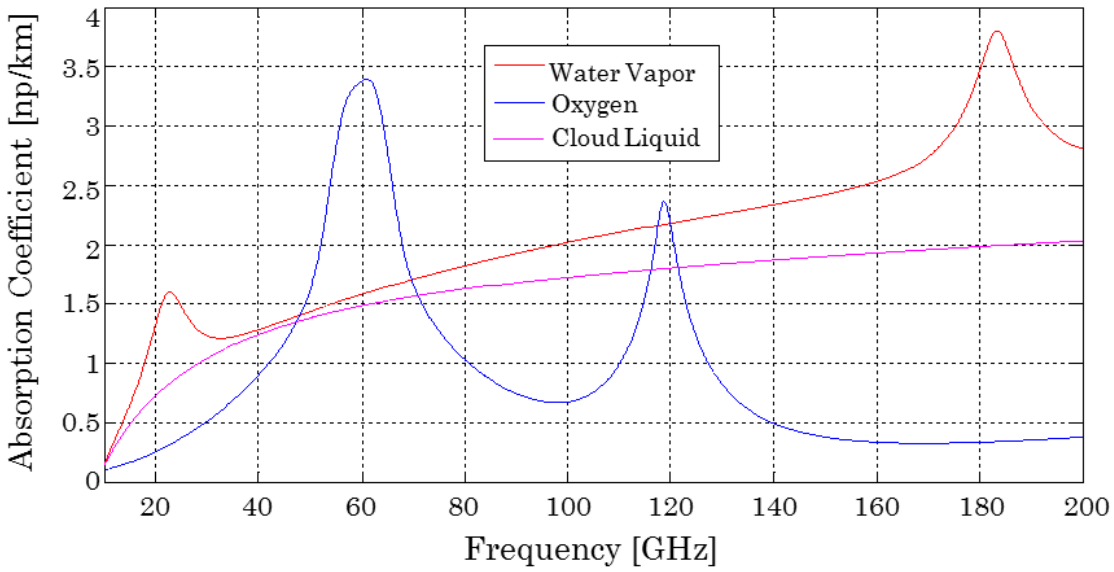


Figure 3: Microwave and Millimeter-Wave Absorption Spectra from 10 to 200 GHz for Water Vapor Density of 15.1 g/m$^3$, a Temperature of 297 K, and a Cloud Liquid Water Density of 0.1 g/m$^3$ at ground level (Sahoo, private communication).

Each peak of absorption is due to the presence of an absorption line, and the frequency ranges between the peaks are referred to as "windows". A radiometer with channels near the peaks is said to have sounding channels. A radiometer with channels in these frequency ranges is said to have window channels because the radiometer will most likely "see" all the way through the atmosphere and be sensitive to emission from the surface. As the attenuation increases, the measurement will penetrate the atmosphere less deeply and will not be sensitive to emission from the surface.

By using measurements in both of these frequency ranges, a variety of atmospheric parameters can be retrieved. Measurements at a number of frequencies close to a

water vapor absorption line allow retrieval of atmospheric water vapor content at a variety of altitudes due to pressure broadening. Measurements at window frequencies allow the characterization of the influence of liquid water and the surface emission. Therefore, a combination of measurements near the absorption lines and window frequencies can be used to retrieve total column, or integrated water vapor.

Oxygen is well mixed in the troposphere, and oxygen absorption line widths change due to pressure and temperature (Iturbide-Sanchez, 2007). Because of this, measurements at multiple frequencies near oxygen absorption lines enable retrievals of atmospheric temperature height profiles.

## 2.2 Radiometer Performance

A radiometer is a passive receiver that is designed to measure a scene's emitted electromagnetic radiation in a selected frequency range. A microwave radiometer measures the portion of the emitted radiation of a scene in the selected range of microwave frequencies. An antenna provides the input to the front end of a radiometer to measure the emitted power, or brightness temperature, $T_B$, and provide an equivalent noise temperature, $T_A$, to the receiver. The equivalent noise temperature of the receiver, $T_{rec}$, of a microwave radiometer is often greater than the antenna temperature (Janssen, 1993). The receiver temperature is caused by the thermal noise, described in the following subsection, generated by its components, including LNAs, mixers, and resistors. If the components generating

thermal noise are in the front end before significant gain stages, it will have a more significant effect than if generated in later stages, as described in sections 2.2.1 and 2.2.2 (Janssen, 1993). The system temperature, $T_{sys}$, is the sum of the receiver and antenna temperatures.

### 2.2.1 Noise

Thermal noise, also known as Nyquist noise, is caused by thermal vibrations of bound charges in a random process with a Gaussian probability density function (PDF) and a mean of zero. Thermal noise is present in all elements with equivalent resistance and needs to be accounted for in system design. The following section discusses how noisy devices are characterized.

Noisy components are characterized by a noise figure, *F*, which describes the degradation of signal-to-noise ratio between the input and output of the device as given in (II.13).

$$F = \frac{S_i / N_i}{S_o / N_o} \tag{II.13}$$

where $S_i$, $N_i$ are input signal and noise powers, respectively, and $S_o$, $N_o$ are output signal and noise powers, respectively. A commonly used way of quantifying noise in a radiometer is noise temperature as shown in (II.14)

$$T_{Rec} = (F - 1)T_o \tag{II.14}$$

where $T_{rec}$ is the noise temperature introduced by the receiver and $T_o$ is the noise temperature of the device defined by the Institute of Electrical and Electronics

Engineers (IEEE) to be 290 K for this definition of noise figure. Analogous to the power of a blackbody radiator, the noise power is described by (II.15).

$$P_{N,rec} = kT_{rec}B \tag{II.15}$$

A noisy receiver with a noise temperature of $T_{\text{rec}}$ can be modeled as a noiseless receiver with an input noise power of $P_{\text{N,rec}}$.

### 2.2.2 Cascaded Noise

The concept of noise figure described in Section 2.2.1 can be extended to describe a multi-component system. Typically such a system consists of a cascade of components. Each component in the system is characterized with its own noise temperature as shown in (II.14). The cascaded noise temperature of the system can be derived from the individual gains and noise temperatures of each component. The cascaded noise figure and equivalent noise temperature of a two-stage system will be derived, as shown in Figure 4.

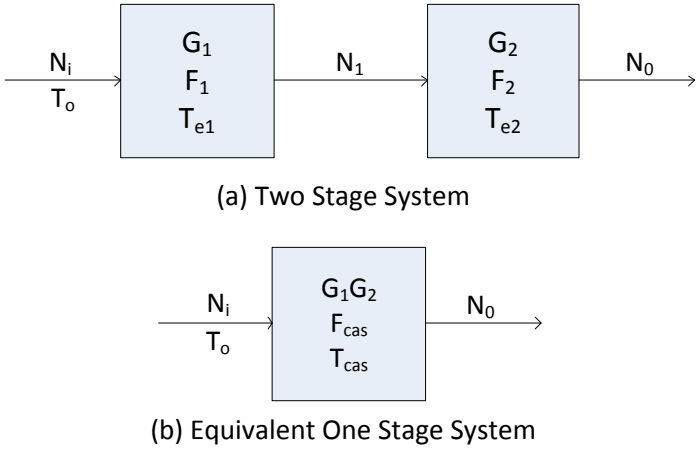


Figure 4: Noise Figure and Noise Temperature of a Cascaded System.

It will be assumed that the components have gains $G_1$ and $G_2$, noise temperatures

$T_{e1}$ and $T_{e2}$, and noise figures $F_1$ and $F_2$, and that the input noise powers are $N_i$ and $N_1$, as shown in Figure 4 above. Using (II.14), and assuming $N_i$ is equal to the antenna temperature $T_A$, the noise power output from the first stage is shown in (II.16) and the noise power output from the second stage is shown in (II.17).

$$N_1 = G_1 k T_A B + G_1 k T_{e1} B \tag{II.16}$$

$$N_o = G_2 N_1 + G_2 k T_{e2} B = G_1 G_2 k B \left( T_A + T_{e1} + \frac{1}{G_1} T_{e2} \right) \tag{II.17}$$

From this, the equivalent noise temperature of the two-stage cascaded system we see that $T_{cas}$ as shown in (II.18) and $F_{cas}$ is the equivalent noise figure, as shown in (II.19). The noise temperature and noise figure of a device or cascaded system are different ways of expressing the same thing. The relationship between noise temperature and noise figure is given in (II.14).

$$T_{cas} = T_{e1} + \frac{1}{G_1} T_{e2} \tag{II.18}$$

$$F_{cas} = F_{e1} + \frac{1}{G_1} (F_2 - 1) \tag{II.19}$$

Using the simplification in (II.18), (II.17) can be reduced to (II.20).

$$N_o = G_1 G_2 k B (T_A + T_{cas}) \tag{II.20}$$

These relationships can be extended to an arbitrary number of cascaded elements as in (II.21) and (II.22). From these it is shown that the most important contribution to the noise of a multi-component system is the noise of the stages up to the first gain-bearing element (Pozar, 2012). To achieve good cascaded noise performance, the stages up to the first gain-bearing element need to have a low noise figure. If they have a gain higher than about ten, this will substantially

mitigate the effects of the noise performance of the components later in the cascade. If the first stage has less than unity gain, not only will it add noise, but it will increase the effects of noise in the stages that follow.

$$T_{cas} = T_{e1} + \frac{1}{G_1} T_{e2} + \frac{1}{G_1 G_2} T_{e3} + \cdots \quad \text{(II.21)}$$

$$F_{cas} = F_{e1} + \frac{1}{G_1}(F_2 - 1) + \frac{1}{G_1 G_2}(F_3 - 1) + \cdots \quad \text{(II.22)}$$

### 2.2.3 Calibration

To determine the antenna temperature from a measured output voltage of a receiver, the radiometer must be calibrated. Calibration usually involves using the radiometer to measure two blackbody emitters, or loads, each at a known temperature. These temperatures are typically referred to as $T_{hot}$ and $T_{cold}$. In this thesis the hot load was a microwave absorber at ambient temperature ≈ 300 K, and the cold load was a microwave absorber cooled with liquid nitrogen, $LN_2$, at ≈ 77 K. The output voltages of the square law detector at the back-end of the radiometer receiver are related to the known measured brightness temperatures. Assuming linearity of the receiver, a linear fit is used between the two points as shown in Figure 5. A Y-factor measurement can be used to determine the noise temperature of a radiometer receiver, as shown in the negative x-intercept in Figure 5 (Pozar, 2012). For a linear receiver, $T_a$ can be determined from

$$T_a = c(v - V_o) \quad \text{(II.23)}$$

where $V_o$ is the offset voltage due to the receiver noise temperature (Janssen, 1993). The radiometer calibration constant, *c,* can then be determined as

$$c = \frac{(T_{hot} - T_{cold})}{(V_{hot} - V_{cold})} \tag{II.24}$$

where $V_{hot}$ and $V_{cold}$ are the measured output voltages corresponding to the $T_{hot}$ and $T_{cold}$ loads, respectively.

This calibration can be performed with any two emitters of known temperature and emissivity. However, as the difference in temperature between the two targets decreases, the accuracy of the calibration in turn worsens. Since the two points are used to determine the slope of the calibration curve, *c*, errors in the derived calibration constant increase as the two points become closer together. If the two points are close together, a small error in one of the values can translate into a large error in the slope.

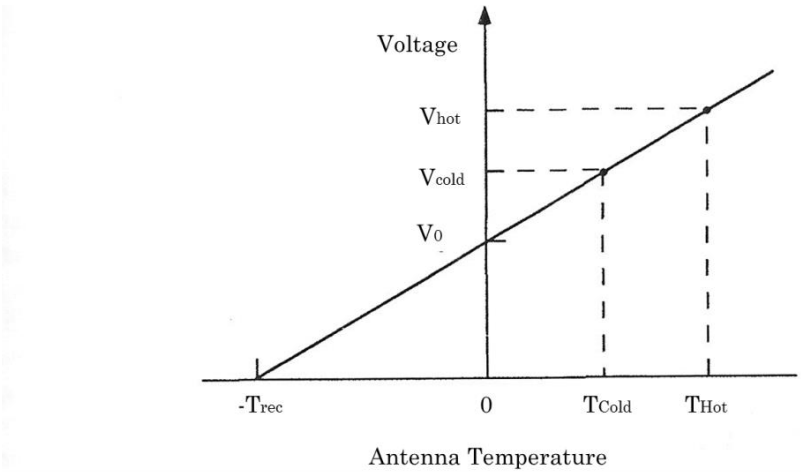


Figure 5: Illustrated Two-Point Calibration of Antenna Temperature Using a Hot and Cold Load. The Calibration Coefficient, *c*, is Given by the Slope (Janssen, 1993).

### 2.2.4 Allan Variance and Stability

Allan variance is intended to estimate the stability of a system due to noise processes as defined in (D. Allan, 1997).

To illustrate this, imagine a set of N radiometer measurements, $x_n$, $x_{n+1}$, and $x_{n+2}$ … $x_N$ taken at the interval $\tau$ while the system is looking at a stable reference input. Ideally, the measurements would have a difference of zero as the scene is emitting a constant power. However, the difference between two measurements will never be zero as non-idealities such as gain fluctuations, and Gaussian and non-Gaussian noise in the system will influence the output voltage of the receiver. To characterize this, the difference between measurements, defined as $y_n$, is calculated as in (II.25) and is averaged with respect to the measurement interval or integration time $\tau$

where D is the first finite difference for the $n^{th}$ interval. In equation (II.25) the two samples being compared are $x_n$ and $x_{n+1}$ so $\tau$ is equal to one.

$$y_n = \frac{(x_{n+1} - x_n)}{\tau} = \frac{(\Delta x_n)}{\tau}, \tau = 1 \tag{II.25}$$

The difference of the difference between measurements can also be calculated as in equation (II.26) where $D^2$ is the difference of the difference or the second difference.

$$\Delta y_n = (y_{n+1} - y_n) = \frac{(\Delta^2 x_n)}{\tau}, \tau = 1 \tag{II.26}$$

This difference between measurements represents the stability of the radiometer receiver. The time-dependence of this measurement fluctuation can then be determined by increasing $\tau$ and taking the difference of averaged measurements as in (II.27) and (II.28). For Allan variance measurements $\tau$ can only be increased up to the point where it averages half the samples of the data because if there are less than two samples then a difference cannot be taken.

$$X_m = \frac{(x_n + x_{n+1})}{\tau}, X_{m+1} = \frac{(x_{n+2} + x_{n+3})}{\tau}, \qquad \tau = 2 \tag{II.27}$$

$$Y_n = \frac{(X_{m+1} - X_m)}{\tau}, \tau = 2 \tag{II.28}$$

If the non-idealities were all Gaussian and of high enough frequency that an entire period is contained in $\tau$, as $\tau$ increased the measurement noise would decrease up to $\tau$ equals infinity. However, since not all non-idealities in a radiometer receiver are

Gaussian, and some occur at low frequencies, a point will be reached where an increase in $\tau$ will result in an increase in the difference between measurements. This increase is mostly due to the mean of the signal changing and not the effects of the additive noise which averaging additional signals corrects. At this point averaging the signal in time at a length $\tau$ is adding more noise to the system. The value of $\tau$ where the Allan variance begins to increase as τ is increased gives the highest resolution integration time for a radiometer. If a radiometer has an integration time higher than this τ, then the measurements will contain mean drifts causing degradation in the radiometric resolution.

The resulting equation to evaluate Allan variation is given in equation (II.29) where $x$ is the individual measurements and each value of $y$ in a set has been averaged over an interval $\tau$ and are taken in adjacent series.

$$\sigma_y^2(\tau) = \frac{1}{2\tau^2}\langle(\Delta^2 x)^2\rangle = \frac{1}{2}\langle(\Delta y)^2\rangle \tag{II.29}$$

Allan deviation can also be used, which is the Allan standard deviation of the signal and is equal to the square root of the Allan variance defined as in equation (II.30).

$$\sqrt{\sigma_y^2(\tau)} = \sigma_y(\tau) = \frac{1}{\sqrt{2}\tau}\langle\Delta^2 x\rangle = \frac{1}{\sqrt{2}}\langle\Delta y\rangle \tag{II.30}$$

A common way of evaluating performance when using Allan variance is to look at the slope of the curve with respect to τ in seconds as seen in Figure 6. Figure 6 has four sections labeled (a) through (d) that correspond to different noise types of the system. Section (a) is the starting point of the graph where the sampling period is

the shortest (minimum $\tau$). This point is the noise present in the measurement at the quickest sample time possible. Section (b) is the area of operation where averaging samples together reduces the noise in the measurement. This section has a slope of -1 when plotted on a log-log scale as the noise fluctuations in the system are occurring quickly so averaging samples will cancel out the Gaussian noise. As the noise fluctuations in the system decrease in frequency section (c) is reached. This section is where the noise fluctuations are slow enough that averaging more samples will increase the noise of the measurement. The x-axis value at the minimum here corresponds to the longest averaging time that will result in a less noisy measurement and the y-axis value at the minimum here gives the minimum variance of the signal at the optimum $\tau$. Section (d) is where the noise begins to increase due to longer averaging. This is often due to low frequency noise such as random walk noise, that when averaged over a small time period is generally quite low. However, when averaged over a long period of time the random walk noise can become quite large numerically thus increasing the noise of the measurement. Random walk noise is usually the sum of multiple factors such as temperature effects, vibrational noise.

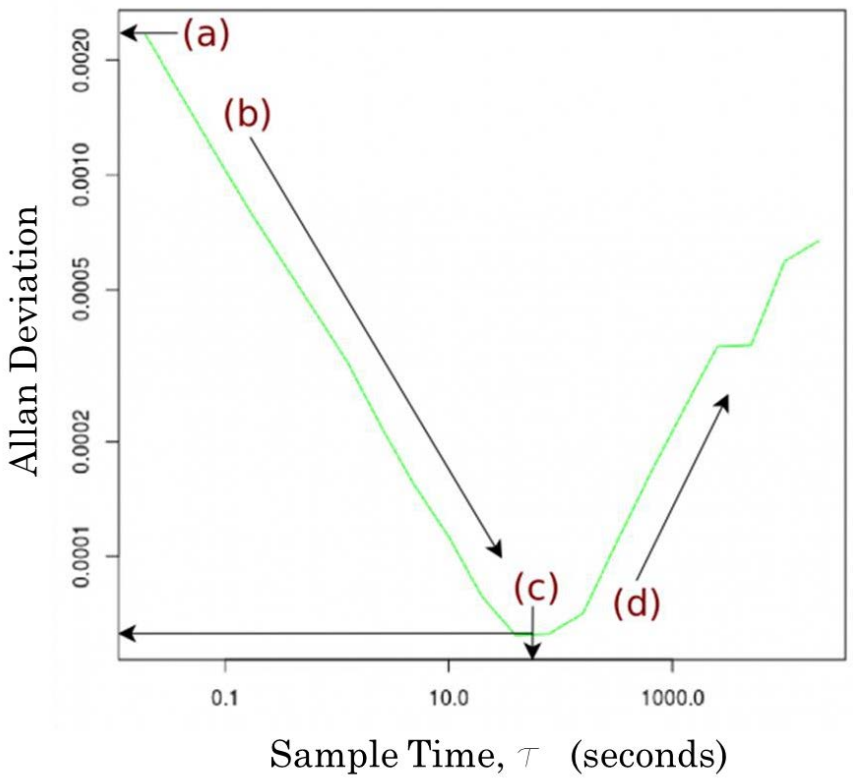


Figure 6: Illustration of the Four Important Sections of an Allan Deviation Plot

Each type of noise has a slope associated with it in an Allan standard deviation plot. White noise or Gaussian noise has a slope of -1/2 and is expected to be caused by additive noise in amplifiers and transistors respectively, this type of noise will dominate at short integration times. Flicker frequency noise, also referred to 1/f noise, has a slope of 0 and is generated in the active amplifying, detecting, and temperature sensing components of the radiometer. Random-walk noise has a slope of +1/2. This noise is often attributed to random short-term changes in temperature of the microwave circuit losses and in amplifier gains that are not fully corrected for in the radiometer system (D V Land, 2007). Both flicker frequency and random walk of frequency noise are associated with long term drifts and their affects can be

reduced by calibrating the instrument in time intervals shorter than the time scale of the drifts (Wiedner, 2002). An example of this is a Dicke switching radiometer. Since the Allan standard deviation is the square root of the Allan variance, the slopes previously presented are all multiplied by two when analyzing Allan variance on a log-log scale.

For the Allan deviation stability analysis of the microwave and mm-wave window radiometers in Sections 5.3.2 and 6.4.2 the slope of the line and the corresponding integration times when the slope changes are primarily used.

## 2.3 Total Power Radiometers

Total power radiometers (TPR) use a square law detector that provides a linear relationship between the output voltage of the receiver and the input brightness temperature of the antenna. The block diagram in Figure 7 shows a typical total power radiometer in a super-heterodyne configuration. The pre-detection section consists of a RF low noise amplifier (LNA), local oscillator (LO) and mixer used for down-conversion, to the intermediate-frequency (IF) stage.

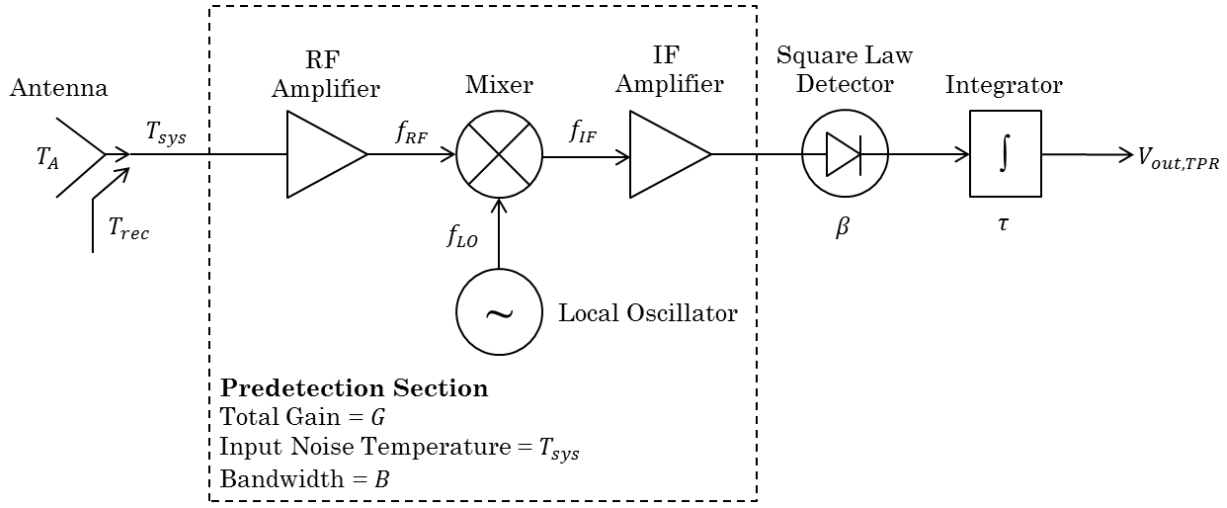


Figure 7: Block Diagram of a Total Power Radiometer (Hadel, 2014).

The antenna views a scene with brightness temperature $T_B$ and measures its radiated power as described in (II.8). This brightness temperature is commonly modeled as a noise temperature input to the system from the antenna and will be referred to as $T_A$. The receiver also introduces noise, $T_{rec}$, into the system as discussed in 2.2. The summation of these two noise sources is labeled as $T_{sys}$ and is shown as the input to the system in Figure 7.

The pre-detection section serves the purpose of amplifying the RF signal centered at $f_{RF}$ with a bandwidth, $B$, to a higher power level. The signal is then down converted to an IF centered at $f_{IF}$ through the use of a mixer and a local oscillator at $f_{LO}$. The signal is again amplified and detected using a square law detector. The square law detector is the preferred method for detection because it results in an output voltage that is linearly proportional to the input power and hence the input temperature (Skou & Le Vine, 2006). The output voltage of the signal can then be expressed as

$$V_{out,TPR} = kBG\beta T_{sys} \tag{II.31}$$

where $B$ is bandwidth of the system in Hz, $G$ is the overall gain of the radiometer, and $\beta$ is the detector sensitivity in V/W.

The output voltage from equation (II.31) is then averaged in time using an integrator, with an integration time of τ to reduce the effects of high frequency noise fluctuations, f>1/τ. In an ideal system, the longer the integration takes place the smoother the output voltage.

A very important metric for determining the performance of a radiometer is a quantity defined as radiometric resolution or $\Delta T_{min}$ (Randa, et al., Aug. 2008). This quantity defines the smallest change in input brightness temperature that can be detected by a change in output voltage (Randa, et al., Aug. 2008). The equation for the radiometric resolution of a TPR is mainly determined by $T_{sys}$, the bandwidth and the integration time as shown in (II.32)

$$\Delta T_{min} = \frac{T_{sys}}{\sqrt{B\tau}} \tag{II.32}$$

Equations (II.31) and (II.32) have been developed for an ideal radiometer where an increase in τ will always result in decrease in $\Delta T_{min}$. This is not the truth in practice as receiver gain changes can be mistakenly identified as changes in input power if the gain fluctuations as shown in (II.33) are sufficiently high. This is also shown in Figure 6 where after region (b) an increase in τ results in an increase in the Allan variance. Where depending on the gain fluctuations, $\Delta G$, the output voltage can differ while $T_{sys}$, and thus $T_A$ remain constant.

$$V_{out,TPR} = kBG\beta T_{sys} + kB\Delta G\beta T_{sys} \tag{II.33}$$

Taking gain fluctuations into account the radiometric resolution for a realizable TPR can be redefined as

$$\Delta T_{TPR} = T_{sys}\sqrt{\frac{1}{B\tau} + \left(\frac{\Delta G}{G}\right)^2} \tag{II.34}$$

Gain fluctuations are often the limiting factor in achieving high radiometric resolution. To compensate for the loss in radiometric resolution due to gain fluctuations another architecture for radiometers will be discussed in the next section.

## 2.4 Dicke Switched Radiometers

Dicke radiometers do not directly measure antenna temperature but instead measure the difference between the antenna temperature and a known reference temperature. This greatly reduces the sensitivity of the instrument to gain and noise temperature instabilities (Skou & Le Vine, 2006). The topology for this type of radiometer is shown in Figure 8.

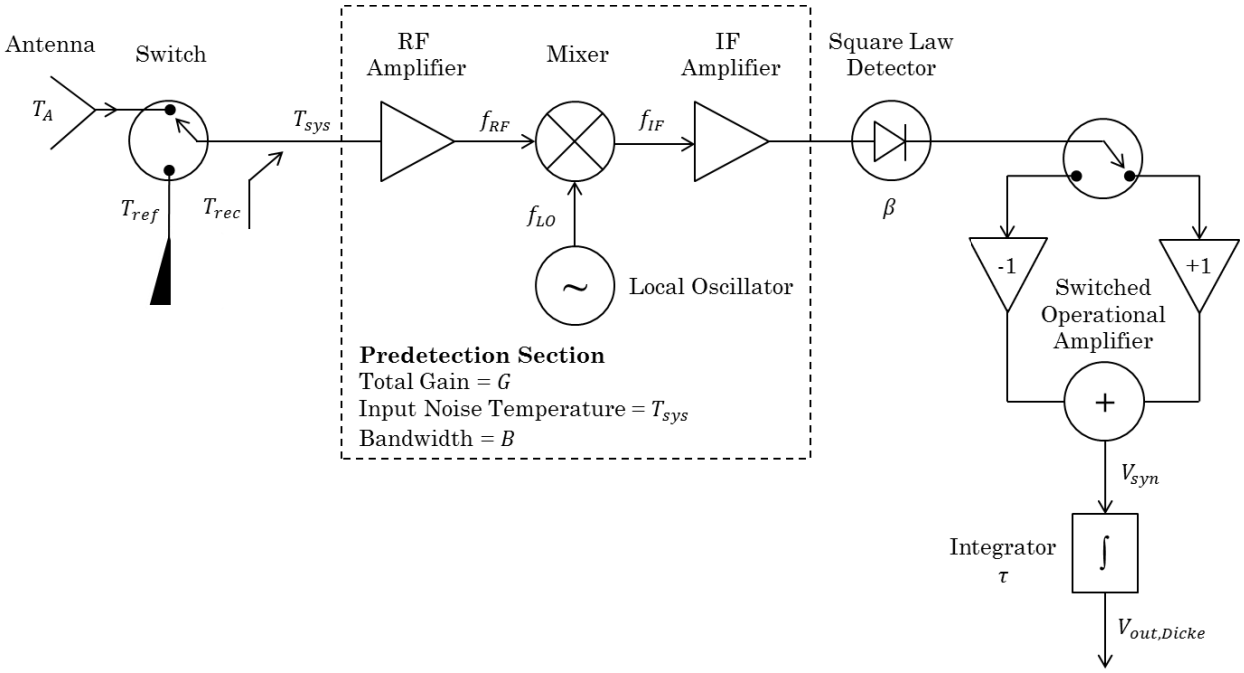


Figure 8: Topology of a Dicke Switched Radiometer (Hadel, 2014)

This is accomplished by using a switch at the input of the receiver that alternates between the antenna and the known reference load, $T_{ref}$. An amplifier that alternates between unity and inverting unity gain is also inserted between the detector and the integrator. By using the unity gain amplifier as both an inverting amplifier and a non-inverting amplifier the noise temperature while looking at the reference can be subtracted from the noise temperature while looking at the antenna cancelling out any gain or system temperature fluctuations. Modern Dicke radiometers do not use a unity gain amplifier but instead accomplish the subtraction of the two signals digitally. Equation (II.35) shows the output voltage of the integrator assuming the switch views the antenna and the reference for equal amounts of time per integration.

$$V_{out,Dicke} = kBG\beta\left(T_A - T_{ref}\right) + kB\Delta G\beta\left(T_A - T_{ref}\right) \tag{II.35}$$

The Dicke switch must be operated at a frequency where $T_A$, $T_{sys}$, and $G$ remain constant (Skou & Le Vine, 2006). The minimum switching frequency can be determined using an Allan variance plot where the maximum amount of time spent looking at each leg is equal to the half of the largest integration time, $\tau$, where the slope of the Allan variance on a log-log plot is equal to -1. Looking at the antenna for only half of the measurement cycle decreases noise from gain fluctuations but increases uncertainty due to viewing the scene for less time. This results in a decrease in ideal radiometric resolution as demonstrated by (II.36) which gives the radiometric resolution for a Dicke radiometer. The factor of two in the numerator of the first term reflects the fact that the radiometer will only be viewing the measured scene for half of the time.

$$\Delta T_{Dicke} = \left[\frac{2(T_A + T_{Rec})^2 + 2\left(T_{Ref} + T_{Rec}\right)^2}{B\tau} + \left(\frac{\Delta G}{G}\right)^2 \left(T_A - T_{Ref}\right)^2\right]^{1/2} \tag{II.36}$$

The radiometer is considered balanced if $T_A$ is equal to $T_{Ref}$. Most Dicke radiometers that are built attempt to be balanced because as $T_{Ref}$ approaches $T_A$ the radiometric resolution improves, moving toward that of a TPR. If the radiometer is assumed to be balanced then the second term in (II.36) becomes zero allowing us to simplify (II.36) to

$$\Delta T_{Dicke} = \left[\frac{2(T_A + T_{Rec})^2 + 2\left(T_{Ref} + T_{Rec}\right)^2}{B\tau}\right]^{1/2} \tag{II.37}$$

continuing with the assumption that $T_A$ is equal to $T_{Ref}$, $T_{Ref}$ can be replaced in (II.37) with $T_A$ simplifying to

$$\Delta T_{Dicke} = 2 * \left[\frac{(T_A + T_{Rec})}{\sqrt{B\tau}}\right] = 2 * \frac{T_{sys}}{\sqrt{B\tau}} \quad \text{(II.38)}$$

which is exactly double the radiometric resolution of a TPR shown in (II.32).

## 2.5 Direct Detection Radiometers

Direct Detection Radiometers can be in a Dicke or TPR configuration but they do not down convert the RF signal to an IF signal for detection. Meaning the radiometer is no longer operating as a super-heterodyne receiver and all phase information is lost. This allows the radiometer to function without a mixer or LO source thus reducing power consumption, size, and the number of system components. If direct detection is to be used the detector diode must operate at the RF frequency of interest, but if this can be accomplished, the impact of the mixer gain on system temperature can be eliminated. Eliminating the mixer can often reduce system temperature as shown by the cascade noise figure presented in 2.2.2.

## 2.6 Radiometric Applications

The past few decades have brought advancements in microwave radiometry and have driven the way for more applications in fields such as oceanography, geophysics, electrical engineering, and atmospheric sciences [2]. Specifically in the field of atmospheric sciences, radiometers have been developed, through collaboration with the Microwave Systems Laboratory (MSL) at Colorado State University (CSU) and the Jet Propulsion Laboratory (JPL) at California Institute of Technology (CalTech), to measure vertical water vapor profiles of the Earth's atmosphere. Previous methods of gathering these profiles have relied on sensors

that operate at visible and infrared wavelengths. The problem with operating at these frequencies is that they cannot penetrate clouds which pose serious problems for accurate weather prediction. Utilizing microwave radiometers gives the advantage of nearly all-weather operation which will shed a great deal of light on weather forecasting, ocean circulation, and phenomena such as hurricanes.

# Chapter III. HAMMR Instrument

This chapter will provide an overview of the HAMMR system and the components used in the system. Additionally, discussions on the design, fabrication, and verification of the HAMMR chassis, the reflectors, and the antenna alignment system are presented.

## 3.1 System Overview

This section presents a brief overview of the HAMMR system, explaining the functionality of the system and basic operating parameters. The sub-systems will be discussed in more detail in later sections. A block diagram of the HAMMR system is shown in Figure 9 including a graphical representation of the optical system.

Radiation from the atmosphere enters HAMMR through an aperture cut into the bottom of the chassis represented in Figure 9 as a hole in the bottom of the diagram. This radiation is reflected off of the scanning flat reflector into an offset paraboloid that focuses the radiation into the three feed horns antennas located at the offset paraboloid's focal plane. The three antennas feed the three radiometer sub-systems used in HAMMR. These radiometer sub-systems include 6 microwave channels at 18.7, 23.8 and 34 GHz with two polarizations for each frequency, 3 millimeter wave window channels at 90, 130, and 168 GHz, and two sounding radiometers with 8 channels each, adjacent to 118 and 183 GHz.

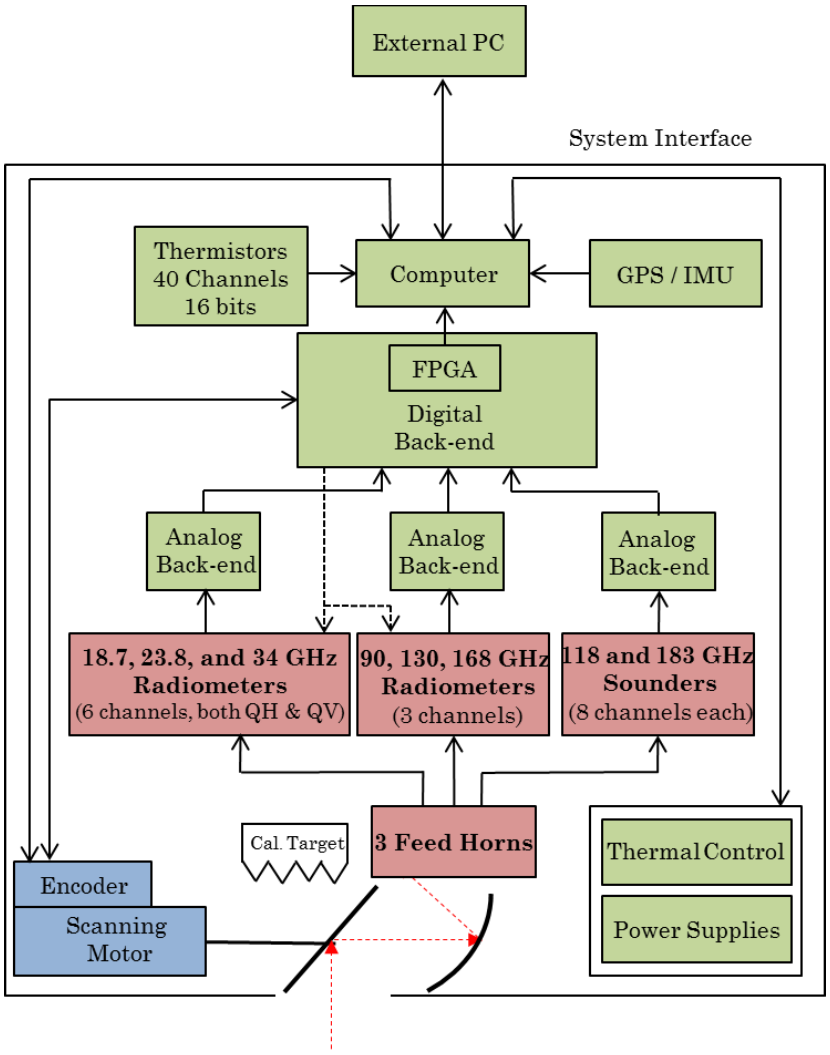


Figure 9: HAMMR System Block Diagram (Reising S. C., et al., 2013).

The output of these radiometers is fed into an Analog Backend Board (ABEB) which performs integration and digitizes the signals for use in the field programmable gate array (FPGA) which then sends the signals to the onboard computer for storage. These sub-systems will be discussed in more detail in section 3.5.

## 3.2 Initial Design

The design for HAMMR was done in stages with the antenna and reflector design coming first and the chassis being designed second. Once the chassis was complete the reflector design was modified and sub-systems were integrated into it as they were chosen or designed. This section covers the initial design of the chassis, offset paraboloid, flat reflector, and motor mount.

### 3.2.1 Chassis

The chassis was designed in Solidworks around initial antenna and reflector geometries provided by Dr. Behrouz Khayatian of JPL shown in Figure 10.

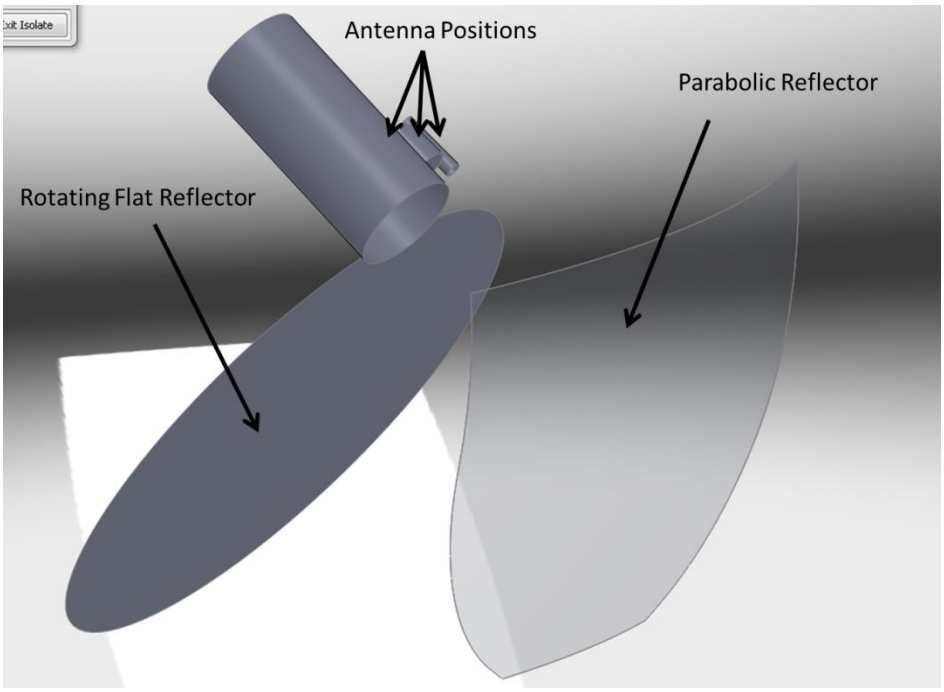


Figure 10: Initial Reflector and Antenna Geometries

The main considerations in the design of the chassis include ensuring that the alignment between reflectors and antennas remains correct, adhering to Federal

Aviation Administration (FAA) requirements for crash loads in the Twin Otter aircraft, making the chassis stiff enough to withstand twisting forces, and minimizing weight and volume without compromising ease of access and maintenance.

The initial design for the HAMMR chassis is shown in Figure 11 with the main sub-systems labeled.

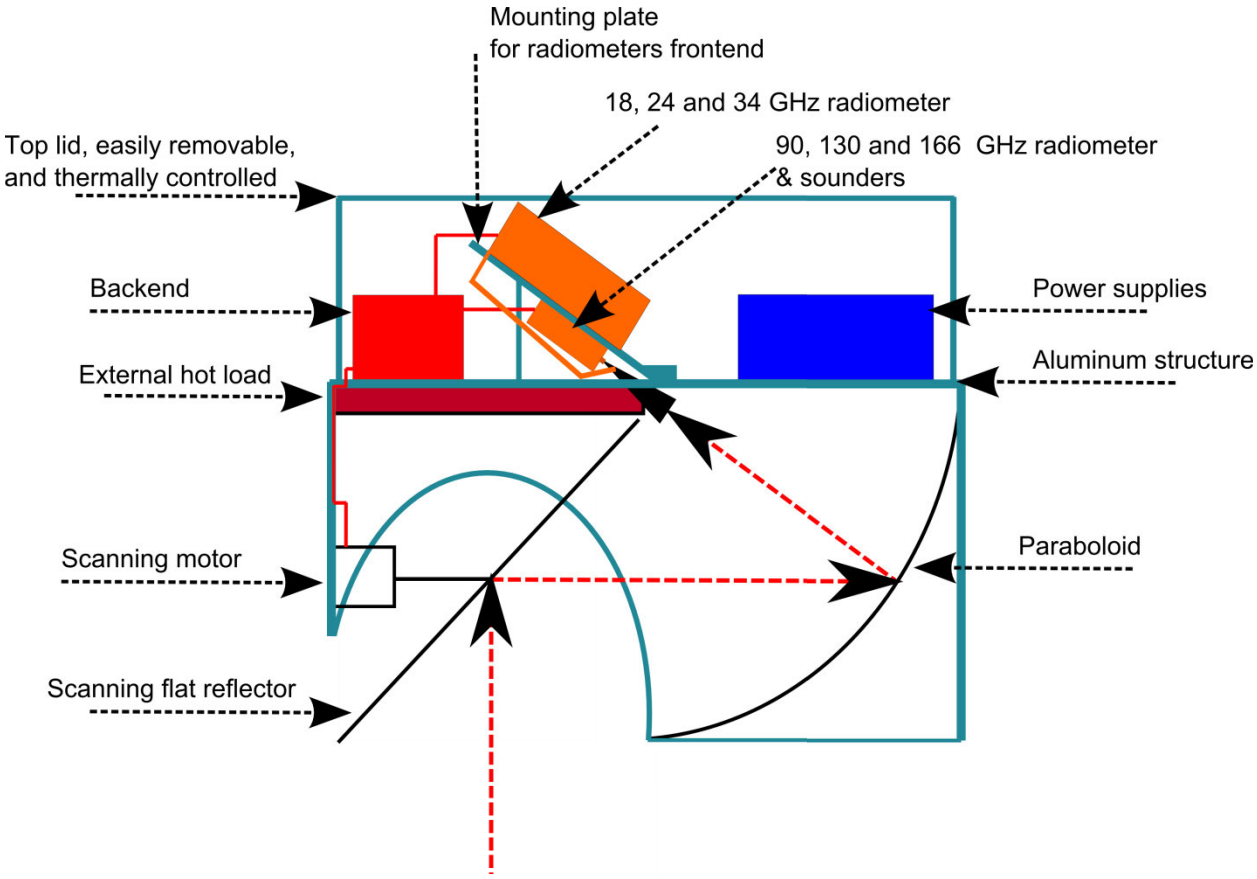


Figure 11: Lateral View of Initial HAMMR Chassis Design.

As the design progressed, certain aspects of the chassis were modified. The bottom was extended to be equal lengths on both sides of the aperture, a middle deck was created to house the power supplies, the alignment for the feed horn horn array was

modified, and mounting points for the paraboloid were designed. These changes were collaboratively designed between CSU and JPL to specify the general chassis layout. The result was the design shown in Figure 12 which was given to ATK Spacecraft Systems and Services (ATK) for the finishing touches. The motor mount, flat reflector, and paraboloid were all designed and fabricated by the National Center for Atmospheric Research (NCAR)'s Earth Observing Laboratory (EOL)'s Design and Fabrication Services (DFS) with input from CSU. The design, fabrication, and integration of these parts will be discussed in detail in proceeding sections.

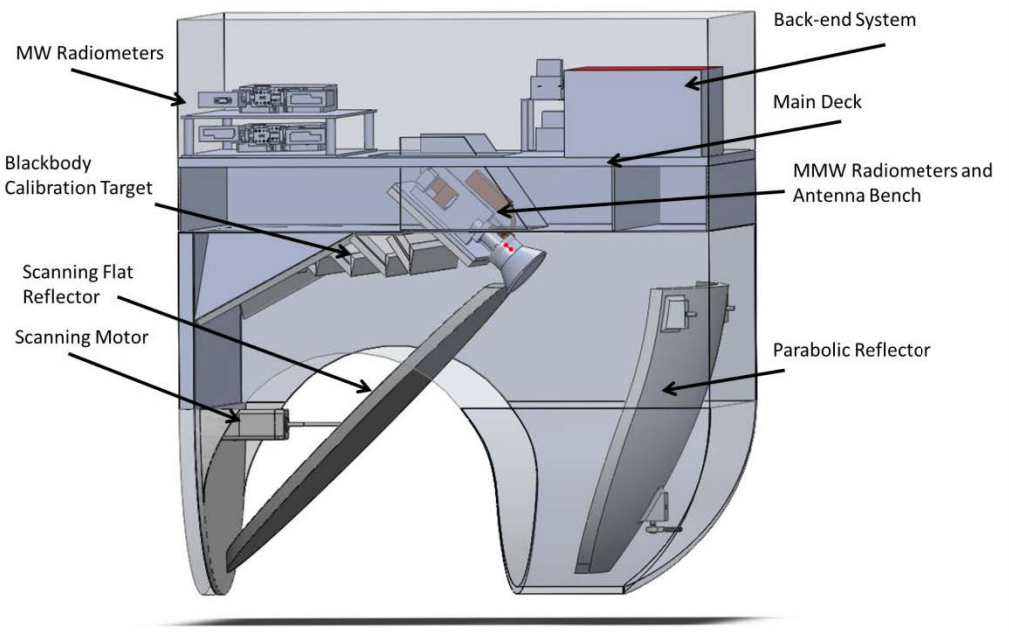


Figure 12: Envelope Design of Chassis Sent To ATK.

ATK, with the input of JPL and CSU, finalized the design adding mounting points, hardware, and stiffening structures as well as choosing material and specifying bend radii for the sheet metal. The design from ATK is shown in Figure 13

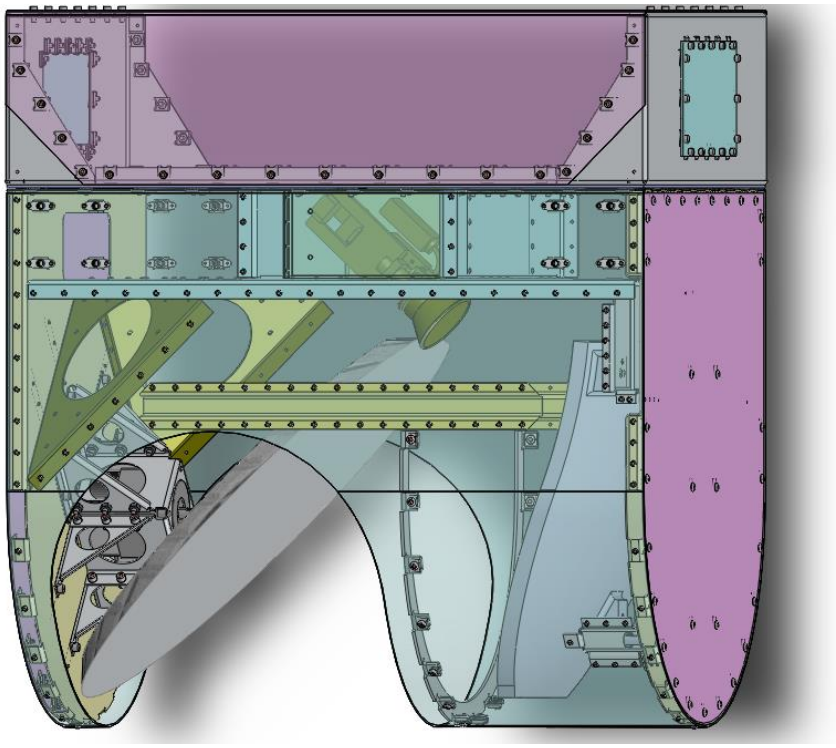

Figure 13: ATK Chassis Design

After making slight modifications to the ATK design the chassis was sent to Dynamic Design and Manufacturing, Inc. in Niwot, CO for fabrication.

### 3.2.2 Offset Paraboloid

The geometry of the offset paraboloid was designed by Dr. Dr. Behrouz Khayatian of JPL to focus the maximum amount of incident energy to the three feed horn antennas as shown in Figure 14.

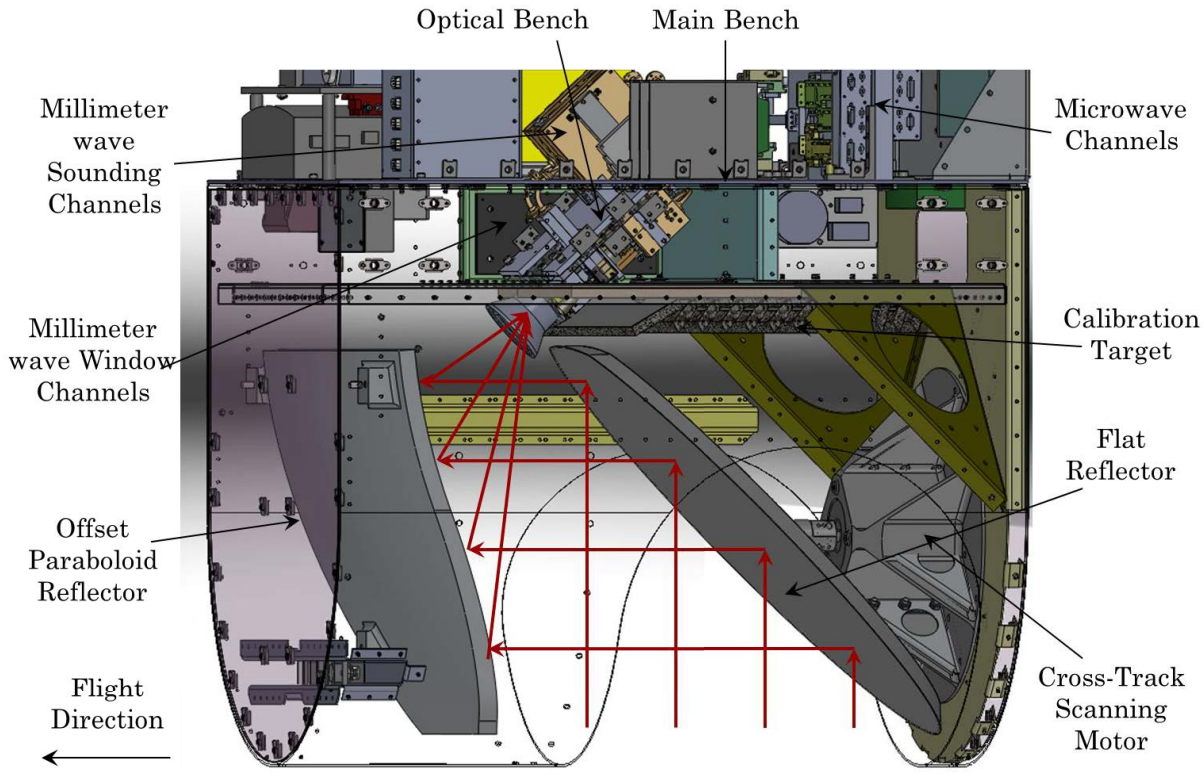


Figure 14: Illustration of Radiation Incident to HAMMR.

A paraboloid is a solid generated by the rotation of a parabola around its axis of symmetry as shown in Figure 15.

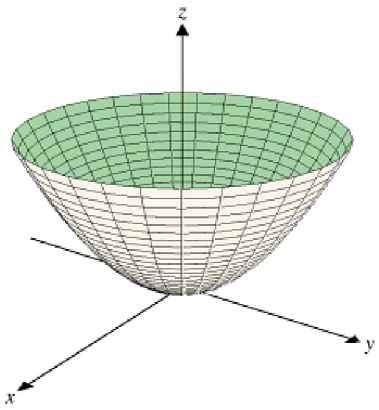


Figure 15: A Parabola Rotated About the Z-Axis to Become a Paraboloid

Paraboloids and parabolas share many of the same defining parameters making the geometry of a paraboloid most easily understood by understanding that of a parabola. Figure 16 illustrates the geometry of a parabola with the diameter equal to $D$, the focal length equal to $F$, the vertical height equal to $H$, and the maximum angle between focal point and the edge of the dish equal to $\theta_o$. The parabola can be described mathematically as in (II.32) and the fundamental parameters can then be related to each other as in (III.2) and (III.3).

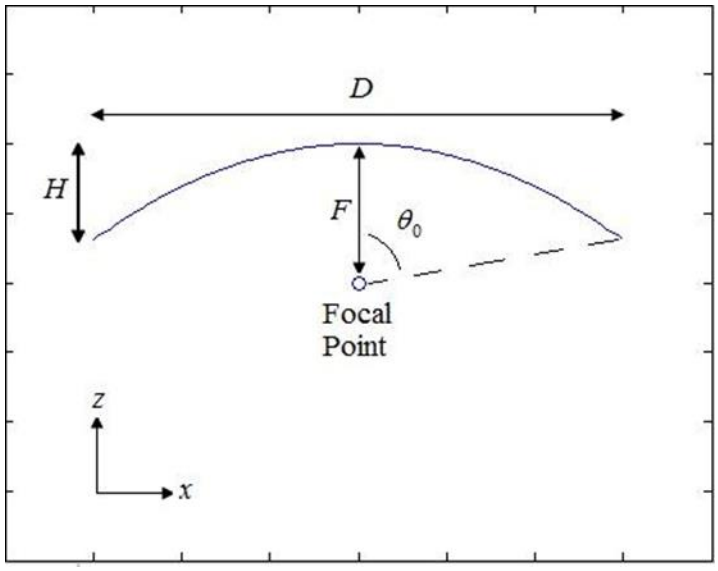


Figure 16: Geometry of a Parabola

$$x^2 = 4F(F - z), |x| \leq \frac{D}{2} \quad \text{(III.1)}$$

$$\frac{F}{D} = \frac{1}{4 * \tan(\frac{\theta_0}{2})} \quad \text{(III.2)}$$

$$F = \frac{D^2}{16H} \quad \text{(III.3)}$$

Because the paraboloid is much bigger than the wavelengths of interest for our system, geometric optics can be used to analyze the parabolic reflector. Figure 17 shows this analysis with two rays being transmitted from the focal point arriving at two separate angles on the reflectors surface.

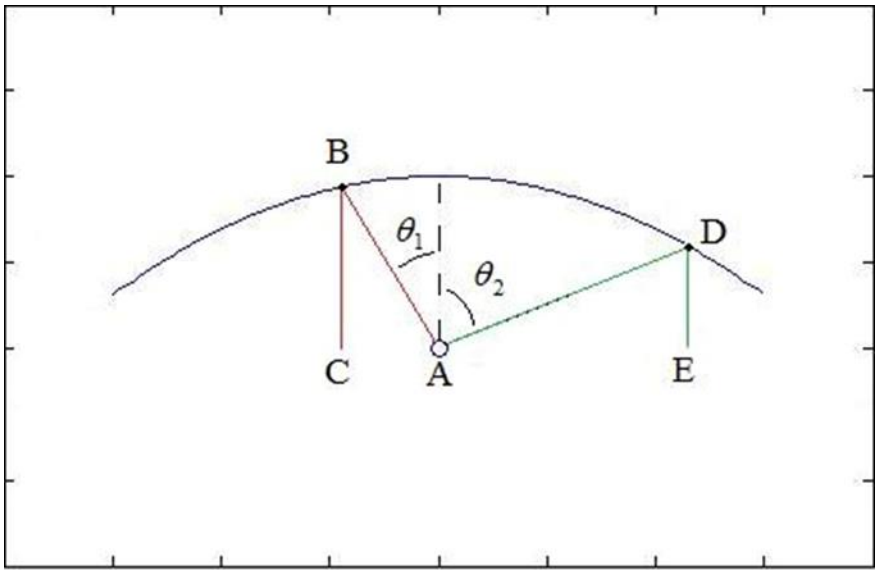


Figure 17: Geometric Optic Analysis of a Parabolic Reflector

Figure 17 illustrates two important facts about parabolic reflectors. The first is that all rays emanating from the focal point will be reflected in the same direction. The second is that the distance each ray travels from the focal point to the reflector to the focal plane of the parabola is constant. This can be proven with geometry and is not shown in this thesis. It can then be concluded that any radiation emitted from the focal point will reach the focal plane travelling in the same direction with the same phase. This conclusion is also valid for radiation emitted from the focal plane and reflected to the focal point making a parabola an ideal shape to focus radiation into an antenna.

To convert this concept to a 3-D space the parabola must be rotated about its axis of symmetry to form a paraboloid as shown in Figure 15.

An offset paraboloid is a section of a complete paraboloid offset from the vertex. This is useful in airborne environments because the reflector does not block the feed horns and the mass and volume of the reflector are reduced when compared to a complete paraboloid. The concept of an offset paraboloid is illustrated in Figure 18 with Q being the position of incoming rays, F being the focal point, and P being the point of reflection.

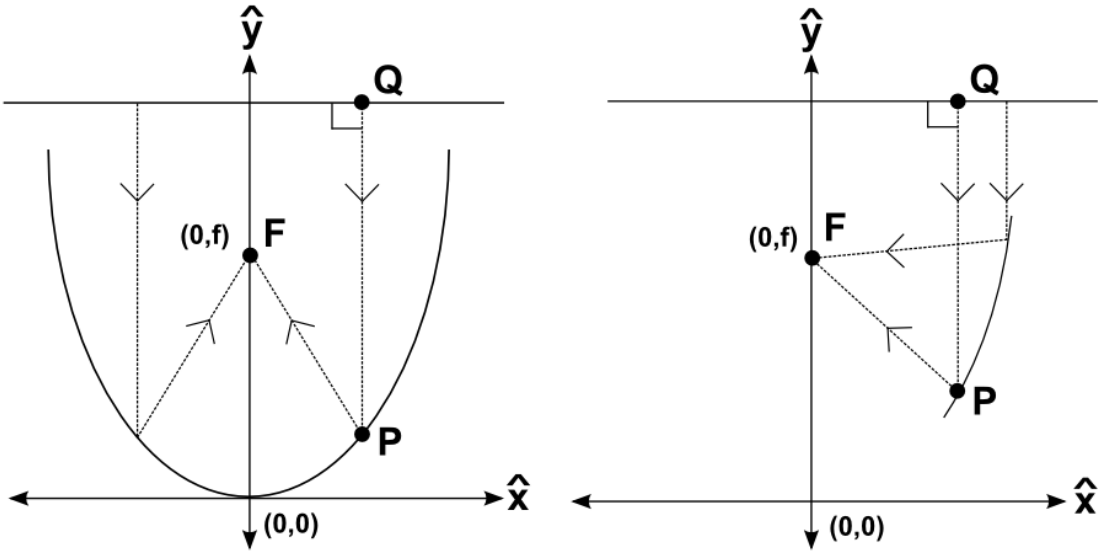


Figure 18: Geometry of Paraboloid (a) and Offset Paraboloid (b) (Nelson, Fall 2013).

Because the paraboloid must be fabricated the surface roughness of the reflector must also be specified. Surface roughness will affect the main beam efficiency defined as the ratio of the power collected from the main beam of the observed scene to the total power collected. This is a concern because when power from the scene is lost it is re-radiated and can be collected by the feed horns causing the antenna temperature to have a large component that is not from the scene. The lost power's

magnitude and direction can also be modulated by the scanning of the flat reflector further adding to the measurement uncertainty.

To define the offset paraboloids required roughness a simulation was done to determine the impact of roughness on antenna efficiency. The roughness was calculated using (III.4) from (Rahmat-Samii, 1998).

$$\eta_{Distortion} = e^{-(4\pi \mathrm{K}\frac{\sigma}{\lambda})^2} \quad \text{(III.4)}$$

Where $\frac{\sigma}{\lambda}$ denotes the surface root mean square (RMS) distortion normalized to wavelength ($\lambda$), $\mathrm{K} = 4\,F/D\,\sqrt{\log(1 + 1/(4\,F/D)^2)}$, and $F/D$ is the ratio between the focal length and the aperture diameter.

Figure 19 shows an analysis of antenna efficiency versus the offset paraboloid surface roughness for various F/D ratios.

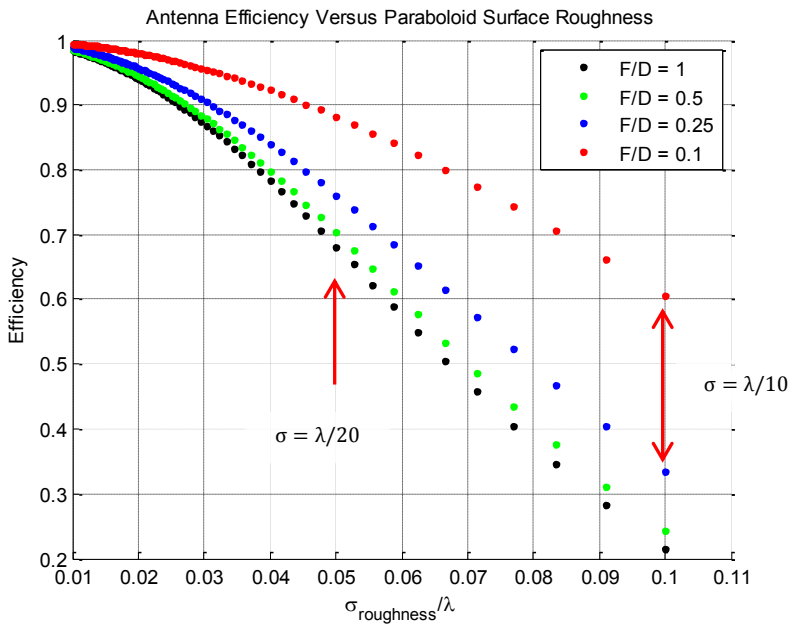


Figure 19: Surface Roughness of the Paraboloid Impact on the Antenna Overall Efficiency for Several Values of F⁄D (Nelson, Fall 2013).

Based on the analysis in Figure 19 a paraboloid with a maximum surface roughness of 0.0508 mm (0.002”) was chosen. At 180 GHz, this surface roughness corresponds to an efficiency of approximately 88%. Based on the geometry and radiation pattern analysis done by Dr. Behrouz Khayatian the following values were chosen to define the paraboloid’s geometry.

- F = 28.58 cm (11.25”)
- D = 50.8 cm (20”)
- F/D = 0.56

### 3.2.3 Flat Reflector and Motor Interface

The flat reflector is used to scan the cross-track swath beneath HAMMR, illustrated in Figure 20, and to redirect this radiation to the feed horn antennas as shown in Figure 14. This is accomplished by attaching the flat reflector to a scanning motor that rotates during flight.

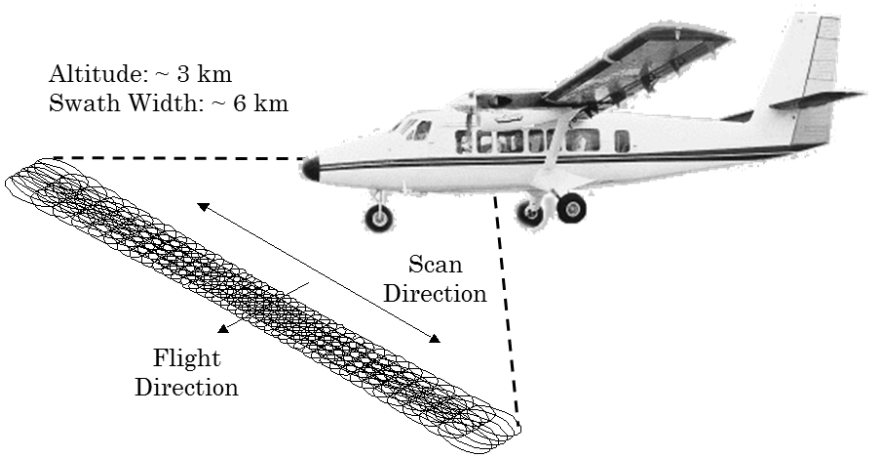


Figure 20: Illustration of Cross-track Scanning from a Twin Otter Aircraft (Reising S. C., et al., 2013).

The original flat reflector geometry was also provided by Dr. Behrouz Khayatian and was changed to its final geometry through a collaborative effort between CSU, JPL, and NCAR's EOL DFS.

Since the flat reflector is a smooth and flat surface the geometry to determine reflections is very simple and is governed by the law of reflection stating that the angle the incident ray makes with the normal is equal to the angle which the reflected ray makes to the same normal. This means that to reflect radiation

entering the aperture of HAMMR into the offset paraboloid the flat reflector must be at a 45° angle with respect to the instrument.

The initial shape provided by JPL for the flat reflector was an ellipse with a minor diameter of 50.8 cm (20”) and a major diameter of 53.85 cm (21.2”). This shape needed to be modified to prevent mechanical interference with the microwave radiometer feed horn and to reduce problems caused by spillover effects. To do this the minor diameter was reduced to 40.64 cm (16”), the major axis was increased to 57.58 cm (22.67”), and the top side of the reflector was trimmed by an arc of radius 44.45 cm (17.5”) on the major axis as seen in Figure 21.

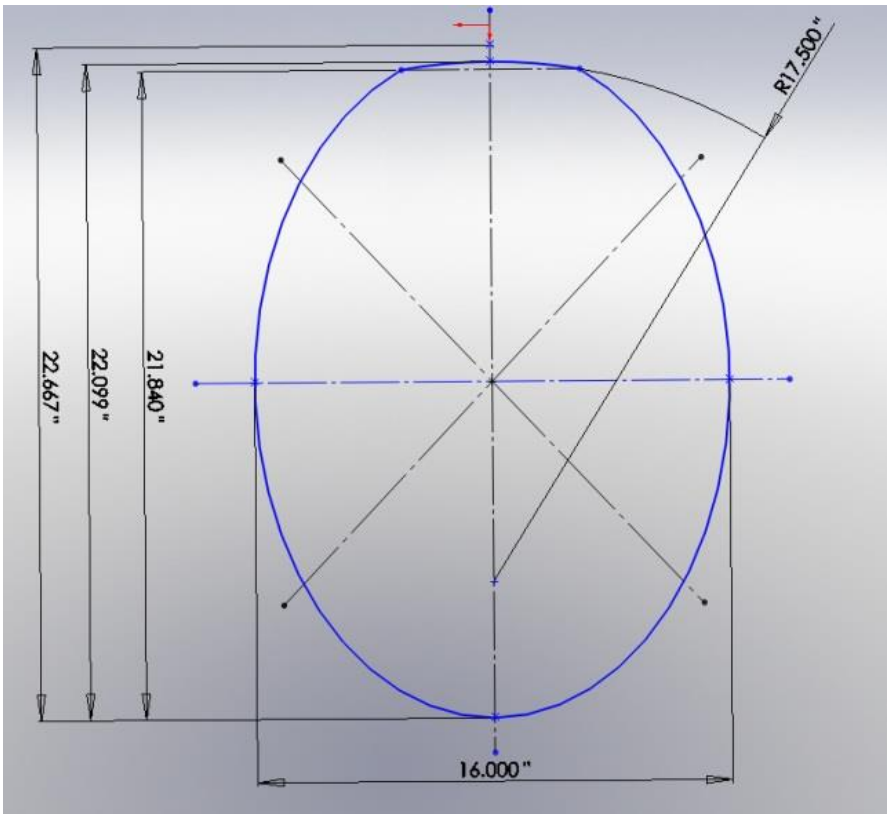


Figure 21: Final Surface Geometry of Scanning Flat Reflector.

The flat reflector must be interfaced with the motor shaft to allow the reflector to scan. This is accomplished through a shaft coupling device that secures the flat reflector to the motor shaft. This part was designed by NCAR's EOL DFS with input from CSU and JPL and will be further referred to as the scanning reflector shaft coupling. The scanning reflector shaft coupling is shown in Figure 22. Since the HAMMR chassis has an open aperture and the flat reflector sits directly above this aperture, special considerations were taken in the design of the scanning reflector shaft coupling to ensure it exceeded all FAA requirements and was resistant to vibration.

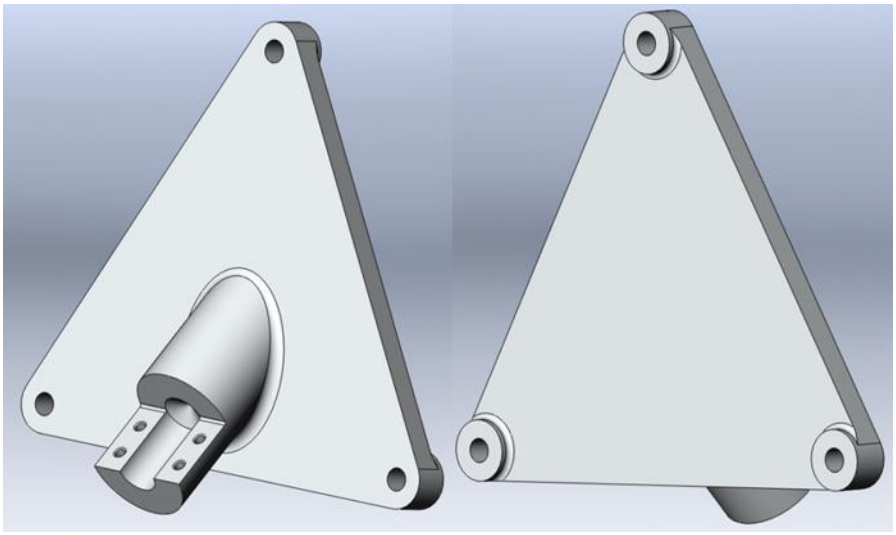

Figure 22: Flat Reflector Shaft Coupling

## 3.3 Fabrication, Integration, and Verification

Once the design of the chassis and reflectors were completed they were fabricated and integrated into the system. The integrated system was then measured and checked to ensure it had been built to specification. The following sections give an overview of this process.

### 3.3.1 Chassis

The HAMMR chassis was fabricated by Dynamic Design in Niwot, CO using 6061-T4 sheet aluminum and is shown below in Figure 23. The fabrication went well with only slight modifications from the original design files.

Figure 23: HAMMR Chassis as Fabricated by Dynamic Design

Once the completed chassis had been received it was taken to NCAR for precise measurements to characterize the fabricated geometry. The main concerns for this were the orthogonality of the walls and reflector mounting points to the main bench shown in Figure 14. If the reflector mounting points and walls were not orthogonal then reflector geometries would need to be reconsidered.

Measurements were taken on a granite table with an RMS flatness of 0.0254 mm (0.001") to ensure that any discrepancies measured were only due to the chassis. Perpendicularity measurements were done using squares and shims as shown in Figure 24 and Figure 25.

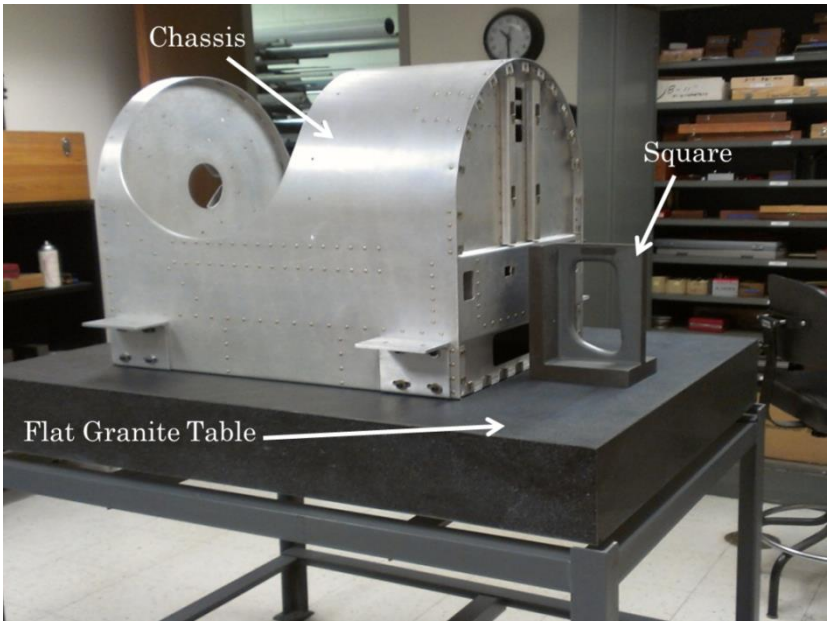


Figure 24: Setup for Characterizing HAMMR Chassis at NCAR.

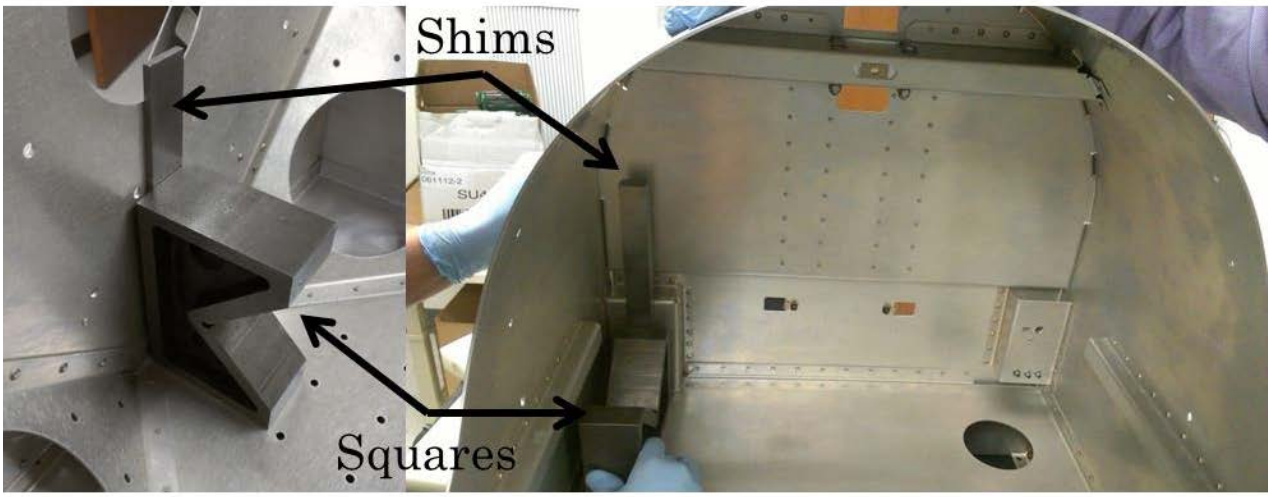


Figure 25: a) Perpendicularity Measurement of the Motor Wall, and,

b) Perpendicularity Measurement of Paraboloid Mounting Point.

The perpendicularity of the fabricated paraboloid mounting points and walls were found to be in good agreement with the 3-D model. Some small discrepancies were measured but everything was found to be within 0.1° of the specified angles.

The distance between the top to the bottom of the main bench was also measured using a depth micrometer. This is important because the top and bottom of the main bench should be parallel to each other and the feed horn antennas are interfaced with these surfaces. Examples of these measurements are shown in Figure 26.

Figure 26: Measurements of Main Deck Geometry at NCAR.

The measurements for this section had a higher deviation than was expected and is summarized in Figure 27, where all distances should be 10.54 cm (4.148”). This shows that there is a peak to valley flatness of about 2.3 mm (0.091”) across the main bench. The pocket that the feed horn antennas will interface to has a peak to valley flatness of 0.5 mm (0.020”). This discrepancy is adjusted for in the feed horn antenna interface discussed in Section 3.4.

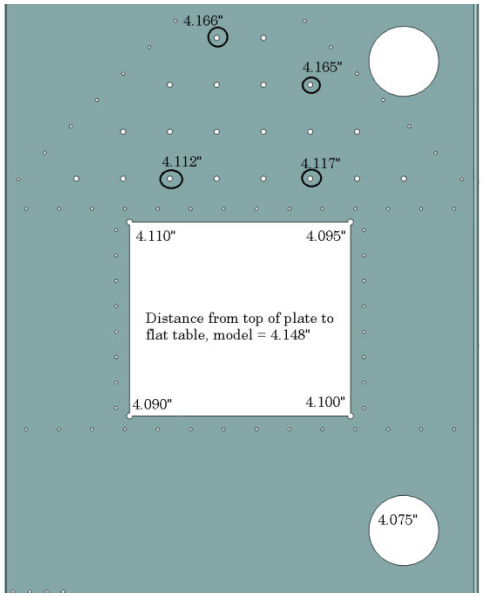


Figure 27: Result of Measurements of Main Deck.

### 3.3.2 Parabolic Reflector

The offset paraboloid was fabricated at NCAR's EOL DFS in Boulder, CO. It was machined from a single piece of 6061-T6511 aluminum and is shown in Figure 28 before being mounted in the chassis. The three interfaces between the offset paraboloid and the chassis as shown in Figure 28.

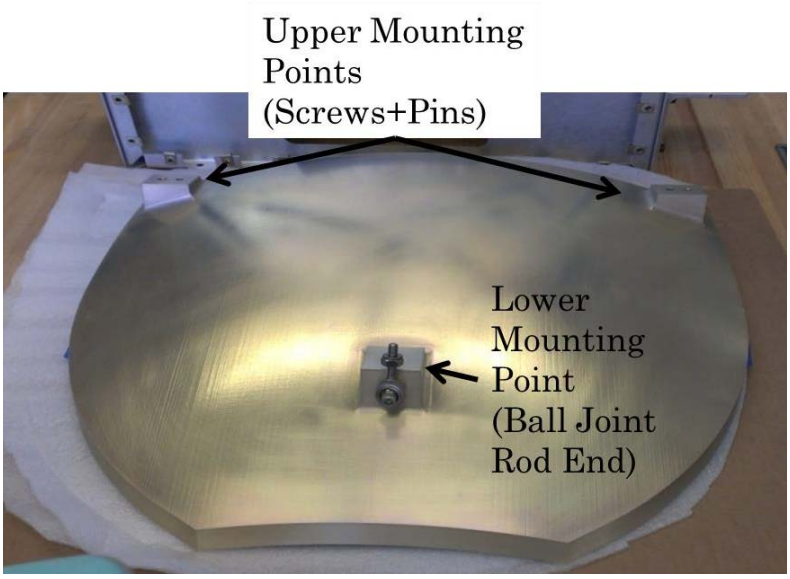


Figure 28: Fabricated Offset Paraboloid Before Chassis Integration.

The integrated offset paraboloid can be seen in Figure 29. To ensure the paraboloid was in the correct spot measurements were done using a depth micrometer between the mounting points and the chassis as shown in Figure 30. These measurements were then compared to values in the 3-D model to ensure their correctness as shown in Figure 31. The three mounting points were found to have a maximum error of 0.127 mm (0.005”).

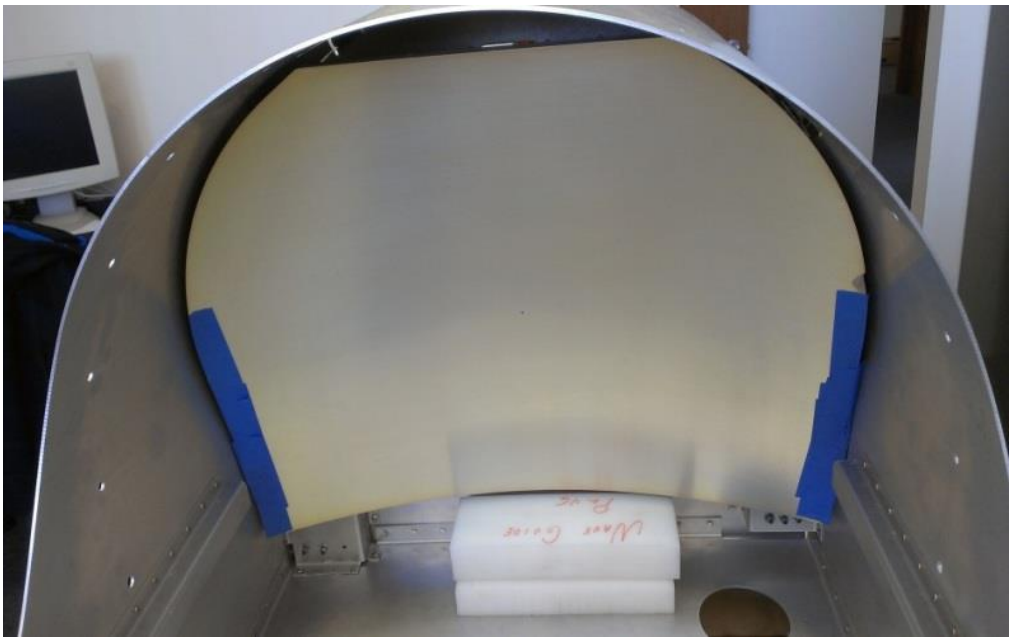

Figure 29: Offset Paraboloid Integrated in HAMMR Chassis.


Figure 30: Depth Micrometer Measurements Used to Characterize Offset of Upper Paraboloid Mounting Points.

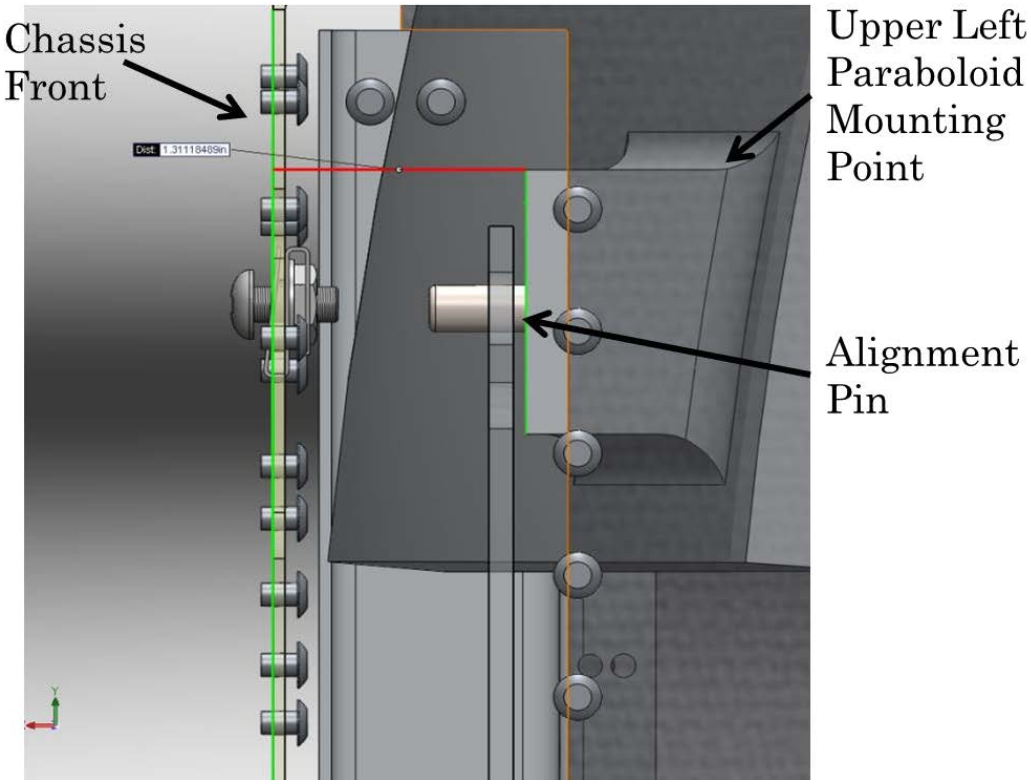


Figure 31: 3-D Model Measurements Used to Verify Paraboloid Position.

Once the position of the mounting points were verified to be correct the position of the four corners of the offset paraboloid with respect to the chassis were verified with custom machined spacers as shown in Figure 32. Figure 32 also shows each dimension that has been verified as correct denoted by green arrows.

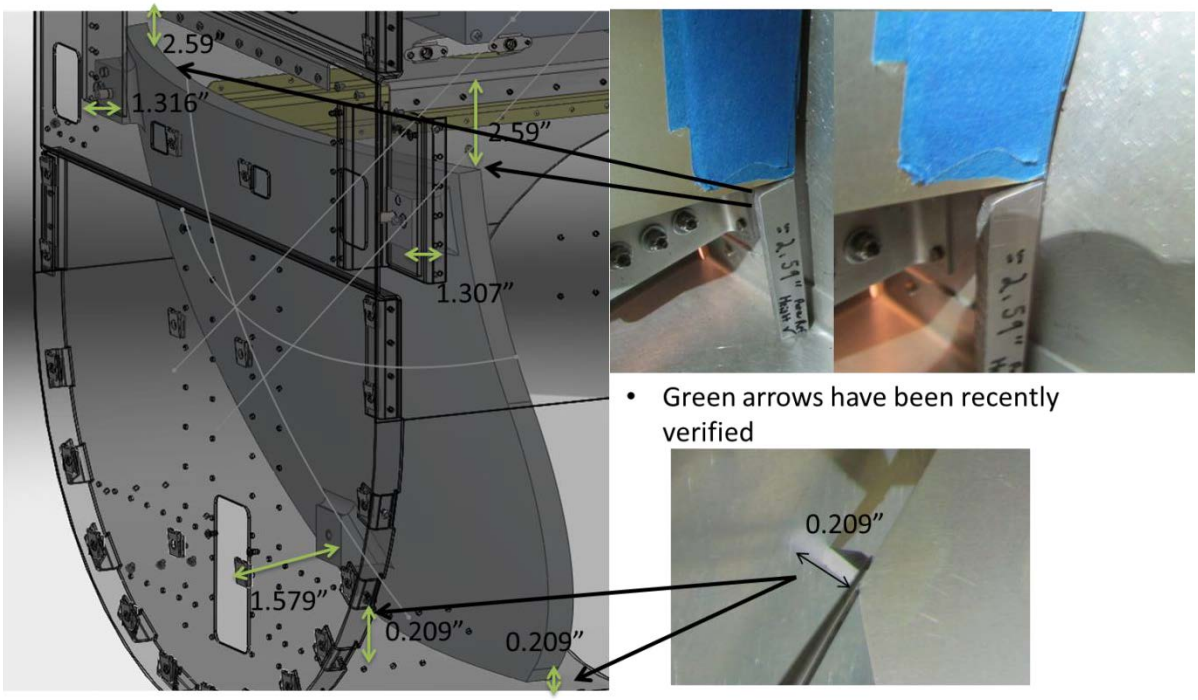


Figure 32: Example of Distance Measurements and Summary of Confirmed Distances for Offset Paraboloid.

### 3.3.3 Flat Reflector and Motor Interface

The scanning flat reflector was also fabricated at NCAR's EOL DFS in Boulder, CO and can be seen in the HAMMR chassis in Figure 33. The scanning flat reflector is made of honeycomb aluminum with polished aluminum faces attached to the front and back. The edges are filled with a green epoxy that resists moisture and thermal expansion/contraction.

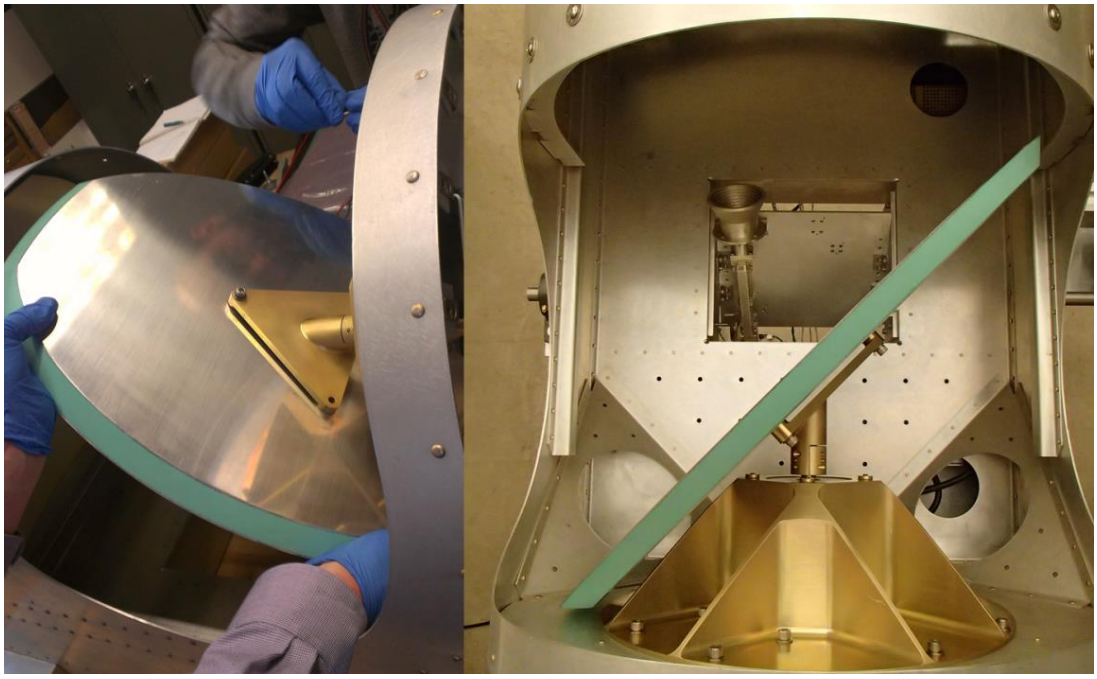

Figure 33: Scanning Flat Reflector Mounted in System

As seen in Figure 33 the scanning flat reflector is attached to the motor shaft through the scanning reflector shaft coupling. The scanning reflector shaft coupling attaches to the scanning flat reflector with three ¼-28 steel socket head cap screws that fasten into three locking helicoil inserts integrated into the flat reflector. For the final configuration these screws are then wire locked together to prevent loosening as seen in Figure 34.

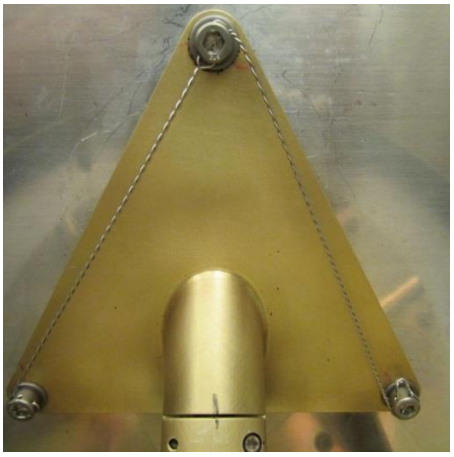

Figure 34: Wire Locked Fasteners on Scanning Flat Reflector

The scanning reflector shaft coupling attaches to the motor shaft with two alignment pins and four 4-40 socket head cap screws that fasten into locking helicoil inserts. A shaft key is used to prevent slippage between the motor shaft and the scanning reflector shaft coupling. These fasteners are shown in Figure 35.

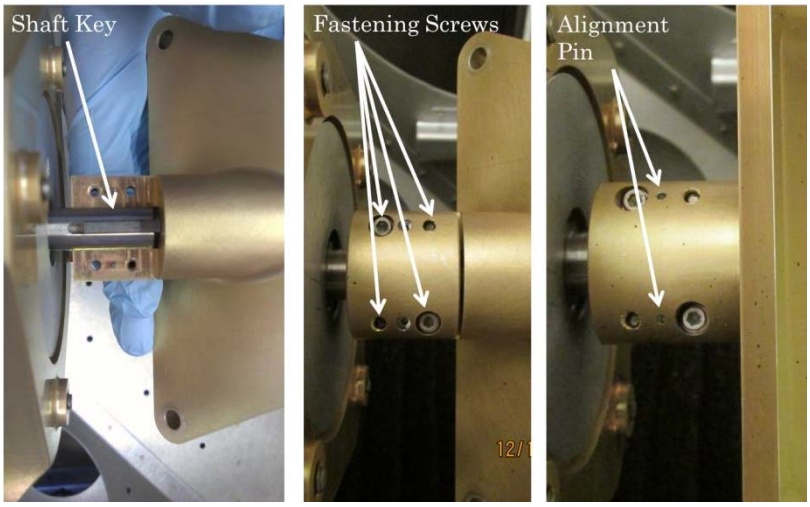


Figure 35: Hardware for Attaching the Scanning Flight Reflector to the Motor Shaft.

Before flying the instrument the interface between the shaft coupling and the motor shaft was tested to ensure reliability. Two primary tests were done to ensure that the scanning reflector shaft coupling would not slip with respect to the motor axis and to ensure vibrations would not cause the 4-40 screws to loosen.

The first test involved removing the shaft key and testing to see if we could overcome the motor stall torque by forcing the motor shaft to spin using the scanning reflector shaft coupling without it slipping. This test was done six times, twice at 0°C, twice at 25°C, and twice at 40°C. No slippage was observed in any of these tests.

The second test involved installing the flat reflector and tightening all fasteners to flight torque values. We then vibrated the mirror by moving the motor back and forth, 1-2°, at various speeds between 10-100 Hz. After about 90 minutes of these

tests we checked to see if any screws had loosened. The test was run twice to ensure reliability of results. To verify that screws were not loosening we marked each screw and the surrounding metal with a line using a marker as seen in Figure 36. If the screw had loosened during the tests the line on the fastener would no longer match the line on the surrounding metal. Figure 36 shows the shaft coupling reflector screws after running two 90 minute tests, it is easily observed that the lines remained continuous.

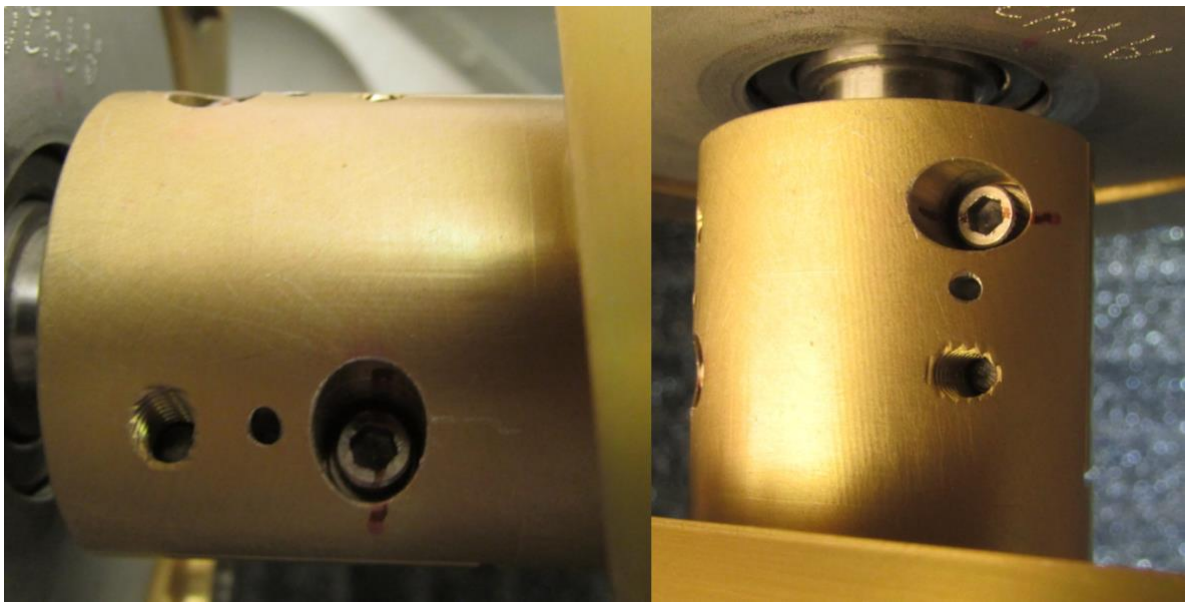

Figure 36: Results of Vibrational Test for Scanning Reflector Shaft Coupling Showing no Misalignment Due to Vibrations.

To ensure that the scanning flat reflector was in the correct position with respect to the chassis two measurements were done. The first measurement checked the minimum clearance between the scanning flat reflector and the microwave feed horn and the second measurement checked the minimum clearance between the

scanning flat reflector and chassis wall as illustrated in Figure 37. Both measurements were found to agree with the 3-D model within 0.51 mm (0.020”). These measurements had an uncertainty of about 0.51 mm (0.02”) due to space limitations in the chassis making these measurements difficult.

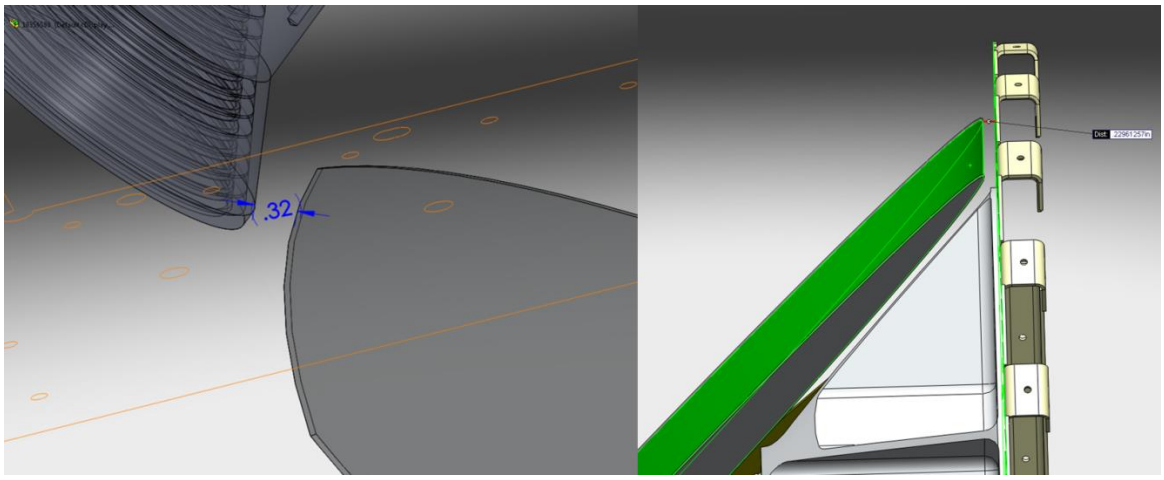


Figure 37: 3-D Representations of Scanning Flat Reflector Position Measurements.

Section 3.4.4 discusses a third method used to verify the motor and hence the scanning flat reflector is in the correct position.

### 3.3.4 HAMMR Cart

Once the fabrication of the HAMMR chassis and reflector sub-systems was completed a mechanism to hold the instrument was needed because the instrument has a rounded bottom. Access to both the top and bottom of the instrument is needed for assembly and maintenance so a cart with a rotation system allowing the instrument to be rotated up to 360° was decided upon. The 3-D Solidworks model of the cart can be seen in Figure 38. The rotation system also aids in the testing,

verification, and calibration of HAMMR as it allows the instrument to view the sky or the ground easily.

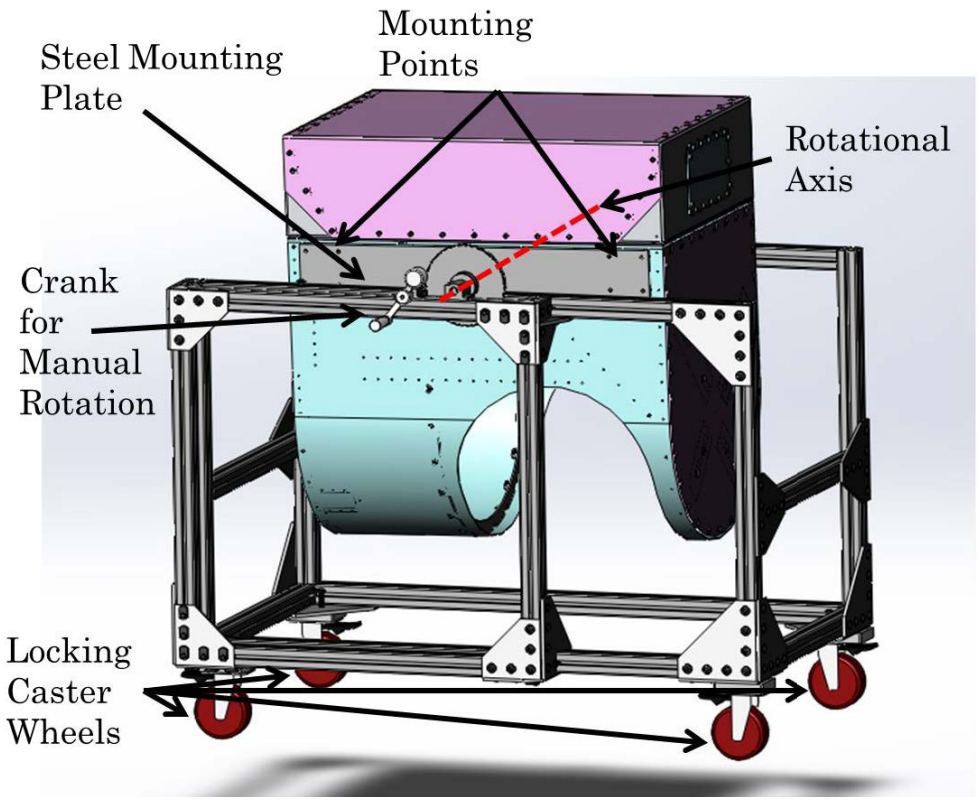


Figure 38: Solidworks Model of Radiometer Cart with Rotating Mechanism.

The cart was made out of 3.81 x 3.81 cm (1.5" x 1.5") extruded T-slot aluminum with four locking caster wheels. The instrument is held to the cart by two steel mounting plates, one on each side, that fasten to the aircraft mounting points in the HAMMR chassis. Steel shafts were then press-fit into the steel plates and welded to shafts providing rotation points. These shafts were then fed through pillow-block linear sleeve bearings for stability and lubrication. The steel shaft on the side of the rotating mechanism is attached to a sprocket using a coupling device and shaft key.

The sprocket is coupled to a worm gear drive and crank that allows for rotation using the crank and prevents unwanted rotation that is more than 2°. The rotating side of the cart is shown in Figure 39.

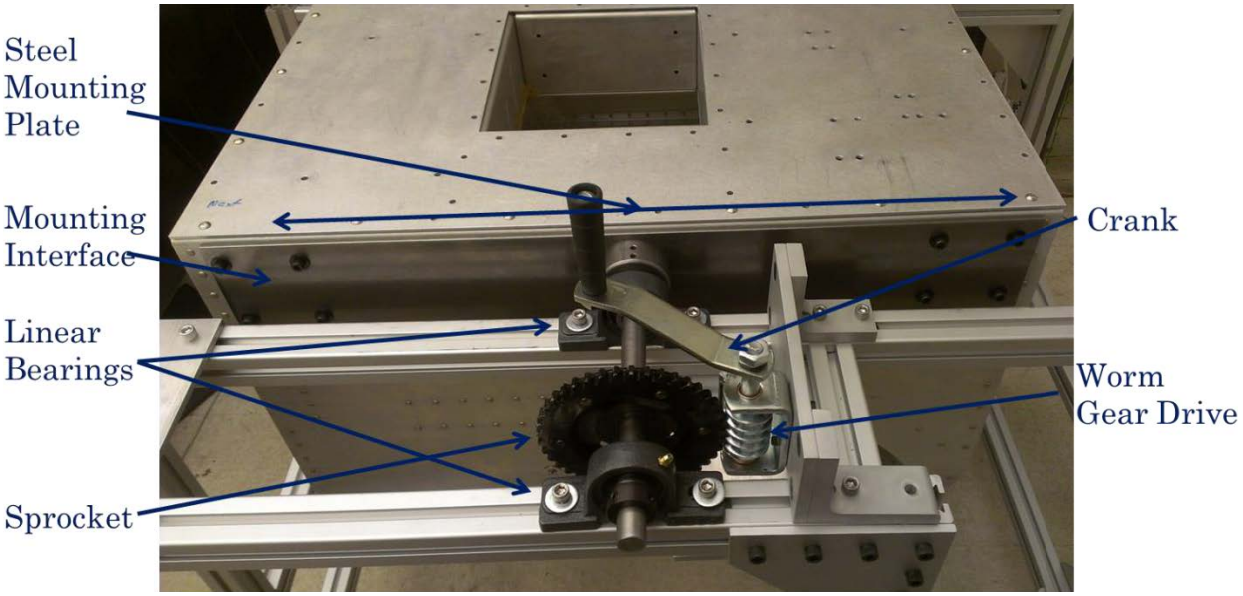


Figure 39: Rotating Mechanism on HAMMR Cart

## 3.4 Feed Horn Antenna Alignment

To ensure the feed horn antennas were properly aligned with the reflectors a mounting and alignment system was designed. All three feed horn antennas were mounted on an aluminum plate referred to as the optical bench. This section details the design of this bench, the hardware used to mount the antennas, and the verification of the antenna's alignment.

### 3.4.1 Optical Bench

The position of the feed horn antennas was defined in the original geometry provided by Dr. Behrouz Khayatian of JPL. The Solidworks model of the optical bench, shown in Figure 40, illustrates how this was accomplished.

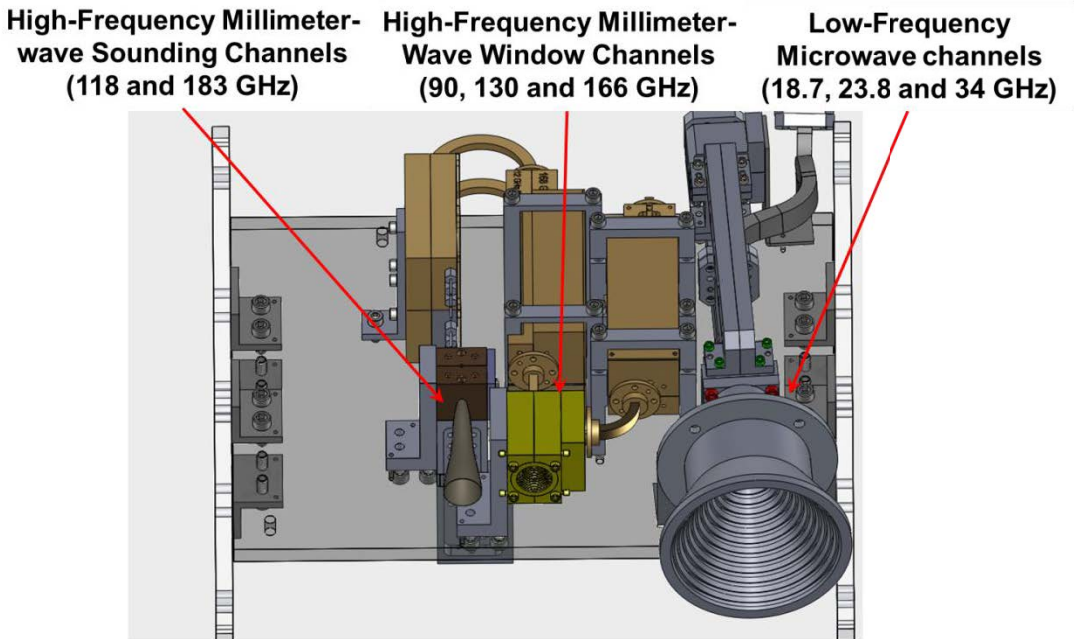


Figure 40: Solidworks Model of the HAMMR Optical Bench

In addition to the feed horn antennas the optical bench also houses the high-frequency millimeter wave window channel receivers. The optical bench is designed to hold the phase center for each feed horn antenna on the focal plane of the offset paraboloid reflector with the most important horn, the tri-frequency horn, at the focal point. This helps maximize the efficiency of each antenna by reducing spillover effects from the reflectors. Figure 41 shows the optical bench with these geometric parameters labeled as well as the linear projection of each feed horn antenna's

aperture normal which illustrates where on the offset paraboloid each feed horn is pointed.

Since only one feed horn can be located directly at the focal point of the offset paraboloid the high-frequency mm-wave window channel feed horn, also called the tri-frequency horn, was selected to be at the focal point. This is because demonstration of the high-frequency mm-wave channels is the focus of IIP-10, so we would like the tri-frequency horn to have the highest efficiency. The high-frequency mm-wave sounding channel's feed horn, also called the quadridge horn, is located very close to offset paraboloids focal point and has an aperture normal that is parallel to that of the tri-frequency horn. Since the feed horn antenna for the microwave channels is so large it had to be located 8 cm (3.15") from the offset paraboloid's focal point. To make up for the large linear offset from the focal point the horn was angled 3.7° toward the outside of the paraboloid as seen in Figure 41. Changing the microwave feed horn orientation helps make up for the linear offset but does not negate it entirely. Due to this offset the microwave channel has an azimuthal and elevation angle offset that is a function of the motor scan angle. This is discussed in detail in Section 3.4.5.

The quad-ridge horn used for the mm-wave sounding channels is offset the other direction from the paraboloid's focal point by 2.7 cm (1.063"). Because this offset is much smaller than the microwave horn offset the sounding horn was left parallel to that of the tri-frequency horn instead of being tilted. Both feed horn offsets are

illustrated in Figure 41 with the black offset representing that of the microwave feed horn and the green offset that of the quad-ridge horn.

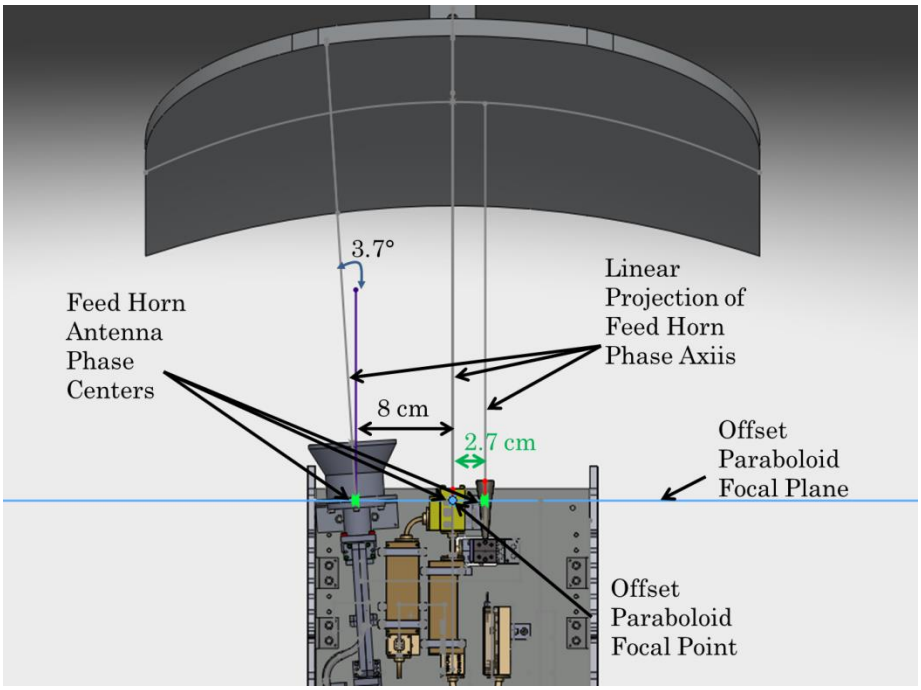


Figure 41: Optical Bench Feed Horn Geometry with Feed Horn Offsets Labeled

The half-power beam width for each radiometer channel used in HAMMR is given in .

Table 1.

Table 1: Half-Power Beam Width of Radiometer Channels in HAMMR (Khayatian, 2011).

| Channel Frequency (GHz) | Beam Width (Degrees) |
|---|---|
| 18.7 | 3.46 |
| 23.8 | 3.06 |
| 34 | 2.14 |
| 90 | 1.36 |
| 130 | 0.44 |
| 168 | 0.34 |
| 118.8 | 0.95 |
| 183.3 | 0.67 |

### 3.4.2 Mounting Hardware

Mounting and aligning the feed horn antennas in the HAMMR chassis required the fabrication of hardware for two interfaces, the antenna to optical bench interface, and the optical bench to chassis interface. Custom hardware was designed and fabricated for both interfaces and will be discussed in this section.

#### 3.4.2.1 Feed Horn Antennas to Optical Bench Interface

The first mounting system discussed will be for the microwave channels. The horn, mounted on the optical bench, with the front and rear mounting brackets is shown in Figure 42. These brackets align precisely with the optical bench through the use of two 0.159 cm (1/16") alignment pins per bracket. The brackets are then interfaced to the feed horn antenna using 3 x 8-32 socket head cap screws and through holes with very tight tolerances allowing for no more than 0.051 mm (0.002") of

misalignment. The bracket to optical bench interfaces are shown in more detail in Figure 43. The exact length and size for all screws can be found in Appendix II.

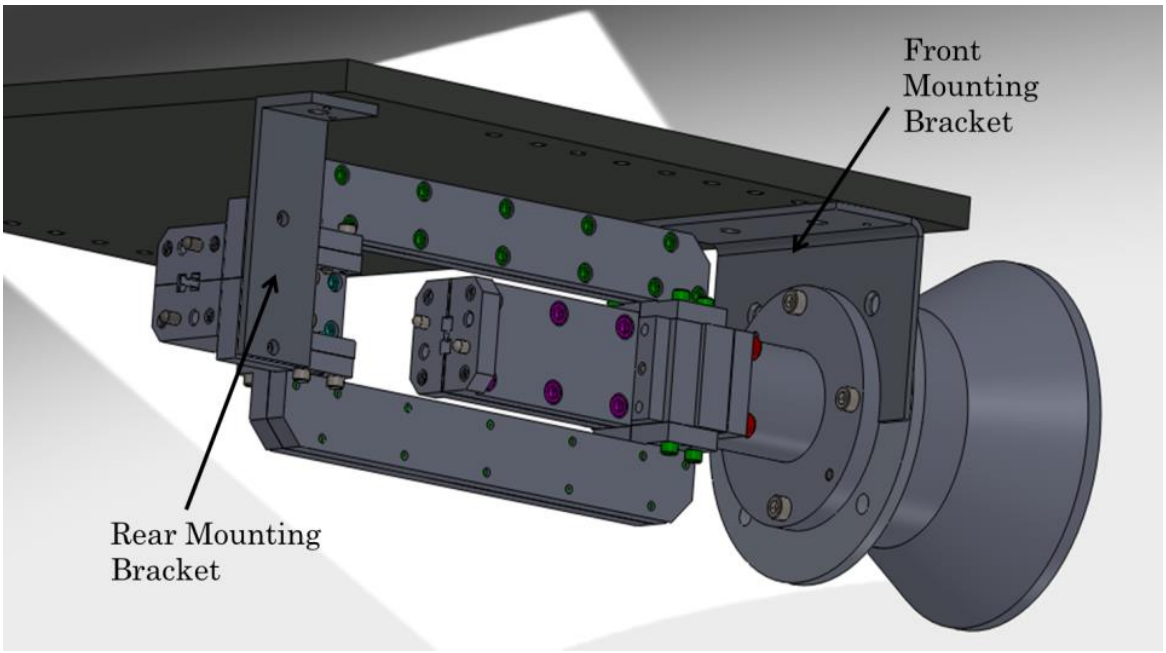


Figure 42: Microwave Channels Feed Horn Mounting

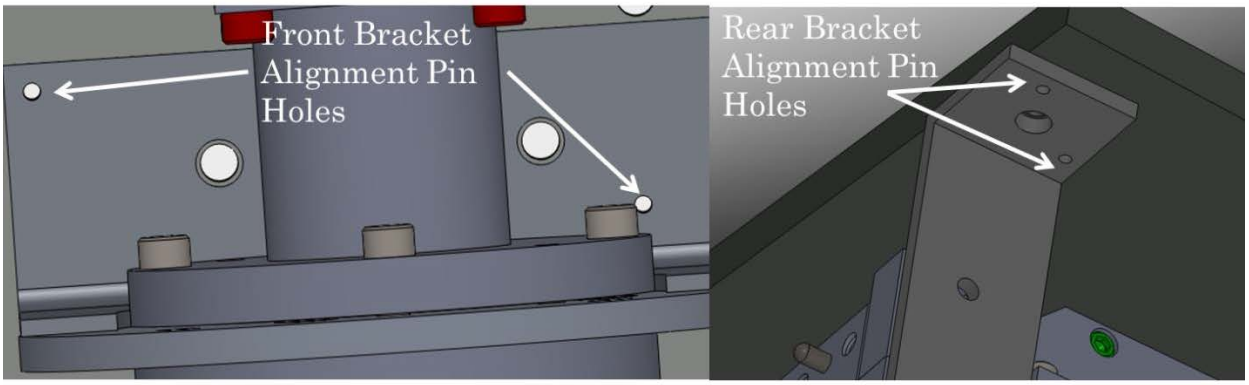


Figure 43: Details of the Microwave Channel's Feed Horn Mounting Hardware,

a) Microwave Feed Horn Front Bracket Optical Bench Interface

b) Microwave Feed Horn Rear Bracket Optical Bench Interface

The high-frequency mm-wave window channel's feed horn antenna required only one mounting bracket due to its small size and can be seen mounted on the optical bench in Figure 44. This bracket uses 4 x 8-32 screws to secure the bracket to the optical bench and two 0.159 cm (1/16") alignment pins to ensure precise alignment as seen in Figure 45. The bracket is then interfaced to the tri-frequency horn with 6 x 2-56 socket head cap screws with precisely machined through holes allowing no more than 0.051 mm (0.002") of misalignment. These screws then fasten into the side of the tri-frequency horn as seen in Figure 44.

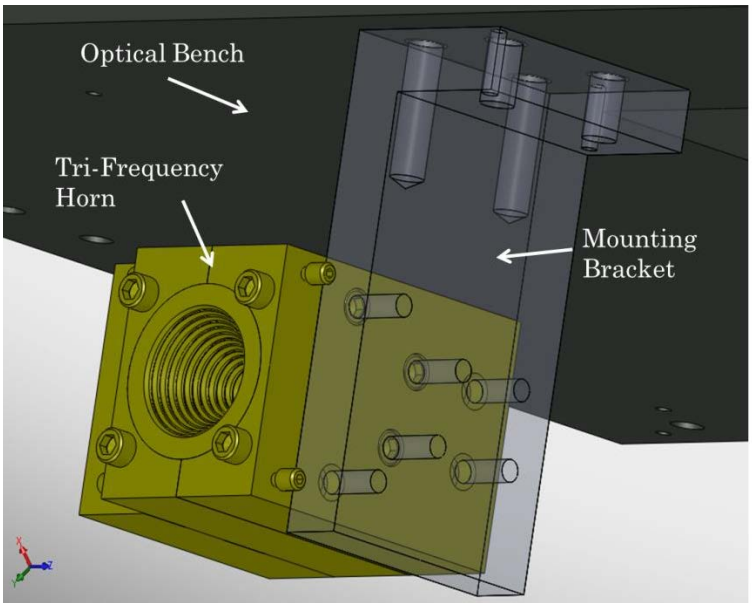


Figure 44: High-Frequency Millimeter-Wave Window Channel's Feed Horn Antenna Mounted on the Optical Bench

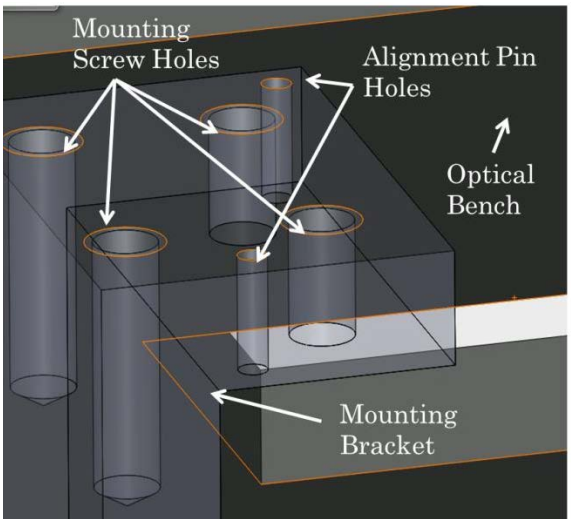


Figure 45: Zoom of Optical Bench to High-Frequency Millimeter-Wave Window Channel's Feed Horn Antenna Interface

The high-frequency mm-wave sounding channel's feed horn or quadridge horn antenna has a mounting structure very similar to that of the tri-frequency horn as

shown in Figure 46. The bracket is attached to the optical bench with 4 x 8-32 socket head cap screws and precise alignment is accomplished through two 0.159 cm (1/16") alignment pins. The bracket is then attached to the horn using 3 x 2-56 socket head cap screws with precisely machined through holes allowing no more than 0.051 mm (0.002") of misalignment.

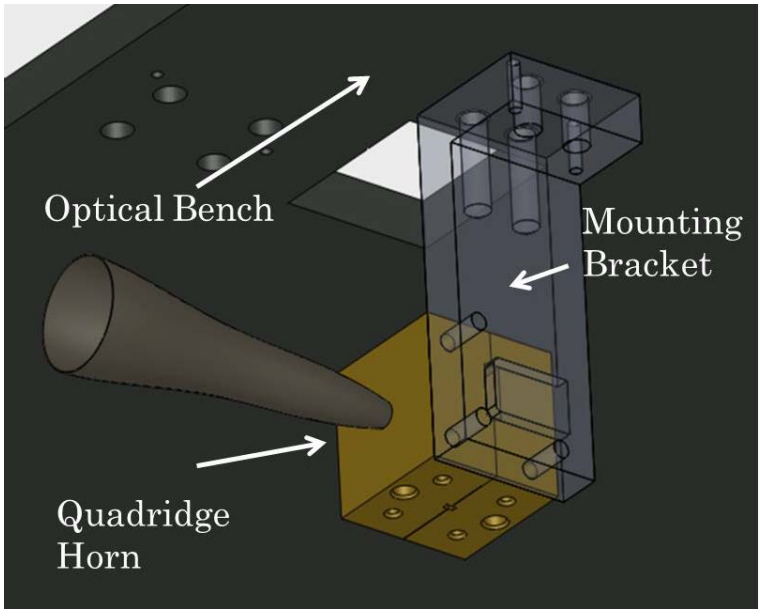


Figure 46: High-Frequency Millimeter-Wave Sounding Channel's Feed Horn Antenna Mounted on the Optical Bench

#### 3.4.2.2 Optical Bench to Chassis Interface

The optical bench sits inside a square cavity within the main bench of HAMMR. Placing the optical bench in this cavity allows it to be removed from the instrument while leaving the main bench in place and gives access to both the top and bottom of the optical bench while it is still in the instrument. To attach the optical bench to the chassis two plates of aluminum referred to as the mounting wings are used.

These wings attach to the cavity through the use of 4 x 10-32 screws per wing as shown on the left side of Figure 47 and Figure 48. The optical bench is then placed on the three lower mounting brackets shown highlighted in blue in Figure 47. These brackets hold the optical bench in place while the alignment discussed in 3.4.3 is completed. Once the optical bench is in the cavity the mounting brackets are attached to the optical bench using 4 x 8-32 socket head cap screws per bracket as seen in Figure 48.

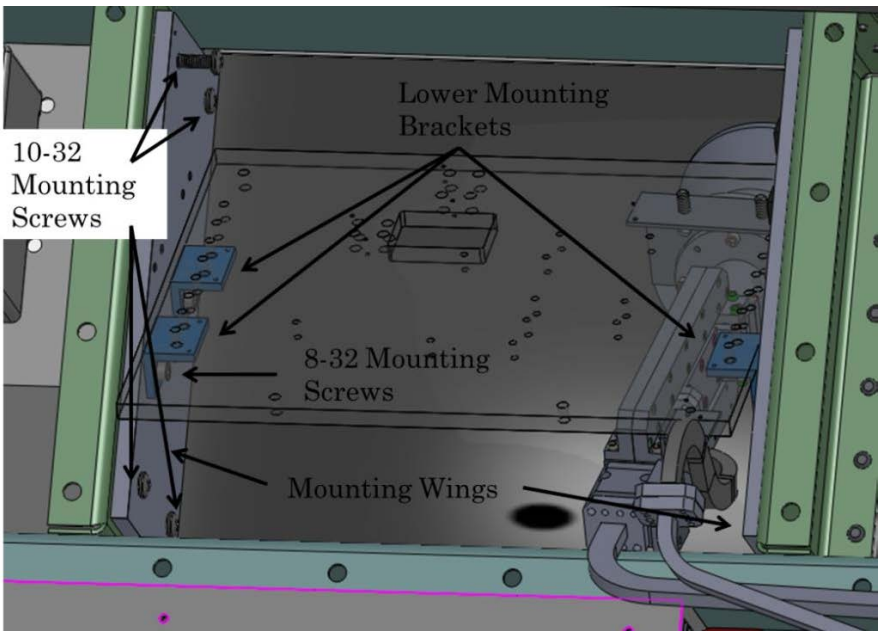


Figure 47: Optical Bench Mounting Hardware

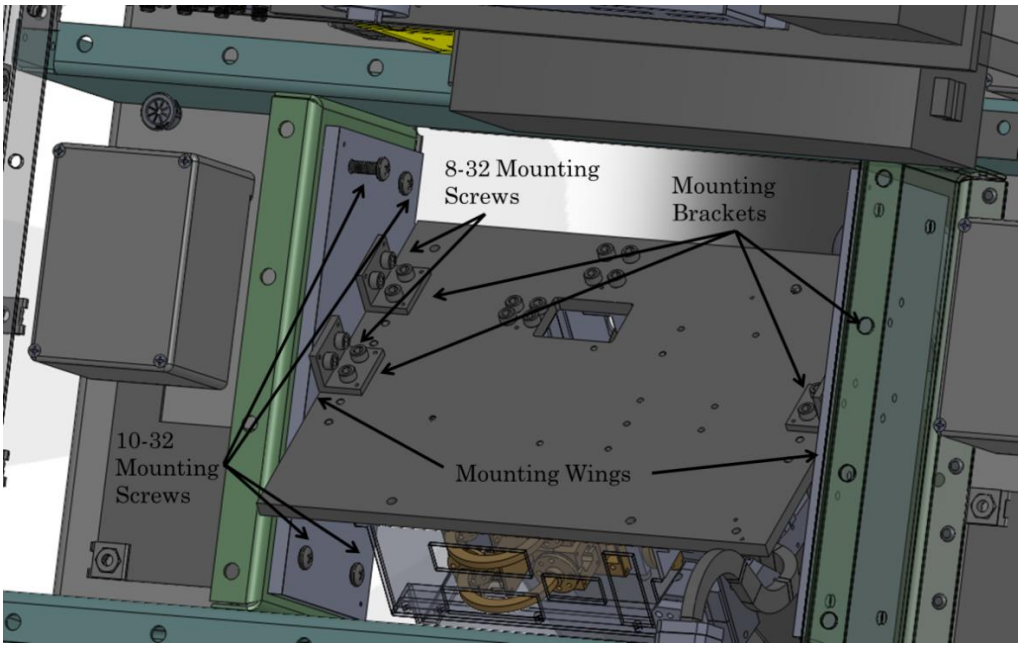


Figure 48: Optical Bench Installed Mounting Hardware

### 3.4.3 Optical Bench Initial Alignment and Repeatability

The optical bench is aligned through the use of three sets of alignment pins as shown in Figure 49. These pins are broken up into three different sets as denoted by color in Figure 49. The first set aligns the mounting wings with the chassis using 2.38 mm (3/32") pins, the second set aligns the mounting brackets with the mounting wings using 1.59 mm (1/16") pins, and the third set aligns the optical bench to the mounting brackets using 1.59 mm (1/16") pins as illustrated in Figure 50 a, b, and c respectively. Once all the pins are in place the screws are tightened and the pins are removed. All pins must be used every time the optical bench is installed. The holes for the alignment pins are matched drilled once alignment has been verified as discussed in 3.4.4.

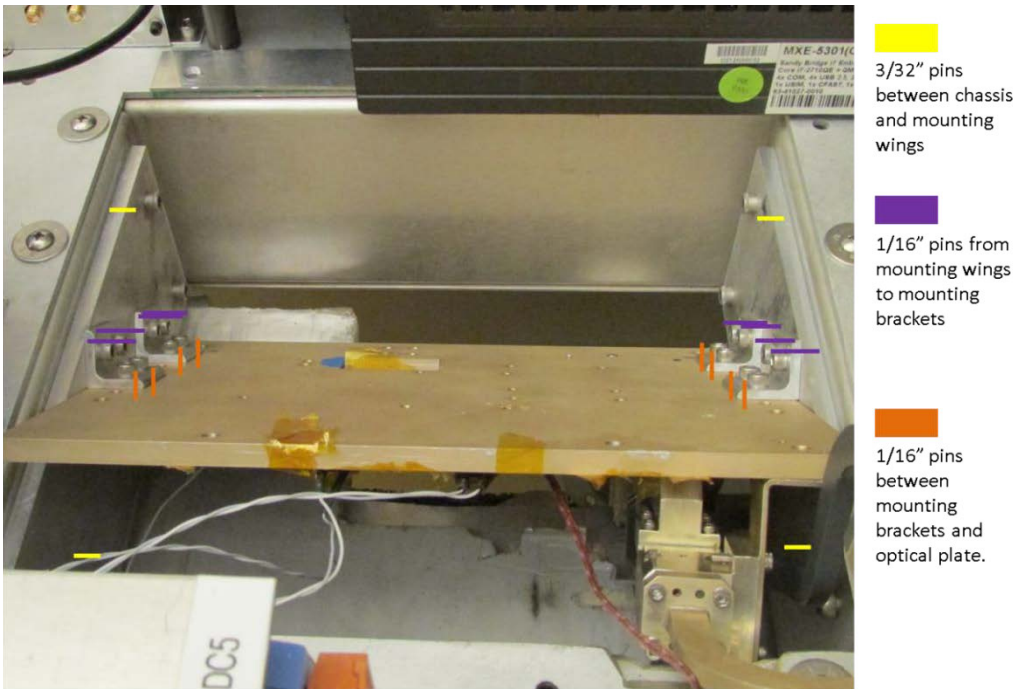


Figure 49: Summary of Optical Bench Alignment Pins


Figure 50: Location of Alignment Pins on Optical Bench

### 3.4.4 Alignment Verification

Before match drilling holes for the alignment pins the alignment of the feed horn antennas must be verified. As seen in 3.3 the location of the offset paraboloid and flat reflectors have been verified with respect to the chassis which means that the optical bench position only needs to be verified with respect to the offset paraboloid. To do this a precision laser was mounted in the exact location and orientation of the tri-frequency horn's aperture normal using a custom fabricated mounting bracket as seen in Figure 51. The location of the laser on the offset paraboloid was then checked to see if it agreed with the projection in the 3-D Solidworks model as shown in Figure 52 a) and b) respectively. The reflection of this laser off of the offset paraboloid onto the motor was also used to verify the position of the motor and hence the flat reflector.

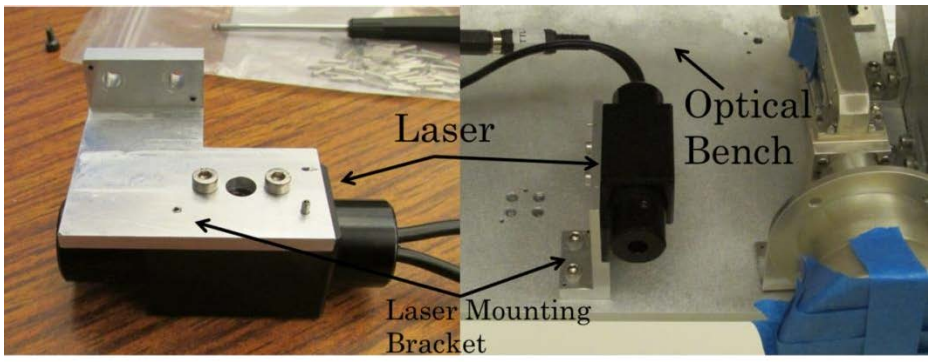


Figure 51: Custom Laser Bracket to Check Optical Bench Antenna Alignment

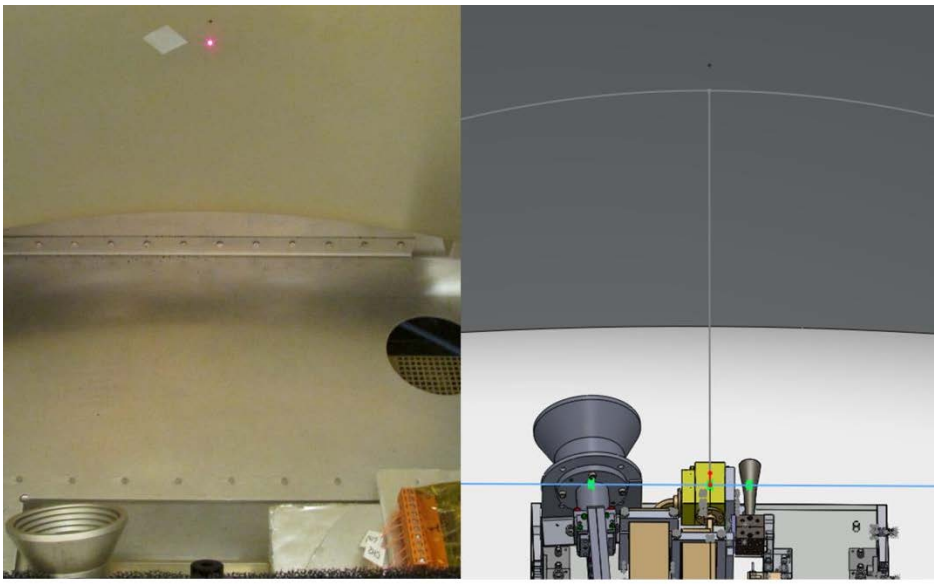

a) b)

Figure 52: Illustration of Alignment Verification, a) Alignment Laser Focused on Offset Paraboloid, b) Projection of Tri-Frequency Horn Phase Axis onto Offset Paraboloid

To determine if the laser spot matched the projection of the tri-frequency horn aperture normal two measurements were used. The first measurement, shown in Figure 53, measures the distance from a 1.59 mm (1/16") fiducial mark manufactured into the offset paraboloid to the laser illumination point. A piece of paper precisely marked to denote 1.97 cm (0.776") was used to measure this distance. Paper was used because the offset paraboloid is a curved surface and the measurement needed to take this into account. It can be seen from Figure 53 that measured value agreed well with the 3-D Solidworks model.

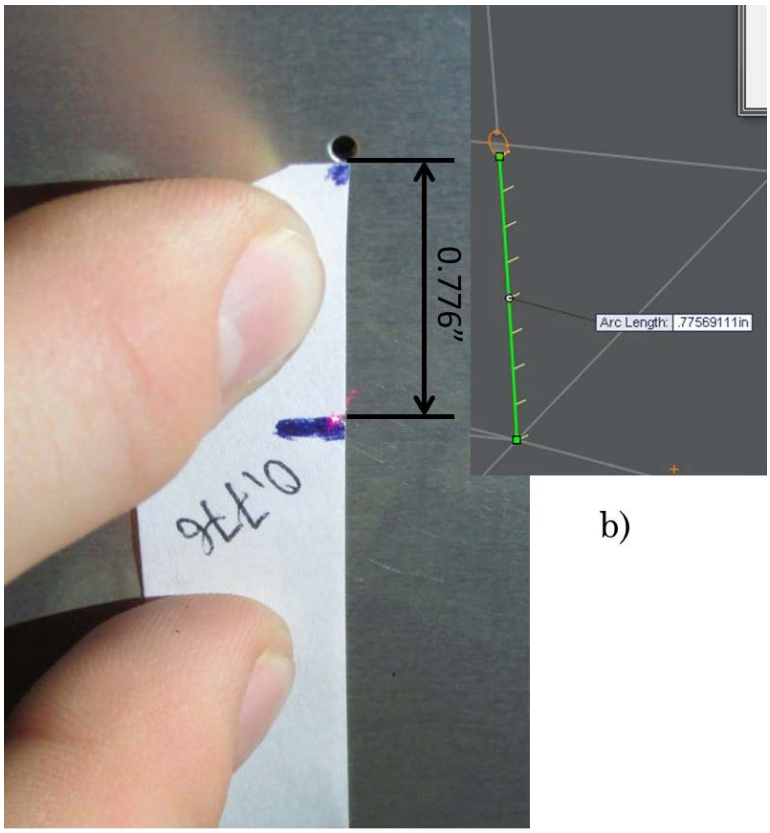


Figure 53: Measurement of Fiducial Mark to Laser Illumination Point on Offset Paraboloid, a) Real Measurement, b) 3-D Solidworks Model Measurement

The second measurement, shown in Figure 54, measured the distance from the laser illumination point to each corner of the paraboloid and compared these values with those of the 3-D Solidworks model. Since the distance for these measurements was so much greater than the distance in the first measurement paper could no longer be used. Instead, string was stretched tight between the laser illumination point and each corner and then measured with 61 cm (24") calipers as shown in Figure 55. This gives the straight line distance between each set of two points. This method of measurement was not extremely accurate but had the highest precision

for any attempted method. Each measurement was completed twice by separate people to ensure consistency.

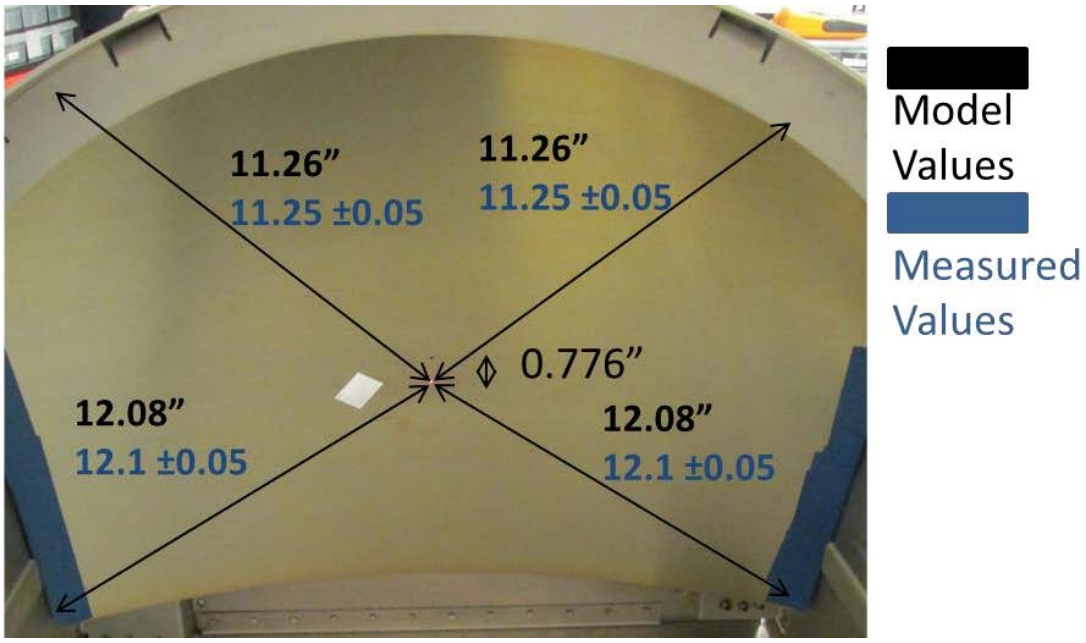


Figure 54: Comparison of Measured and Modeled Values for the Distance Between the Laser Illumination Point and each Corner of the Offset Paraboloid.

Figure 55: Illustration of Measurement Technique Used to Determine the Distance Between the Laser Illumination Point and each Corner of the Offset Paraboloid.

Figure 54 shows that the results of these measurements match well with the 3-D Solidworks model.

### 3.4.5 Feed Horn Angular Beam Offsets

Due to the microwave and mm-wave sounding feed horn antennas being offset from the parabolic reflector's focal point as discussed in Section 3.4.1 the feed horn beams are not all parallel to each other when exiting the HAMMR chassis aperture. This section will detail the calculations used to determine the angular beam offset and the correction that is applied in the retrieval algorithm. Because the microwave feed horn is offset from the focal point by 8 cm, as illustrated in Figure 56, the beam needs a correction for both elevation and azimuth angles that are a function of motor angle. The correction provided in this section only corrects for the change in elevation angle.. The mm-wave sounding channels have the same correction but for

a linear offset of 2.7 cm (1.063”) in the opposite direction and the mm-wave window channels need no correction as the mm-wave window feed horn is located at the offset paraboloids focal point.

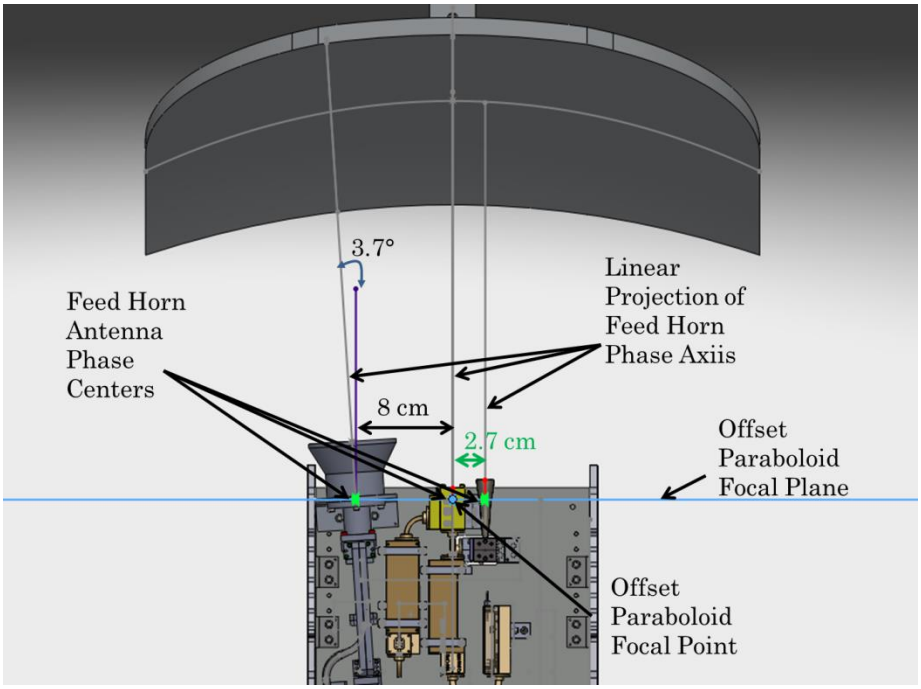


Figure 56: Optical Bench Feed Horn Geometry with Feed Horn Offsets Labeled

The microwave feed horn is also tilted 3.7° to help negate the effects of the 8 cm (3.15”) linear offset. Figure 57 illustrates how tilting the horn helps to correct for this offset. The dotted red line in Figure 57 represents the un-tilted beam, which is pointed off to the side of the optical bench and thus the side of the HAMMR chassis. If the beam was left in this orientation a large portion of the energy seen by the horn would not be from the flat reflector. The green lines represent the beam after being tilted. The tilted beam is pointed onto the left side of the optical bench and thus into the flat reflector. Having the beam better centered on the flat reflector

allows a higher portion of the energy seen by the antenna to come from the flat reflector and thus the measured scene as well as preventing modulation of the measured signal from a varying area of illumination on the flat reflector as it scans. The mm-wave sounding feed horn is not tilted as the offset is much smaller.

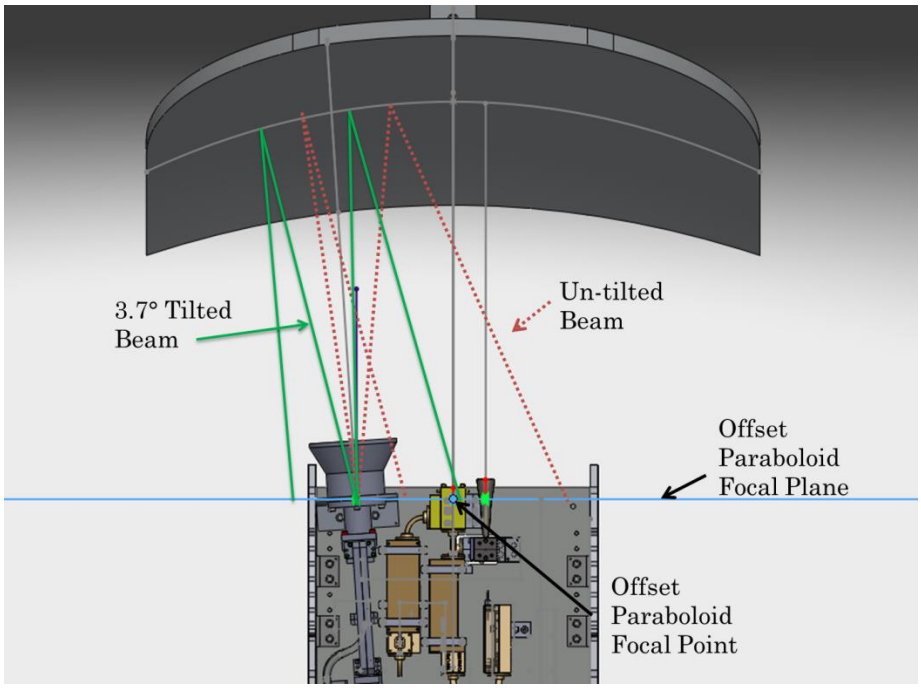


Figure 57: Diagram of the Effects of Tilting the Microwave Feed Horn Meant for Illustrative Purposes which is not Geometrically Accurate

The angle of the microwave feed horn beam reflecting from the parabolic reflector can be calculated by taking the arctangent of the linear offset divided by the focal distance of the parabolic reflector as illustrated in Figure 58. The angular offset calculated for the microwave and mm-wave sounding feed horns is 15.64° and 5.4° respectively. Knowing this value along with the flat reflector angle gives us the means for calculated the corrected elevation angle.

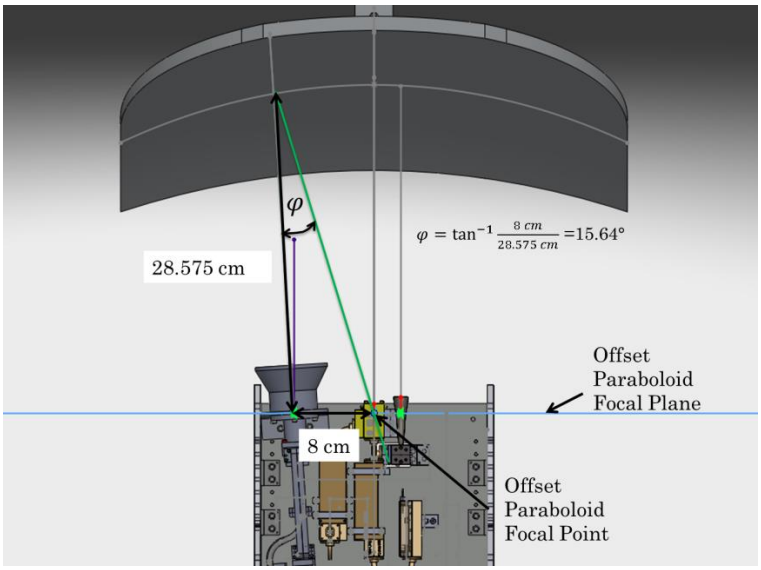


Figure 58: Illustration of Parabolic Angular Beam Offset for Microwave Channel

The first step in calculating the corrected elevation angle is to define a spherical coordinate system that describes this geometry. To do this a standard spherical coordinate transformation is used resulting in equations (III.5), (III.6), and (III.7) where θ is equal to the motor position angle and φ is equal to the angle of the microwave feed horn beam reflecting from the parabolic reflector. These equations describe the $\hat{x}$, $\hat{y}$, and $\hat{z}$ coordinates of a point in the center of the microwave feed horn beam on the flat reflector as it spins as illustrated in Figure 59 this point will describe a circle parallel to the xy plane. The effect of the linear feed horn offset is that perimeter defined by P while the motor scans is no longer a circle parallel to the xy plane as in Figure 59, but is now a 3D ellipse with a $\hat{z}$ coordinate.

$$z_p = \cos(\varphi) \tag{III.5}$$

$$y_p = \sin(\varphi) * \sin(\theta) \tag{III.6}$$

$$x_p = \sin(\varphi) * \cos(\theta) \tag{III.7}$$

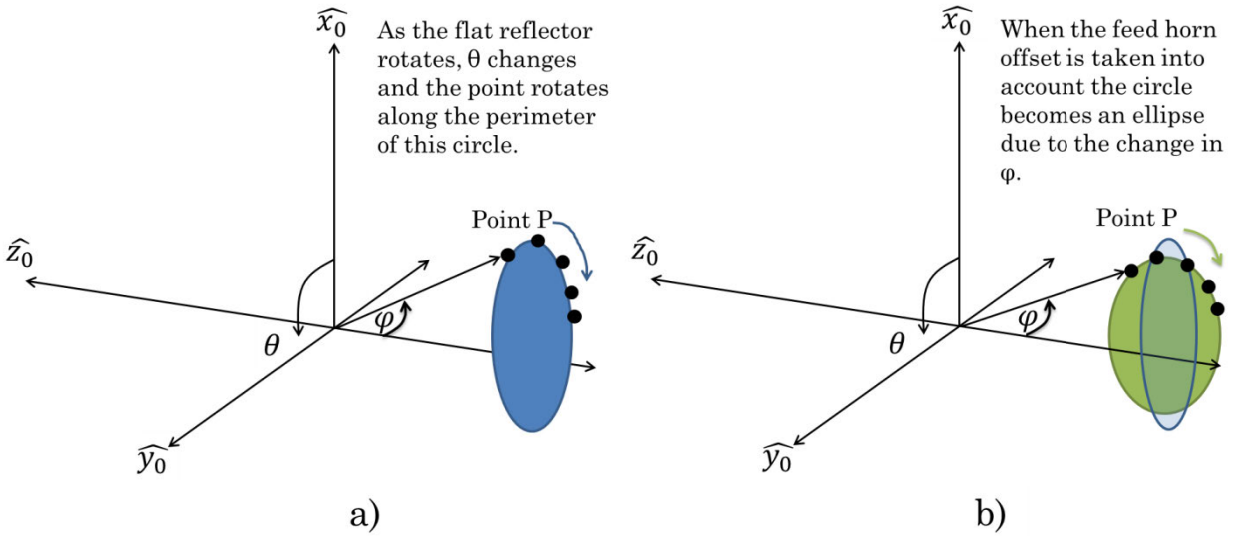


Figure 59: Illustration of the Effect of Offsetting the Microwave Feed Horn Shown by a Projection of the Feed Horn Beam onto the Flat Reflector, a) No Offset, b) 8 cm Linear Offset from Focal Point

The coordinate transformation must then take into account the angle change from reflecting off the flat reflector which is oriented at 45° to the offset paraboloid resulting in a 90° coordinate change. This will redefine the axes so z represents the motor axis, y represents the zenith/nadir axis, and x represents the side-to-side axis. This transformation is shown in equations (III.8), (III.9), and (III.10) and illustrated in Figure 60.

$$x_1 = \cos(\varphi) \tag{III.8}$$

$$y_1 = \sin(\varphi) * \sin(\theta) \quad \text{(III.9)}$$

$$z_1 = \sin(\varphi) * \cos(\theta) \quad \text{(III.10)}$$

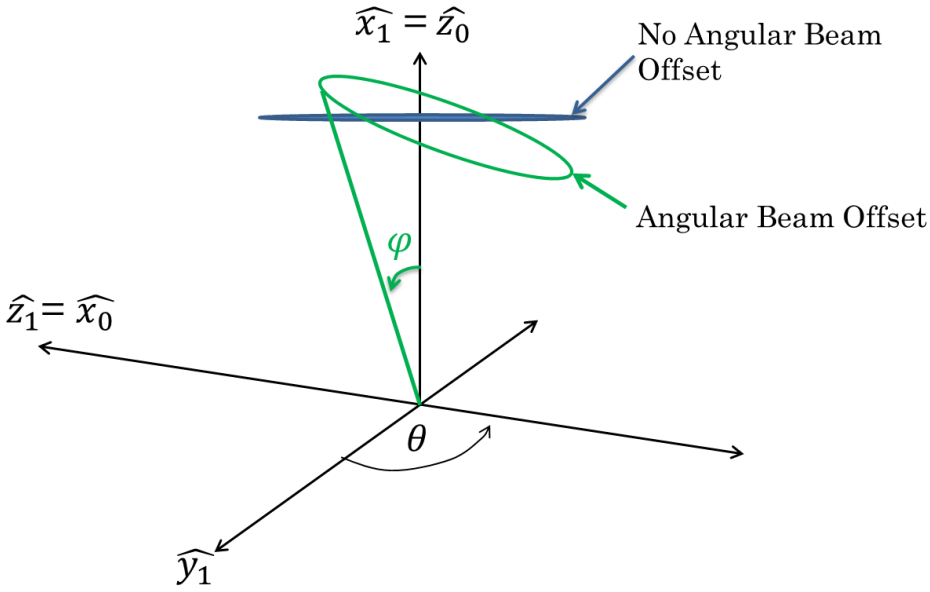


Figure 60: Coordinate System after the Reflection off the Flat Reflector

The coordinate system must then be projected onto the earth's surface using the transformations described in equations (III.11), (III.12), and (III.13) and illustrated in Figure 61.

$$\text{Motor Axis} => z' = \sin(\varphi) * \cos(\varphi) \quad \text{(III.11)}$$

$$\text{Zenith} => y' = \sin(\varphi) * \sin(\theta) * \cos(\theta) - \cos(\varphi) * \sin(\theta) \quad \text{(III.12)}$$

$$\text{Side-Side} => x' = \cos(\varphi) * \cos(\theta) + \sin(\varphi)\sin^2(\theta) \quad \text{(III.13)}$$

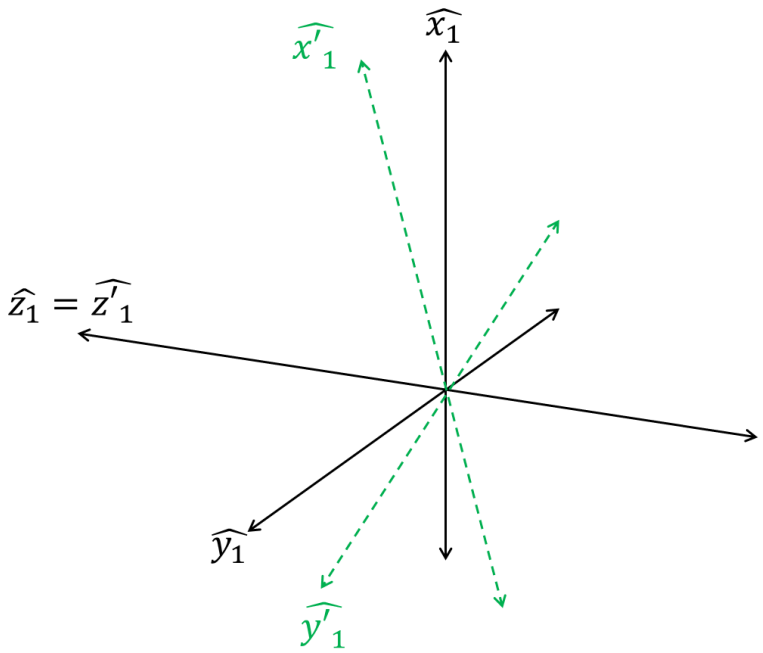


Figure 61: Final Coordinate System for Projecting Microwave Feed Horn Beam onto the Earth

The beam elevation angle can then be found by taking the Arcsin of y', since it is the zenith/nadir axis as in equation (III.14). This correction can be used for both the microwave and mm-wave sounding channels using their respective angular offsets.

$$\text{Elevation Angle} = \sin^{-1}(y') \tag{III.14}$$

These transformation equations can then be applied in the retrieval algorithm to compensate for the microwave feed horn linear offset and angular tilt. The corrected elevation angle and angular elevation correction for one channel in each frequency set are presented in Figure 62, Figure 63, and Figure 64 for the 18 GHz QV microwave channel, the 90 GHz mm-wave window channel, and the 183-3 GHz mm-wave sounding channel respectively. The mm-wave window channels have no

angular correction as the tri-frequency horn is located at the focal point of the offset paraboloid.

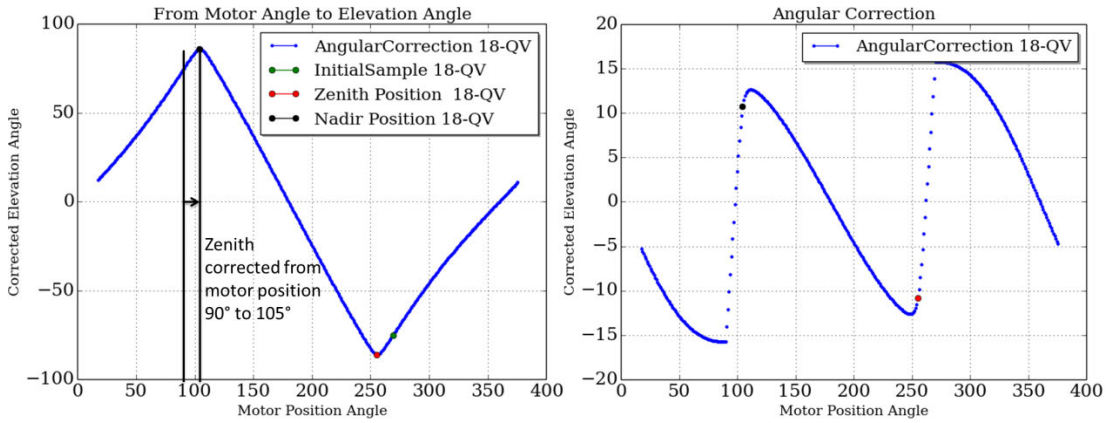


a) b)

Figure 62: a) Corrected Elevation Angle with Respect to Motor Position Angle for the 18 GHz QV Microwave Channel, b) Angular Correction of Elevation Angle with Respect to Motor Position Angle for the 18 GHz QV Microwave Channel

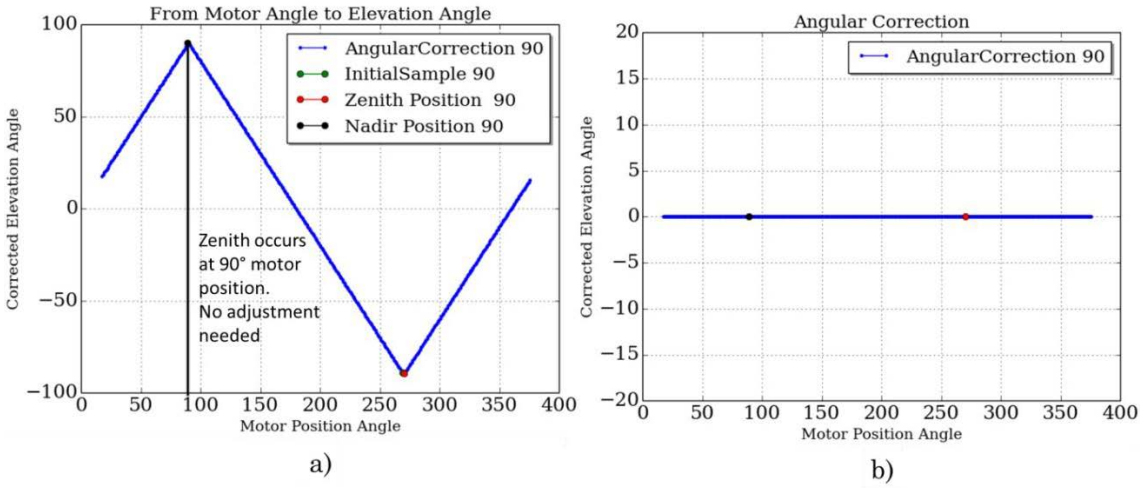


Figure 63: a) Corrected Elevation Angle with Respect to Motor Position Angle for the 90 GHz Millimeter-Wave Window Channel, b) Angular Correction of Elevation Angle with Respect to Motor Position Angle for the 90 GHz Millimeter-Wave Window Channel

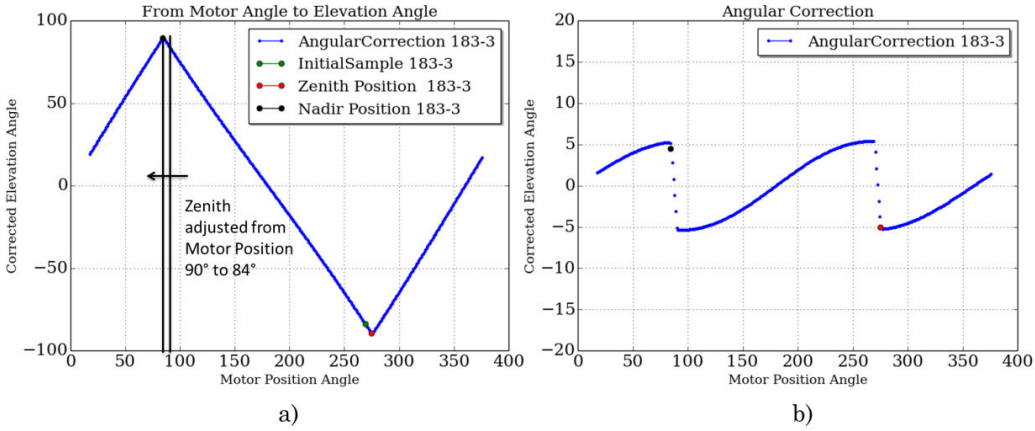


Figure 64: a) Corrected Elevation Angle with Respect to Motor Position Angle for the 183-3 GHz Millimeter-Wave Sounding Channel, b) Angular Correction of Elevation Angle with Respect to Motor Position Angle for the 183-3 GHz Millimeter-Wave Sounding Channel

## 3.5 HAMMR Components

In addition to the radiometers and reflectors the HAMMR chassis contains hardware for converting alternating current (AC) to direct current (DC), temperature sensing and control, motor control and monitoring, analog to digital conversion, and data conditioning. HAMMR also contains an internal computer that can be remotely logged into allowing the operator to configure the acquisition sequence and access data files.

### 3.5.1 Power Supplies and Distribution

The power supplies in HAMMR are all positioned beneath the main bench. This was done to reduce the amount of electromagnetic interference (EMI) that could be coupled into the radiometers and data cables from the switching power supply noise. HAMMR uses a locking 20 Amp AC power inlet that is internally distributed to the AC-DC power supplies shown in Figure 65. The HAMMR system contains a total of seven AC-DC power supplies at -12, -5, +7, +12, +15, +16, and +48 Volts described in Table 2.

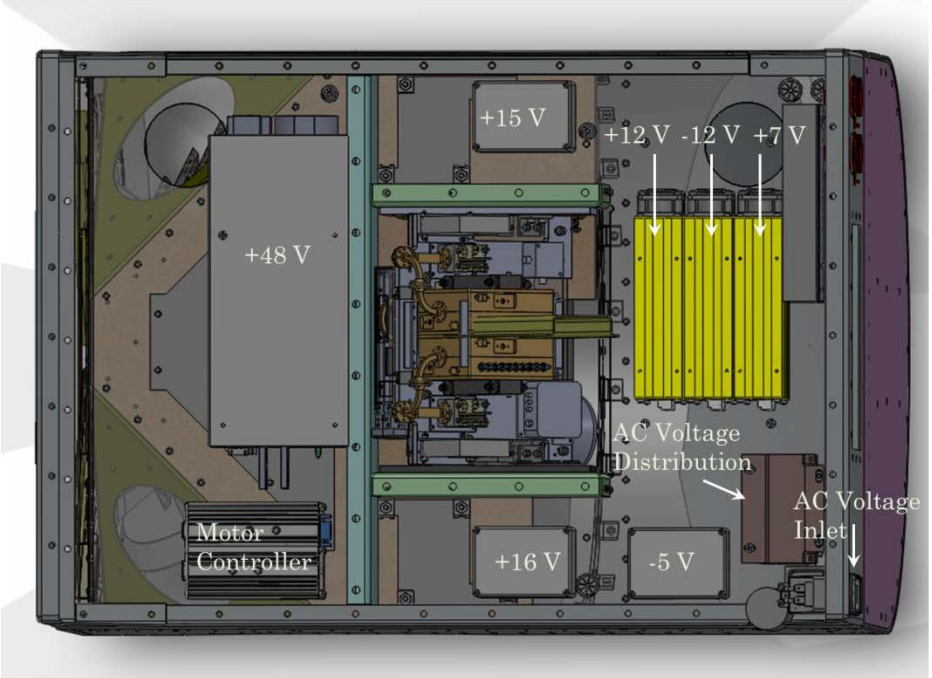


Figure 65: Physical Layout of HAMMR Power Supplies and AC Distribution.

The DC output of these supplies is then distributed via a fused distribution block to the HAMMR sub-systems as shown in Figure 66. This type of distribution was chosen so that for each sub-system, every input voltage has a fuse. This is advantageous because the fuses help prevent damage if a short occurs. In addition, the current for each sub-system voltage can be measured by bypassing the fuse with a current meter which allows the operator to easily verify if a piece of hardware is malfunctioning.

Each piece of the block, except for the voltage return sections, has a colored circle on it. The colored circle designates which size of fuse belongs in that piece. The voltage returns are not fused so they have no designator. A map showing where each piece of the DC distribution provides power and what size of fuse it employs is

shown in Figure 67. Appendix I presents a broken up version of Figure 67 for ease of reading. Fuses were chosen to be as close to 200% of expected current draw as possible. In a future version of HAMMR this could be implemented using a printed circuit board PCB with D-subminiature-9 (DB-9) connectors for each sub-system. Implementing the DC distribution with a PCB would reduce debugging capabilities but would make the instrument cleaner and less prone to assembly errors.

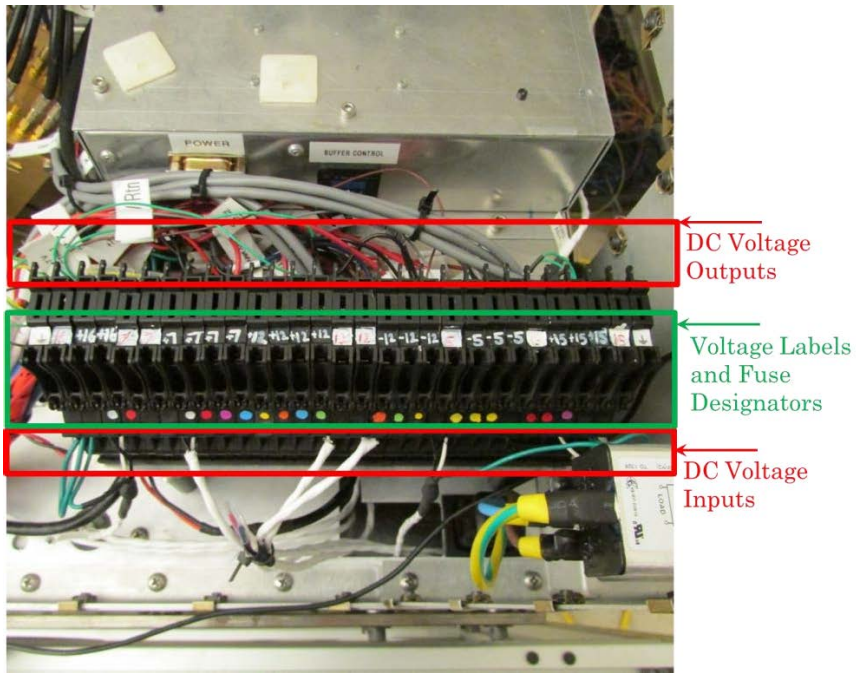


Figure 66: DC Voltage Distribution Block.

| +7 V | | -5 V | | +12 V | | -12 V | | +15 V | | +16 V | |
|---|---|---|---|---|---|---|---|---|---|---|---|
| Current (A) | Sub-System | Current (A) | Sub-System | Current (A) | Sub-System | Current (A) | Sub-System | Current (A) | Sub-System | Current (A) | Sub-System |
| 0.7 | | 0.05 | | 0.07 | | 0.07 | | 0.05 | AMRs + Window | 0.6 | FPGA |
| 0.7 | AMRs | 0.05 | AMRs | 0.07 | AMRs | 0.07 | AMRs | 0.025 | NSs | | |
| 0.4 | Window | 0.06 | Window | 0.25 x 7 = 1.75 | ABEB | 0.25 x 7 = 1.75 | ABEB | 0.125 | DROs + OP Amp | | |
| 0.2 | Sounder (OMT) | 0.05 | | 1.35 | Freq Mult | 0.1 | Window | 5 x 0.075 = 0.375 | Thermistors + SND CLK | | |
| 0.4 | | 0.05 | Sounder | 0.1 | Window | | | | | | |
| 0.4 | Sounders | | | | | | | | | | |

| | |
|---|---|
| 0.25A | X 3 |
| 0.315A | X 2 |
| 0.5A | X 3 |
| 1A | X 2 |
| 1.6A | X 2 |
| 3A | X 2 |
| 4A | X 2 |

Figure 67: DC Distribution List

Table 2 gives a summary of the power supplies used in HAMMR and Appendix I shows the sub-systems that use these voltages and the expected current draw for each sub-system in more detail. Each power supply was tested for large transients when powering the instrument on or off before integration and were found to have less than 1 volt of deviation from the nominal value.

Table 2: Summary of AC-DC Power Supplies in HAMMR

| Model # | Manufacturer | V_out (V) | I_out (A) 40 to 71°C | Ripple (mV) P- | Ripple (mV) | Price ($) | Supply Type |
|---|---|---|---|---|---|---|---|
| W7FT850 | Acopian | +7 | 5.9 | 50.0 | 10 | 225 | Switching |
| W12FT910 | Acopian | +11.5 | 6.3 | 100.0 | 15 | 255 | Switching |
| W12FT910 | Acopian | -11.5 | 6.3 | 100.0 | 15 | 255 | Switching |
| SE-1000-48 | Mean Well | +48 | 20.8 | 200.0 | 283 | 259 | Switching |
| 5EB150 | Acopian | -5 | 1.5 | 0.7 | 1 | 171 | Linear |
| 15EB100 | Acopian | +15 | 1.0 | 0.7 | 1 | 171 | Linear |
| 16EB90 | Acopian | +16 | 0.9 | 0.7 | 1 | 171 | Linear |

The +7, +12, and -12 volt power supplies were originally linear supplies but were changed to switching supplies due to a 60 Hz noise problem further discussed in Section 7.4.

### 3.5.2 Temperature Sensing

HAMMR contains 40 thermistors spaced throughout the various sub-systems. The thermistors have a resistance that changes with physical temperature. This change in resistance corresponds to a change in voltage across the thermistor, the thermistor voltages are monitored by five SuperLogics 8017, 16-bit, data acquisition modules (Superlogics, 2010). These modules digitize the voltages and send them to the internal computer through RS-485. The two types of thermistors used in HAMMR are 5 kΩ thermistors from US Sensors (Digi-Key, 2014) and Measurement Specialties (Measurement Specialties, 2014). The voltages are converted to temperatures using an equation specified by US Sensors given in (Digi-Key, 2014) and by an equation provided by Dr. Sharmila Padmanabhan of JPL respectively. Figure 68 shows the SuperLogics 8017 data acquisition module and US Sensors thermistor used in HAMMR. Table 3 shows where each thermistor goes in the system, what type of thermistor is used, the resolution for each thermistor, and the reference number for each thermistor in the data processing code. The position of the SuperLogics 8017 data acquisition modules is shown in Figure 69.

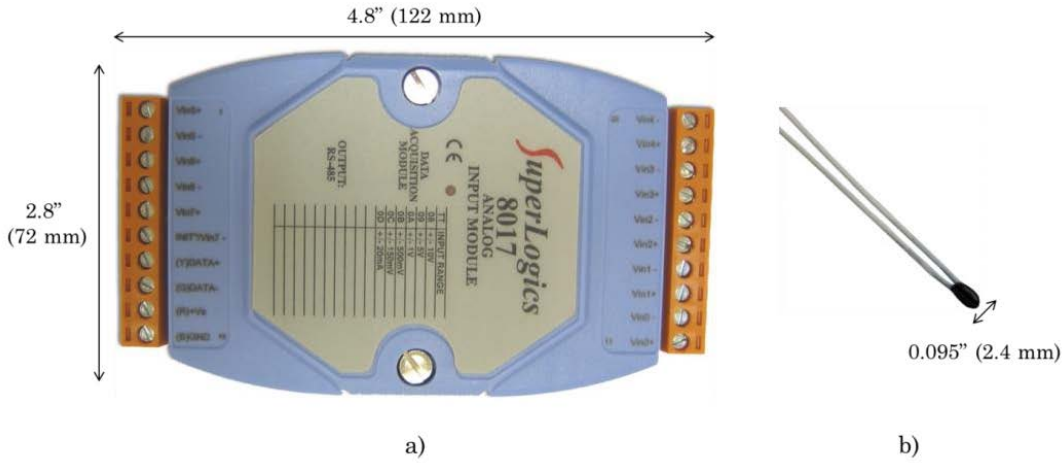


Figure 68: a) Superlogic 8017 Digitizer (Digi-Key, 2014) and b) Thermistor (Superlogics, 2010)

Table 3: Map of HAMMR Thermistor Numbers and Location

| Digitizer# | D.Number | S.Number | Name | Type | Resolution | Model - NTC |
|---|---|---|---|---|---|---|
| 1 | 1 | **8** | BB Target 0 - Upper Left (Base) | Thermistor - 5 kΩ | 0.1° C | KS502J2 (615-1073-ND) |
| | 2 | **9** | BB Target 1 - Lower Left (Tip) | Thermistor - 5 kΩ | 0.1° C | KS502J2 (615-1073-ND) |
| | 3 | **10** | BB Target 2 - Center (Middle) | Thermistor - 5 kΩ | 0.1° C | KS502J2 (615-1073-ND) |
| | 4 | **11** | BB Target 3 - Bottom Left (Base) | Thermistor - 5 kΩ | 0.1° C | KS502J2 (615-1073-ND) |
| | 5 | **12** | BB Target 4 - Bottom Right (Tip) | Thermistor - 5 kΩ | 0.1° C | KS502J2 (615-1073-ND) |
| | 6 | **13** | BB Target 5 - Upper Right (Tip) | Thermistor - 5 kΩ | 0.1° C | KS502J2 (615-1073-ND) |
| | 7 | **14** | BB Target 6 - Lower Right (Base) | Thermistor - 5 kΩ | 0.1° C | KS502J2 (615-1073-ND) |
| | 8 | **15** | BB Target 7 - Top (Middle) | Thermistor - 5 kΩ | 0.1° C | KS502J2 (615-1073-ND) |
| 2 | 1 | **16** | AMR-(Ch18/Ch24)-Internal QV | Thermistor - 5 kΩ | 0.1° C | 44906 (S311P18-06S7R6) |
| | 2 | **17** | AMR-Ch34-Internal QV | Thermistor - 5 kΩ | 0.1° C | 44906 (S311P18-06S7R6) |
| | 3 | **18** | AMR-(Ch18/Ch24)-External QH | Thermistor - 5 kΩ | 0.1° C | 44906 (S311P18-06S7R6) |
| | 4 | **19** | AMR-Ch34-External QH | Thermistor - 5 kΩ | 0.1° C | 44906 (S311P18-06S7R6) |
| | 5 | **20** | AMR-NS-18/24H brn | Thermistor - 5 kΩ | 0.1° C | 44907 (S311P18-06S7R6) |
| | 6 | **21** | AMR-NS-34H grn | Thermistor - 5 kΩ | 0.1° C | 44908 (S311P18-06S7R6) |
| | 7 | **22** | AMR-NS-18/24V blue | Thermistor - 5 kΩ | 0.1° C | 44909 (S311P18-06S7R6) |
| | 8 | **23** | AMR-NS-34V orng | Thermistor - 5 kΩ | 0.1° C | 44910 (S311P18-06S7R6) |
| 3 | 1 | **24** | 12V Power Supply chamber | Thermistor - 5 kΩ | 0.1° C | KS502J2 (615-1073-ND) |
| | 2 | **25** | 12V Power Supply chamber | Thermistor - 5 kΩ | 0.1° C | KS502J2 (615-1073-ND) |
| | 3 | **26** | BACKSIDE-PARABOLOID1 (bot) | Thermistor - 5 kΩ | 0.1° C | KS502J2 (615-1073-ND) |
| | 4 | **27** | BACKSIDE-PARABOLOID2 (mid) | Thermistor - 5 kΩ | 0.1° C | KS502J2 (615-1073-ND) |
| | 5 | **28** | BACKSIDE-PARABOLOID3 (top) | Thermistor - 5 kΩ | 0.1° C | KS502J2 (615-1073-ND) |
| | 6 | **29** | Motor Controller GRN | Thermistor - 5 kΩ | 0.1° C | KS502J2 (615-1073-ND) |
| | 7 | **30** | Motor BLUE | Thermistor - 5 kΩ | 0.1° C | KS502J2 (615-1073-ND) |
| | 8 | **31** | Motor PSU BROWN | Thermistor - 5 kΩ | 0.1° C | KS502J2 (615-1073-ND) |
| 4 | 1 | **32** | ACT-MCM90 | Thermistor - 5 kΩ | 0.1° C | KS502J2 (615-1073-ND) |
| | 2 | **33** | ACT-MCM130 | Thermistor - 5 kΩ | 0.1° C | KS502J2 (615-1073-ND) |
| | 3 | **34** | ACT-MCM166 | Thermistor - 5 kΩ | 0.1° C | KS502J2 (615-1073-ND) |
| | 4 | **35** | SOUNDER118 External | Thermistor - 5 kΩ | 0.1° C | KS502J2 (615-1073-ND) |
| | 5 | **36** | SOUNDER-Multiplier 118 | Thermistor - 5 kΩ | 0.1° C | KS502J2 (615-1073-ND) |
| | 6 | **37** | ABEB External | Thermistor - 5 kΩ | 0.1° C | KS502J2 (615-1073-ND) |
| | 7 | **38** | SOUNDER183 External | Thermistor - 5 kΩ | 0.1° C | KS502J2 (615-1073-ND) |
| | 8 | **39** | SOUNDER-Multiplier 183 | Thermistor - 5 kΩ | 0.1° C | KS502J2 (615-1073-ND) |
| 5 | 1 | **0** | OPTICALBENCH-AMR (1&2) | Thermistor - 5 kΩ | 0.1° C | KS502J2 (615-1073-ND) |
| | 2 | **1** | OPTICALBENCH-ACT (3&4) | Thermistor - 5 kΩ | 0.1° C | KS502J2 (615-1073-ND) |
| | 3 | **2** | OPTICALBENCH-SOUNDER (5&6) | Thermistor - 5 kΩ | 0.1° C | KS502J2 (615-1073-ND) |
| | 4 | **3** | Optical Bench Box Ambient (7&8) | Thermistor - 5 kΩ | 0.1° C | KS502J2 (615-1073-ND) |
| | 5 | **4** | Attach as Needed | Thermistor - 5 kΩ | 0.1° C | KS502J2 (615-1073-ND) |
| | 6 | **5** | Attach as Needed | Thermistor - 5 kΩ | 0.1° C | KS502J2 (615-1073-ND) |
| | 7 | **6** | Attach as Needed | Thermistor - 5 kΩ | 0.1° C | KS502J2 (615-1073-ND) |
| | 8 | **7** | Attach as Needed | Thermistor - 5 kΩ | 0.1° C | KS502J2 (615-1073-ND) |

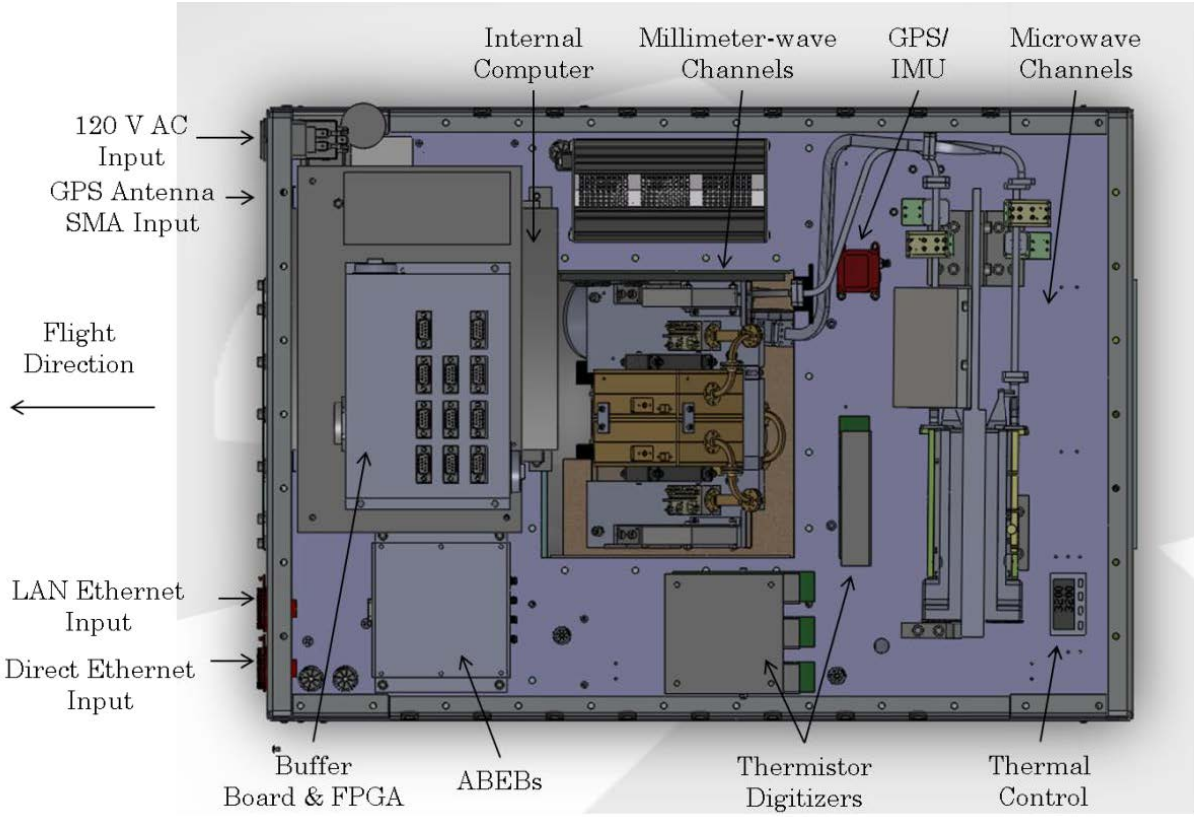


Figure 69: Physical Layout of HAMMR Sub-Systems

### 3.5.3 Global Positioning and Inertial Measurement Unit

To record HAMMR's global position and attitude in terms of latitude, longitude, and altitude and roll, pitch, and yaw respectively HAMMR uses the IG-500N from SBG Systems (SBG Systems). The IG-500N is a global positioning system (GPS) and inertial measurement unit (IMU) integrated into a single module shown in Figure 70. The IG-500N can measure roll, pitch, and yaw to within 0.45° and latitude, longitude, and altitude to within 3 meters at 16 Hz (SPG Systems). This data is then sent to the internal computer through USB to be stored in the acquisition files.


Figure 70: SBG Systems IG-500N GPS IMU (SPG Systems)

The IG-500N uses a Wi-Sys Communications Inc. WS3910 High Gain, Low Noise GPS Antenna (Wi-Sys Communications Inc., 2014) that mounts to the top of the aircraft and is connected to HAMMR through a subminiature version A (SMA) input shown on the left side of Figure 69. Figure 71 shows the GPS antenna as received from SBG Systems. To comply with aircraft regulations the co-axial cable output of the antenna was changed to an RG-142 cable.

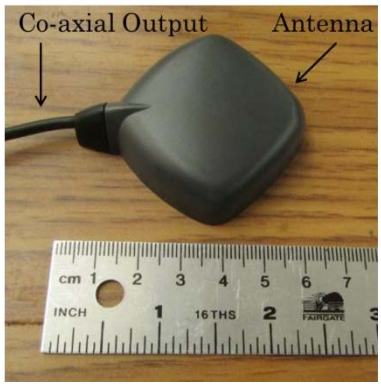


Figure 71: Wi-Sys Communications Inc. WS3910 High Gain, Low Noise GPS Antenna (Wi-Sys Communications Inc., 2014).

### 3.5.4 Scanning Motor

The force to scan the scanning flat reflector comes from a QCI-A34HK-1 NEMA-34 servo motor from Quick Controls Inc. shown in Figure 72. The QCI-A34HK-1 has 700 oz-in of continuous torque and an optical encoder with a resolution of 16000 counts per revolution that records the precise position of the motor at all times (Quicksilver Controls Inc., 2014). The motor is controlled by a SilverSterling S3-IG controller also from Quick Controls Inc. (Quick Silver Controls, Inc., 2011) shown in Figure 73. This controller runs the software that controls the motor and communicates with the HAMMR onboard computer to change the motor program and monitor motor parameters in real time. The S3-IG controller also uses power from the +48 V Mean Well power supply to run the motor.

Figure 72: Quick Controls Inc. QCI-A34HK-1 Servo Motor (Quicksilver Controls Inc., 2014)


Figure 73: Quick Controls Inc. SilverSterling S3-IG Controller (Quick Silver Controls, Inc., 2011).

### 3.5.5 Signal Processing and Digital Back-end

The signal conditioning and digital portion of the HAMMR system consists of analog back-end boards (ABEBs), a digital buffer board, a field programmable gate array (FPGA), and an internal computer. These systems digitize the analog signals from the radiometers, send and receive control signals for the radiometers and motor, and synchronize the outputs from the HAMMR sub-systems to be stored in the final acquisition files. The ABEBs and digital back-end board were designed, fabricated and tested by Scott Nelson and Dr. Xavier Bosch-Lluis of the CSU MSL. Detailed discussions of the design and testing of the entire digital and analog back-end can be found in (Nelson, Fall 2013).

#### 3.5.5.1 Analog Back-End Boards (ABEBs)

The output of the radiometers is an analog signal that must be digititized before being stored in the internal computer. Each ABEB, shown in Figure 74, integrates the radiometer output in time, amplifies the analog signal, and digitizes the signal before sending the signal to the digital buffer board. A total of 7 ABEBs providing 28 channels is used in the HAMMR system and can be seen in their final configuration in Figure 75 a).

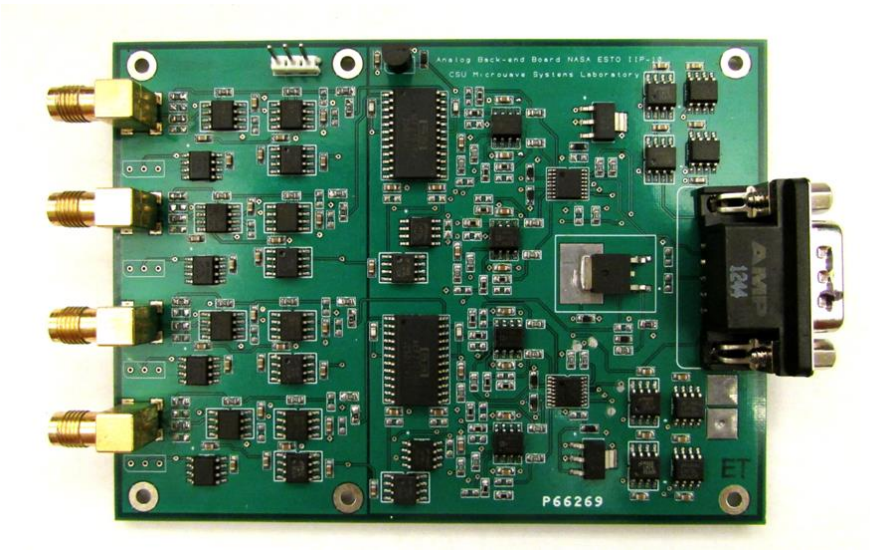


Figure 74: Analog Back-End Board (Nelson, Fall 2013)

#### 3.5.5.2 Digital Buffer Board and FPGA

The digital buffer board is controlled by the FPGA and is used to issue control signals to the radiometers, ABEBs, and motor and drives them at the appropriate voltage levels. It also buffers radiometer data as it is read by the FPGA. The digital buffer board interfaces directly with the FPGA and can be seen in Figure 75 b).

The FPGA used in HAMMR is a BeMicro SDK FPGA and can be seen in Figure 75 c).

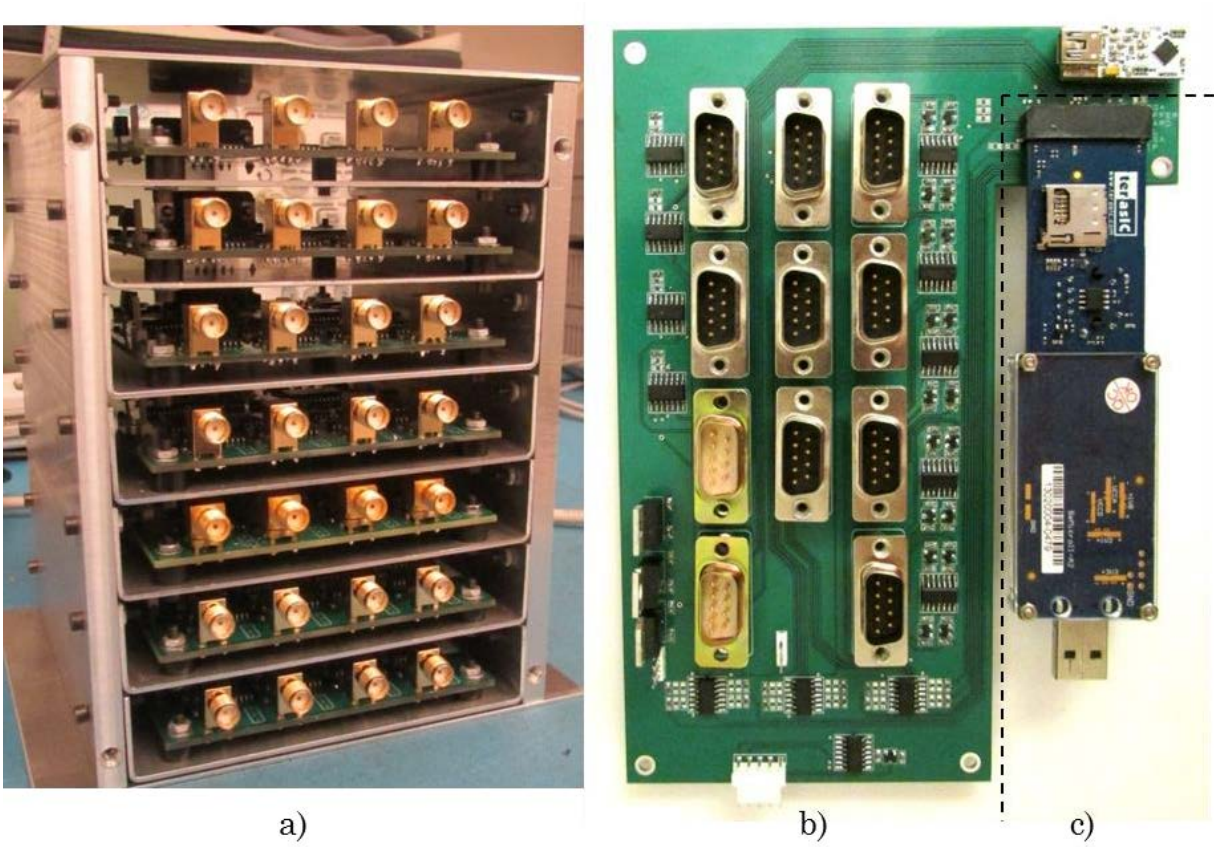


Figure 75: Overview of the Signal Conditioning and Digitizing Sub-System, a) ABEB Stack in Internal Chassis, b) Buffer Board, and c) FPGA (Nelson, Fall 2013)

#### 3.5.5.3 Internal Computer

The internal computer in HAMMR is a MXE-5301 from Media Wave PC seen in Figure 76. This computer features an i7-2710QE processor, 8 GB of DDR3 memory, 6 USB ports, and 4 Ethernet ports (Mediawave PC, Inc.). It is powered by an AC-DC rectifier that is mounted separately in the system. The MXE-5301 was tested running at 100% load between -20 and 60° C by Media Wave PC before it was shipped out. The hard drive in the MXE-5301 was upgraded to a Samsung 840 Pro

Series Solid State Drive (SSD) to add resistance to vibration and increase the speed of the system. This is particularly advantageous for the start and shutdown times for the computer which limit how quickly acquisitions can be started and the instrument can be powered off respectively. The MXE-5301 was chosen because it has fast hardware, a large number of Ethernet and USB ports, and because it is a compact ruggedized system that is passively cooled.


Figure 76: The MXE-5301 Used as the Internal Computer in HAMMR (Mediawave PC, Inc.).

# Chapter IV. Blackbody Calibration Target

For the IIP-10 project a blackbody calibration target is needed to perform end to end calibration of the radiometer channels and to verify the accuracy of the internal calibration methods by providing a stable reference brightness temperature that can be used in the calibration method explained in Section 2.2.3 to convert measured voltages to brightness temperatures. This chapter discusses the design, fabrication, and verification of this target.

## 4.1 Background

The purpose of this calibration target is to create a close approximation of a blackbody. A blackbody is a body that emits electromagnetic radiation according to Planck's law, meaning that it emits a brightness temperature proportional to its physical temperature. This brightness temperature is used to perform external calibration of the radiometers across the entire range of operating frequencies (18-183 GHz). This is accomplished by creating a structure that absorbs all incident energy on it and emits a known brightness temperature across a desired bandwidth for a given physical temperature.

There are three parameters that define how electromagnetic energy interacts with a dielectric material in this situation, effective emissivity ($e_e$), effective reflectivity ($\Gamma_e$), and effective transmissivity ($U_e$). Effective here refers to a steady-state solution that takes into account all multiple reflections within the dielectric. For a material

in thermodynamic equilibrium the sum of these three quantities will be equal to one (F. Ulaby, 1982).

$$e_e + \Gamma_e + \Upsilon_e = 1 \qquad \text{(IV.1)}$$

For the following analysis two major assumptions are made. The first is that the microwave absorber material, Eccosorb HR-10, used in this target is an opaque material, $U_e$=0. This is a valid approximation for anything with a metal base layer as metal has a $U_e$ equal to zero.

The second assumption is that we can use a geometrical optics (GO) approximation for this analysis. GO is an excellent assumption when the wavelength is small compared with the size of the structures that the energy is interacting with. The simplification in GO analysis comes from the disregard of scattering effects such as diffraction and interference and the assumption that all reflections are specular.

Specular reflection is described by Fesnel reflection laws when the reflecting boundary is perfectly smooth and is illustrated in Figure 77 a). The specular component of a reflection is often referred to as the coherent scattering component. As the reflecting surface becomes rougher the reflection becomes less specular and the scattered components, also known as the diffuse or incoherent components, increase in energy (F. Ticconi, 2011). Figure 77 b) and c) show the relative contributions of coherent scattering components for slightly rough and very rough surfaces respectively.

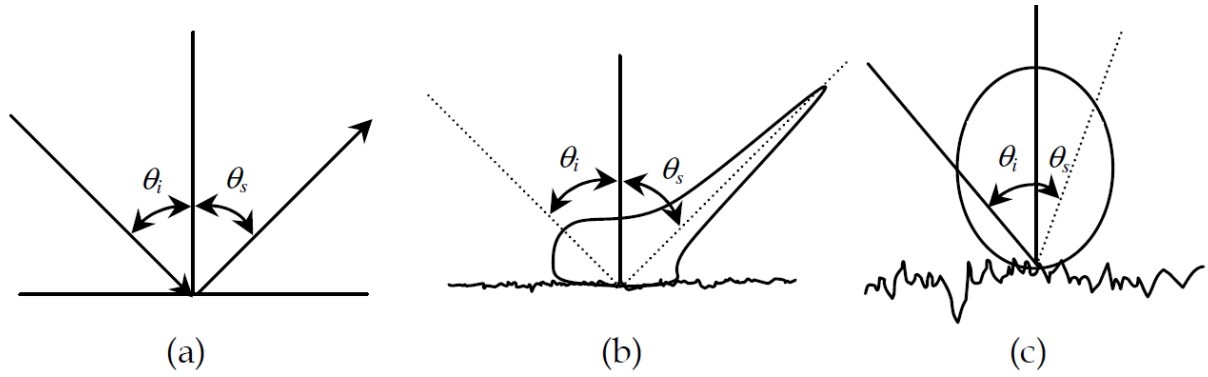


Figure 77: Relative contributions of coherent and diffuse scattering components for different surface-roughness conditions, a) specular, b) slightly rough, c) very rough (F. Ticconi, 2011)

If we make the approximation that the then it can be easily shown why this geometry for the calibration target will be effective.

Using arbitrary numbers, thus setting $e_e = 0.8$, $|\Gamma_{abs}|^2 = 0.2$ and the power of the incident wave as $P_{in}$ Figure 78 shows what happens to radiation incident on the calibration target.

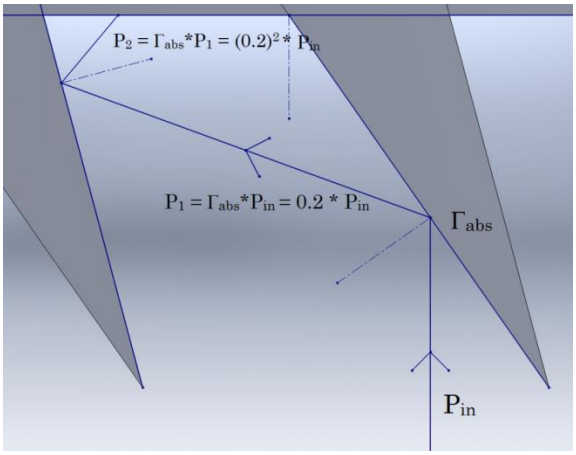


Figure 78: Illustration of Angle Dependencies

The power is reduced by a factor of $|\Gamma_{abs}|^2$ every bounce so if $|\Gamma_{abs}|^2$= 0.2 then ten bounces would reduce the power of the outgoing wave to $P_{ref}$ = $P_{in}$ * $(0.2)^{10}$, or by -70 dB.

$$P_1 = |\Gamma_{abs}|^2 * P_{in} = 0.2 * P_{in} \quad \text{(IV.2)}$$

$$P_2 = |\Gamma_{abs}|^2 * P_1 = 0.2^2 * P_{in} \quad \text{(IV.3)}$$

## 4.2 Design

Figure 79 shows a side view of the calibration target showing five critical design parameters, i.e., D, the distance between each tooth, H, the height of each tooth, BH, the height of the base layer of absorber, Theta1, the angle between the flat surface and the back of the tooth, Theta2, the angle between the flat surface and the front of the tooth, and T, the thickness of the tooth at H = H/2.

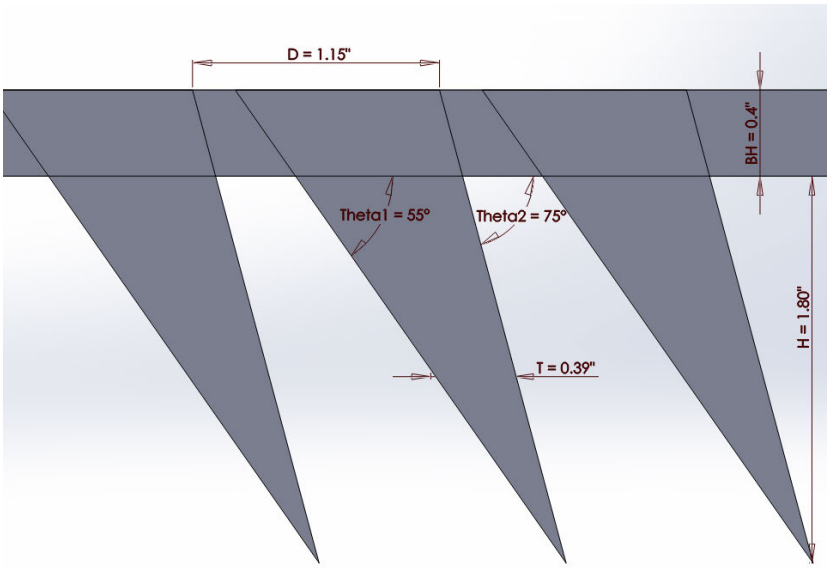


Figure 79: Side view of the Calibration Target with Dimensions Labeled

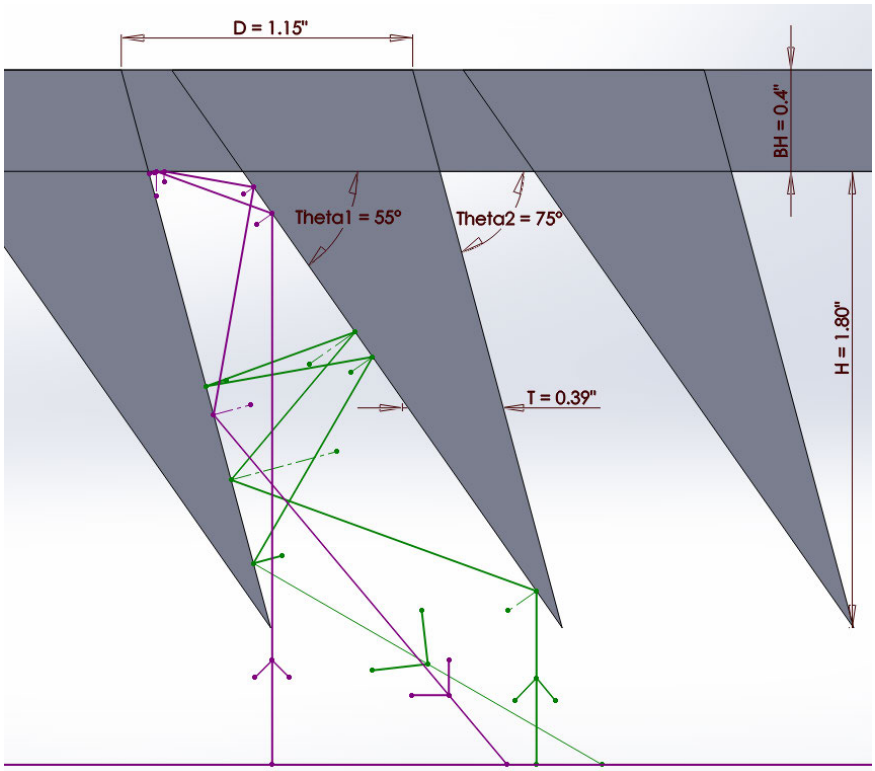


Figure 80: Geometric Optics Ray Trace of Two Limiting Cases

Figure 80 shows a Geometrical Optics (GO) analysis of two electromagnetic waves orthogonally incident on the base layer of the calibration target. The two waves shown (green and magenta) enter the calibration target in the two limiting cases with respect to tooth position. The magenta wave enters just in front of a tooth tip and the green wave enters directly behind the tooth tip. Any other waves will be between these two cases. The waves reflect from the surface of the teeth with the angle of incidence equal to the angle of reflection. The reflected wave is attenuated on each bounce until it is reflected back out of the calibration target. The attenuation upon each bounce depends on the reflectivity of the tooth material, in this case Eccosorb HR, which is a function of the thickness of the material and the electromagnetic frequency. Each wave will bounce a number of times and then will leave the calibration target. The total wave attenuation is a function of the reflectivity, BH, H, Theta1, Theta2, and D.

The reflectivity in dB of Eccosorb HR up to about 67 GHz is shown in Figure 81, where HR-10 and HR-25 have thicknesses of 0.4" and 1" respectively. The reflectivity of Eccosorb HR above 67 GHz is not provided by the manufacturer which was a source of uncertainty for this design.

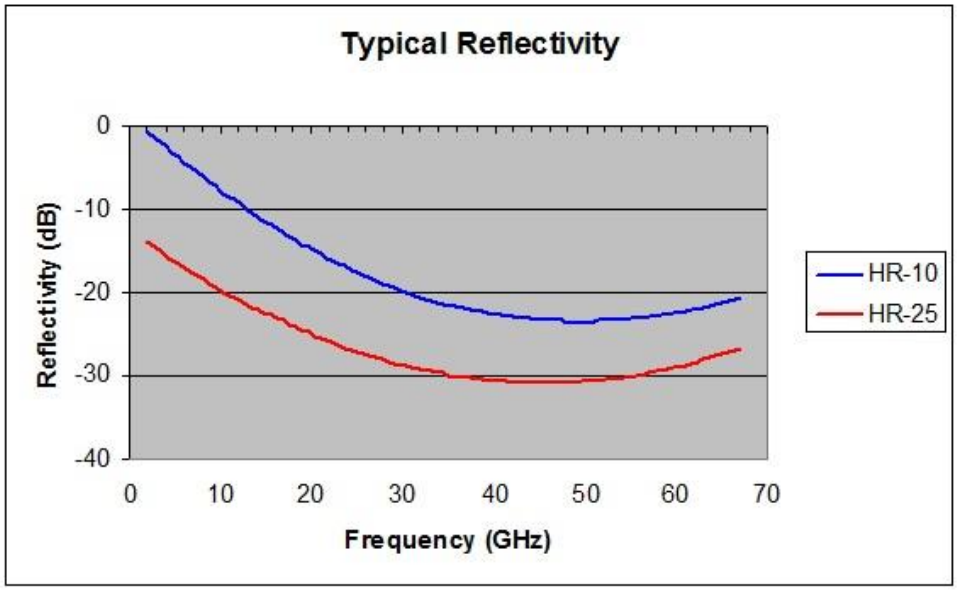


Figure 81: Reflectivity of Eccosorb HR. (Emerson & Cuming, 2013)

Using these values, the power attenuation for a certain number of bounces at 18 GHz has been calculated and is shown in Table 4.

Table 4: Power Attenuation for Different Absorber Thicknesses

| Eccosorb Thickness | Emissivity | Emissivity after 3 Bounces | Emissivity after 5 Bounces | Emissivity after 7 Bounces |
|---|---|---|---|---|
| 0.4" | 0.949881277 | 0.999874107 | 0.999999684 | 0.999999999 |
| 1" | 0.996018928 | 0.999999937 | 1.000000000 | 1.000000000 |

### 4.2.1 Analysis of Design Parameters

This section presents an analysis of the six primary design parameters and how they affect the target performance.

#### 4.2.1.1 Distance Between Teeth (D)

This design parameter is important because we do not want any waves to bounce directly back out of the calibration target without multiple reflections as is shown in Figure 82. A smaller D also means that the wave will bounce more times because it will not travel as far upward between bounces. The distance between teeth will only have an effect as wavelength decreases below 2D for normal pyramidal absorbers that are not tilted (Kuester, 1994), so the design should keep $D > \lambda_{18GHz}/2$ as a minimum value.

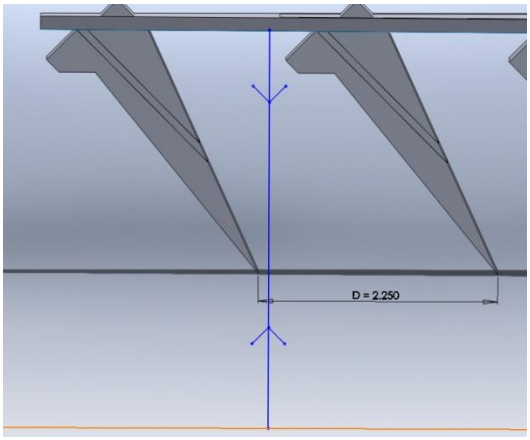


Figure 82: Unwanted Ray Path if D is Too Large

#### 4.2.1.2 Theta1 ($\theta_1$)

$\theta_1$ has considerable effects on the thickness of the tooth (T) as well as how the waves will bounce. It defines the slope of the first surface that a wave will hit and therefore has a large impact on the total number of reflections that the wave will have before leaving the calibration target. There will be further discussion on this

in the next section. For this configuration $\theta_1$ can vary between 0-90°, based on the initial GO analysis the optimal range will be somewhere between 50° and 80°.

#### 4.2.1.3 Theta2 ($\theta_2$)

$\theta_2$ has an equally important effect on T and the number of bounces a wave will experience as $\theta_1$ does. For this configuration $\theta_2$ can vary between 0-90°, based on the initial GO analysis the optimal range will be somewhere between 65° and 85°.

#### 4.2.1.4 Thickness (T)

The thickness of the tooth is very important because if T is not thick enough, the signal will not have enough attenuation. This can be negated by ensuring that each wave will have a high number of bounces before leaving the target, as the power of the signal is greatly reduced after each bounce.

A source of uncertainty is the dependence of thickness and incidence angle on the Eccosorb's reflectivity. If the reflectivity becomes too low as T decreases then the transmissivity will increase and waves will pass right through the tips of the teeth. This could possibly be compensated for by making the base layer resemble a saw tooth as opposed to being flat. The angled sections would change the angle of reflection allowing the wave to bounce more thus increasing the attenuation.

#### 4.2.1.5 Tooth Height (H)

The height of the target influences the number of total bounces the wave undergoes before exiting the target. The larger H is, the more bounces the wave will experience; however, H is limited by the envelope of the spinning flat reflector. The

maximum value H+BH can be is 2.2" which allows for a 0.25" clearance between the calibration target and the flat reflector.

#### 4.2.1.6 Thickness of Base Layer (BH)

Destructive and constructive interference that occur because of multiple reflections within the wedges are an important consideration in the design of a calibration target. Varying the thickness of the base layer of absorber can change the frequency dependent reflection coefficient of the absorber (Kuester, 1994). Increasing this thickness decreases the reflection at low frequencies while slightly increasing it at higher frequencies (Kuester, 1994).

### 4.2.2 Summary of Design Parameter Analysis

The analyses of these parameters have yielded seven main design considerations.

**1.** The end of the teeth must be cut into a sharp point to avoid a single reflection off of the bottom of the tooth out of the calibration target.

**2.** There is a potential problem if a ray hits the tooth on the thinnest edge and goes straight through to the base layer. The ray could then bounce directly off of the base layer and back through the tip of the tooth undergoing very little attenuation.

**3.** The distance between the teeth cannot be too large or the rays will only reflect once off of the flat top of the reflector and then out of the calibration target as shown in Figure 4.

**4.** The angle $\theta_1$ must be >45° so that the incident rays will reflect upwards into the calibration target. The angle $\theta_2$ must always be greater than $\theta_1$ in order to maintain a pointed tooth tip.

**5.** Following Snell's law the ray will be reflected off the first tooth at an angle equal to $\theta_1$. It will then hit the adjacent tooth with an incidence angle equal to $[\theta_1 - (\theta_2 - \theta_1)]$ and will reflect at that same angle. This continues on until the incidence angle drops below 90° or the wave bounces off of the base layer at the top. This is shown in Figure 5.

**6.** The height of the teeth (H) plus the height of the base layer (BH) must be ≤ 2.2". This is limited by the envelope of the spinning flat reflector. We want the B+BH = 2.6 cm (2.2").

**7.** The number of reflections is controlled by the parameters H, BH, D, $\theta_1$, and $\theta_2$. We want to balance these parameters to obtain the maximum number of reflections possible.

### 4.2.3 Parameter Interdependencies

There are some important relationships between $\theta_1$ and $\theta_2$ that should be discussed. These relationships are illustrated in Figure 83. If a wave is coming straight up into the calibration target (blue line in Figure 83) then it will hit the absorber material at an incidence angle equal to $\theta_1$. Following Snell's law it will be reflected at an angle equal to $\theta_1$. It will then hit the adjacent tooth with an incidence angle equal to

$\theta_1$ - ($\theta_2$ - $\theta_1$) and will reflect at the same angle. This continues on until the incidence angle drops below 90° or the wave bounces off of the base layer at the top. As D become larger the waves travel further upward towards the base between each bounce leading to less overall bounces, therefore by reducing D we will increase the number of bounces.

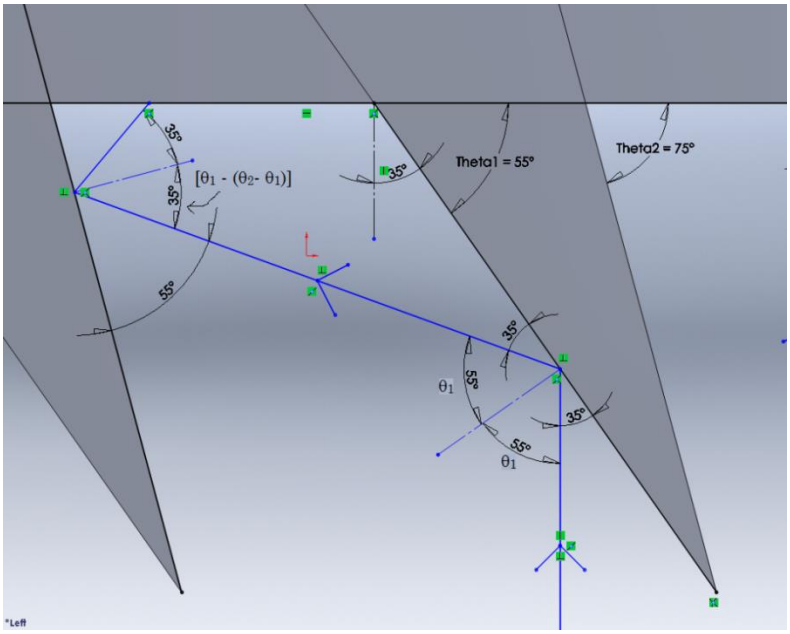


Figure 83: Illustration of Angle Dependencies

Based on this initial GO analysis the calibration target should be designed to minimize D and the difference between $\theta_2$ and $\theta_1$ while maintaining geometries that allow the target to work at all frequencies.

### 4.2.4 Thermal Considerations

Thermal gradients can be a problem in a blackbody calibration target as the emitted energy of the target is proportional to the physical temperature of the target. In

order to monitor the physical temperature of the target eight thermistors were embedded in the microwave absorber at various heights throughout the target giving temperature readings once every second. The locations and heights of these thermistors are shown in Figure 84.

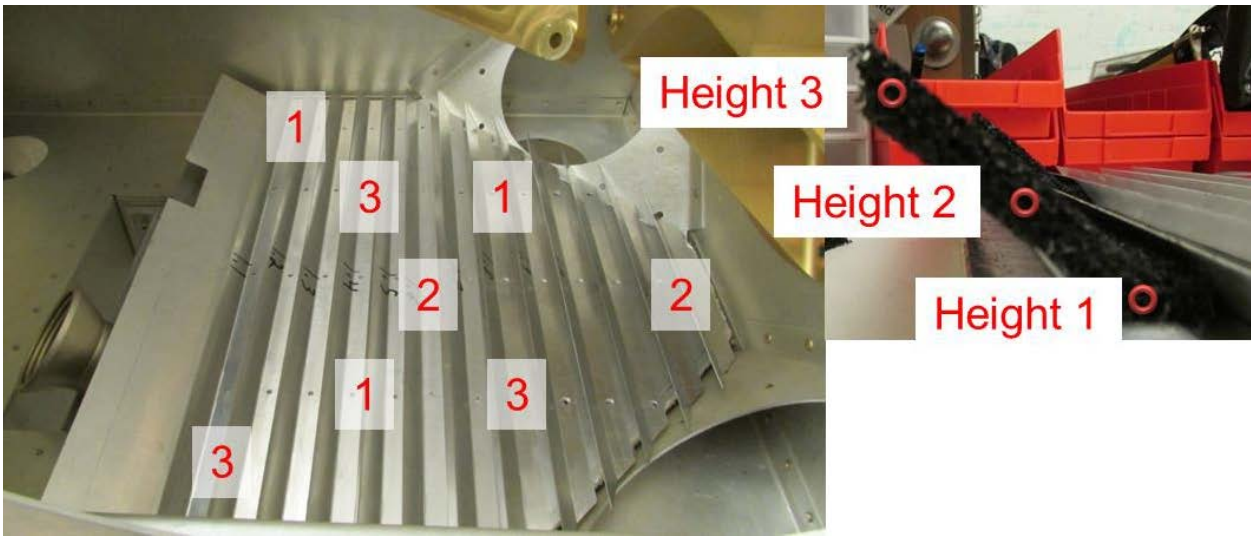


Figure 84: Picture of Fabricated Calibration Target Indicating Where Thermistors Were Placed, Where the Numbers Indicate Thermistor Height

To mitigate thermal gradients a base layer of insulation was used prevent thermal gradients caused from electronics and power supplies mounted in the main bench of the HAMMR chassis. To further thermally isolate the blackbody calibration target plastic screws were used to attach the target to the HAMMR chassis.

## 4.3 Fabrication

As fabrication of the calibration target began, certain design parameters needed to be changed due to the feasibility of cutting the microwave absorber. The design

was modified to match what is shown in Figure 85 and the following materials were used.

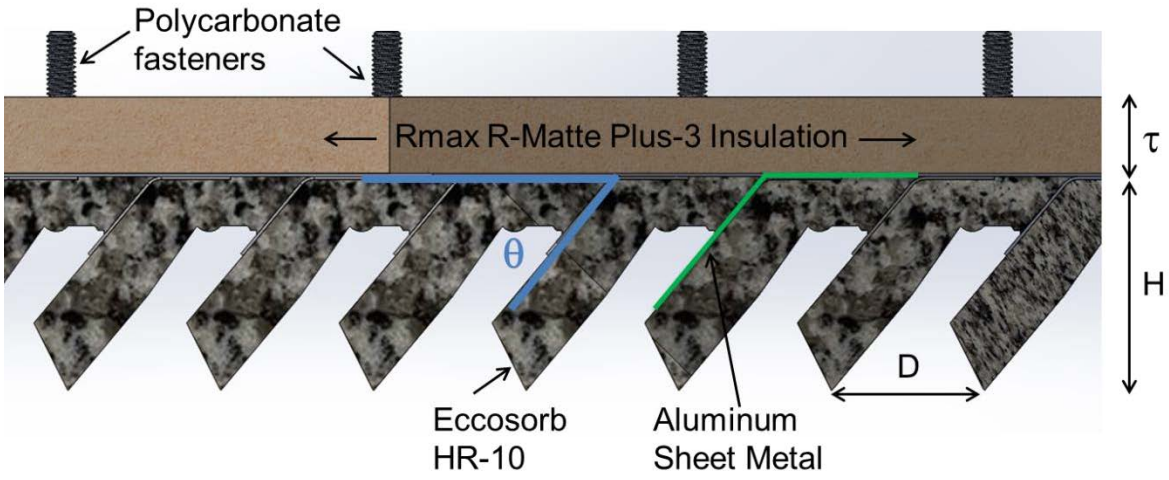


Figure 85: Solidworks Model of Blackbody Calibration Target with Major Design Parameters Labeled.

The base layer represented by τ is Rmax R-Matte Plus-3 insulation, which is a common household insulator. The purpose of the insulator is to thermally isolate the calibration target from the HAMMR chassis. This will help prevent thermal gradients cause by the heat of power supplies and other electronics. The final thickness of this material is 1.25 cm (0.5").

To secure the target to the chassis polycarbonate fasteners were used. These fasteners are thermal insulators and help reduce the thermal transfer between the HAMMR chassis and the target.

Support and structure for the microwave absorber is provided by aluminum sheet metal tabs riveted to a flat aluminum sheet. The tabs have a vertical height H, of

3.95 cm (1.56”). This dimension is constrained by the available space in the HAMMR chassis. The lengths of the tabs was calculated so that the space between the tips of the absorbers, D, is equal to 2.54 cm (1”). These tabs were bent at a 60° angle represented by the blue θ shown in Figure 85. The completed sheet metal and insulation portion of the target before microwave absorber has been added can be seen in Figure 86.

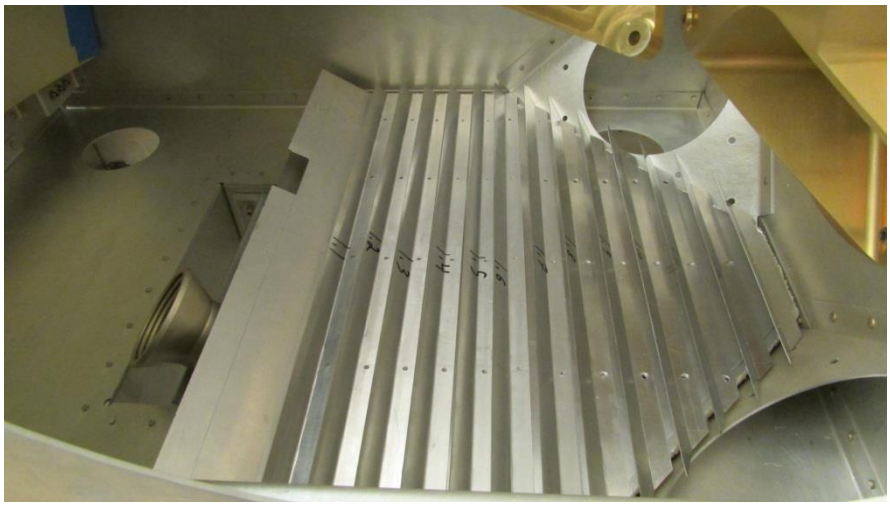

Figure 86: Sheet Metal Target Before Eccosorb HR was Added

The Eccosorb HR was then cut to the right dimensions by using a table saw with an angled blade with a piece of heavy foam on top as shown in Figure 87.

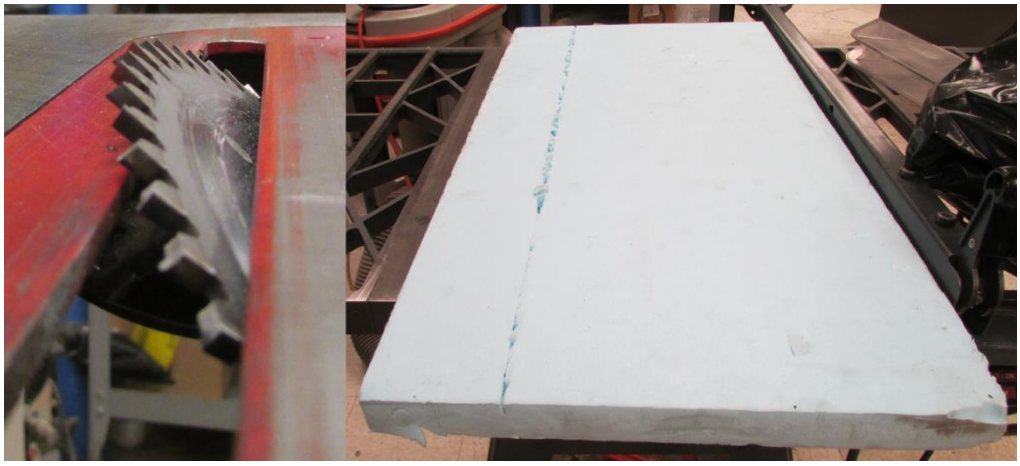

Figure 87: Setup Used to Cut the Eccosorb HR Microwave Absorber

This method of cutting Eccosorb HR results in consistent and repeatable cuts that meet the tooth sharpness requirements for the target. Many other methods were attempted to cut the Eccosorb, such as using a razor blade or hack saw with a mechanical guide but these methods do not result in sufficient repeatability or smoothness.

After cutting the Eccosorb the thermistor wiring was routed and glued into place leaving the thermistors in the correct location as shown in Figure 88 with the thermistors circled in red. The Eccosorb HR was then affixed to the sheet metal structure of the target using Emerson & Cuming Eccostock 13-111NF Contact Adhesive. These steps can be seen in Figure 89 and Figure 90. The target mounted in the system can be seen in Figure 91.

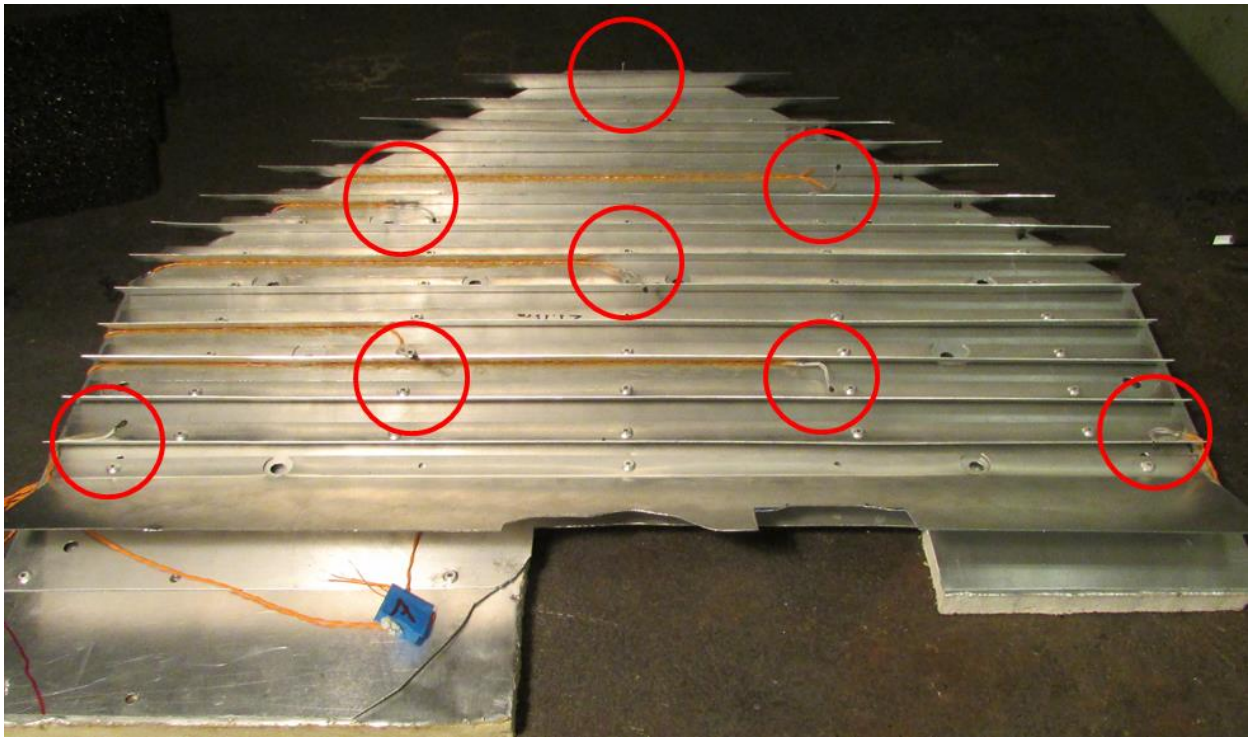

Figure 88: Calibration Target with Thermistors Installed Before Eccosorb was Added

Figure 89: Process of Gluing Eccosorb to Target (1/2)

Figure 90: Process of Gluing Eccosorb to Target (2/2)

Figure 91: Calibration Target In Chassis

Once the target was finalized Eccosorb HR-10 was glued to the inside of the chassis to minimize unwanted internal reflections and external radiation while viewing the target. This is shown in Figure 92.

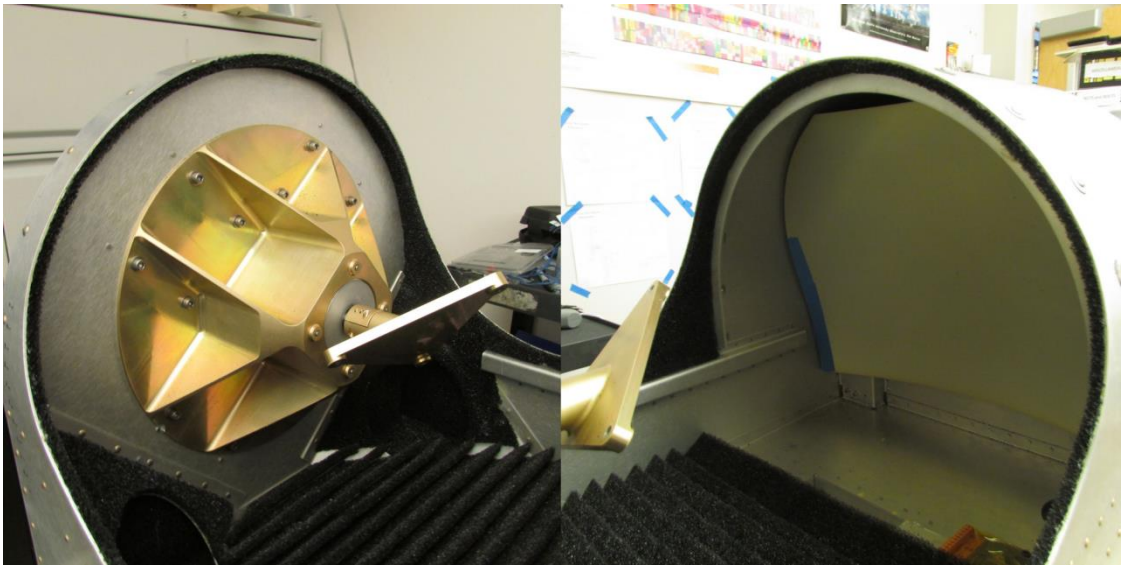

Figure 92: Inside of Chassis Lined with Eccosorb HR-10

## 4.4 Verification of Performance

To evaluate the performance of the internal blackbody calibration target a comparison was done between the internal calibration target with a final thickness of 5.2 cm (2.05") and a pyramidal absorber with pyramid dimensions of 7 x 7 x 15.5 cm (2.75 x 2.75 x 6.1") and a base thickness of 5 cm (1.96"). The following sections present results measured in antenna temperature vs motor position angle averaged over 29 seconds. The standard deviation is calculated using 10° of motor position angle data.

The goal of the calibration target is to present a brightness temperature that is constant across a range of motor position angles and to have a ratio of measured antenna temperature to physical temperature that is close to one.

The results for all radiometer channels are summarized in Table 5.

Table 5: Summary of Antenna Temperature Standard Deviation of the Internal and Pyramidal Calibration Targets for All Radiometer Channels

| Radiometer | Frequency | Internal Target Standard Deviation | Pyramidal Target Standard Deviation |
|---|---|---|---|
| **Microwave QV** | 18.7 GHz | 0.3 | 0.3 |
| | 23.8 GHZ | 0.2 | 0.1 |
| | 34.0 GHz | 0.3 | 0.4 |
| **Microwave QH** | 18.7 GHz | 0.4 | 0.5 |
| | 23.8 GHZ | 0.3 | 0.2 |
| | 34.0 GHz | 0.2 | 0.1 |
| **Millimeter-Wave Window** | 90 GHz | 0.2 | 0.2 |
| | 130 GHz | N/A | N/A |
| | 168 GHz | 0.6 | 1 |
| **Millimeter-Wave Sounding 118.75 GHz** | 0 MHz | N/A | N/A |
| | 250 MHz | 0.4 | 0.6 |
| | 500 MHz | 0.2 | 0.5 |
| | +1 GHz | 0.2 | 0.2 |
| | +2 GHz | 0.3 | 0.5 |
| | +3 GHz | 0.3 | 0.5 |
| | +4 GHz | 0.3 | 0.7 |
| | +5 GHz | 0.2 | 0.7 |
| | +6 GHz | N/A | N/A |
| | +7 GHz | N/A | N/A |
| | +8 GHz | N/A | N/A |
| **Millimeter-Wave Sounding 183.31 GHz** | -1GHz | 0.4 | 0.5 |
| | -2 GHz | 0.3 | 0.4 |
| | -3 GHz | 0.4 | 0.3 |
| | -4 GHz | 0.3 | 0.2 |
| | -5 GHz | 0.2 | 0.4 |
| | -6 GHz | 0.3 | 0.3 |
| | -7 GHz | 0.4 | 0.3 |
| | -8 GHz | 0.2 | 0.4 |

### 4.4.1 Microwave Radiometers

Figure 93 shows the antenna temperature vs motor position angle for both polarizations of the 18.7, 23.8, and 34.0 GHz microwave radiometer channels. The QV polarization is shown by the blue line and the QH polarization is shown by the cyan line. The internal calibration target had an antenna temperature standard

deviation within 0.1 K of the values for the pyramidal absorber for all frequencies and polarizations. This shows that the internal calibration target can successfully be used for calibration of the microwave channels.

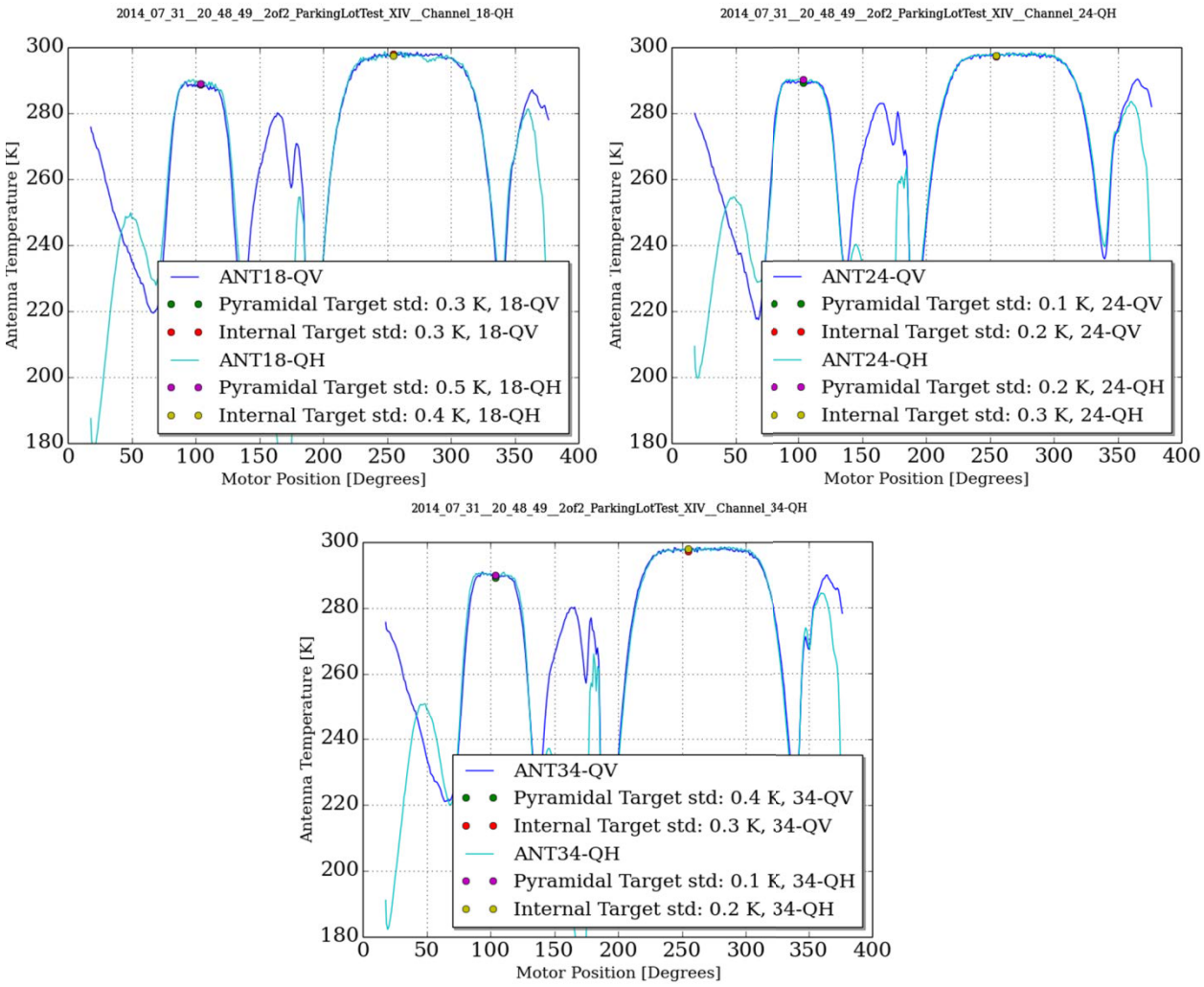


Figure 93: Antenna Temperature vs Motor Position Angle for QV and QH Polarizations of the 18.7, 23.8, and 34.0 GHz Microwave Channels

### 4.4.2 Millimeter-Wave Window Radiometers

Figure 94 shows the antenna temperature vs motor position angle for the 90, 130, and 168 GHz mm-wave window channels. For this test the 130 GHz channel was

not functional. At 90 GHz the internal and pyramidal targets had the same antenna temperature standard deviation and for 168 GHz the internal target performed much better than the pyramidal. These results show that the internal calibration target can successfully be used for calibration of the mm-wave window channels.

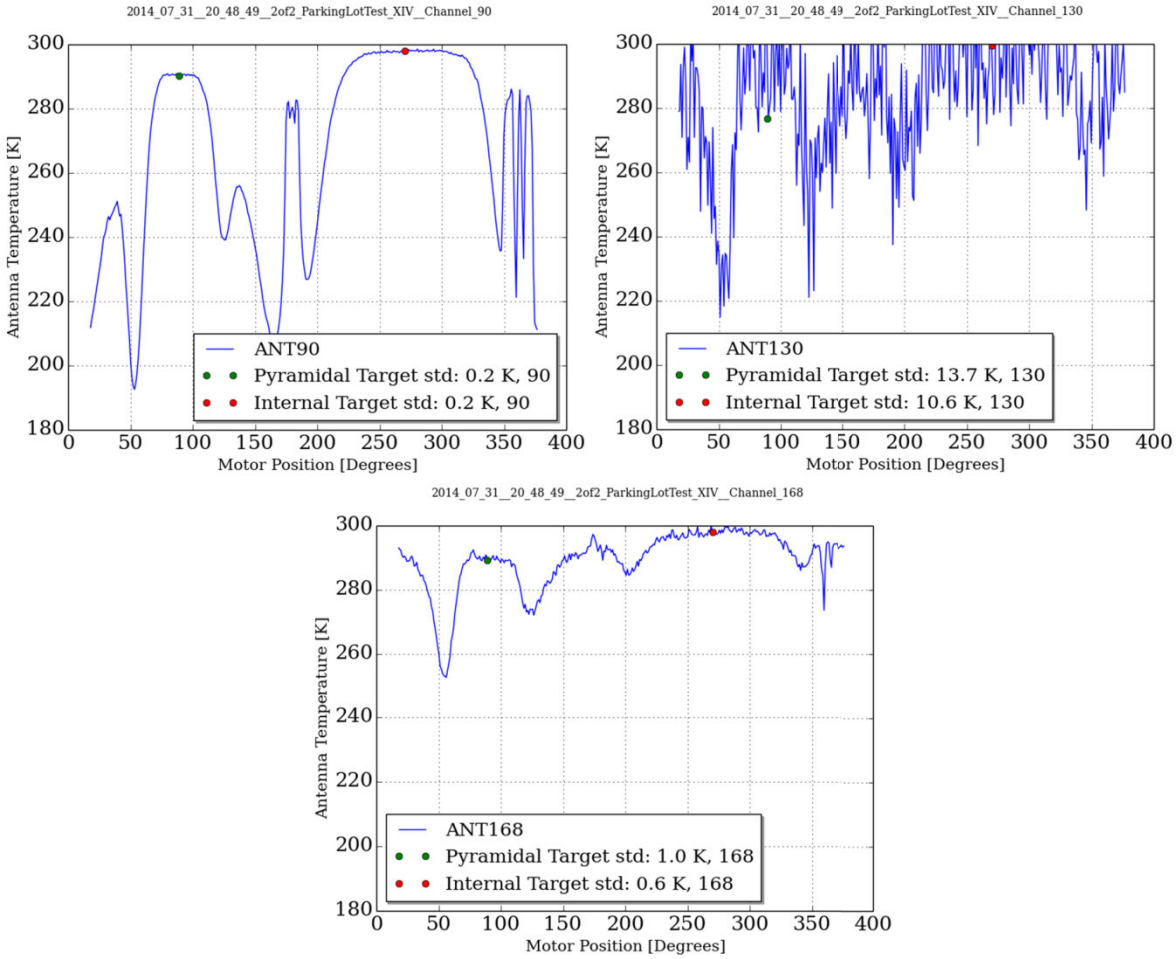


Figure 94: Antenna Temperature vs Motor Position Angle for the 90, 130, and 168 GHz Millimeter-Wave Window Channels

### 4.4.3 Millimeter-Wave Sounding Radiometers

Figure 95 shows the antenna temperature vs motor position angle for the 118.75 GHz mm-wave oxygen sounding channels. For every channel the internal

calibration target had an equal or lower antenna temperature standard deviation than the pyramidal target showing that the internal calibration target can successfully be used for calibration of the mm-wave window channels.

Figure 96 shows the antenna temperature vs motor position angle for the 183.31 GHz mm-wave water vapor sounding channels. The internal calibration target did not outperform the pyramidal target with respect to antenna temperature standard deviation for every channel. However, the internal target did have an antenna temperature standard deviation equal to or lower than the pyramidal target for five out of the eight channels. When the antenna temperature standard deviation of all channels is summed the internal target outperforms the pyramidal target by 0.3 K. showing that the internal calibration target can successfully be used for calibration of the mm-wave window channels.

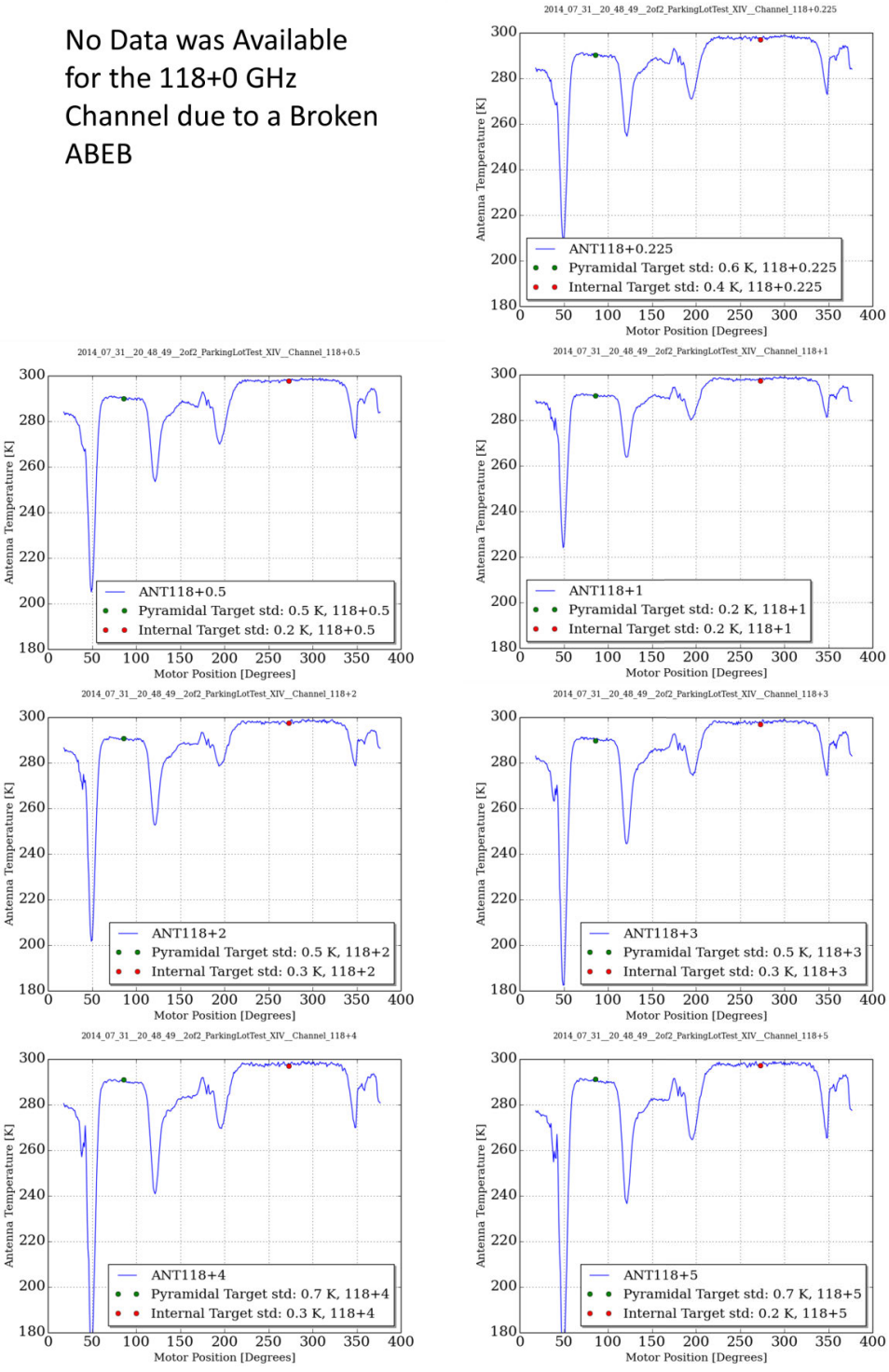


Figure 95: Antenna Temperature vs Motor Position Angle for the 118.75 GHz Millimeter-Wave Oxygen Sounding Channels

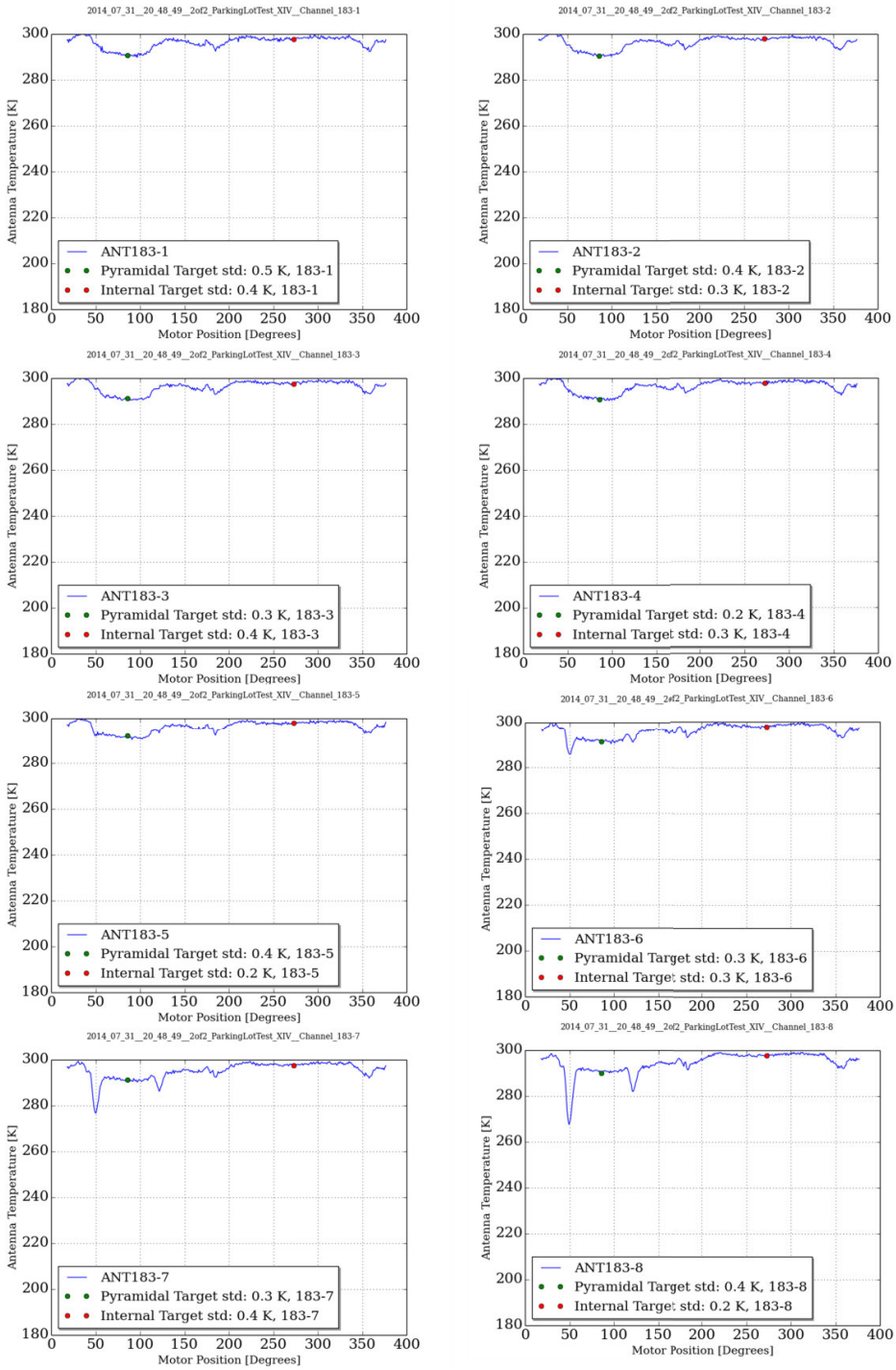


Figure 96: Antenna Temperature vs Motor Position Angle for the 183.31 GHz Millimeter-Wave Water Vapor Sounding Channels

### 4.4.4 Comparison of Antenna Temperature Vs Physical Temperature

Another metric of performance for the internal calibration target is the ratio of measured antenna temperature to physical temperature. This ratio should be close to one and is important because as this ratio decreases the resolution of the radiometer calibration is reduced. This is because if the ratio is very low, say 0.1, the antenna temperature is not very sensitive to changes in physical temperature. For example a ratio of 0.1 with a physical target temperature of 300 K would only produce an antenna temperature of 30 K. If the physical temperature rose to 305 K the resulting antenna temperature would be 30.5 K which can be very difficult to distinguish without a good calibration. As this antenna temperature is used to calibrate the instrument it is very important to have a good ratio.

Figure 97 and Figure 98 present the ratio of antenna temperature to physical temperature for all radiometer channels used in HAMMR. During these tests the 130 GHz radiometer was not functional so the results for that channel are not present. Because the internal calibration target is usually used to calibrate the instrument, the calibration for these plots was done by using a pyramidal absorber at ambient temperature instead of the internal calibration target as the hot load. Figure 98 shows that the ratio of antenna temperature to physical temperature for all radiometer channels is above 0.965 demonstrating that the target is well suited for use in calibration for all frequencies.

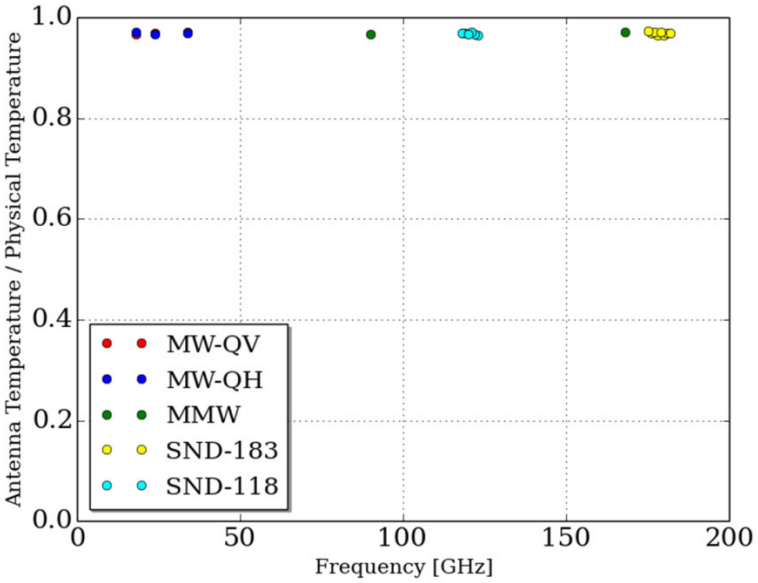


Figure 97: Antenna Temperature Divided by Physical Temperature of Internal Calibration Target for All Radiometer Channels

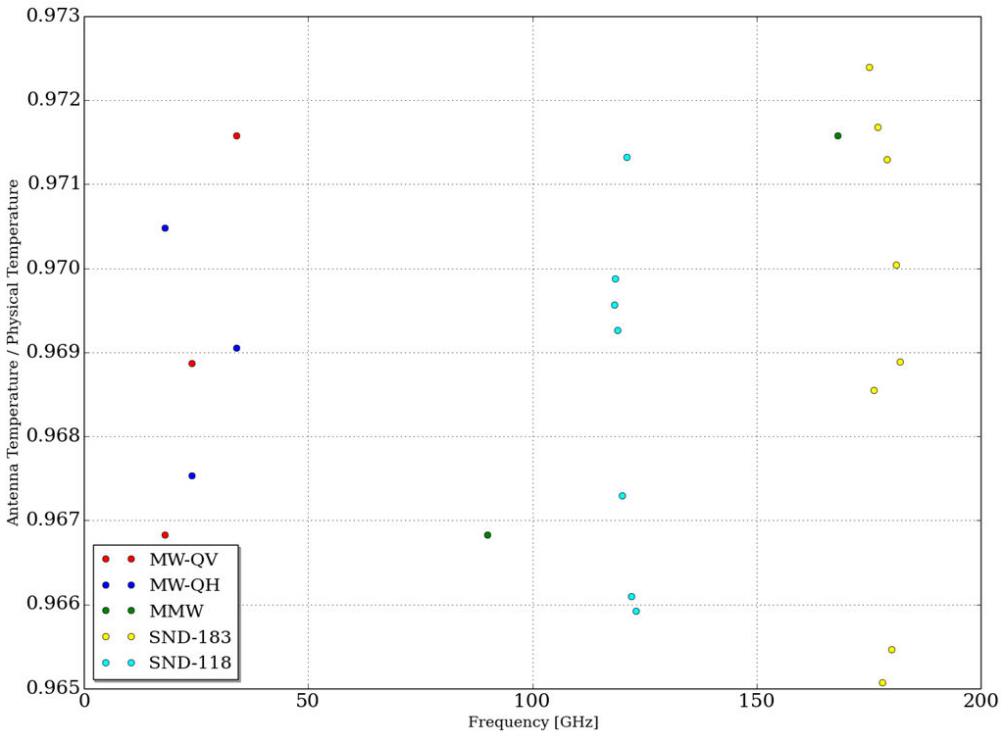


Figure 98: Zoom of Antenna Temperature Divided by Physical Temperature of Internal Calibration Target for All Radiometer Channels

### 4.4.5 Thermal Analysis

The physical temperature of the calibration target is designed to be homogenous and stable across the target. The mean temperature, mean temperature standard deviation, minimum, and maximum temperatures of the calibration target for two tests are presented in Table 6. The mean temperature of the target stayed pretty consistent on the ground and in flight with a standard deviation of 1.08 and 1.06 °C respectively. The calibration target temperature was much colder in flight than on the ground. One of the biggest obstacles in keeping the internal calibration target temperature homogenous across its face is that when the flat reflector begins to rotate a breeze is created across the target that introduces thermal gradients.

Table 6: Mean Temperature, Standard Deviation and Temperature Minimum of the Internal Calibration Target as a Whole for Both a Ground and Flight Test

| | Mean Temperature (°C) | Standard Deviation (°C) | Minimum Temperature (°C) | Maximum Temperature (°C) | Largest Temperature Difference (°C) |
|---|---|---|---|---|---|
| **Parking Lot Test** | 28.2 | 1.08 | 26.63 | 29.7 | 3.02 |
| **Lake Powell Flight** | 16.31 | 1.06 | 15.21 | 18.67 | 3.46 |

The temperature of each internal calibration target thermistor with respect to the center thermistor temperature was also analyzed and presented in Table 7. It was found that the center area of the target was the coldest. The bottom left of the target has an analog to digital converter for digitizing the thermistor voltages that creates heat causing that area of the target to be the hottest. The left side of the target had the highest temperatures due to the wind created by the scanning of the

flat reflector. Overall the thermal performance of the target is good enough to be used in the radiometer calibrations.

Table 7: Mean Difference of Temperature for Each Thermistor and the Center Thermistor of the Internal Calibration Target for Both a Ground and Flight Test

| | Parking Lot Test | | Lake Powell Flight | |
|---|---|---|---|---|
| | Mean Difference in Temperature from Center Thermistor (°C) | Standard Deviation of Temperature Difference from Center Thermistor (°C) | Mean Difference in Temperature from Center Thermistor (°C) | Standard Deviation of Temperature Difference from Center Thermistor (°C) |
| **Thermistor 1** | 2.6 | 0.065 | 1.45 | 0.098 |
| **Thermistor 2** | 0.75 | 0.092 | 0.23 | 0.116 |
| **Thermistor 3** | 0 | 0.094 | 0 | 0.11 |
| **Thermistor 4** | 2.8 | 0.046 | 3.46 | 0.085 |
| **Thermistor 5** | 0.89 | 0.078 | 1.19 | 0.1 |
| **Thermistor 6** | -0.22 | 0.093 | 0.12 | 0.122 |
| **Thermistor 7** | 2.23 | 0.084 | 1.59 | 0..117 |
| **Thermistor 8** | 1.53 | 0.1 | 0.79 | 0.107 |
| **Sum** | 11.02 | 0.652 | 8.83 | 0.738 |

### 4.4.6 Performance Summary

Based on the results presented in Sections 4.4.1-4.4.5 the internal calibration target used in the instrument performs well in regards to antenna temperature flatness with respect to motor position angle, thermal homogeneity, and the ratio of antenna temperature to physical temperature. These analyses prove that this target will provide an accurate point to use in the calibration of all HAMMR radiometer channels.

# Chapter V. Microwave Radiometer Channels

One of the main goals of HAMMR is to demonstrate improved spatial resolution over that of currently deployed microwave radiometers for the retrieval of wet-tropospheric path delay through the use of mm-wave radiometers. In order to provide a direct comparison microwave and mm-wave radiometers are used simultaneously in HAMMR. The microwave radiometers have been well characterized and retrieval algorithms have been developed for Jason-1 and Jason-2 to retrieve wet-tropospheric path delay measurements using these frequencies. Because these radiometers and their retrieval algorithms are well characterized, including them in HAMMR provides means of data verification and simultaneous comparison for determining the potential for improvement in spatial resolution of wet-tropospheric path delay retrieval from microwave to mm-wave radiometer measurements.

## 5.1 System Overview

The microwave channels are the lowest frequency channels in HAMMR and include two orthogonal linear polarizations of channels at 18.7, 23.8, and 34.0 GHz. These radiometers are based off the Advanced Microwave Radiometers (AMRs) currently deployed on OSTM/Jason-2 (Jet Propulsion Laboratory) with minor improvements done by JPL for this project. The two polarizations are labeled quasi-vertical (QV) and quasi-horizontal (QH) because as the flat reflector rotates during the scan, the

polarization basis rotates as well making neither channel have a purely vertical or horizontal polarity.

The 23.8 GHz channel is in close proximity to the water vapor absorption line at 22.235 GHz and is one of the least sensitive frequencies to pressure broadening for this absorption line (Voronin & Voronina, 2002). This makes 23.8 GHz useful for determining integrated water vapor while used in conjunction with other channels, such as 34 GHz. The highest frequency, 34 GHz, has the greatest absorption due to cloud liquid water of the three microwave channels used in HAMMR and is used to correct for non-precipitating clouds (National Aeronautics and Space Administration, 2010). While the lowest frequency channel, 18.7 GHz has the least amount of absorption due to water vapor making it the most sensitive to the surface. The addition of an 18.7 GHz channel helps the algorithm compensate for surface effects such as roughening due to wind at the sea surface and whitecaps. The QV and QH are measured at all three frequencies because the ratio of the polarized brightness temperatures helps to validate the off-nadir sea surface microwave emission using well-understood models that take into account the sea surface wind speed and related factors (Baumgardner, et al., 2014).

## 5.2 Microwave Receiver Architecture

The microwave radiometers are direct detection Dicke radiometers built and designed by JPL. Figure 99 shows an overall block diagram illustrating the signal path and Figure 100 shows the signal path in the microwave receiver. The EM

energy is coupled from the atmosphere to the microwave feed horn as a voltage signal. The signal then propagates through waveguide until it reaches the orthomode transducer (OMT) which separates the QV and QH polarizations that then propagate to separate radiometers. The QV and QH signal paths are identical. After the OMT, the signal reaches the directional coupler which is used to couple in energy from two noise sources used in internal calibration. One noise source is tuned for 18.7 and 23.8 GHz and the other is tuned for 34.0 GHz. The role of these noise sources in internal calibration is discussed in detail in Section 5.4.

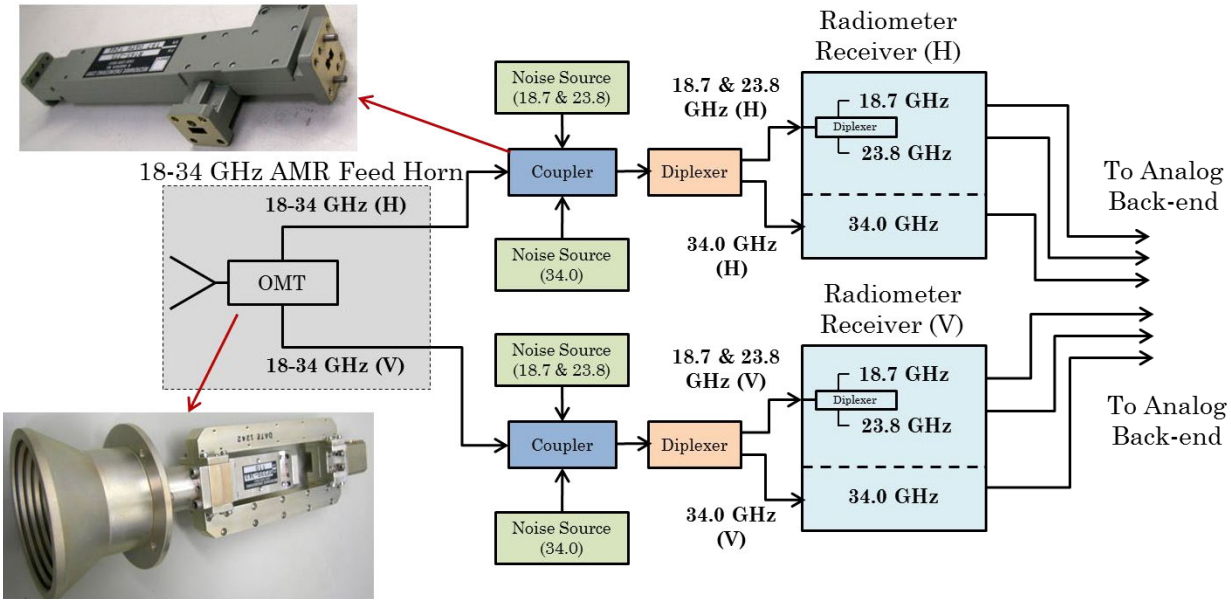


Figure 99: Microwave Radiometer Channel Block Diagram (Reising S. , et al., 2013)

After the directional coupler a diplexer is used to split the signal into two waveguide-bands. Where WR-42 is used for the 34 GHz signal and WR-28 is used for the 18.7 and 23.8 GHz signals. The 34 GHz signal is then fed into the 34 GHz

receiver while the WR-28 band is diplexed again to separate the 18.7 and 23.8 GHz signals before routing them to their respective receivers.

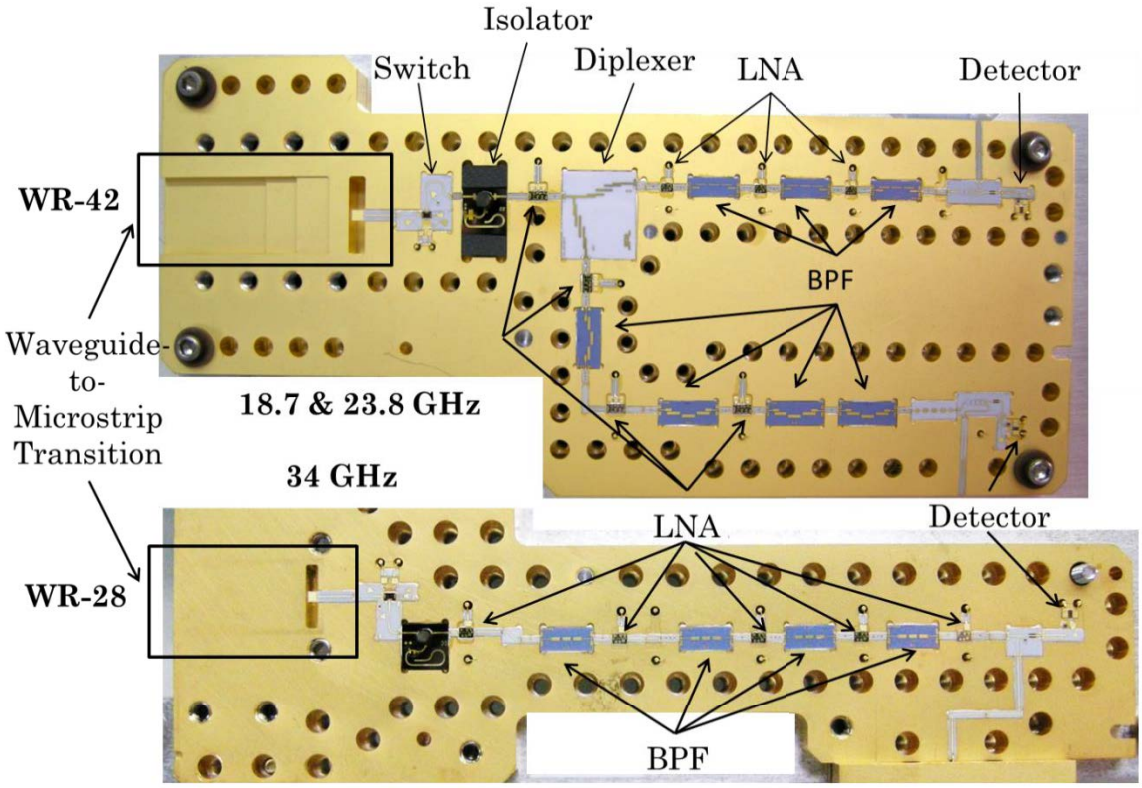


Figure 100: Populated Microwave Radiometer Channel Receiver (Reising S. , et al., 2013)

The first component in the microwave receivers is a waveguide to microstrip transition shown in Figure 100. This transition couples the EM fields in the waveguide to surface waves on the microstrip transmission lines. The signal is then input to the Dicke switch at the front end of the receiver chain. An isolator is used after the Dicke switch to prevent the receiver from emitting any significant reflected RF radiation. Band pass filters (BPFs) and low noise amplifiers (LNAs) are then used to isolate the frequency band of interest and bring it to the correct power

level to be detected by the diode detector at the end of the receiver chain shown on the right side of Figure 100. The diode detector is designed to operate in the square-law region to ensure there is a linear relationship between input RF power and output voltage. The output of the diode detector is input to a video amplifier that provides baseband amplification before routing the signal through a coaxial cable to the input of the analog back-end board (ABEB) for signal conditioning and digitization.

Figure 101 shows a 3-D CAD illustration of the two microwave receivers integrated in the HAMMR chassis. The receivers are the exact same but are mounted as mirror images of each other with the QH receiver closer to the aft of HAMMR and the QV closer to the fore. The receivers are mounted to a large aluminum plate to help increase thermal stability.

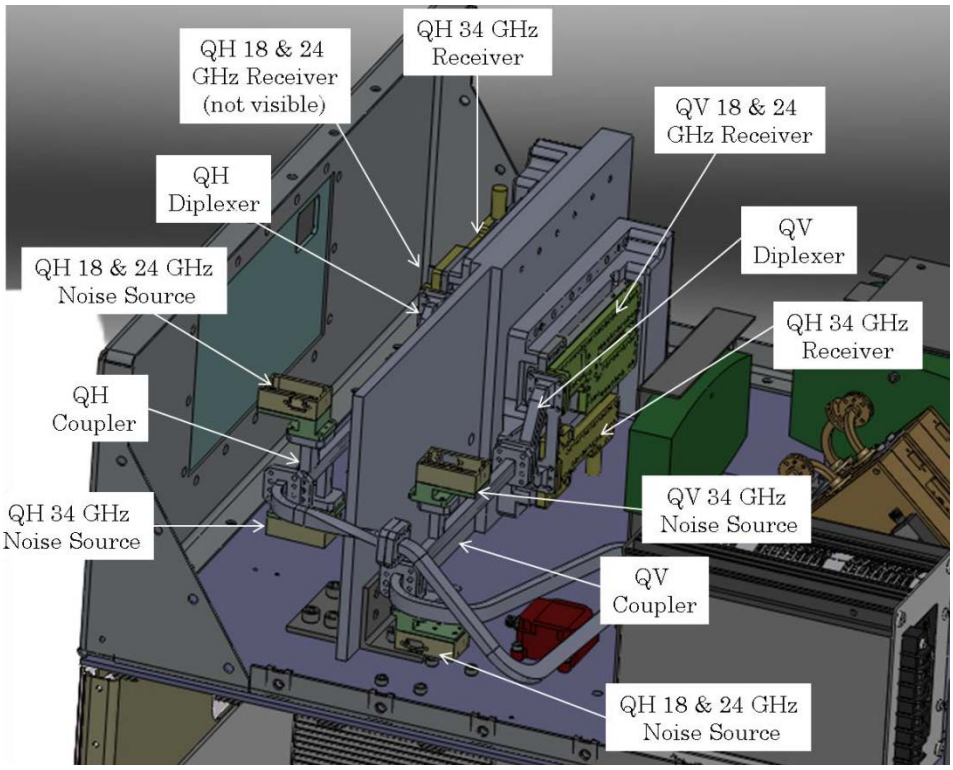


Figure 101: CAD Model of HAMMR Microwave Radiometer Channels

## 5.3 Laboratory Tests and Performance

This section will discuss the performance of the microwave radiometers in the context of system noise temperature and stability as measured by Allan variance (Vernotte, 2014). The impact of offsetting the microwave feed horn from the focal point of the paraboloid will also be analyzed.

### 5.3.1 Receiver Noise Temperature

The receiver noise temperature was determined by performing a Y-factor measurement as detailed in Section 2.2.3 and (Pozar, 2012). The hot load was a microwave absorber at ambient temperature, 290 K, and the cold load was

microwave absorber cooled with liquid nitrogen (LN2), 77 K. The measurements were performed at JPL and the resulting values are summarized in Table 8 and Table 9. These values were as expected and show that the microwave radiometers were assembled correctly.

Table 8: QH-Polarization Microwave Radiometer Performance (Measured)

| **Frequency (GHz)** | **Receiver Noise Temperature (K)** | **3 dB Bandwidth (MHz)** |
|---|---|---|
| 18.7 | 550 | 192 |
| 23.8 | 570 | 368 |
| 34 | 620 | 767 |

Table 9: QV-Polarization Microwave Radiometer Performance (Measured)

| **Frequency (GHz)** | **Receiver Noise Temperature (K)** | **3 dB Bandwidth (MHz)** |
|---|---|---|
| 18.7 | 550 | 187 |
| 23.8 | 570 | 471 |
| 34 | 620 | 753 |

Because the QH and QV microwave receivers have the same components and architecture any variance in receiver noise temperature and 3 dB bandwidth should be due to manufacturing and assembly tolerances.

### 5.3.2 Allan Variance and Stability

A plot of the Allan variance for the QH and QV microwave radiometer channels are shown in Figure 102 and Figure 103 respectively. The plots show the measured values for Allan variance for each channel as dots and the ideal values as a solid line. Each channel is represented by a different color with 18.7 GHz in red, 23.8 GHz in black, and 34.0 GHz in blue for both polarizations. A discussion on the theory of Allan variance measurements is presented in Section 2.2.4.

The QH horizontal channels, shown in Figure 102, show that the 18.7 GHz channel is the most stable followed by the 23.8 GHz and 34 GHz channels respectively. The slope of the 18.7, 23.8, and 34.0 GHz channels deviates from -1 at an integration time of approximately 400, 159, and 63 milliseconds respectively. The location where the slope deviates from -1 and begins to approach -1/2 is the integration time where the lower frequency noise components begin to adversely affect the noise of the measurement. At this point the integration time should be reduced or Dicke switching should be used to lower the overall noise of the measurements.

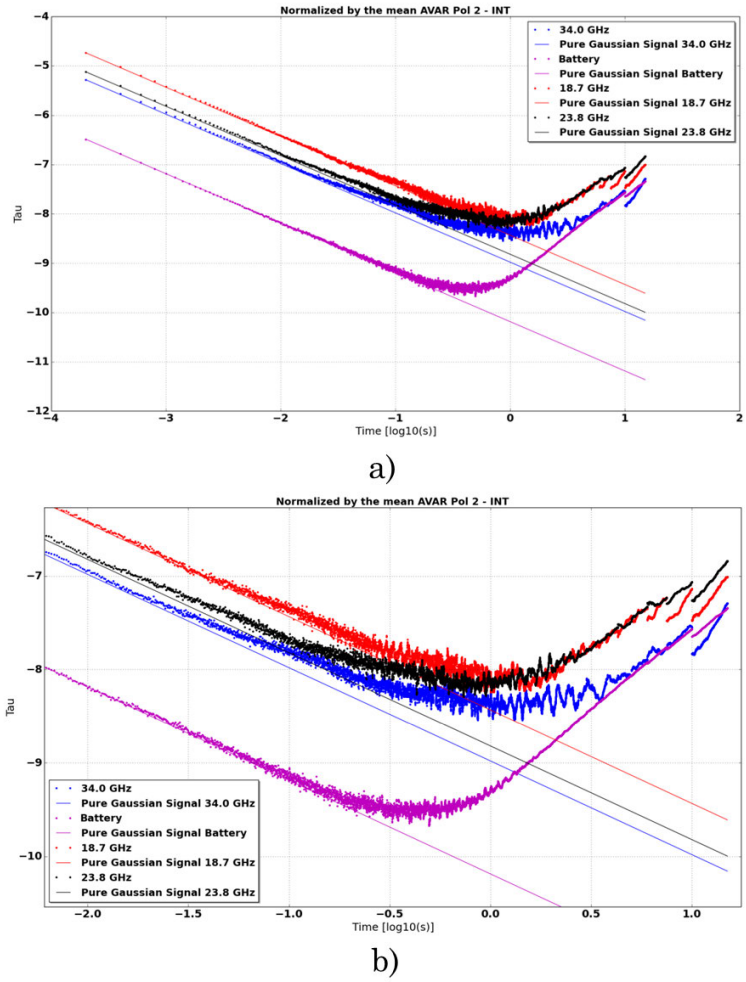


Figure 102: Lab Measurement of Allan Variance for QH Microwave Radiometer Channels, a) Full Measurement Range, b) Zoom of the Region of Interest

The QV horizontal channels, shown in Figure 103, show that the 18.7 GHz channel is the most stable followed by the 23.8 GHz and 34 GHz channels respectively. The slope of the 18.7, 23.8, and 34.0 GHz channels significantly deviates from -1 at an integration time of approximately 355, 100, and 79 milliseconds respectively. The location where the slope deviates from -1 is the integration time where the lower frequency noise components begin to adversely affect the noise of the measurement.

At this point the integration time should be reduced or Dicke switching should be used to lower the overall noise of the measurements.

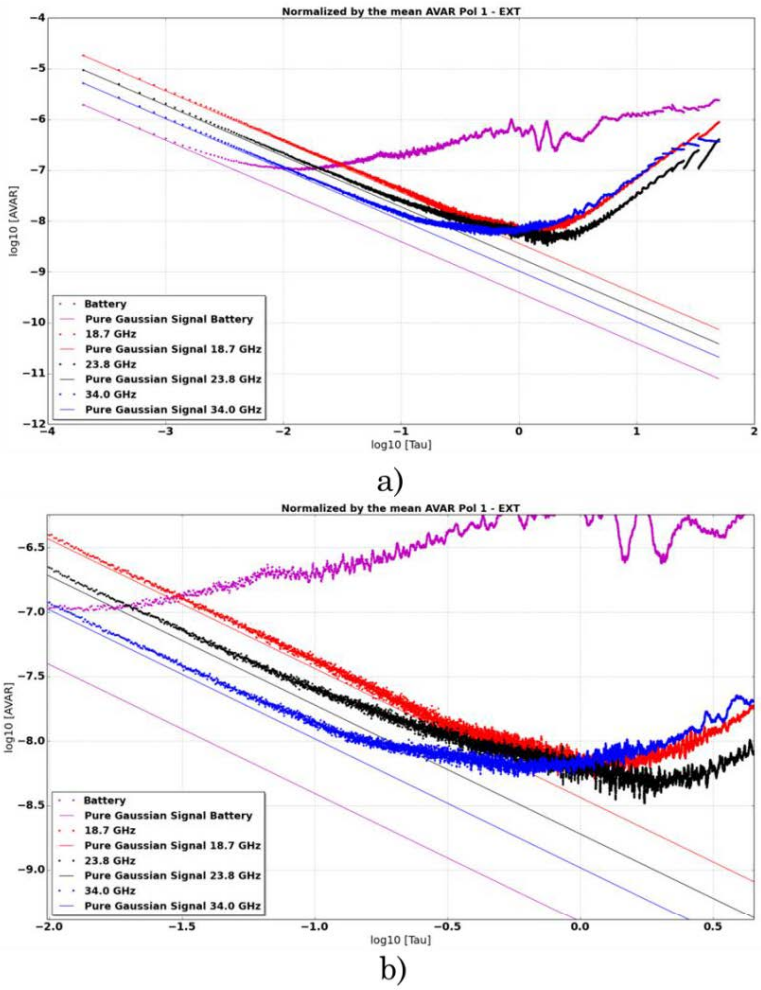


Figure 103: Lab Measurement of Allan Variance for QV Microwave Radiometer Channels, a) Full Measurement Range, b) Zoom of the Region of Interest

## 5.4 Internal Calibration

The internal calibration is accomplished through a similar approach as was discussed in Section 2.2.3 but instead of using external targets, noise diodes with known noise temperatures are coupled into the receiver input via a directional

coupler. These noise diodes present two temperature points for a linear system calibration. However, since the antenna temperature is unknown during these calibrations one cannot just take the measured voltage while firing a noise diode and assume it corresponds to the noise temperature of that noise source. A difference in the detected voltages while the noise diodes are being fired must be used. Although the antenna and receiver temperatures are unknown they are assumed to remain constant throughout the internal calibration sequence as the whole sequence takes less than 10 ms. This calibration cannot be done while looking at the Dicke reference, $T_{REF}$, as the noise diodes are located before the Dicke switch in the receiver chain so no power from the noise diodes would be seen in the measurement.

During the internal calibration sequence three different noise sources are fired. Each noise source consists of two noise diodes, one at the 18.7 and 23.8 GHz band and one at the 34 GHz band. Each noise source has a different noise temperature that it injects into the receivers which are shown in

Table 10.

Table 10: Noise Temperatures at Microwave Receivers for Each Noise Source

| **Frequency (GHz)** | **NS1 (K)** | **NS2 (K)** | **NS3 (K)** |
|---|---|---|---|
| 18.7 | 120 | 114 | 143 |
| 34 | 71 | 63 | 60 |
| 23.8 | 156 | 146.5 | 162 |

Equations (II.35), (V.2), and (V.3) describe the contributors to the detected voltages while firing each noise source.

$$V_{NS_1}\,\alpha\,T_A + T_{REC} + T_{NS1} \tag{V.1}$$

$$V_{NS_2}\,\alpha\,T_A + T_{REC} + T_{NS2} \tag{V.2}$$

$$V_{NS_3}\,\alpha\,T_A + T_{REC} + T_{NS3} \tag{V.3}$$

Since there are two unkowns per equation, $T_A$ and $T_{REC}$, a system of equations must be used to establish the calibration constant. This is shown in equations (V.4), (V.5), and (V.6).

$$C_{21} = \frac{T_{NS2} - T_{NS1}}{V_{NS2} - V_{NS1}} \tag{V.4}$$

$$C_{32} = \frac{T_{NS3} - T_{NS2}}{V_{NS3} - V_{NS2}} \tag{V.5}$$

$$C_{31} = \frac{T_{NS3} - T_{NS1}}{V_{NS3} - V_{NS1}} \tag{V.6}$$

Once the calibration constant is calculated the calibration line can be found using the standard equation for a line given in equation (V.7), as in Figure 104, and setting $y = T_B$, $y_0 = T_{REF}$, $m = C$, $x = V$, *and* $x_0 = V_{REF}$. Equation (V.7) then becomes (V.8), where $T_B$ and $V$ are the measured voltage and brightness temperature while a particular noise source is firing. $T_{REF}$ and $V_{REF}$ are the measured physical temperature and voltage of the Dicke reference respectively.

$$y - y_0 = m(x - x_0) \tag{V.7}$$

$$T_B - T_{REF} = C(V - V_{REF}) \tag{V.8}$$

Rearranging (V.8) and considering the case of measuring $C_{21}$ yields equation (V.9) which can be rearranged to yield equation (V.10) where the first term in parenthesis is $T_{SYS}$ and the second term is $T_{REC}$.

$$T_B = C_{21}(V - V_{REF}) + T_{REF} = \frac{T_{NS2} - T_{NS1}}{V_{NS2} - V_{NS1}}\,(V - V_{REF}) + T_{REF} \tag{V.9}$$

$$T_B = \left(\frac{T_{NS2} - T_{NS1}}{V_{NS2} - V_{NS1}} * V\right) + \left(T_{REF} - \frac{T_{NS2} - T_{NS1}}{V_{NS2} - V_{NS1}} V_{REF}\right) = T_{SYS} - T_{REC} \tag{V.10}$$

This equation can now be solved for brightness temperature as all the variables in the equation are known. Solving either (V.4), (V.5), or (V.6) yields the slope of the line and the point defined by $(x_0,y_0)$ is given by looking at the reference load. These two values allow us to solve for the calibration line that relates a measured voltage to a brightness temperature. Only two noise sources are required to perform this calibration so the third source was added for redundancy and increased accuracy.

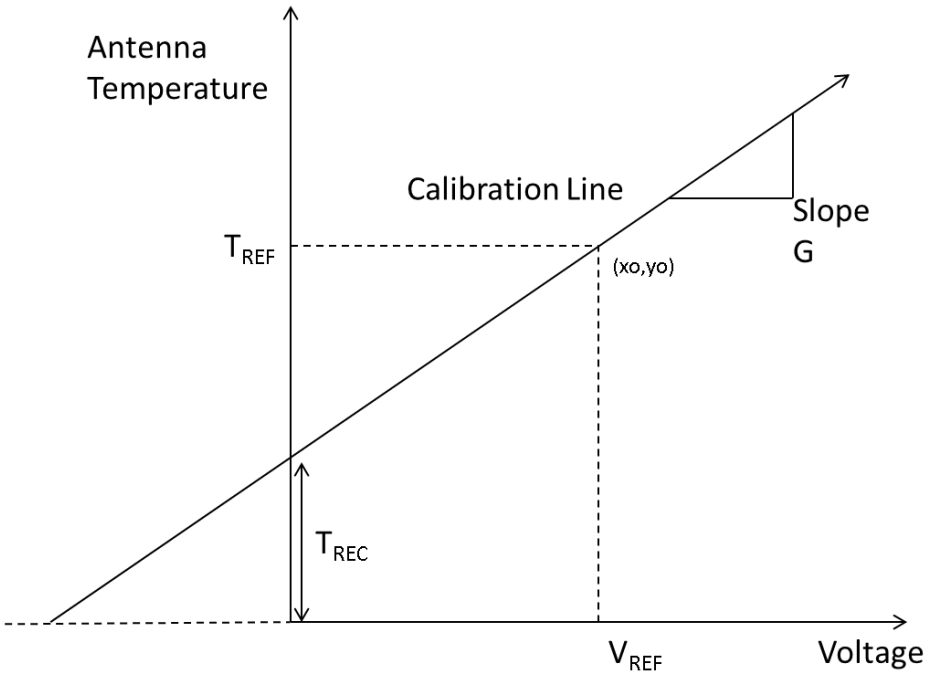


Figure 104: Graphical Representation of the Internal Calibration for the Microwave Receivers

# Chapter VI. Millimeter-Wave Window Channels

HAMMR contains two sets of mm-wave radiometers, the mm-wave window radiometers and the mm-wave sounding radiometers. This chapter discusses the architecture, integration, characterization, and calibration of the mm-wave window channels.

## 6.1 System Overview

The mm-wave window channels are located in the frequency "windows" between water vapor absorption lines at 90, 130, and 168 GHz. These frequencies were chosen to retrieve the maximum amount of information content on wet-tropospheric path delay. The mm-wave window channels have a much larger bandwidth compared to the microwave channels and are more sensitive to integrated water vapor. This is because the absorption, and therefore emission, of the atmosphere is much greater at mm-wave than microwave frequencies as can be seen in Figure 3. The higher absorption makes the mm-wave frequencies less sensitive to surface emission so the measured brightness temperature will be much different at mm-wave than microwave frequencies. The development of the mm-wave window channels is discussed in detail in (Albers, Fall 2012).

## 6.2 Development Previous to IIP-10

The mm-wave window channels are all direct detection Dicke radiometers similar to the microwave radiometers previously discussed in Section 5.1. The initial design

for the mm-wave window channels and the fabrication of laboratory prototypes was completed in ACT-08 along with the design of the tri-frequency feed horn used by these channels (Reising, et al., 2011). Figure 105 shows the block diagram for the mm-wave windows radiometers and Figure 106 shows a picture of the tri-frequency horn.

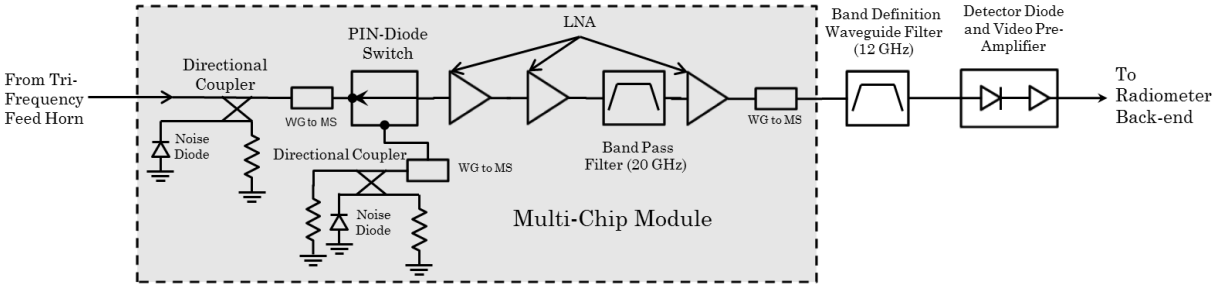


Figure 105: mm-wave Radiometers Block Diagram

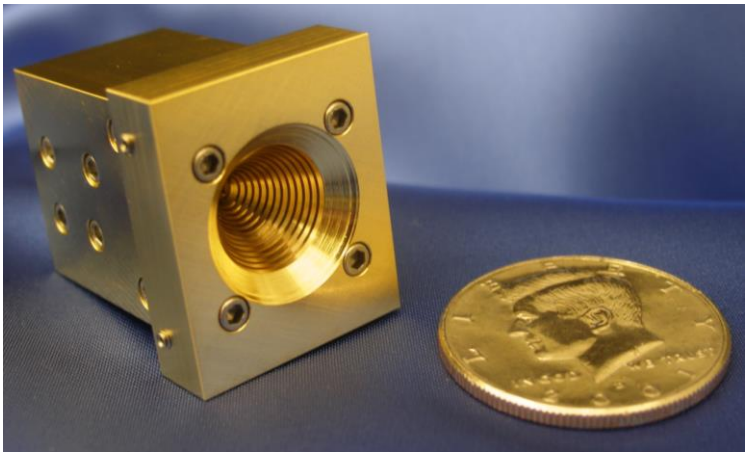

Figure 106: Tri-Frequency Horn with a Half Dollar as Reference (Reising, et al., 2011)

Under ACT-08 the single pole double throw PIN diode switch, shown with its performance in Figure 107, was also developed for use as the Dicke switch in the

mm-wave receivers. Figure 108 shows the laboratory prototype for the 90 GHz receiver multi-chip module (MCM), where the majority of the radiometer's RF components are housed, with the PIN diode switch installed. Each mm-wave window radiometer has an MCM that contains the entire RF receiver.

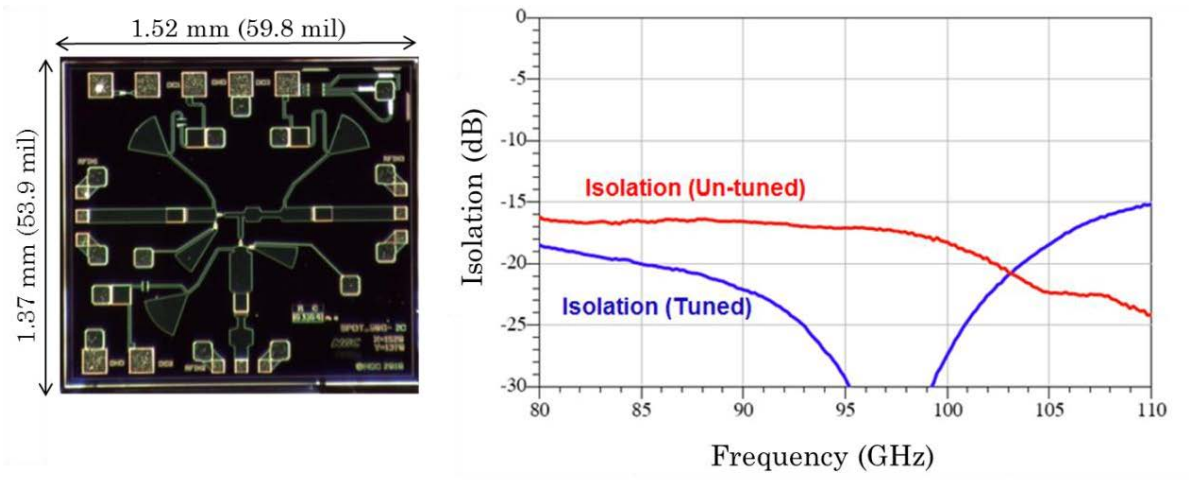


Figure 107: ACT-08 PIN Diode SPDT (Johnson & Hadel, 2012)

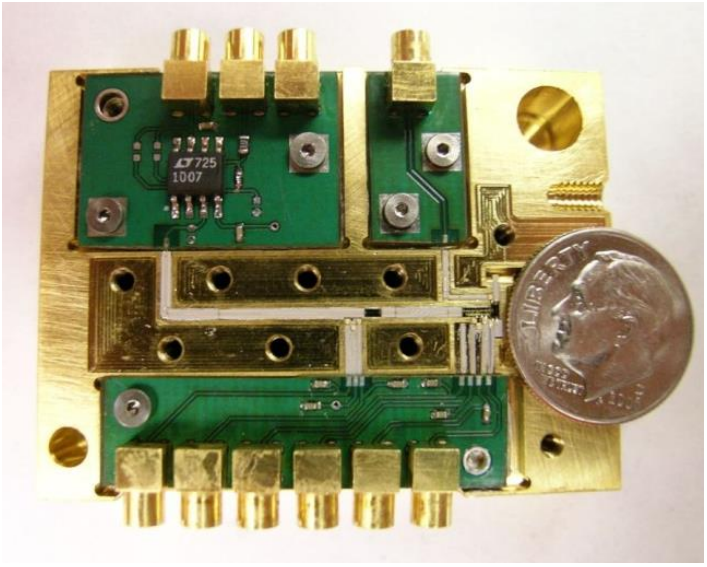

Figure 108: ACT-08 90 GHz Multi-Chip Module Lab Prototype with a Dime as Reference (Lee, Spring 2012), (Albers, Fall 2012)

## 6.3 Millimeter-Wave Window Receiver Architecture

The receiver design from ACT-08 was slightly modified for airborne use in IIP-10. These changes were primarily implemented by Victoria Hadel of CSU's MSL and are discussed in detail in (Hadel, 2014). A brief overview of the changes and the resulting system architecture will be given in this section.

Figure 109 illustrates the three major changes made during IIP-10 to the ACT-08 mm-wave window radiometers. These include the addition of a second input port to measure the PIN diode switch symmetry, the integration into the MCM of a directional coupler and noise diodes to reduce size, mass and insertion losses, and the conversion of the band definition BPF from microstrip to waveguide to lessen insertion loss and better define the frequency band that is diode detected for each receiver.

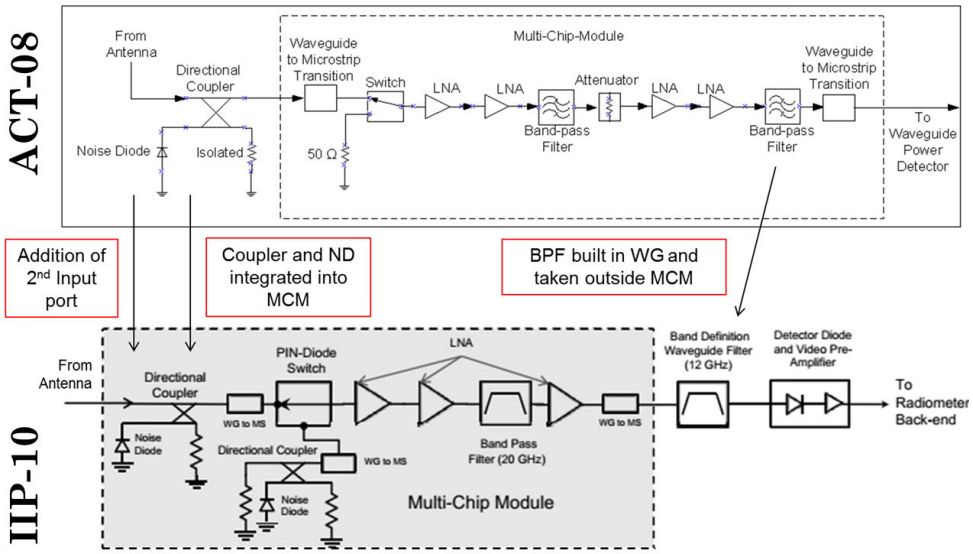


Figure 109: Major Modifications to ACT-08 mm-Wave Window Radiometers

Figure 110 shows the block diagram for the 168 GHz mm-wave receiver as well as a picture showing the populated RF trench. The signal path for the mm-wave window receivers is very similar to that of the microwave receivers discussed in Section Section 5.1.

The tri-frequency horn developed under ACT-08 is used at the front end of the mm-wave radiometers. The RF signal from the antenna enters the MCM through a directional coupler that is used for internal calibration. Similar to the microwave radiometers, noise is injected into the receiver front end via a noise diode at the coupled port of the directional coupler. The injected noise is used to perform an internal calibration as detailed in Section 2.2.3. The RF signal is then coupled onto a microstrip transmission line by a waveguide to microstrip transition which feeds into the PIN diode SPDT switch used for Dicke switching.

Subsequent to the Dicke Switch are three LNAs and a BPF used to avoid saturation of the last LNA. The RF signal is then coupled back into waveguide before leaving the MCM and entering the waveguide band definition filter which defines the bandwidth of the radiometer. Immediately following the band definition filter the signal enters the diode detector block where it is diode detected to baseband frequency and amplified via a video amplifier. The amplified baseband signal is then input to the ABEB via coaxial cable for further amplification, integration, and digitization.

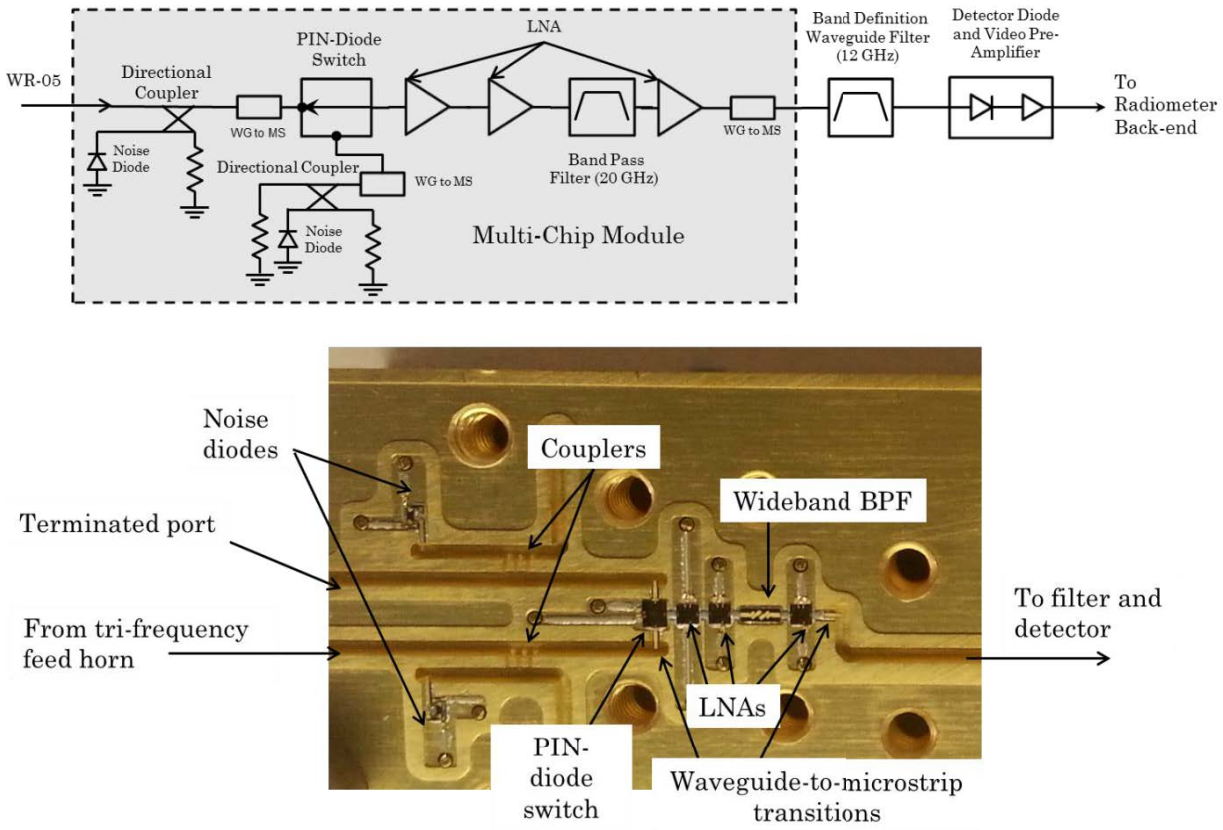


Figure 110: Original Block Diagram Design and 168 GHz Populated MCM

The three finished mm-wave window MCMs can be seen in Figure 111 with their final dimensions and weights given in Table 11.

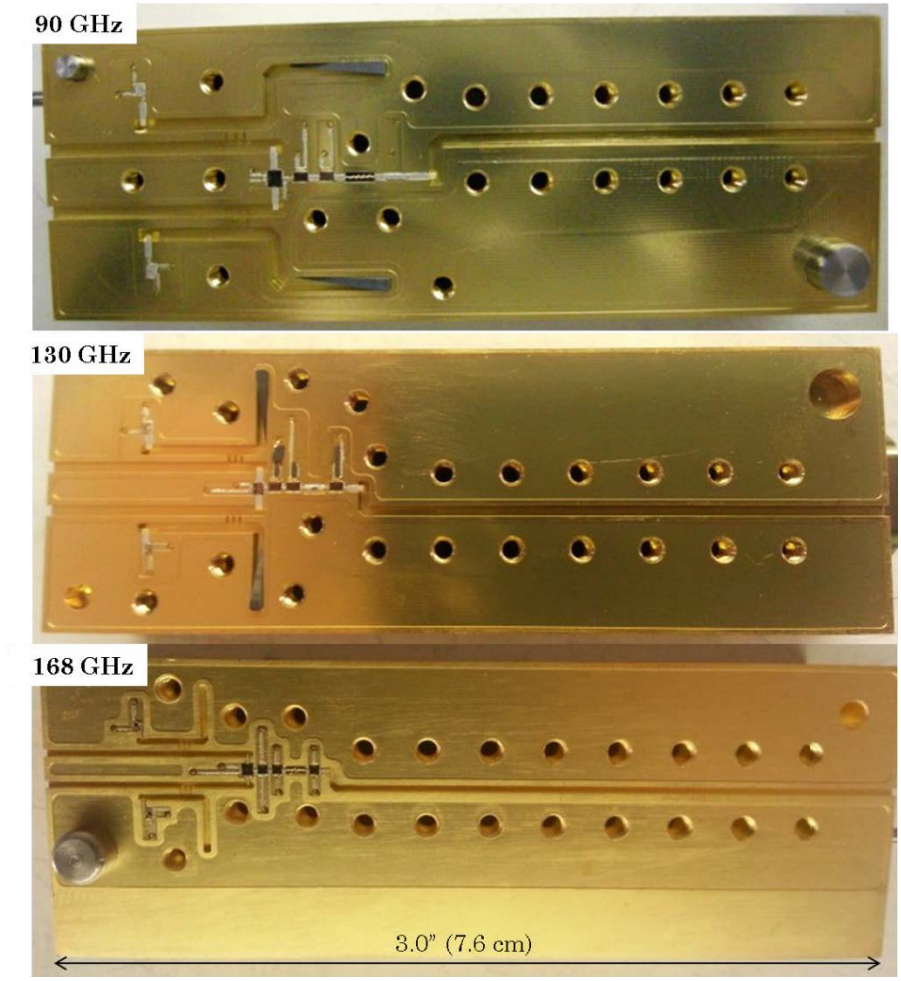


Figure 111: Assembled mm-Wave Multi-Chip Modules

Table 11: Outer Dimensions and Weight of mm-Wave MCMs

| Radiometer Center Frequency | Length | Width | Height | Weight (g) |
|---|---|---|---|---|
| 90 GHz | 2.9" (74 mm) | 1.1" (28 mm) | 1.1" (28 mm) | 523 |
| 130 GHz | 3.0" (76 mm) | 1.0" (25 mm) | 1.1" (28 mm) | 522 |
| 168 GHz | 3.0" (76 mm) | 1.1" (28 mm) | 1.1" (28 mm) | 498 |

To secure the mm-wave window receivers to the optical bench a set of custom brackets were designed by Victoria Hadel shown in Figure 112.

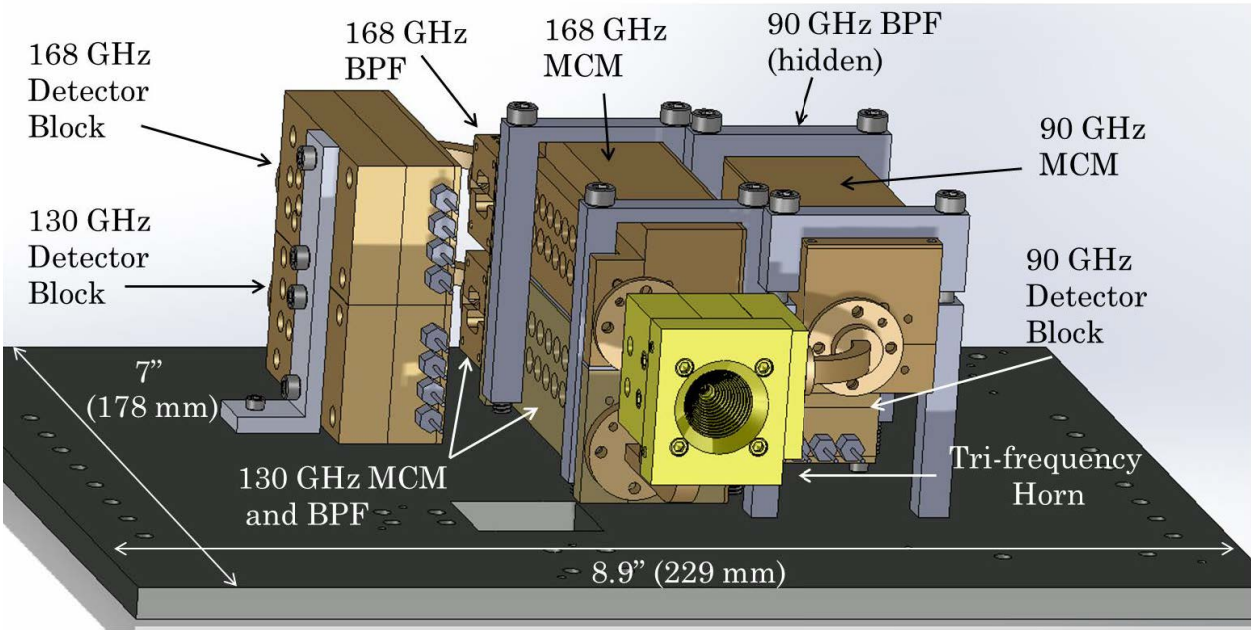


Figure 112: Millimeter-Wave Window Optical Bench Layout

## 6.4 Laboratory Tests and Performance

This section will discuss the performance of the mm-wave window radiometers in the context of system noise temperature, gain and stability as measured by Allan variance.

### 6.4.1 Gain and Receiver Noise Temperature

Y-factor measurements were performed at JPL to determine the receiver noise temperature and gain across each channel's respective frequency band. Each channel was measured individually with a standard gain horn as the waveguide

assembly to connect the tri-frequency to the MCMs was not finished. The diode detector modules were still being fabricated as well so the RF output of the MCMs were down converted using a mixer and fed into a power detector as shown in Figure 113. The Y-factor measurements allowed the receiver gain and noise temperatures to be calculated and the results for the 90, 130, and 168 GHz receivers are shown in Figure 114, Figure 115, and Figure 116 respectively and summarized in Table 13.

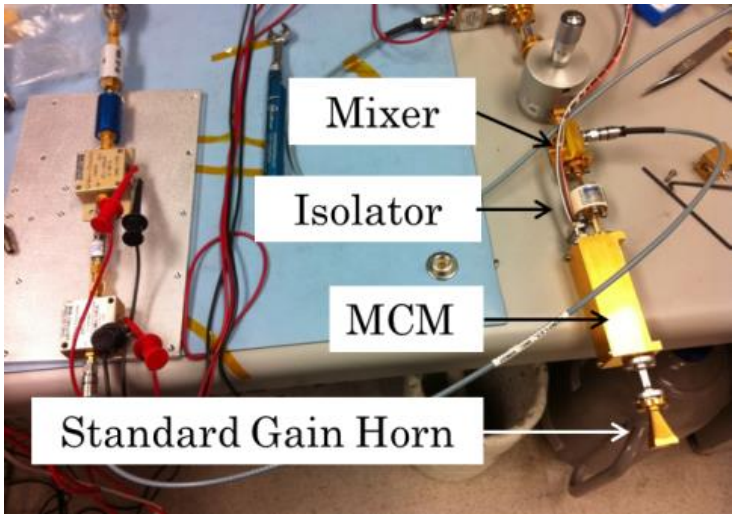


Figure 113: mm-Wave Radiometer Y-Factor Measurements Test Bench

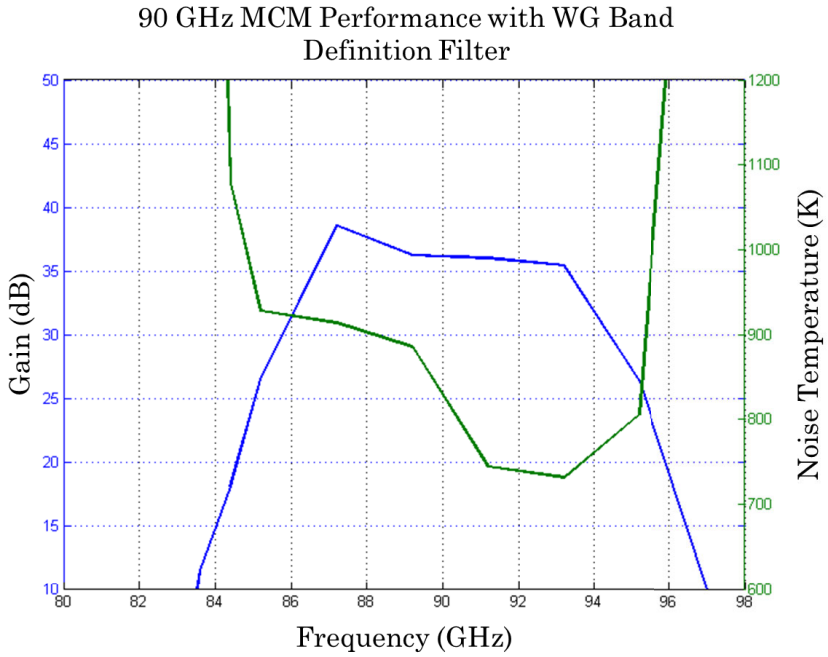


Figure 114: 90 GHz MCM Performance with WG Band Definition Filter

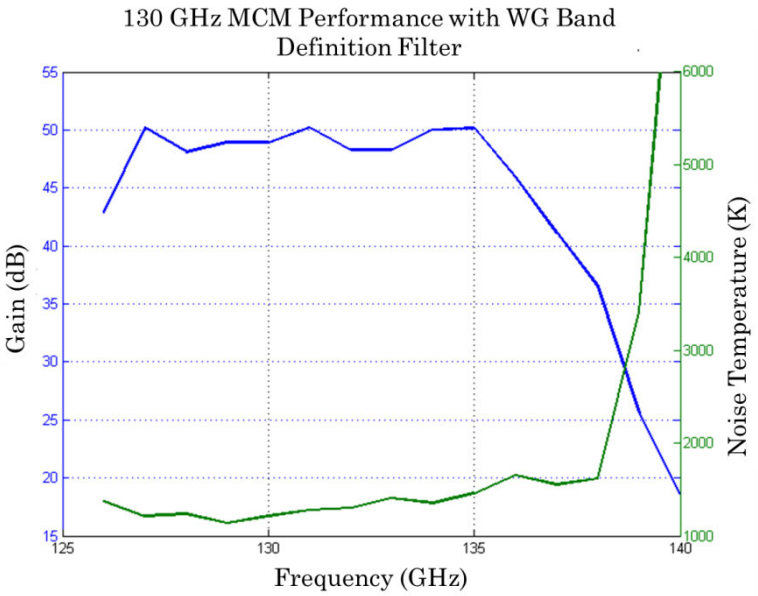


Figure 115: 130 GHz MCM Performance with WG Band Definition Filter

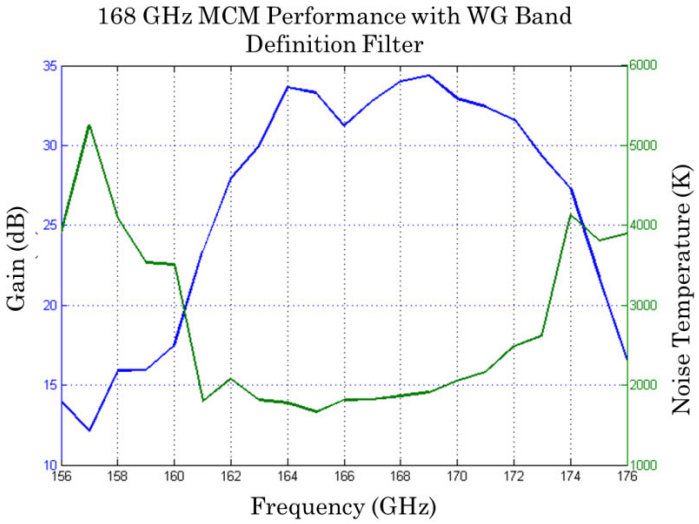


Figure 116: 168 GHz MCM Performance with WG Band Definition Filter

Table 12: Summary of MCM Initial Lab Performance

| Channel Frequency (GHz) | Average Gain (dB) | Average Noise Temperature (K) |
|---|---|---|
| 90 | 36.5 | 818.7 |
| 130 | 46.8 | 1369.5 |
| 168 | 31.1 | 2142.7 |

Once the fabrication of the diode detector modules and waveguide assembly were complete the three mm-wave window receivers were tested together with the tri-frequency horn and backend from HAMMR at JPL as shown in Figure 117.

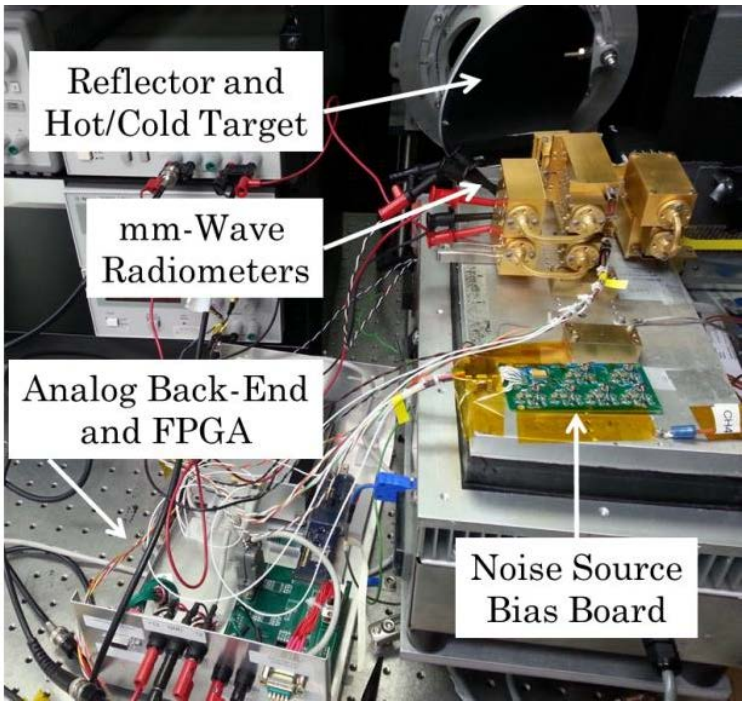


Figure 117: Test Bench for Full System Laboratory Measurements

The testing for the mm-wave window receivers involved Y-factor measurements while firing the noise diodes used for internal calibration. The results of these tests for the 90, 130, and 168 GHz receivers are shown in Figure 118, Figure 119, and Figure 120 respectively and summarized in Table 13.

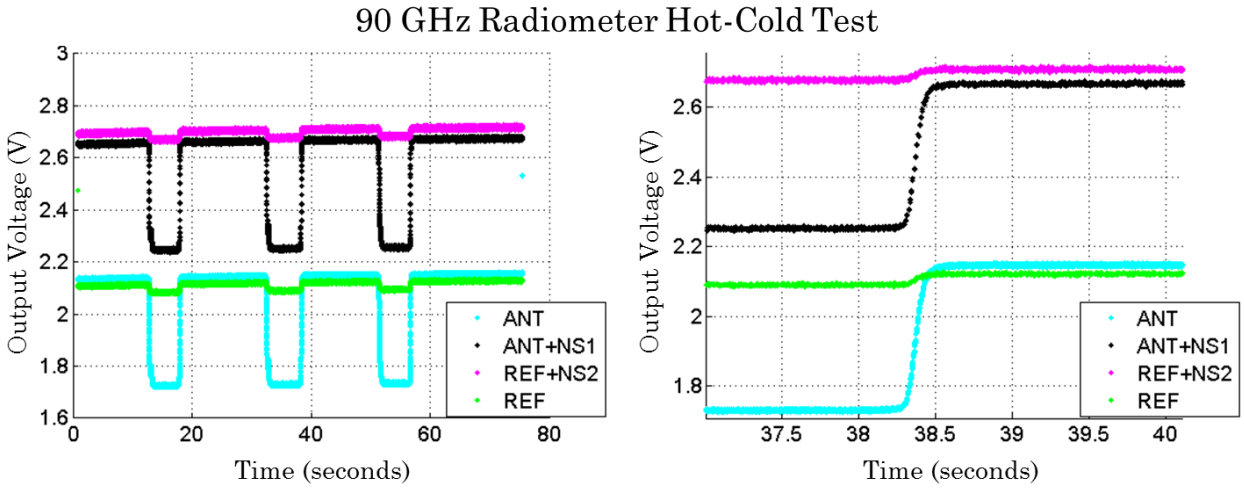


Figure 118: 90 GHz Radiometer Hot-Cold Measurements with Two Different Time-Scales

The right side of Figure 118 shows an excellent example of switch leakage at approximately 38.5 seconds. Here the antenna scene changes from a cold to a hot load with a difference of about 200 K. During this transition it can be seen that the output voltage while looking at the reference also increases. The increase in temperature is caused by some of the power from the antenna port leaking into the reference port while the radiometer is looking at the reference. This leakage can cause problems with calibration and overall performance of the radiometer due to the uncertainty of how much energy is leaking from the off port. If the switch is well

characterized the leakage can be calibrated out but due to time and budget constraints the switches were not characterized.

For all three receivers the output voltage while viewing the reference load (REF) and the output voltage while viewing a hot load with the antenna (ANT) should be the same. The 90 GHz receiver shows a discrepancy that is small enough to be accounted for in post processing.

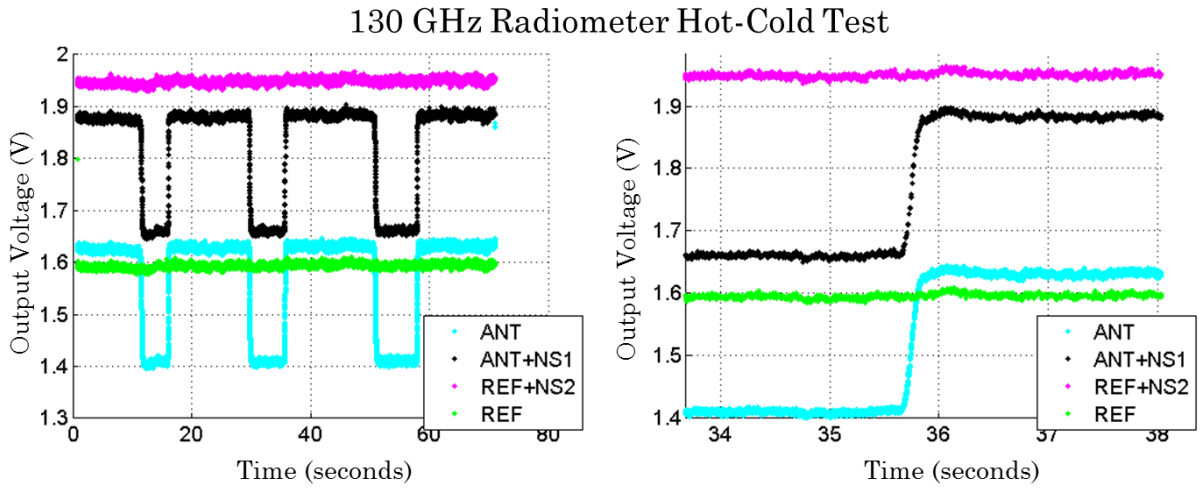


Figure 119: 130 GHz Radiometer Hot-Cold Measurements with Two Different Time-Scales

The 130 GHz receiver does not show the same switch leakage problem as the 90 GHz receiver but the difference between the output voltage of REF and ANT is larger than that of the 90 GHz receiver.

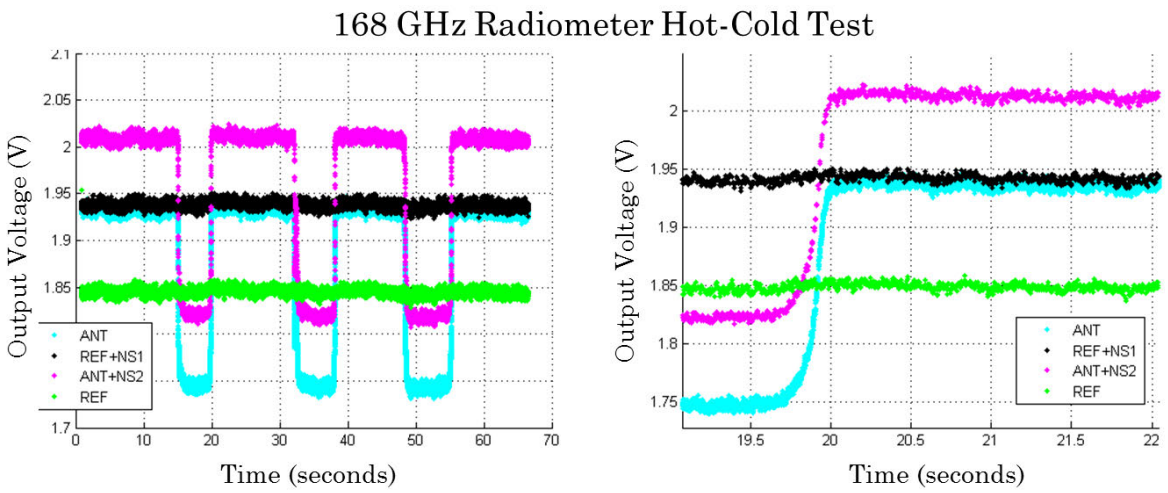


Figure 120: 168 GHz mm-wave Radiometer Hot-Cold Measurements with Two Different Time-Scales

The 168 GHz receiver shows no noticeable switch leakage problems but the difference between ANT and REF is very large.

The hypothesis for why the 130 and 168 GHz receivers see a lower voltage when viewing REF than ANT while looking at am ambient target is that the insertion loss on the switch reference leg is much higher than that of the antenna leg causing the measured voltage while looking at REF to have greater attenuation than when looking at ANT.

Table 13: Summarized Performance of Millimeter-Wave Window Radiometers

| **Radiometer** | **$T_{sys}$ (K)** | **Gain (K/Volt)** | **$T_{ref}$ (K)** |
|---|---|---|---|
| 90 GHz | 816 | 514 | 281 |
| 130 GHz | 1310 | 982 | 255 |
| 168 GHz | 2672 | 1524 | 160 |

The discrepancies between Table 12 and Table 13 stem from the difference in antenna and waveguides being used between the two experiments. For the measurements used to calculate the values in Table 12, the system was setup with a standard gain horn attached to only one receiver at a time with minimal waveguides. For the measurements used to calculate the values in Table 13 all three receivers were attached to the tri-frequency horn in their final flight configuration. This caused a slight increase in the average noise temperatures of the 90 and 130 GHz receivers. However, the 168 GHz receiver saw an increase in average noise temperature of approximately 400K due to these additional components.

### 6.4.2 Allan Standard Deviation and Stability

A plot of the Allan deviation for 90, 130, and 168 GHz channels are shown in Figure 121. The plot shows the measured values for Allan standard deviation for each channel represented by a different color with 90 GHz in red, 130 GHz in green, and

168 GHz in black. A discussion on the theory of Allan standard deviation measurements is presented in Section 2.2.4.

The channels, shown in Figure 121, show that the 90 GHz channel is the least noisy followed by the 130 GHz and 168 GHz channels respectively. The slope of 90, 130, and 168 GHz channels deviates from -1 at an integration time of approximately 25, 2, and 1.3 milliseconds respectively. The location where the slope deviates from -1 and begins to approach -1/2 is the integration time where the lower frequency noise components begin to adversely affect the noise of the measurement. At this point the integration time should be reduced or Dicke switching should be used to lower the overall noise of the measurements.

The conclusion of this test is that the 90 GHz channel is the most stable with the slope reaching 0 at an integration time of about 25 ms. This can be seen in Section 8.4.2.4 where the 90 GHz has the least amount of noise in the retrieval. The 130 and 168 GHz channels reach a slope of zero at a about 12 ms. However, the slope of the Allan deviation for these two channels slowly changes from -1 to 0 over the span of $\tau$ ranging from 1.3 to 12 ms. This means that the Gaussian or White noise in the measurement is being reduced by integrating more samples but a significant amount of noise from other processes are being introduced into the measurement by integrating over this time period. This introduces uncertainty into the measurement that is not desired. Operating the 130 and 168 GHz radiometers in Dicke mode will improve the stability of both receivers.

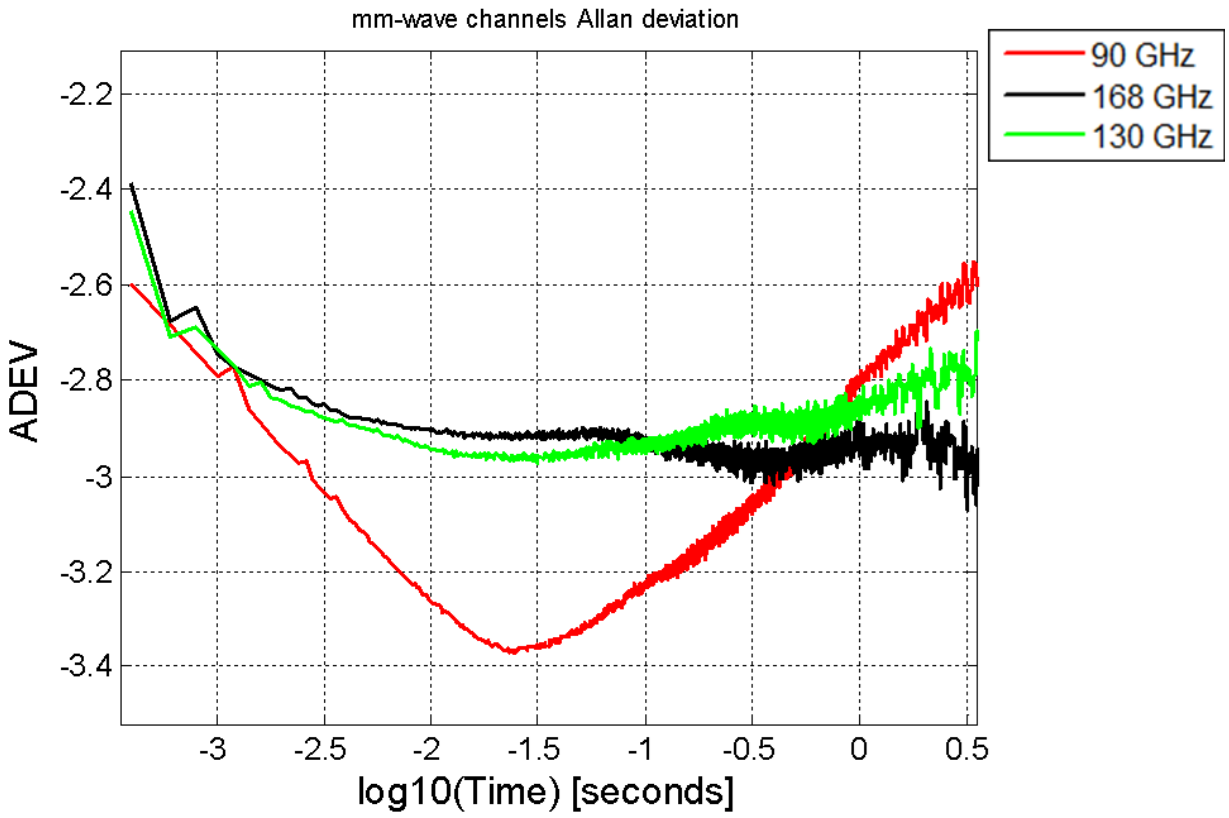


Figure 121: Lab Measurements of Allan Standard Deviation for the Millimeter-Wave Window Channels at 90, 130, and 168 GHz.

## 6.5 Internal Calibration

The internal calibration for the mm-wave window channels is accomplished through the use of two noise sources similar to that of the microwave channels discussed in Section 5.4 with a one difference. The difference is that for the microwave channels all noise sources are coupled into the antenna leg before the PIN Dicke switch. For the mm-wave window channels one noise source is coupled to the antenna leg before the PIN Dicke switch and the other is coupled to the reference leg before the PIN

Dicke switch. This means, that unlike the equations for the calibration constant in Section 5.4, the calibration constant cannot be calculated using the ratio of temperature to measured voltage for two noise sources. Instead, the ratio of antenna temperature to measured voltage with and without the noise source firing, or the ratio of noise temperature when looking at the Dicke reference with and without the noise source firing must be used. Equations (II.35), (V.2), (V.3), and (VI.4) describe the contributors to the measured voltage for each acquisition position.

$$V_{NS_1} \alpha\, T_A + T_{REC} + T_{NS_1} \tag{VI.1}$$

$$V_{ANT} \alpha\, T_A + T_{REC} \tag{VI.2}$$

$$V_{NS_2} \alpha\, T_{REF} + T_{REC} + T_{NS_2} \tag{VI.3}$$

$$V_{REF} \alpha\, T_{REF} + T_{REC} \tag{VI.4}$$

Using these relationships two different calibration constants, $C_{ANT}$ and $C_{REF}$, can be calculated as shown in equations (V.4) and (V.5) respectively.

$$C_{ANT} = \frac{(T_A + T_{REC} + T_{NS_1}) - (T_A + T_{REC})}{V_{NS_1} - V_{ANT}} = \frac{T_{NS_1} - 0}{V_{NS_1} - V_{ANT}} \tag{VI.5}$$

$$C_{REF} = \frac{(T_{REF} + T_{REC} + T_{NS_2}) - (T_{REF} + T_{REC})}{V_{NS_2} - V_{REF}} = \frac{T_{NS_2} - 0}{V_{NS_2} - V_{REF}} \tag{VI.6}$$

Following the steps outlined in Section 5.4 the measured brightness temperature can then be calculated using equations (V.9) and (V.10) where $C_{ANT}$ and $C_{REF}$ can be substituted for each other.

$$T_B = C_{ANT}(V - V_{REF}) + T_{REF} = \frac{T_{NS_1} - 0}{V_{NS_1} - V_{ANT}}(V - V_{REF}) + T_{REF} \tag{VI.7}$$

$$T_B = \left(\frac{T_{NS_1} - 0}{V_{NS_1} - V_{ANT}} * V\right) + \left(T_{REF} - \frac{T_{NS_1} - 0}{V_{NS_1} - V_{ANT}} V_{REF}\right) = T_{SYS} - T_{REC} \tag{VI.8}$$

# Chapter VII. Millimeter-Wave Sounding Channels

HAMMR contains two sets of millimeter-wave radiometers, the millimeter-wave window radiometers and the millimeter-wave sounding radiometers. This chapter discusses the architecture, integration, characterization, and calibration of the millimeter-wave sounding channels.

## 7.1 System Overview

The millimeter-wave sounding channels contain two frequency sets. Each set contains eight digitized channels with 1 GHz of bandwidth per channel. The channels are located on the upper sideband (USB) of the 118.75 GHz oxygen absorption line and the lower sideband (LSB) of the 183.31 GHz water vapor absorption line. These particular frequency sets where chosen to maximize information content while adhering to the band limitations of the feed horn.

The 118.75 GHz sounder, also called the temperature sounder, has eight channels offset 1 GHz apart above the 118.75 oxygen absorption line and three channels offset at 0, 0.25, and 0.5 GHz above the 118.75 oxygen absorption line. Since the peak of the absorption line is at 118.75 GHz as the channels move away in frequency from this peak they will be attenuated less and will therefore penetrate further into the atmosphere. This allows the retrieval algorithm to construct a vertical temperature profile of the observed scene. Measuring brightness temperature near the oxygen absorption line allows the retrieval of atmospheric

temperature because the volume mixing ratio of oxygen is essentially independent of location and time; therefore, any changes in the measured brightness temperature will be due to changes in the physical temperature of the atmosphere (von Engeln & Buhler, 2002). Only eight of the eleven channels are digitized because some channels provide redundant information.

The 183.31 GHz sounder, also called the water vapor sounder, contains eight channels offset 1 GHz apart below the 183.31 GHz water vapor absorption line. Similar to the temperature sounder, each channel will penetrate further into the atmosphere as its' center frequency is spaced further from the 183.31 absorption line resulting in a vertical profile of the water vapor density in the atmosphere.

## 7.2 Millimeter-Wave Sounder Receiver Architecture

The sounder receivers are built using a super-heterodyne topology as opposed to the direct detection topology of the microwave and millimeter-wave window channels. The difference between these two topologies is discussed in more detail in Sections 2.3, 2.4, and 2.5. The block diagram for the sounding receivers can be seen in Figure 122. The sounding receivers share the same architecture with the only difference being the operating frequency of the individual components, so only one receiver will be included in the following discussion.

The quad-ridge feed horn, seen in Figure 123 a), is used at the front end of the sounding receivers. This feed horn contains an OMT for separation of orthogonal polarizations and an LNA at each output of the OMT for amplification. HAMMR

only uses one polarization for the mm-wave sounding channels so the second output of the quad-ridge horn OMT is terminated. Subsequent to the quad-ridge horn is a custom diplexer designed by Victoria Hadel to separate the 118.75 and 183.31 GHz frequency bands. The diplexer design is discussed in detail in (Hadel, 2014) and was specifically designed to have physical dimensions that allow for the use of standard waveguide pieces in the sounding subsystem.

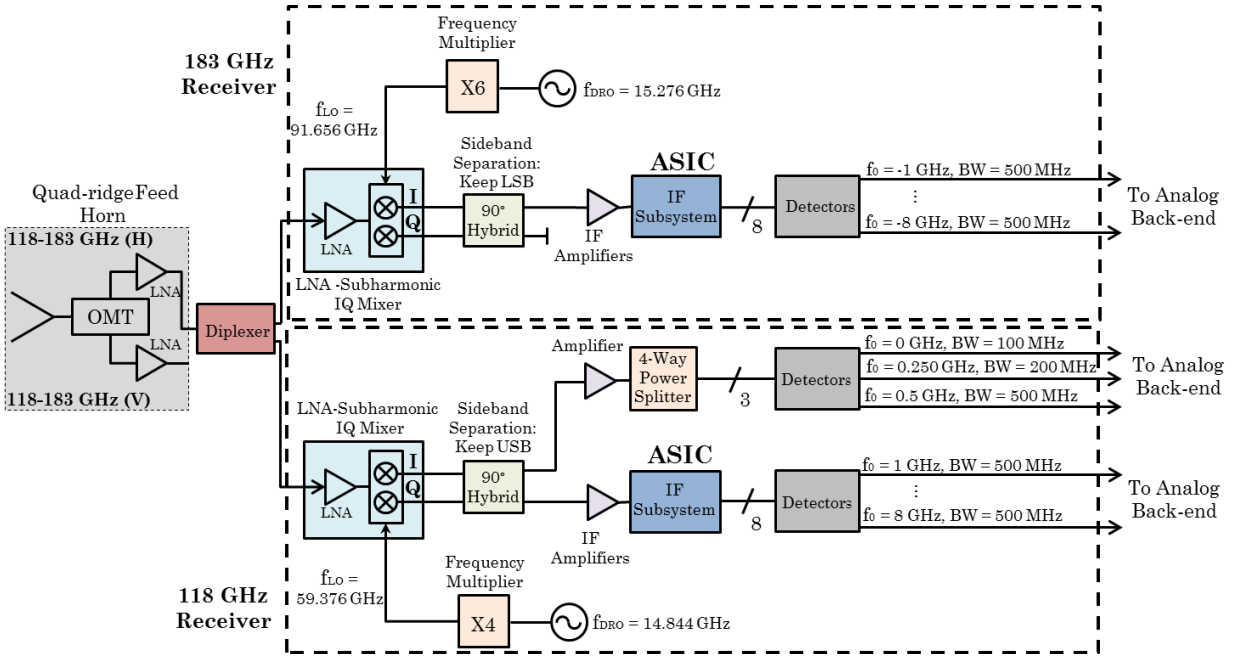


Figure 122: Millimeter-Wave Sounding Radiometer Block Diagram

The output of the diplexer feeds into the sounder receiver input. The first component in the sounder receiver amplifies and down converts the RF signal via an LNA and subharmonic IQ mixer. An externally generated local oscillator (LO) signal is input into the subharmonic mixer to accomplish the down conversion. The LNA and subharmonic mixer are housed in a single device called the miniature

monolithic microwave integrated circuit (MMIC) low mass/power radiometer (MIMRAM) (Kangaslahti, A., Lambrigsten, & Pukala, 2007). Developed as part of the Geostationary Synthetic Thinned Aperture Radiometer (GeoSTAR) IIP project as shown in Figure 124.

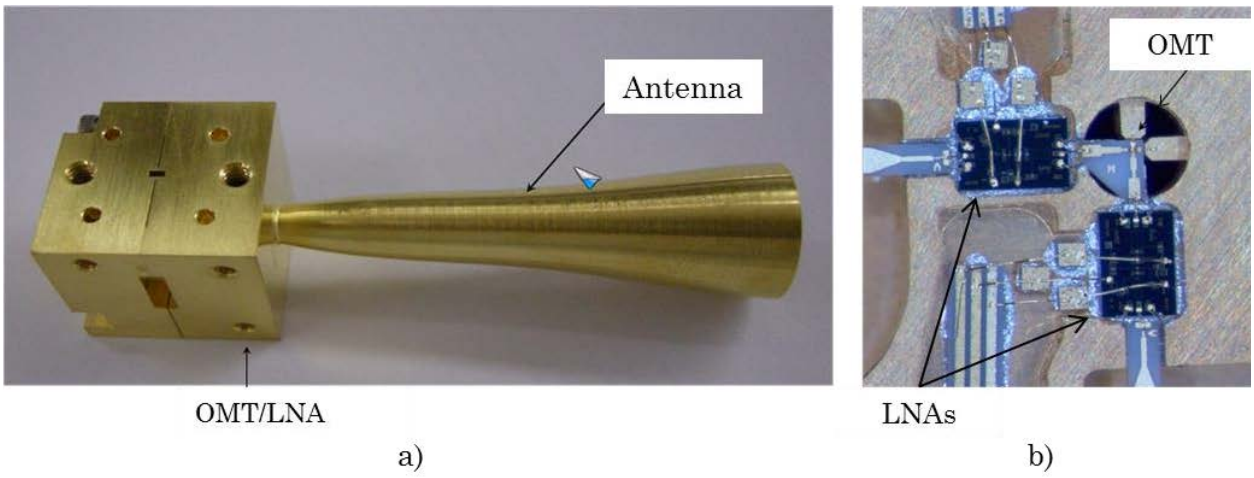


Figure 123: a) Quad-Ridge Horn and b) Inside Quad-Ridge Horn Receiver

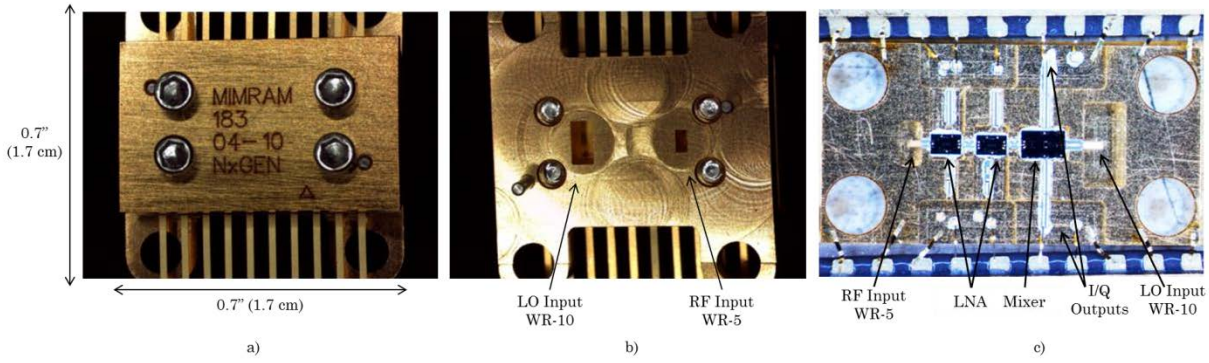


Figure 124: a) Top of 183 GHz MIMRAM b) Bottom of 183 GHz MIMRAM c) Populated 183 GHz MIMRAM

After down conversion the RF signal is output as two individual signals with 90° of phase separation designated as I and Q (Ulaby, Moore, & Fung, 1981). Both the I

and Q signals are output from the MIMRAM to identical IF chains containing a low pass filter and three IF amplifiers each as shown in Figure 125.

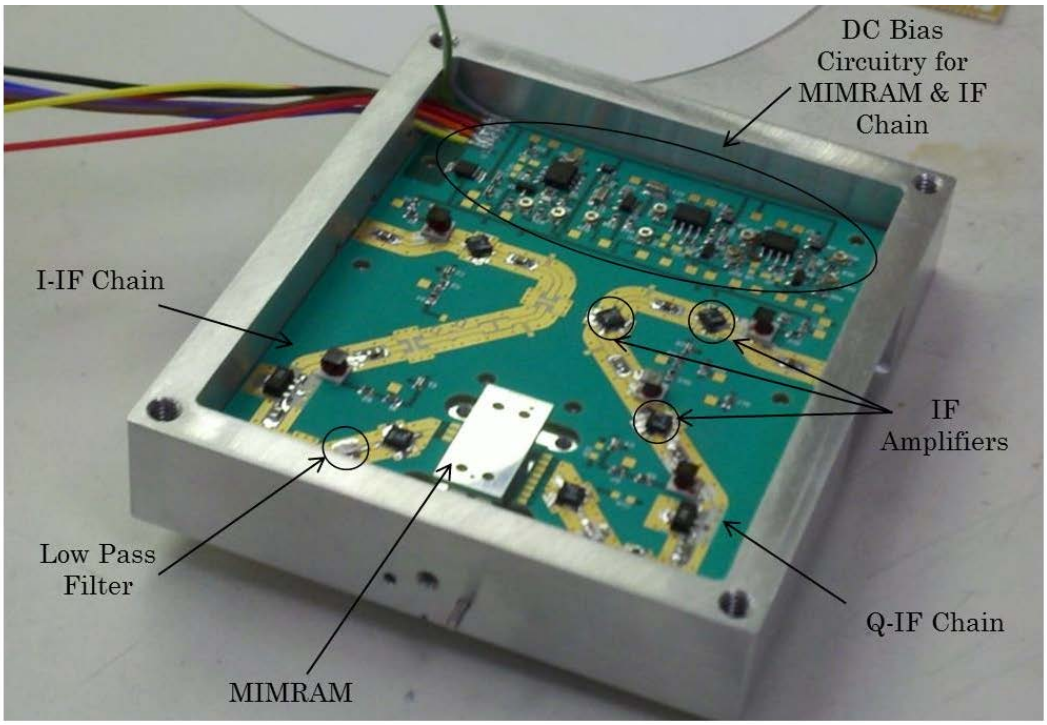


Figure 125: Millimeter-Wave Sounder Radiometer IF Board

The output of the IF chains are fed into a 90° hybrid coupler (Microwave Communications Laboratories, Inc., 2010) through two equal length coaxial cables. The 90° hybrid coupler accomplishes image rejection of the two signals through phase cancellation which results in two single sideband (SSB) signals at the output. This is desired because the oxygen sounding receiver only uses the USB and the water vapor sounding receiver only uses the LSB of the detected signals. These sidebands are removed because they are outside the frequency range of the quad-ridge horn and including them would increase the noise of the system. Additionally, the 118.75 GHz sounder has three channels that are output directly from the 90°

coupler. These channels are measured before the application-specific integrated circuit (ASIC) to allow the frequency spacing between them to be less than 1 GHz. Inline coaxial filters are used to set the offsets frequencies of these three channels to 0, 250, and 500 MHz. An 18 dB external LNA (Mini Circuits) is used to amplify these three channels and a four way power splitter is used to separate them, the external LNA and power splitter are referred to as the offset channel components.

After the 90° hybrid coupler the SSB signal is input to an ASIC spectrometer developed by Prof. Behzad Razavi of the University of California Los Angeles (UCLA) for the IIP-10 project. The ASIC divides the SSB signal into eight frequency bands offset in increments of 1 GHz from the center frequencies of 118.75 and 183.31 GHz. The offset and center frequency for each channel used in the sounding radiometers are given in Table 14 and

Table 15 for the 118.75, and 183.31 GHz center frequencies respectively.

Table 14: Temperature Sounding ASIC Offset Channel Frequencies

| Frequency Set | Channel | Offset Frequency |
|---|---|---|
| 118.75 GHz | 1 | +1 GHz |
| | 2 | +2 GHz |
| | 3 | +3 GHz |
| | 4 | +4 GHz |
| | 5 | +5 GHz |
| | 6 | +6 GHz |
| | 7 | +7 GHz |
| | 8 | +8 GHz |

Table 15: Water Vapor Sounding ASIC Offset Channel Frequencies

| Frequency Set | Channel | Offset Frequency |
|---|---|---|
| 183.31 GHz | 1 | -1 GHz |
| | 2 | -2 GHz |
| | 3 | -3 GHz |
| | 4 | -4 GHz |
| | 5 | -5 GHz |
| | 6 | -6 GHz |
| | 7 | -7 GHz |
| | 8 | -8 GHz |

SMC coaxial cables (Amphenol Connex) are used at the ASIC outputs to transmit the signal to the ABEBs for further amplification, integration, and digitization. Inline 500 MHz low pass filters and attenuators are used along these cables to define the bandwidth being detected and to bring the signal to the proper power level so the diode detectors will operate in the square-law region. The Schottky diode detectors for the sounder channels are also inline coaxial components placed directly before the ABEB inputs. The diode detectors were manufactured by Eclipse Microwave as part number EZM0120PA3 (Eclipse Microwave, 2014). It is important to notice that each output channel has an effective bandwidth of 1 GHz due to the negative frequency component from the down conversion folding over.

The sounder modules could not be built to specification due to time and budget constraints at JPL. This resulted in a much larger system as the LO chain and post ASIC filtering, attenuation, and diode detection had to be done external to the system. An additional bench called the sounder bench was designed to sit on top of

the optical bench to house the mm-wave sounding receivers. The additional volume of this sub-system caused mechanical issues in the HAMMR chassis mostly related to ease of access and reflector alignment. The labeled components and physical layout of the mm-wave sounding receivers can be seen in Figure 126 with the inputs and outputs of the receivers shown in Figure 127 a), and b).

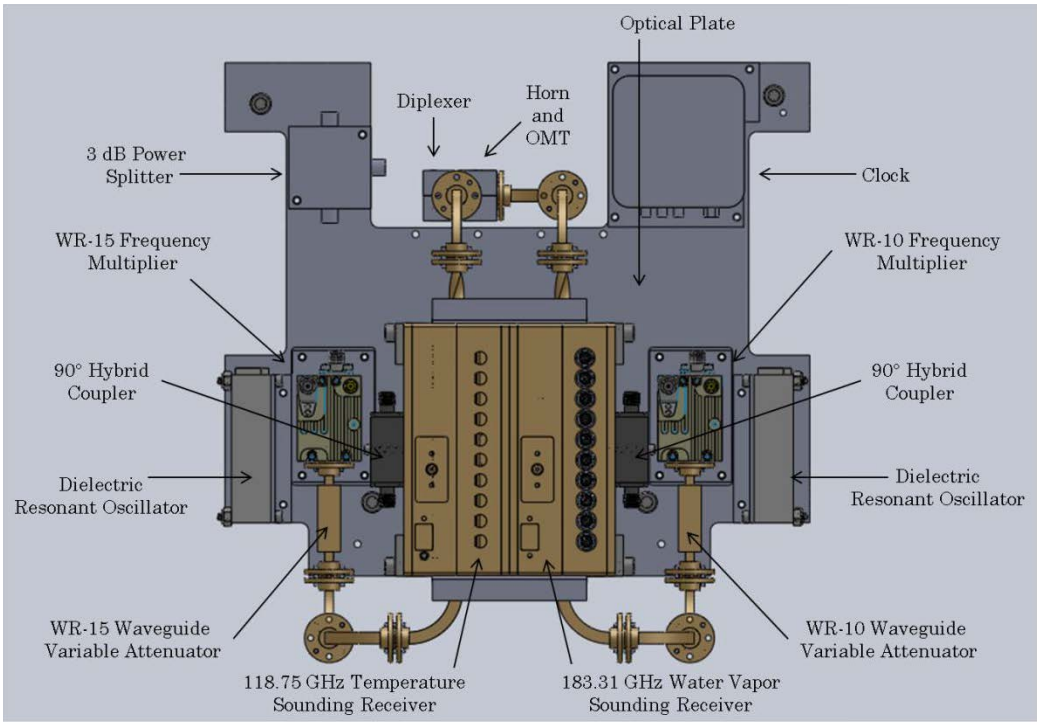


Figure 126: Millimeter-Wave Sounding Radiometer Components

As seen in Figure 126 the LO for the initial down conversion is external to the sounding receivers. The LO signal is generated by the Dielectric Resonant Oscillator (DRO) (Miteq) seen on the left and right sides of Figure 126. The DRO signal is then multiplied by the WR-15 and WR-10 frequency multipliers (Millitech) before entering the sounder receivers through a waveguide port shown in Figure 127 a). The 100 MHz clock (Wenzel Associates, Inc.) in the upper right portion of

Figure 126 generates a clock signal used in the ASIC. The clock signal goes from the clock to the 3 dB power splitter (Mini Circuits) before being fed into the ASIC clock SMA input shown in Figure 127 a).

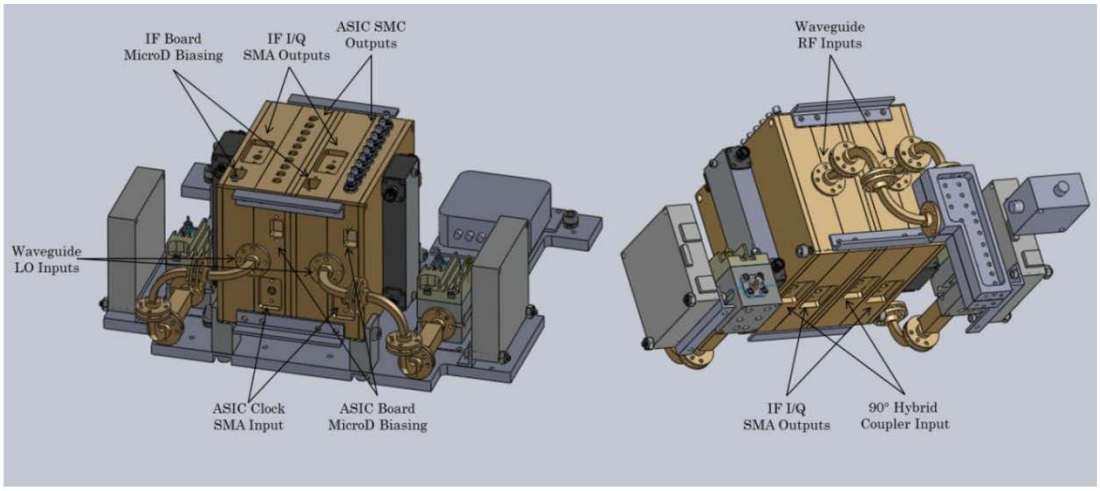


Figure 127: a) mm-Wave Sounding Radiometers Front Face Inputs b) mm-Wave Sounding Radiometers Back Face Inputs

The mm-wave sounding sub-system can be seen fully integrated in the HAMMR chassis in Figure 128 including the offset channel components.

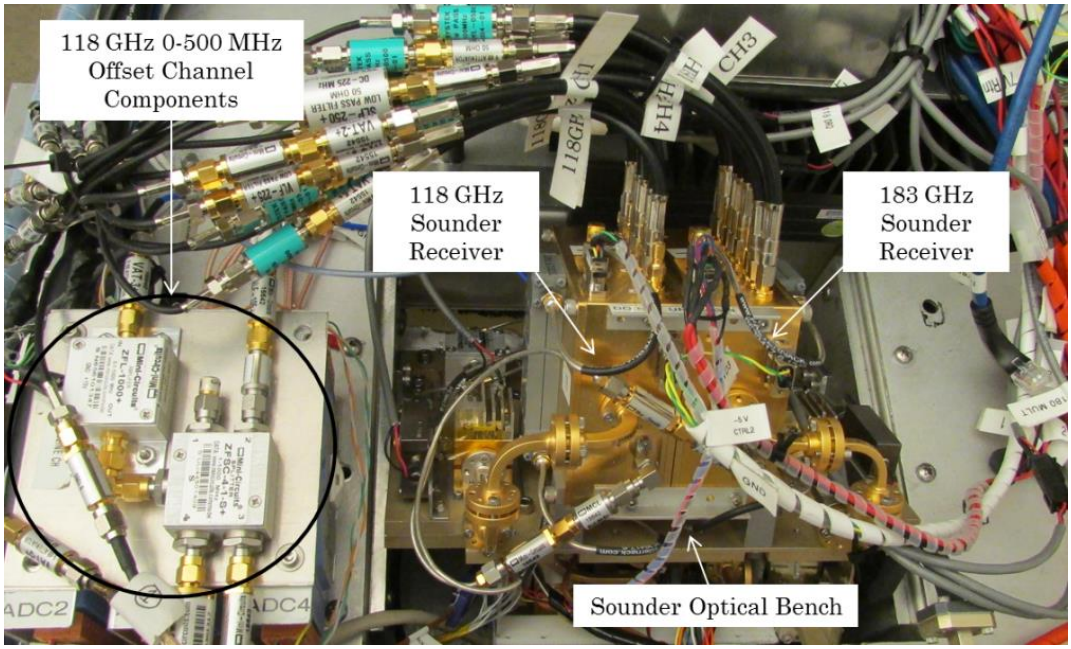


Figure 128: Assembled Millimeter-Wave Sounders in HAMMR

## 7.3 Performance

After the mm-wave sounding receivers had been assembled they were tested to ensure that the output power for each channel was consistent when looking at a stable load. This helps to ensure that the output power is at a level where the diode detector will work in the square-law region for each channel. The setup for these tests is shown in Figure 129.

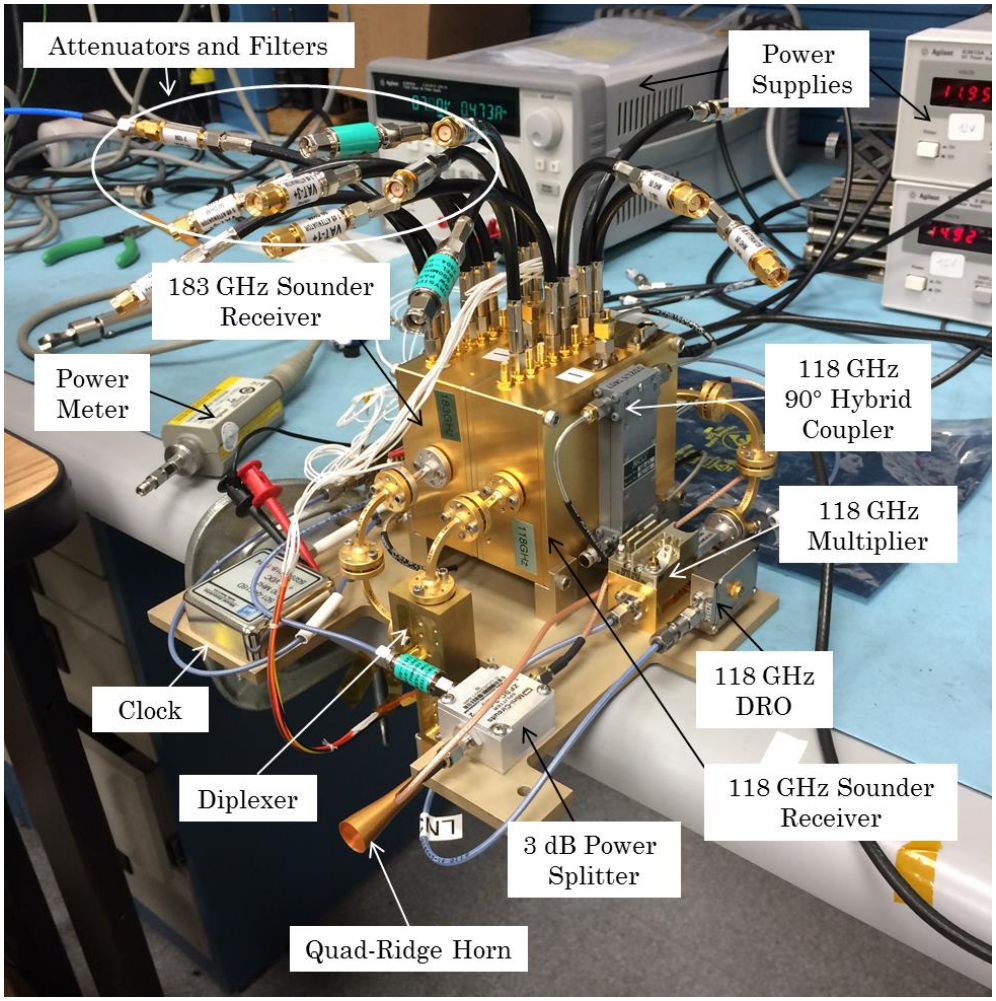


Figure 129: Millimeter-Wave Sounder Power Level Test Setup

Table 16 illustrates the output power for each sounder output.

Table 16: Sounder Channels Measured Output Power Levels

| Center Frequency | Offset Frequency | Filter Type | Measured Power Level (dBm) |
|---|---|---|---|
| 118.75 | 0 MHz | 100 MHz LPF | -27.7 |
| | 250 MHz | 200 MHz BPF | -27.4 |
| | 500 MHz | 300 MHz BPF | -27.5 |
| | +1 GHz | 250 MHz LPF | -27.5 |
| | +2 GHz | 250 MHz LPF | -27.4 |
| | +3 GHz | 500 MHz LPF | -27.6 |
| | +4 GHz | 500 MHz LPF | -27.6 |
| | +5 GHz | 500 MHz LPF | -29.5 |
| | +6 GHz | 500 MHz LPF | Not Connected |
| | +7 GHz | 500 MHz LPF | Not Connected |
| | +8 GHz | 500 MHz LPF | Not Connected |
| 183.31 | -1 GHz | 250 MHz LPF | -28.3 |
| | -2 GHz | 500 MHz LPF | -28.1 |
| | -3 GHz | 500 MHz LPF | -28.2 |
| | -4 GHz | 500 MHz LPF | -27.6 |
| | -5 GHz | 500 MHz LPF | -27.6 |
| | -6 GHz | 500 MHz LPF | -27.8 |
| | -7 GHz | 500 MHz LPF | -27.7 |
| | -8 GHz | 500 MHz LPF | -28.7 |

### 7.3.1 Receiver Noise Temperature

Once the mm-wave sounding sub-system had been installed and the output powers for each channel were verified a Y-factor test was done to characterize the receiver noise temperature for each channel shown in Table 17.

Table 17: Sounder Channels Average Noise Temperature

| Center Frequency | Offset Frequency | Average Noise Temperature (K) |
|---|---|---|
| 118.75 GHz | 0 MHz | N/A |
| | 250 MHz | 492 |
| | 500 MHz | 427 |
| | +1 GHz | 558 |
| | +2 GHz | 535 |
| | +3 GHz | 536 |
| | +4 GHz | 535 |
| | +5 GHz | 540 |
| | +6 GHz | NC |
| | +7 GHz | NC |
| | +8 GHz | NC |
| 183.31 GHz | -1GHz | 1323 |
| | -2 GHz | 1341 |
| | -3 GHz | 1349 |
| | -4 GHz | 1441 |
| | -5 GHz | 1422 |
| | -6 GHz | 1434 |
| | -7 GHz | 1210 |
| | -8 GHz | 1230 |

Table 17 shows that the average noise temperature for each sounder channel is quite good. It is hypothesized that the 183.31 GHz channels have higher noise temperatures than the 118.75 GHz channels because the LNAs and perhaps the mixer in the 183.31 GHz MIMRAM have higher noise figures.

## 7.4 60 Hz Noise

After integration, initial testing showed a large amount of noise in the sounder channels as illustrated for the 118 + 3 GHz channel in Figure 130. Initially it was

thought that the noise was being caused by oscillations in the ABEB. However, while troubleshooting it was found that the noise was coming from three different sources; a 20 kHz and harmonics oscillation from the oscilloscope that was being coupled through the wall power to the instrument, 120 Hz oscillation caused by the fluorescent lights in the laboratory, and a 60 Hz and harmonics oscillation being caused by the linear power supplies in the instrument.

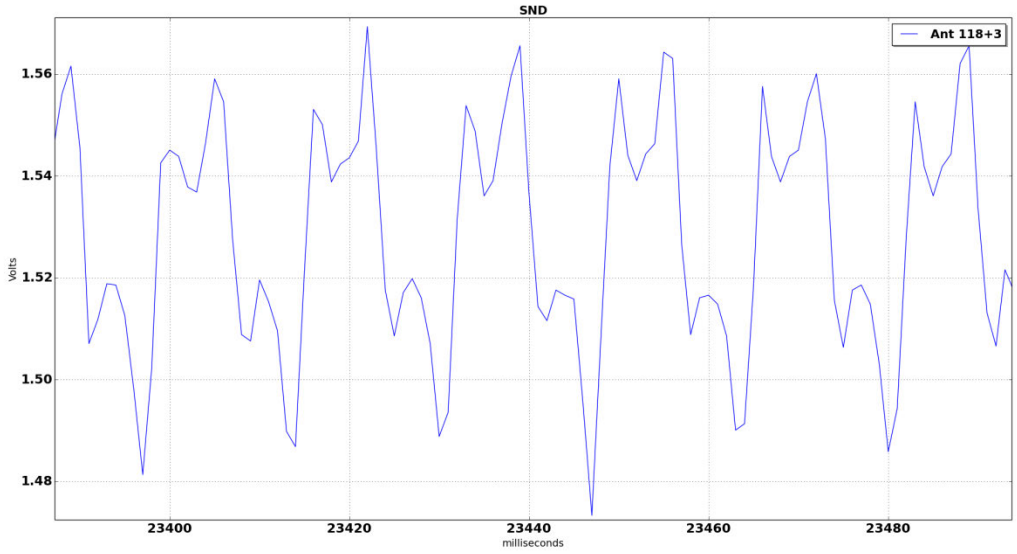


Figure 130: Initial Voltage Waveform of Sounding Channel 118+3 GHz

The first two noise components, from the oscilloscope and fluorescent lights, were easily eliminated by turning them off but the noise from the linear power supplies was much harder to correct. We first had to establish if the noise was being coupled to the coaxial cables via magnetic fields from the transformers or if there was a ground loop causing these oscillations. To do this we tested the +7 V linear power supply in four different positions and orientations as shown in Figure 131. The results for this test are shown as fast Fourier transforms (FFTs) of the voltage

signals for power supply positions 1, 2, 3, and 4 in Figure 132 a), b), c) and d) respectively.

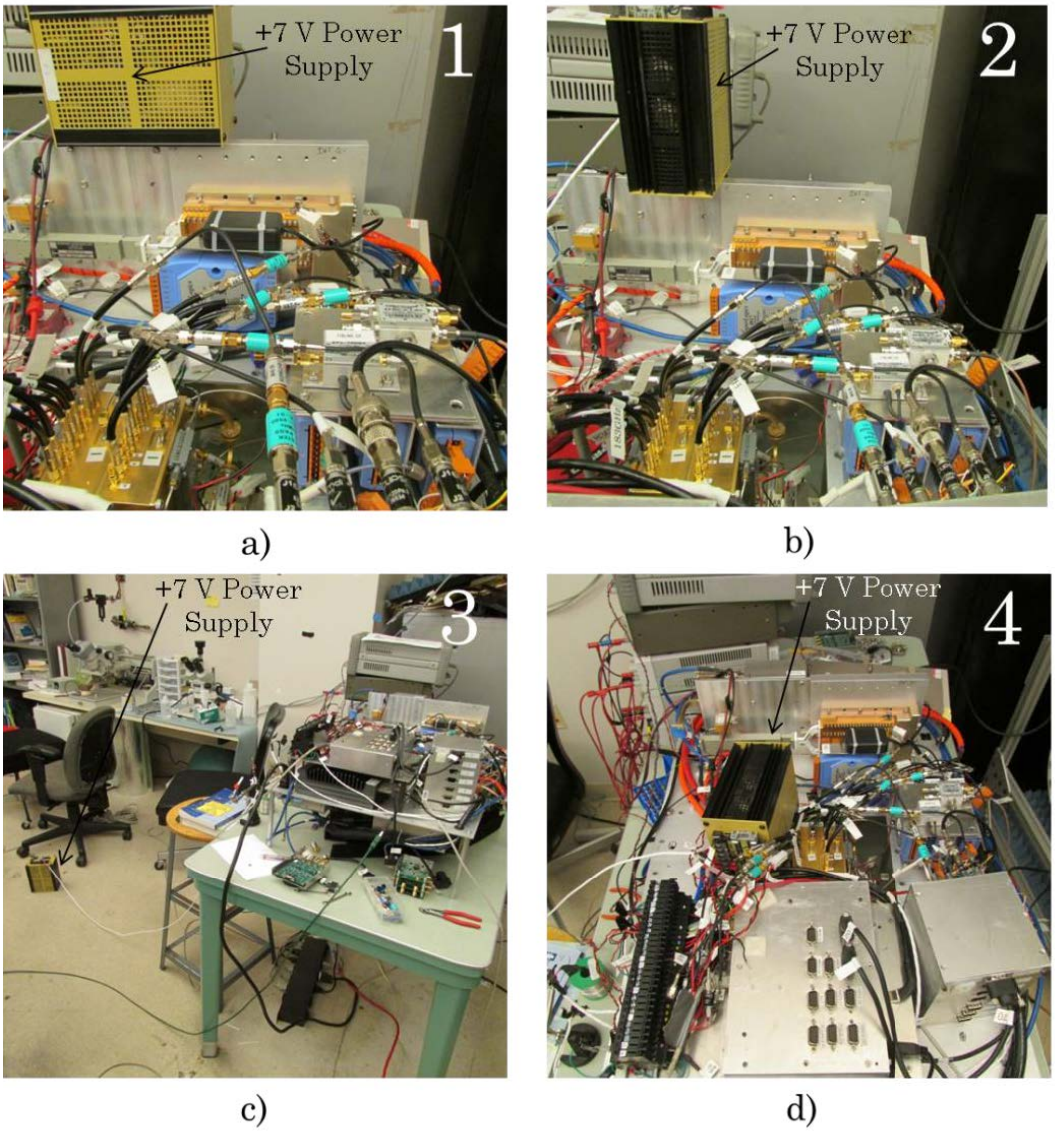


Figure 131: Power Supply Orientations to Test Source of 60 Hz Noise Coupling

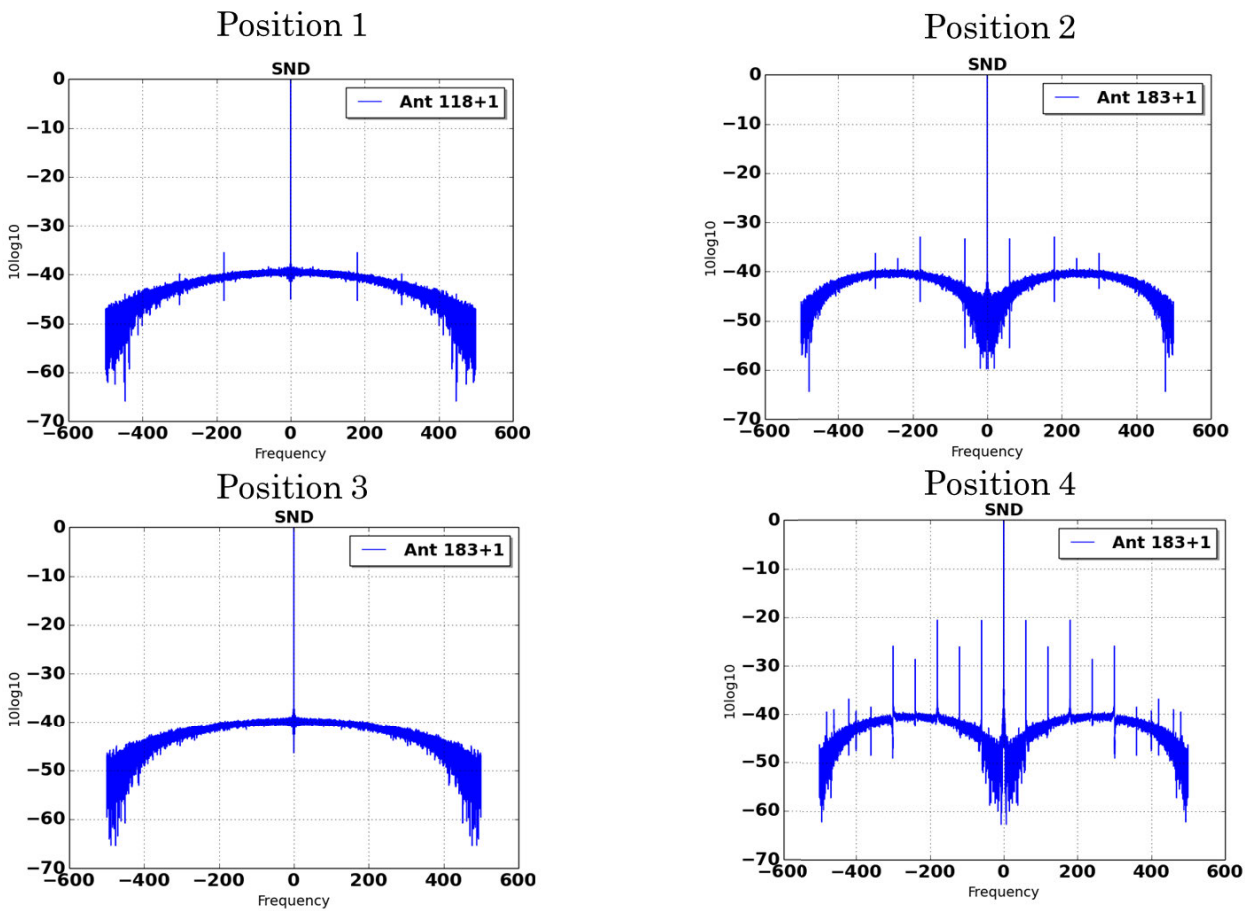


Figure 132: Fast Fourier Transforms of Measured Voltage for Sounding Channel 183+1 GHz with the +7 V Power Supply in Four Different Positions

Figure 132 shows that the orientation and distance of the power supply to the sounder channels makes a large difference which allows us to conclude that the magnetic fields from the linear power supply transformers are causing the problem. This test was done while monitoring four different sounder channels with cables in different orientations. It was found that the orientation and distance of the cable with respect to the power supply has the largest effect in the amount of 60 Hz noise and its harmonics that is detected. This test was repeated with a switching power

supply for a laptop and regardless of position or orientation no noise within 40 dB of the detected signal was measured. Various types of shielding were implemented to try and further reduce the 60 Hz noise components but none were successful.

To solve this problem, the three biggest linear power supplies, -12, +12, and +7 V were removed and replaced with switching power supplies at these voltages. Inline coaxial DC blocking capacitors were also added before each diode detector to attenuate the 60 Hz signal that was being coupled from the remaining smaller, -5, +15, and +16 V linear power supplies.

The result of these changes is shown in voltage with respect to time in Figure 133. It can be seen when comparing with Figure 130 that the peak to peak voltage of the noise has reduced from about 90 mV to about 30 mV.

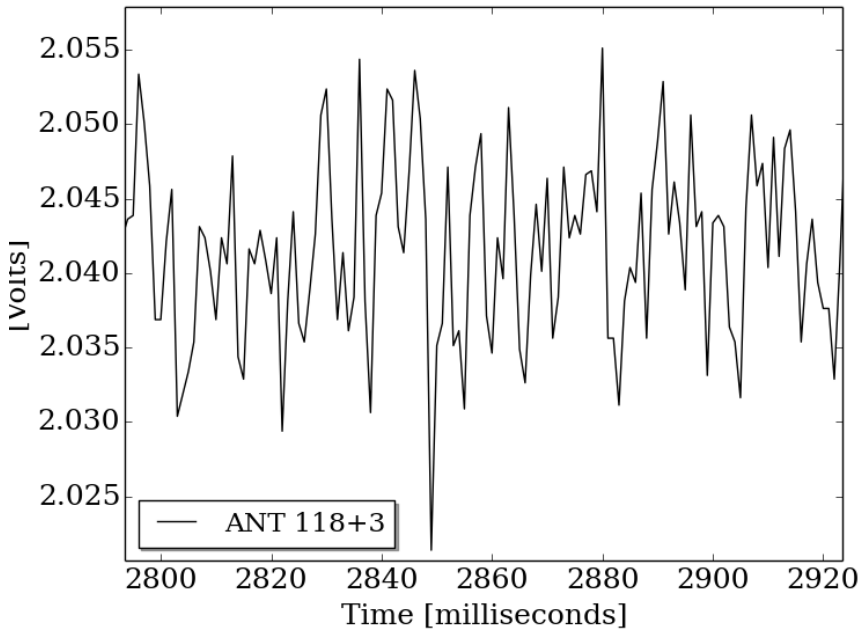


Figure 133: Voltage Waveform of Sounding Channel 118+3 GHz after Modifications

However, when the signal is averaged over time the 60 Hz oscillations again become distinguishable as shown by the blue line in Figure 134. The data is still good though, because enough noise was removed that post processing digital filtering can remove the 60 Hz component of the signal as shown by the green line in Figure 134.

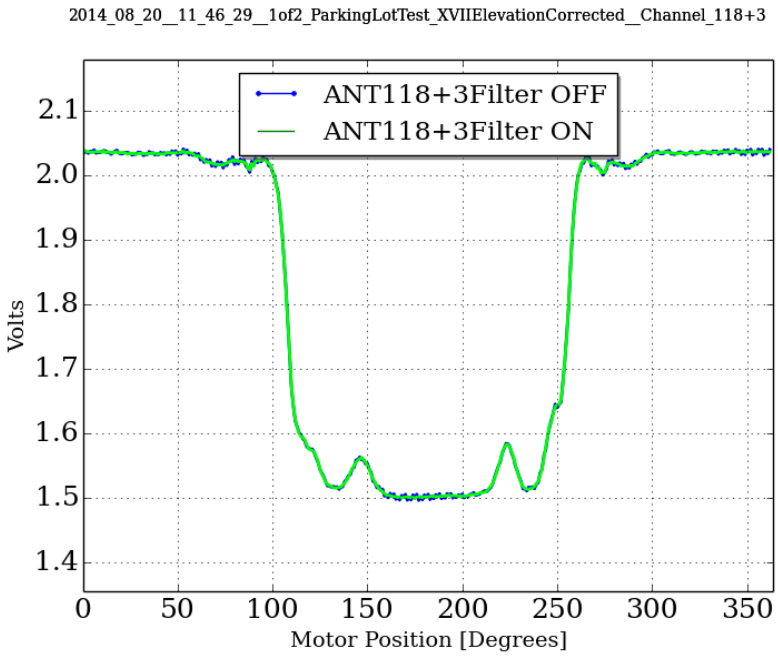


Figure 134: 118+3 GHz Output in Final Configuration with and Without Post Processing Filter

Figure 135 a) and b) show two zoomed in portions if Figure 134 to better illustrate the effects of the filtering and time averaging on the sounder signal.

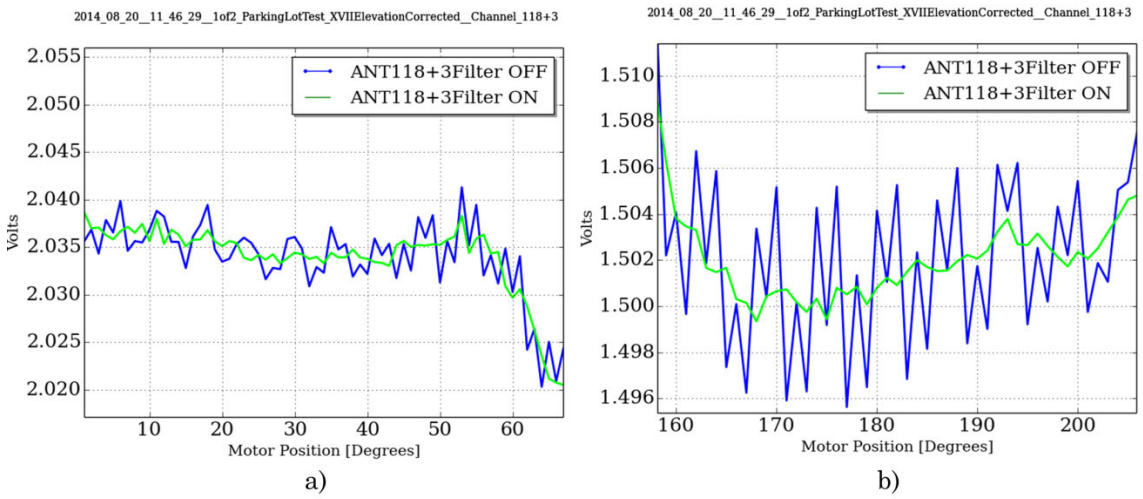


Figure 135: Zoomed in 118+3 GHz Output in Final Configuration with and Without Post Processing Filter

To further correct this problem the remaining -5, +15, and +16 V linear power supplies could be swapped for switching power supplies at the same voltages.

## 7.5 Oxygen Sounder Spectrum Debugging

When running tipping curve tests discussed in Section 8.2 it was noticed that the 118 GHz oxygen sounder offset channels were not measuring the expected brightness temperatures as seen in Figure 136 with the red dots being measured temperatures and the blue line being the expected values with respect to frequency.

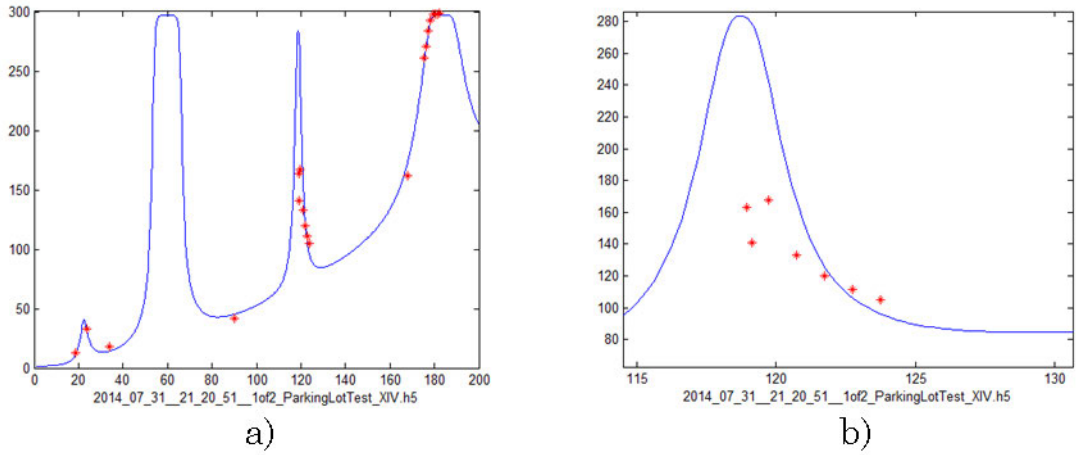


Figure 136: Measured (dots) vs. Expected Brightness Temperatures (lines) with no Waveguide Attenuation, a) All Channels, b) Zoom of 118 GHz Sounding Channels

The discrepancy in measured vs expected brightness temperatures is believed to be caused by intermodulation distortion in the MIMRAM subharmonic mixer. The intermodulation distortion is caused by the RF power input to the mixer being too high. To confirm this hypothesis, a piece of anti-static bag was glued to a ring terminal and inserted across the RF waveguide diplexer output to act as an attenuator as seen in Figure 137. This "waveguide attenuator" added approximately 8 dB of attenuation of the RF signal before the mixer. The results of tipping curve tests done with the 8 dB "attenuator" are shown in Figure 138.


Figure 137: Antistatic Bag Attenuator across the Diplexer Waveguide Output

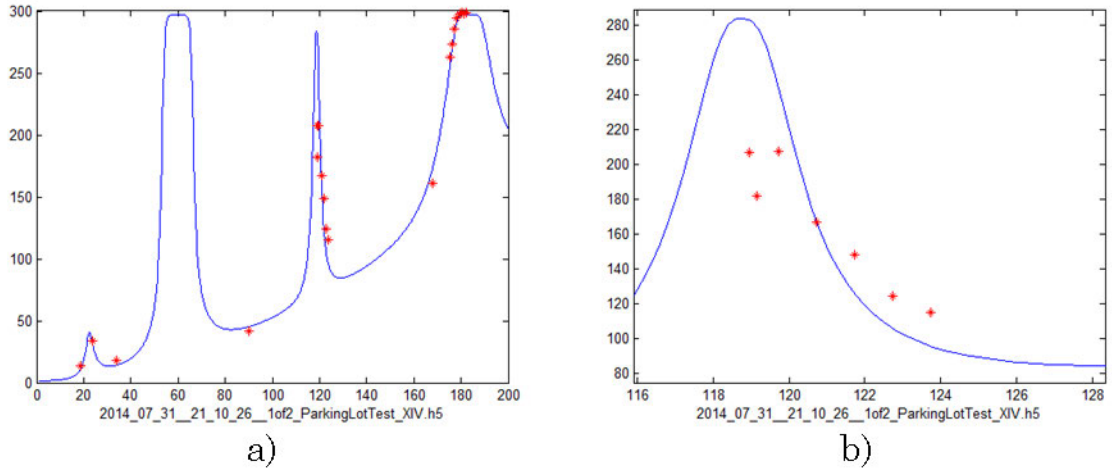


Figure 138: Measured vs. Expected Brightness Temperatures with 8dB of Waveguide Attenuation, a) All Channels, b) Zoom of 118 GHz Sounding Channels

Figure 138 shows that with an added 8 dB of attenuation on the RF signal before the subharmonic mixer, the measured brightness temperatures better match the expected values. To correct this problem the 118 GHz receiver will be sent to JPL and attenuator pads will be installed before the mixer on the RF signal path in the

MIMRAM. This should provide sufficient attenuation to keep the intermodulation distortion in the subharmonic mixer negligible.

# Chapter VIII. HAMMR Characterization and Calibration

This chapter will discuss the tests used to validate, characterize and calibrate HAMMR. The tests discussed in this chapter were run with all sub-systems integrated in the chassis.

## 8.1 Instrument Setup

For these tests the instrument was assembled in its' final flight configuration. Each radiometer channel has its' own acquisition sequence which defines how much time is spent looking at the antenna (ANT), dicke reference load (REF), and noise sources (NS#). The ratio of time spent between looking at the ANT and either the REF or NSs influences the radiometric resolution for that channel. As more time is spent looking at ANT the ideal radiometric resolution increases but noise from gain fluctuations can become more prominent decreasing the radiometric resolution, as explained in Section 2.2.3. A balance must be found in the acquisition sequence to optimize time spent looking at each source. For all tests the motor scans at 1 Hz, 60 rotations per minute, and the acquisition sequence for each radiometer is as shown in Table 18.

Table 18: Acquisition Sequence for Parking Lot Tests

| Radiometer | Integration Time (ms) | Acquisition Sequence |
|---|---|---|
| Microwave | 0.2 | 1 ms REF |
| | | 6 ms ANT |
| | | 1 ms NS1 |
| | | 1 ms NS2 |
| | | 1 ms NS3 |
| Microwave | 0.2 | 1 ms REF |
| | | 6 ms ANT |
| | | 1 ms NS1 |
| | | 1 ms NS2 |
| Sounders | 1 | 1 ms ANT |

## 8.2 Parking Lot Tests

Before installing HAMMR in an aircraft, tests were done in the CSU Lory Student Center parking lot to characterize the radiometer sub-systems and to determine if a scan bias was present in any channel due to the HAMMR chassis. To accomplish this tip curves were measured and an LN2 target was viewed for calibration.

### 8.2.1 Tip Curve Measurements

The first tests done were tipping curve measurements used to ensure that the radiometer is operating in a linear region and measuring expected voltage levels. A tip curve measurement involves looking straight up into the sky and then scanning the beam towards the horizon. While looking straight up into the air, often referred to as the zenith position, the radiometer should see a low brightness temperature corresponding to one atmosphere. As the radiometer scans, the beam angle changes

and the radiometer sees more atmosphere which should correspond to a higher brightness temperature as illustrated in Figure 139. The expected values for the different scan angles are calculated using the radiative transfer model discussed in Section 2.1.2 based off atmospheric parameters such as temperature and pressure. Since these values cannot be known without launching a radiosonde these tests are approximate and cannot be used for final validation or calibration.

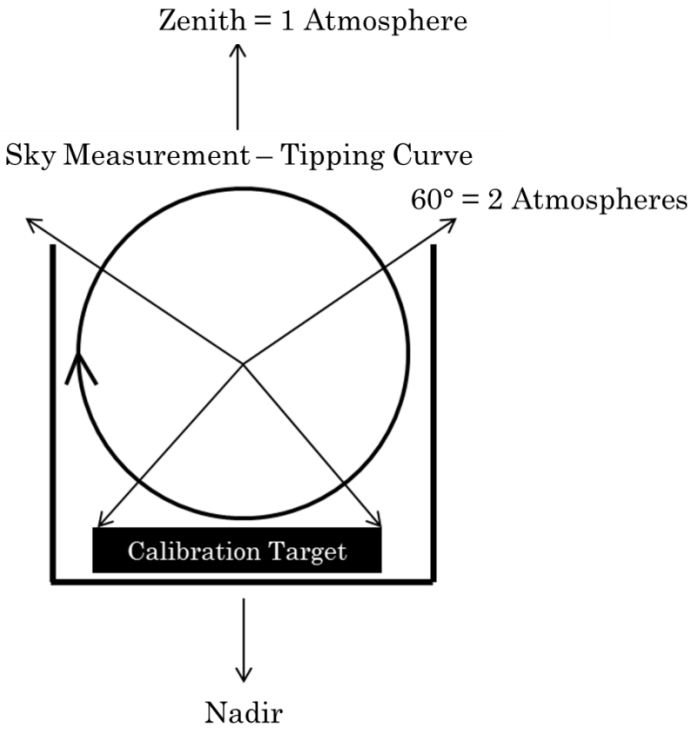


Figure 139: Illustration of HAMMR Performing a Tipping Curve Measurement

For the tipping curve measurements HAMMR was set up in the rotational cart described in Section 3.3.4 as seen in Figure 140. The instrument views the sky, scanning from left to right as shown in Figure 141. For these measurements the brightness temperature at zenith should be the minimum and it should increase

symmetrically with scan angle. The results for the tipping curve measurements performed on July 22, 2014 are presented below in sub-sections for each frequency set. The results are presented with each side of the tipping curve measurement folded over on itself to aid in evaluating scan symmetry and the ideal tipping curve values shown in red. The top of each figure also shows the receiver noise temperature calculated using the presented tipping curve.

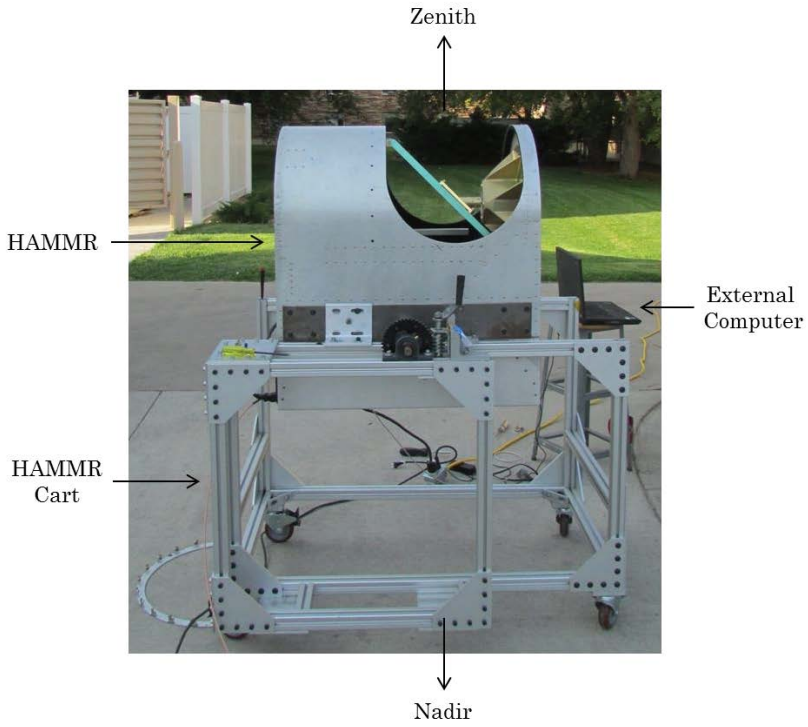


Figure 140: HAMMR Outdoor Ground Test Setup

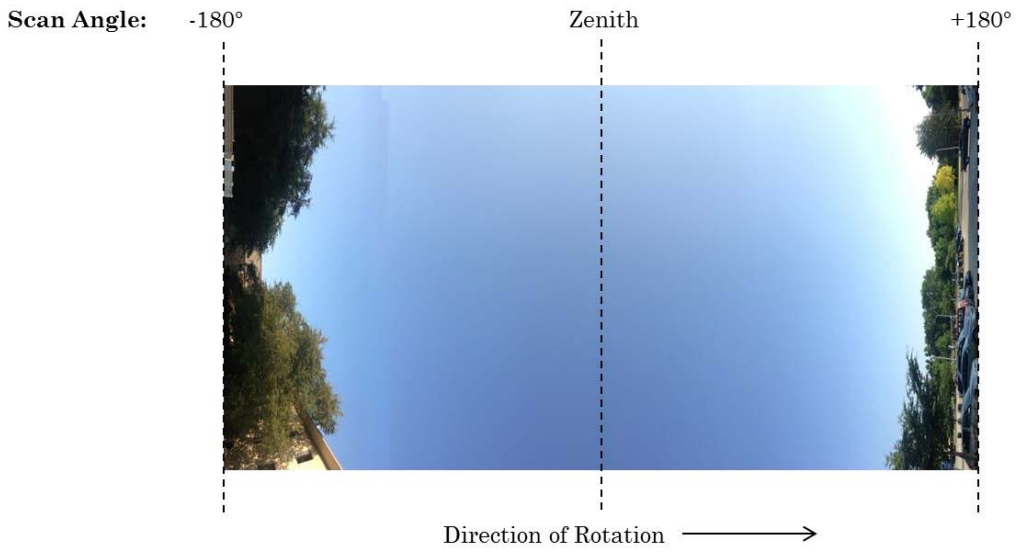


Figure 141: Sky Observed by HAMMR during Outdoor Ground Measurements

#### 8.2.1.1 Microwave Radiometers

The microwave radiometers results are shown in Figure 142 with the QH and QV radiometers shown on the left and right side respectively. Both microwave radiometers have an obvious asymmetry for every channel. This asymmetry is due to the beam offset detailed in section BEAM OFFSET SECTION causing the microwave feed horn beam to view the chassis on the first half of the scan. This can be corrected by trimming the HAMMR chassis aperture to no longer obstruct the feed horn beam during the scan. The side of the scan not affected by the beam offset shows excellent agreement with expected values and the calculated receiver noise temperature match LN2 calibrations quite well. The receiver noise temperatures for the microwave channels are calculated using only the unobstructed half of the scan.

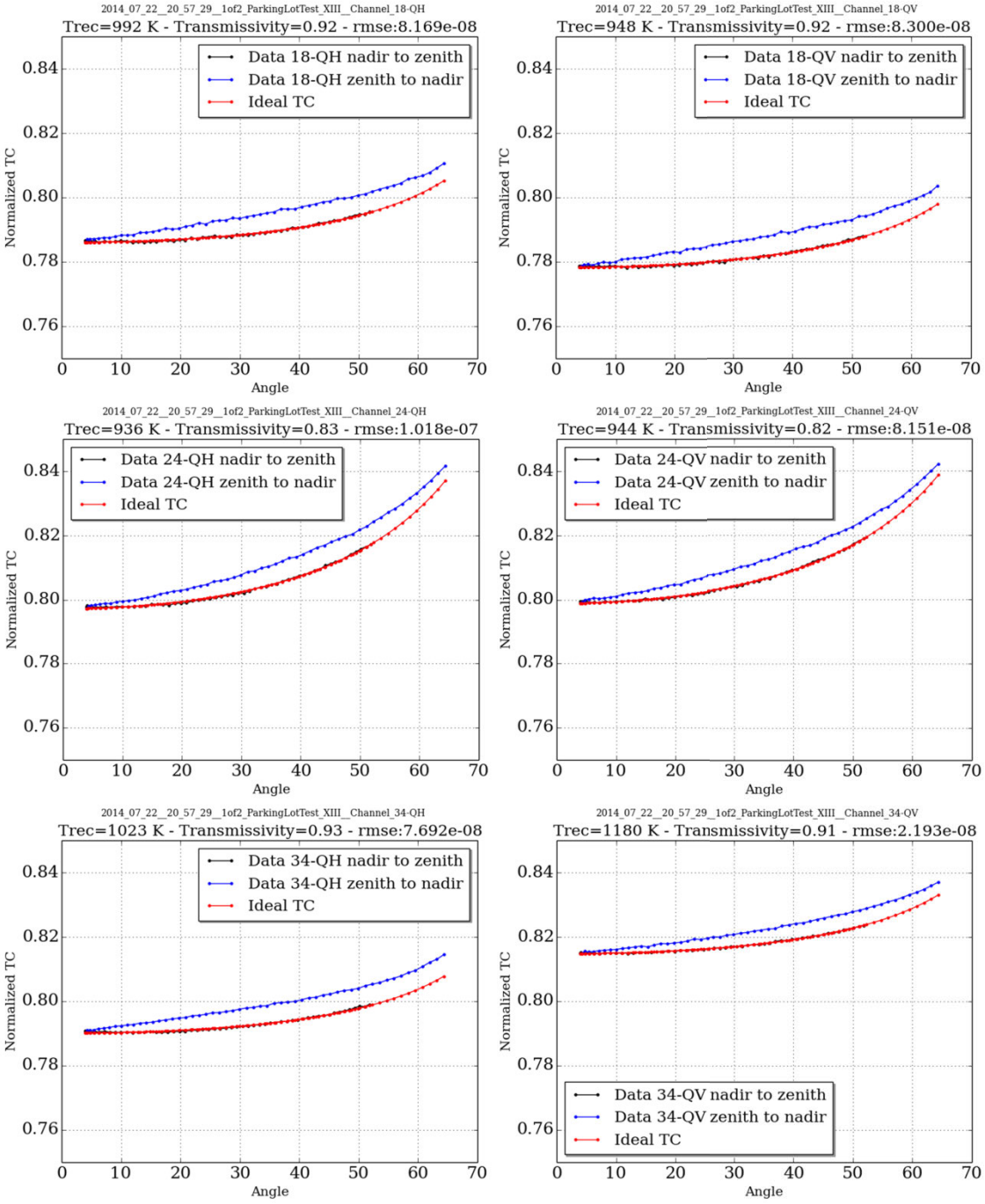


Figure 142: Results of a Tipping Curve Measurement Performed on July 22, 2014 for the Microwave Radiometers QH (left) and QV (right) Polarizations

#### 8.2.1.2 Millimeter-Wave Window Radiometers

The mm-wave window channels tipping curve results are shown in Figure 143 with a), b), and c) representing the 90, 130, and 168 GHz channels respectively. All mm-wave window channels show great symmetry and agree well with the ideal tipping curve values. The noise temperatures calculated for these channels is a little higher than expected most likely due to errors in atmospheric assumptions or the receivers operating at a higher physical temperature.

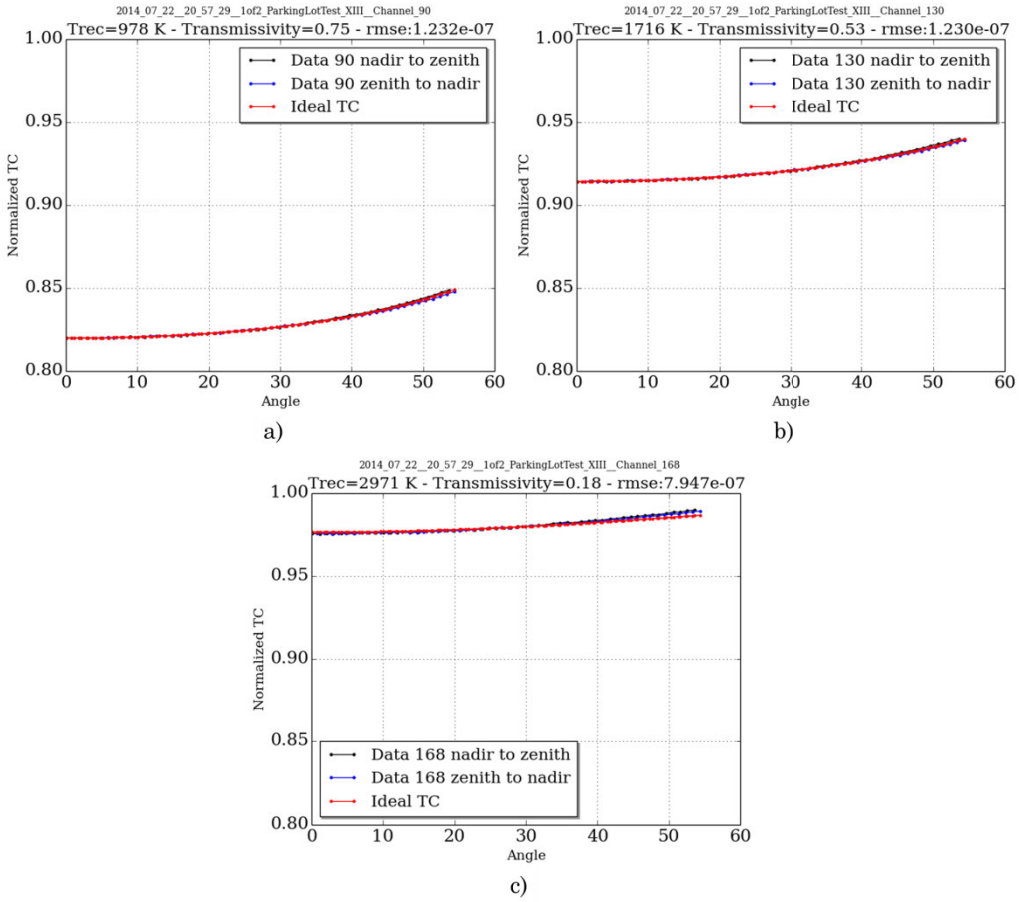


Figure 143: Results of a Tipping Curve Measurement Performed on July 22, 2014 for the Millimeter-Wave Window Channels, a) 90 GHz, b) 130 GHz, and c) 168 GHz

#### 8.2.1.3 Millimeter-Wave Sounding Radiometers

The mm-wave 118.75 GHz oxygen sounding channels tipping curve results are shown in Figure 144 and Figure 145. The 118+0 GHz channel has no data because the ABEB for that channel had not yet been fixed at the time of this test. The 118 GHz channels shows good symmetry and agree well with the ideal tipping curve values. The calculated receiver noise temperatures match well with those presented in Section 7.3.1 for the four most offset channels shown in Figure 145. The channels

shown in Figure 144 show higher noise temperatures due to the frequency spectrum problem discussed in Section 7.5.

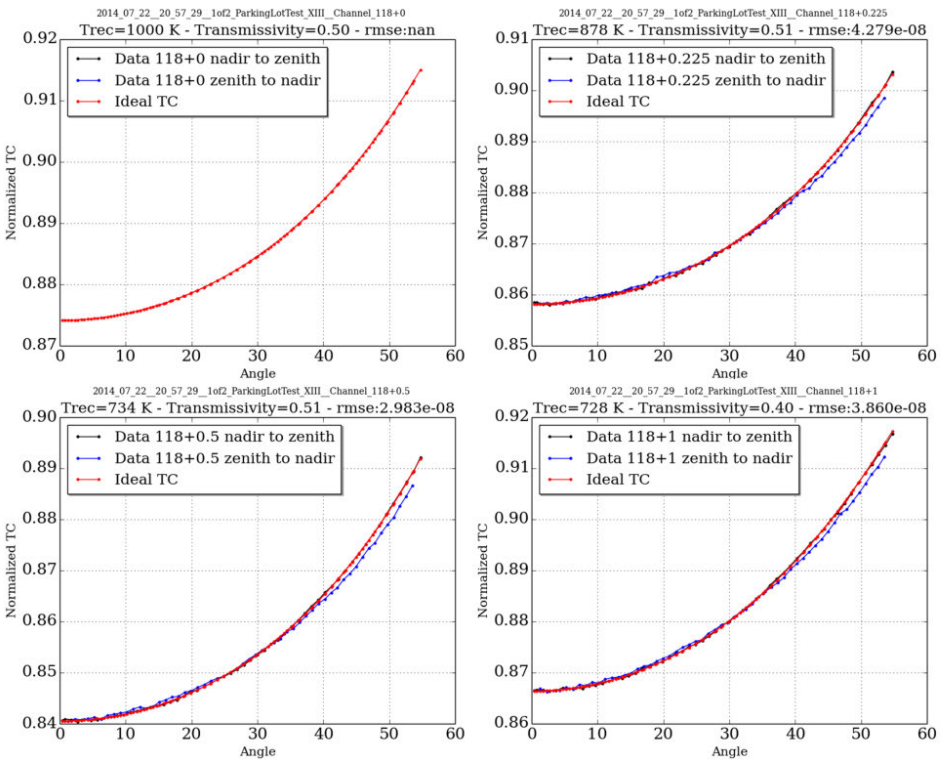


Figure 144: Results of a Tipping Curve Measurement Performed on July 22, 2014 for the Millimeter-Wave Sounding Channels 118+0, 118+0.225, 118+0.5, and 118+1 GHz

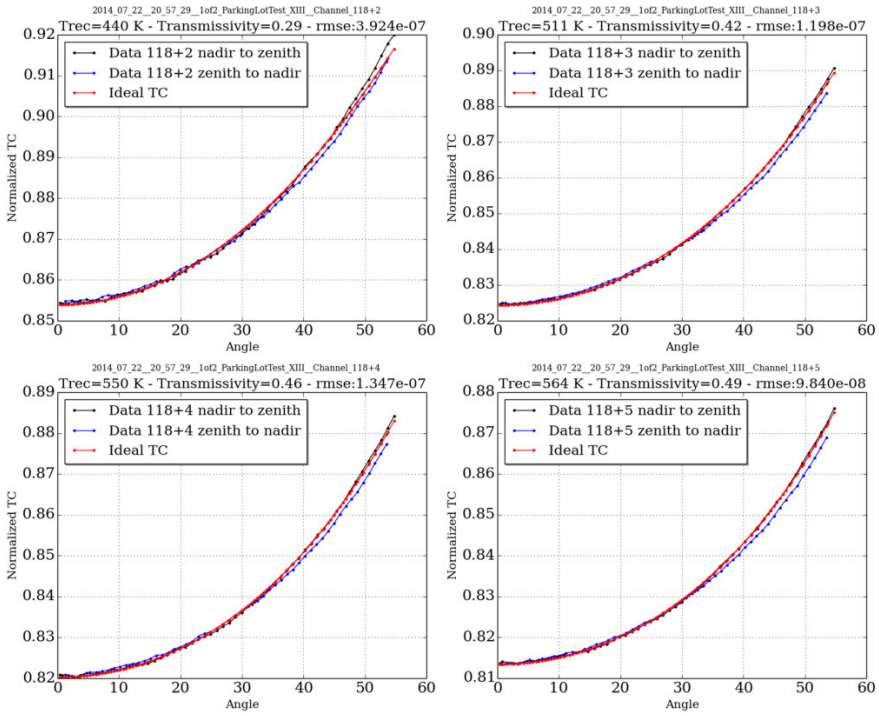


Figure 145: Results of a Tipping Curve Measurement Performed on July 22, 2014 for the Millimeter-Wave Sounding Channels 118+2, 118+3, 118+4, and 118+5 GHz

The mm-wave 183.31 GHz water vapor sounding channels tipping curve results are shown in Figure 146 and Figure 147. All the 183.31 GHz sounding channels were saturated during this experiment due to the high absorption due to water vapor at these frequencies which is why the measured values are practically flat for the first few offset channels. As the channel offsets increase the data begins to converge to the expected values indicating that the channels are saturated. The receiver noise temperatures calculated during this experiment for these channels is extremely high due to the channels being saturated.

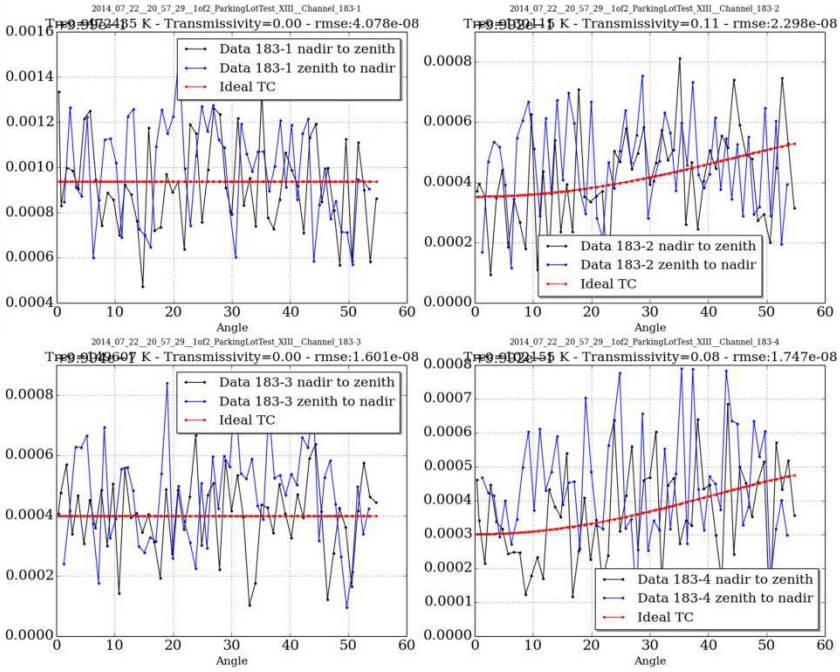


Figure 146: Results of a Tipping Curve Measurement Performed on July 22, 2014 for the Millimeter-Wave Sounding Channels 183-1, 183-2, 183-3, and 183-4 GHz

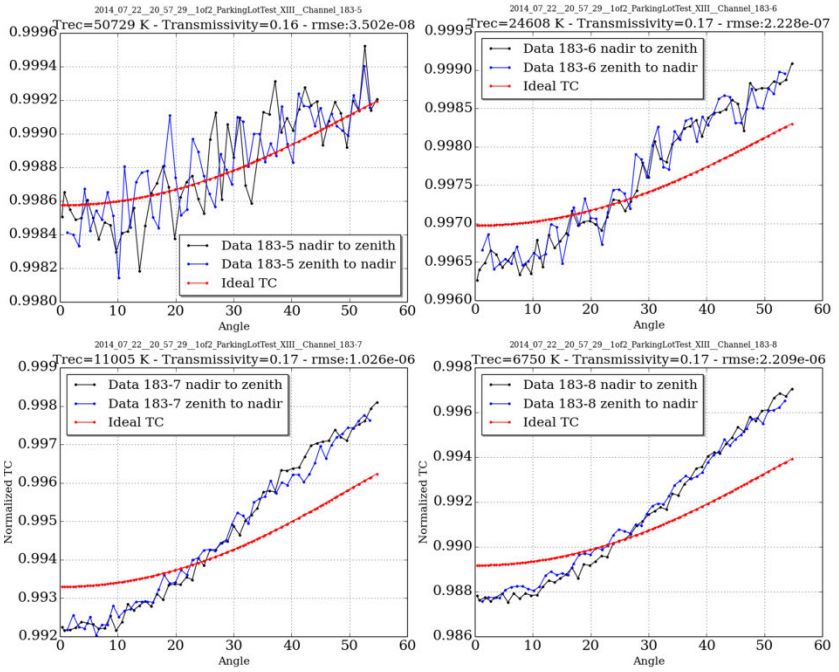


Figure 147: Results of a Tipping Curve Measurement Performed on July 22, 2014 for the Millimeter-Wave Sounding Channels 183-5, 183-6, 183-7, and 183-8 GHz

These tests showed a problem with the spectrum of the oxygen sounder channels where some offset frequencies were not measuring the expected brightness temperature. The debugging and solution for this problem is discussed in detail in Section 7.5.

### 8.2.2 Liquid Nitrogen Calibration

For Y-factor calibration an LN2 calibration target, made from a Styrofoam cooler with LN2 cooled microwave absorber at the bottom, as seen in Figure 148 was used. To ensure that all the energy measured by the radiometers is coming from the microwave absorber, the walls of the cooler were lined with aluminum foil.

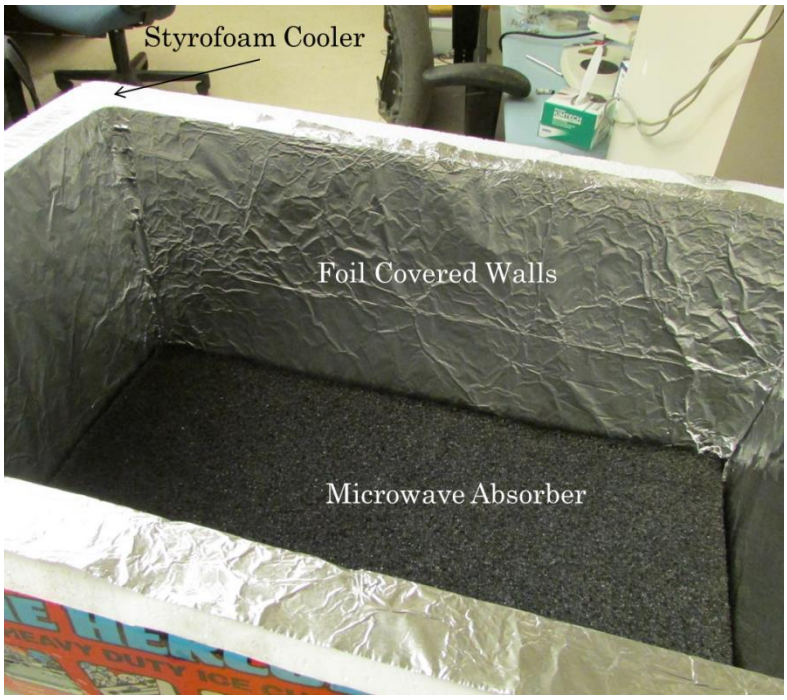


Figure 148: Styrofoam Cooler Calibration Target

To use the target HAMMR is rotated 180° to view the Styrofoam LN2 calibration target as seen in Figure 149. However, since the HAMMR aperture curves upward from the bottom of the instrument, cardboard flaps covered in aluminum foil were fabricated to isolate these measurements from ambient radiation. The flaps being used during a calibration are shown in Figure 150.

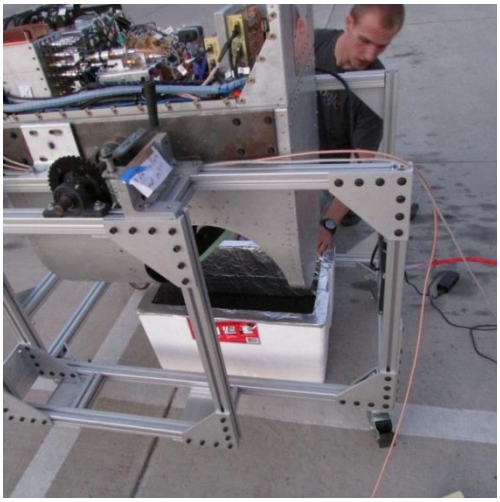

Figure 149: HAMMR Viewing the Styrofoam LN2 Calibration Target

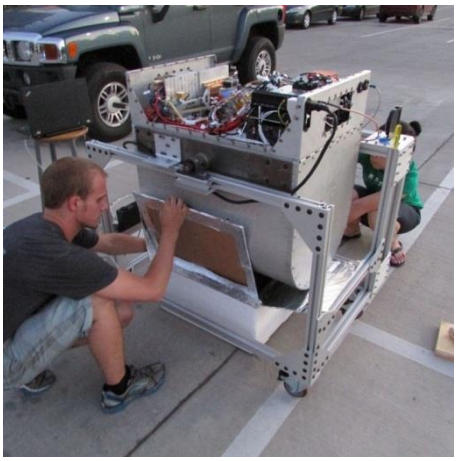

Figure 150: HAMMR Viewing the Styrofoam LN2 Calibration Target with Cardboard Flaps in Use

The LN2 calibration test provides a two-point calibration, or Y-factor, along with the internal blackbody calibration target discussed in Chapter IV, that is used in conjunction with the tipping curve measurements to validate radiometer performance. These tests can also be used to validate the internal calibration of the microwave and mm-wave window radiometers.

The results of these tests are given in the following sub-sections organized by frequency sets. For each frequency set only one channel is shown as the LN2 calibration target results are very similar for the other channels in each frequency set.

#### 8.2.2.1 Microwave Radiometers

The results for the 18 GHz QV microwave channel are presented in Figure 151 a) and b). The results show that the LN2 target remains stable enough for a good calibration across a 15° scan angle.

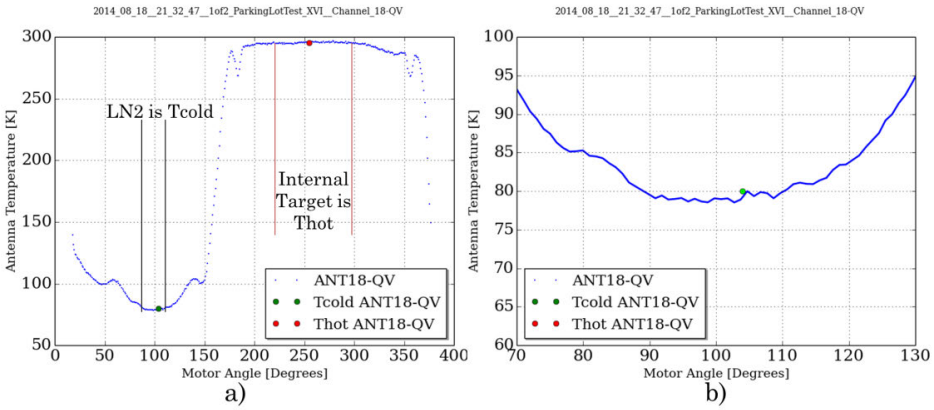


Figure 151: Results of a LN2 Calibration for the 18 GHz QV Microwave Channel, a) With No Zoom, b) Zoomed on the Portion of the Scan While Viewing the LN2

#### 8.2.2.2 Millimeter-Wave Window Radiometers

The results for the 90 GHz mm-wave window channel are presented in Figure 152 a) and b). The results show that the LN2 target remains stable enough for a good calibration across a 20° scan angle.

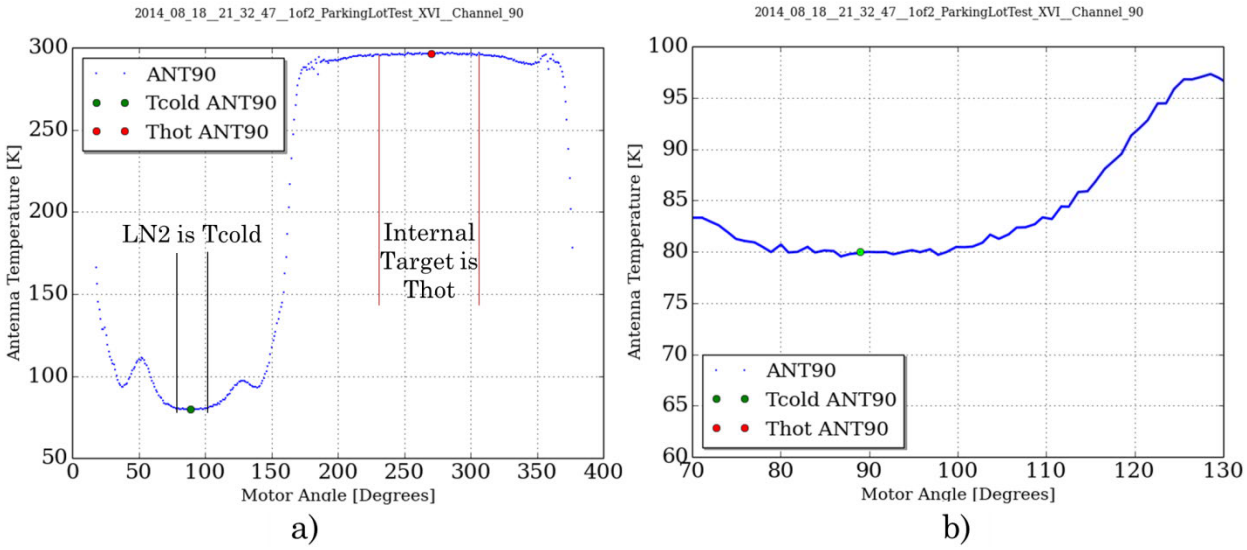


Figure 152: Results of a LN2 Calibration for the 90 GHz Millimeter-Wave Window Channel, a) With No Zoom, b) Zoomed on the Portion of the Scan While Viewing the LN2

#### 8.2.2.3 Millimeter-Wave Sounding Radiometers

The results for the 118+2 GHz mm-wave sounding channel are presented in Figure 152 a) and b). The results show that the LN2 target remains stable enough for a good calibration across a 25° scan angle.

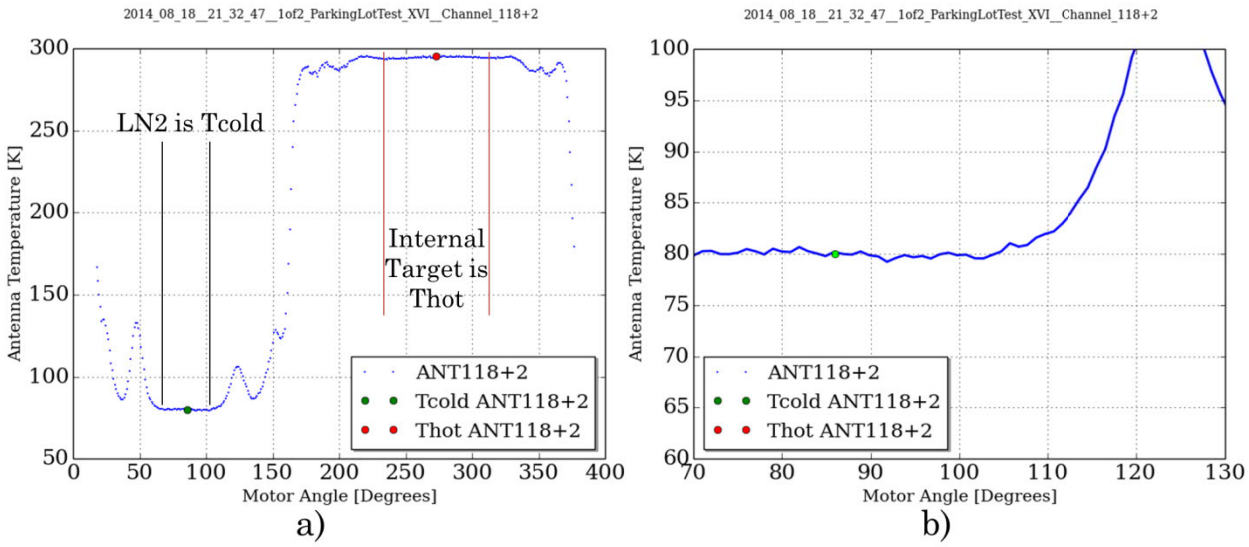


Figure 153: Results of a LN2 Calibration for the 118+2 GHz Millimeter-Wave Sounding Channel, a) With No Zoom, b) Zoomed on the Portion of the Scan While Viewing the LN2

### 8.2.3 Cart Tilting Test

To determine if the HAMMR chassis is obstructing any antenna beams as they exit the instrument aperture a test where the instrument was tipped while taking a tipping curve was done.

If the chassis is interfering with the antenna beam for only a portion of the scan this would be difficult to detect using tipping curve measurements without a radiosonde. To determine if this type of scan bias exists in the system the entire instrument was tilted on its scan axis and tipping curve measurements were taken. This ensures that measurements are consistent between the tilted and un-tilted scans. An example of this would be to look at the measured voltage while looking at

zenith and then tilt the instrument 12° and compare the initial zenith measurement to the -12° measurement when the instrument is tilted. The two measured voltages should agree exactly.

The setup for these measurements is shown in Figure 154, with the inclinometer measurements for the two tilt tests shown in Figure 155 a) and b).


Figure 154: Setup for Tilt Scan Bias Experiment


a) b)

Figure 155: Inclinometer Reading for Two Tilt Scan Bias Tests

The results for the tests are presented in the following subsections. Only data for one channel of the microwave channels, one channel of the mm-wave window channels, and one channel of the mm-wave sounding channels are shown. For each radiometer set only the channel with the largest 3 dB bandwidth is shown as it will be the most heavily affected channel. To conserve space only one polarization of the 18 GHz microwave channel is shown.

#### 8.2.3.1 Microwave Channel Results

The results of the tilt test for the 18 GHz QV microwave channel are shown in Figure 156. Figure 156 a) shows the results of the three tests with no angular correction while b) shows the results of the three tests corrected to have the same zenith angle. If the instrument had no scan bias the three lines in b) would be almost on top of each other.

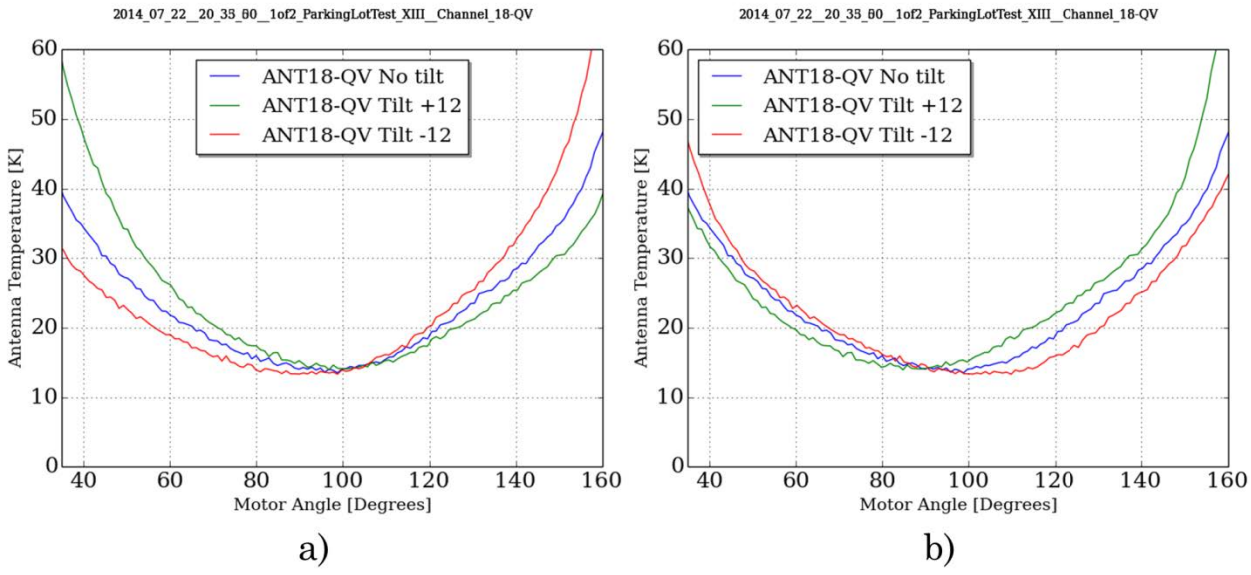


Figure 156: Results of the Tilt Test for the 18 GHz QV Microwave Channel, a) With No Correction, b) Corrected to Have the Same Zenith Angle

As Figure 156 b) shows there is a scan bias present in the microwave channels. We believe that this bias is primarily due to the beam offset discussed in Section 3.4.5 as one side of the scan, 100-160°, shows the most disagreement between tests. An additional source of error for these tests is that when the instrument is tilted 12° the scan on the side that it is tilted to will begin to be contaminated by things close to the horizon 12° sooner. These tests will be redone after the HAMMR chassis aperture has been trimmed.

#### 8.2.3.2 Millimeter-Wave Window Channel Results

The results of the tilt test for the 90 GHz mm-wave window channel are shown in Figure 157. Figure 157 a) shows the results of the three tests with no angular

correction while b) shows the results of the three tests corrected to have the same zenith angle.

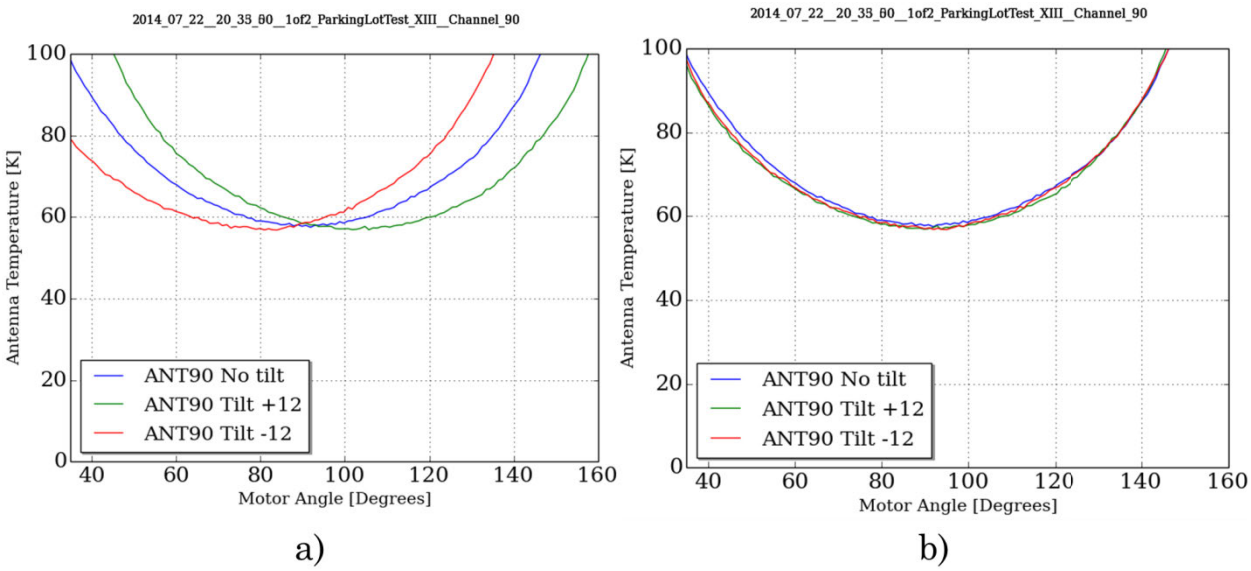


Figure 157: Results of the Tilt Test for the 90 GHz Millimeter-Wave Window Channel, a) With No Correction, b) Corrected to Have the Same Zenith Angle

Figure 157 b) shows that there is no scan bias present in the mm-wave window channels. There is a small disagreement between antenna temperatures due to system gain fluctuations during the time between when the LN2 was viewed for calibration and when the data was taken.

#### 8.2.3.3 Millimeter-Wave Sounding Channel Results

The results of the tilt test for the 118.75 GHz mm-wave oxygen sounding channel are shown in Figure 158. Figure 158 a) shows the results of the three tests with no angular correction while b) shows the results of the three tests corrected to have the same zenith angle.

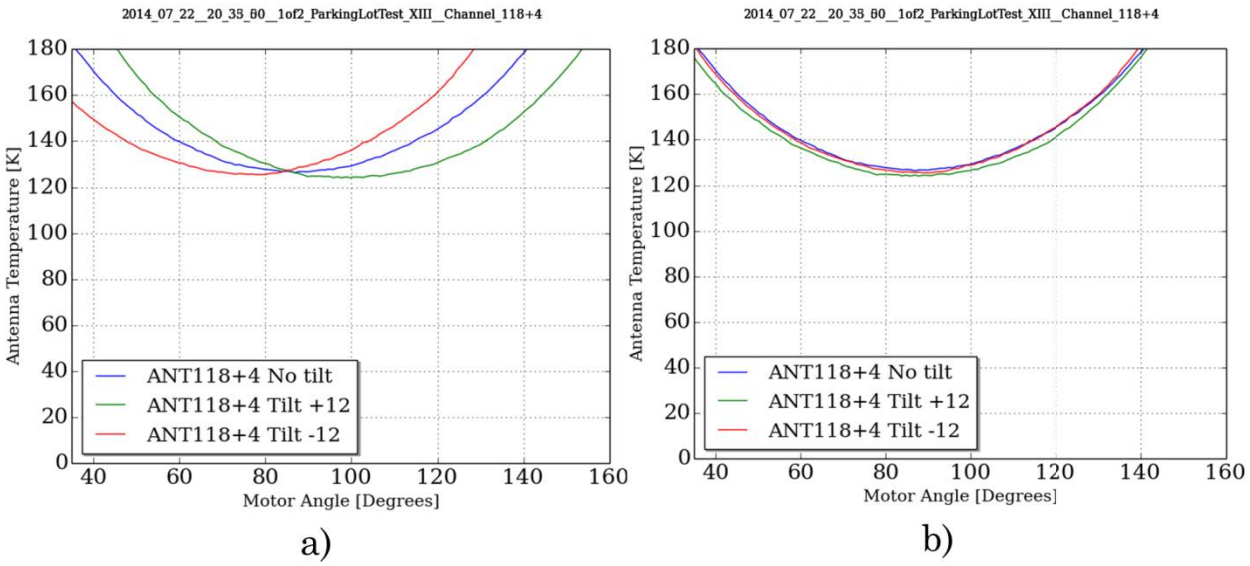


Figure 158: Results of the Tilt Test for the 118.75 GHz Millimeter-Wave Oxygen Sounding Channel, a) With No Correction, b) Corrected to Have the Same Zenith Angle

Figure 158 b) shows that there is no scan bias present in the mm-wave window channels. There is a two kelvin difference in the antenna temperatures for the +12° tilt due to system gain fluctuations during the time between when the LN2 was viewed for calibration and when the data was taken.

## 8.3 Twin Otter Aircraft

In July 2014 the team at CSU brought HAMMR to Twin Otter International LLC. (TOIL) in Grand Junction, Colorado for aircraft integration and airborne demonstration. TOIL has a fleet of Twin Otter aircrafts specifically modified for testing scientific instruments including onboard 115 V AC power and an instrument port in the floor of the aircraft.

Mechanics at TOIL built a mechanical brace interface to hold HAMMR in the Twin Otter and had an FAA Designated Engineering Representative sign off that both the instrument and the interface meet FAA safety requirements. Once the mechanical brace interface was completed HAMMR was mounted in the aircraft using a manual floor crane as seen in Figure 159. The mechanical brace interface holds the top of the instrument above the cabin floor to ensure ease of access to the instrument for maintenance and is attached to rails on the floor of the Twin Otter aircraft via four mounting points shown in Figure 160. Figure 160 also shows the three external connections, power, GPS antenna input, and Ethernet to external computer, needed to operate the instrument in flight.


Figure 159: CSU Team Guiding HAMMR into the Nadir Port on the Twin Otter Aircraft

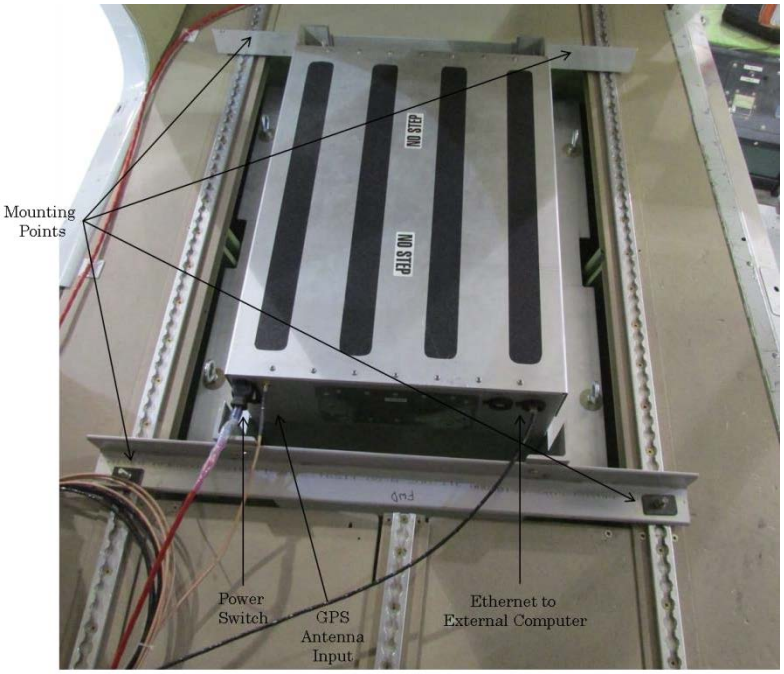


Figure 160: Top of HAMMR Mounted in Twin Otter

Once HAMMR was integrated into the Twin Otter aircraft two fairings, mounted fore and aft, were fabricated by TOIL to increase the aerodynamics of HAMMR. A third fairing or "wind dam" was also fabricated and mounted just in front of the chassis aperture. This is beneficial as it diverts air away from the chassis aperture which reduces turbulence and mechanical forces on the spinning flat reflector. The "wind dam" also reduces the amount of airflow in the bottom part of the HAMMR chassis which reduces temperature gradients in the radiometers and internal blackbody calibration target. The three fairings integrated with HAMMR while mounted in a Twin Otter are shown in Figure 161.

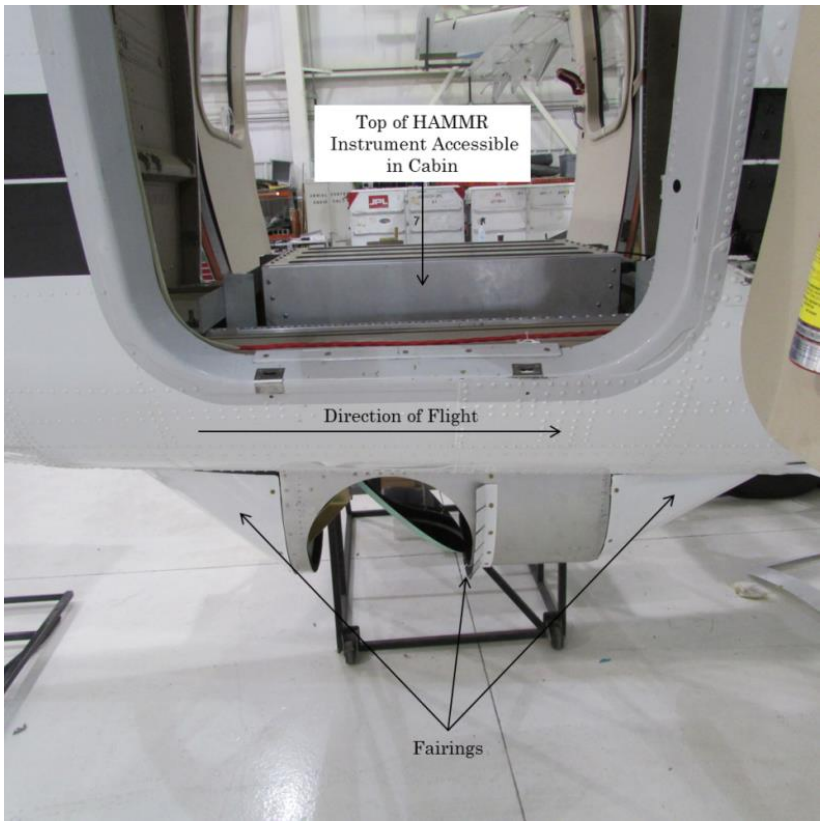


Figure 161: HAMMR in Twin Otter with Fairings

A desk with a power strip was mounted in the Twin Otter cabin to house the laptop used to operate the instrument during flight. The power switch on the power strip also provides a redundant point for powering off the instrument in case of an emergency. The final configuration of HAMMR mounted in the Twin Otter aircraft can be seen in Figure 162 where the Twin Otter is being prepared for takeoff.


Figure 162: Twin Otter and HAMMR Being Prepared for Takeoff

## 8.4 Airborne Demonstration

The airborne demonstration of HAMMR has two phases. The first phase, called the engineering flights, is to verify instrument functionality on an airborne platform. The major concerns for the engineering flights are motor errors, overheating, temperature stability, vibrational effects, and radiometer functionality. The second phase which will be conducted in fall of 2014 will focus primarily on the retrieval of brightness temperatures and the verification of measured results. This chapter only contains results for the first phase or engineering flights.

### 8.4.1 Blue Mesa Reservoir

The first day of flights were done over Blue Mesa Reservoir near Gunnison, Colorado on July 9, 2014. Blue Mesa Reservoir was chosen because it is close to

Grand Junction and is the largest body of water in Colorado (Wikipedia, 2014). The primary concern for the first day of flights was to verify functionality of the system and to monitor the motor error before flying out to Lake Powell in Utah.

#### 8.4.1.1 Blue Mesa Reservoir Flight Plan

The flight plan for Blue Mesa Reservoir is broken up into two stages. The first stage involved the Twin Otter aircraft circling the Grand Junction airport while motor position and system functionality were tested. If any problems were encountered that could not be fixed in flight the Twin Otter would land and necessary adjustments would be made. If the system was functioning properly the team would continue on to the Blue Mesa Reservoir to take brightness temperature measurements. A flight path was decided upon that would maximize the time over water, have areas where both land and water were being observed simultaneously, and include land to water transitions. The flight path, with the critical paths shown in red, is shown in Figure 163 with the waypoints marked with latitude and longitude. Each critical path was repeated three times to allow verification of measurement repeatability.

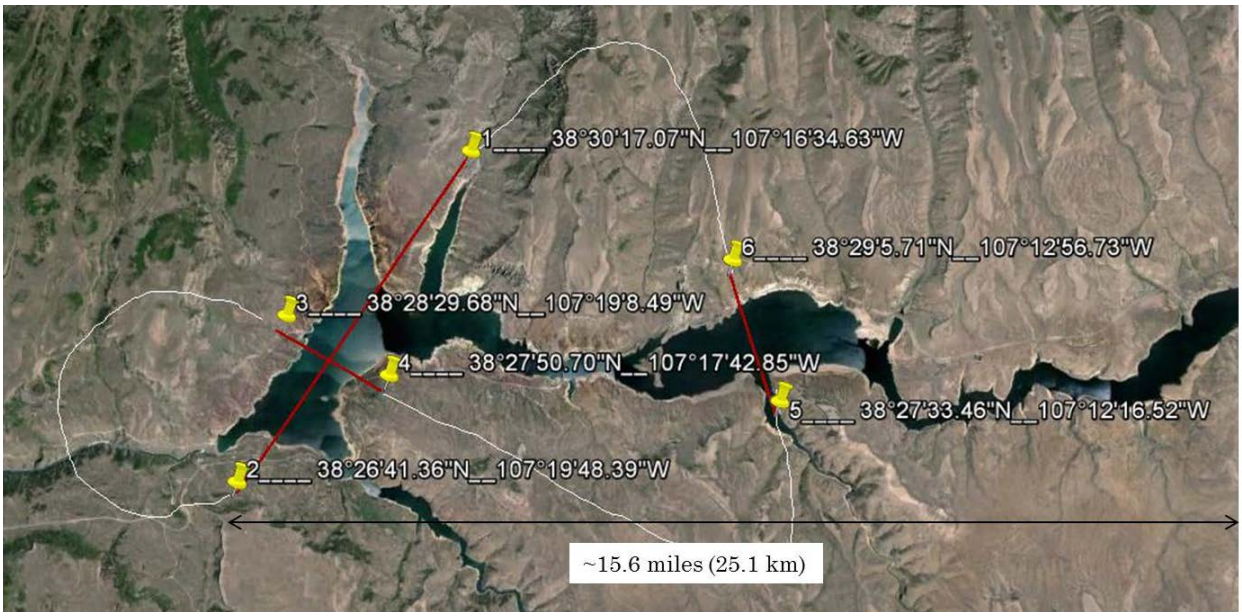


Figure 163: Blue Mesa Reservoir Flight Path

On the critical paths the Twin Otter was flown at an altitude of approximately 3 km (10,000 feet) above mean sea level (AMSL). A set of priorities was given to the pilots so they could determine the optimal attitude and speed of the plane to follow the critical paths with the least amount of variation. The priorities were that the aircraft should fly at the lowest speeds possible while maintaining pitch and roll deviations less than ±10°, no requirement for yaw was given. The average speed of the aircraft for these measurements was about 80 knots (92 mph). The GPS/IMU module in the instrument records all of these parameters at 16 Hz.

#### 8.4.1.2 Motor Position Error

The first test done on the Blue Mesa Reservoir flights was to test the motor position error while in flight. To do this the motor was controlled using Quicksilver's proprietary motor control software QuickControl (Quicksilver Controls, Inc., 2014).

As discussed in Section 3.5.4 the motor has an encoder that discretizes each 360° revolution into 16000 counts of 0.0225° each. The motor controller stores the measured and expected count values in the Current Position Error register which can be viewed in the software and recorded to a text file. By comparing the measured value with the expected value the motor position error can be found.

Tests were done in the lab at CSU to determine the motor position error with no external forces. The average motor position error in the lab was determined to be 10 counts or 0.225°. The goal for in-flight motor position error was 50 counts or 1.125°.

To test the in-flight motor position error the scanning reflector was programmed to hold position at zenith, rotate at 1 Hz, and then to hold position at zenith over a five minute period. The motor position error was logged to a text file and plotted in counts, with the three command periods labeled as seen in Figure 164.

The results of this test show that the average motor position error remained far below 50 counts and had a higher average error for the periods where the motor was holding a position than when spinning. The average error for holding the zenith position was 14.8 counts (0.3°) and while spinning at 1 Hz was 9.1 counts (0.2°). This confirms that the scanning motor can maintain a scanning speed of 1 Hz (60 RPM) during flight while maintaining negligible error.

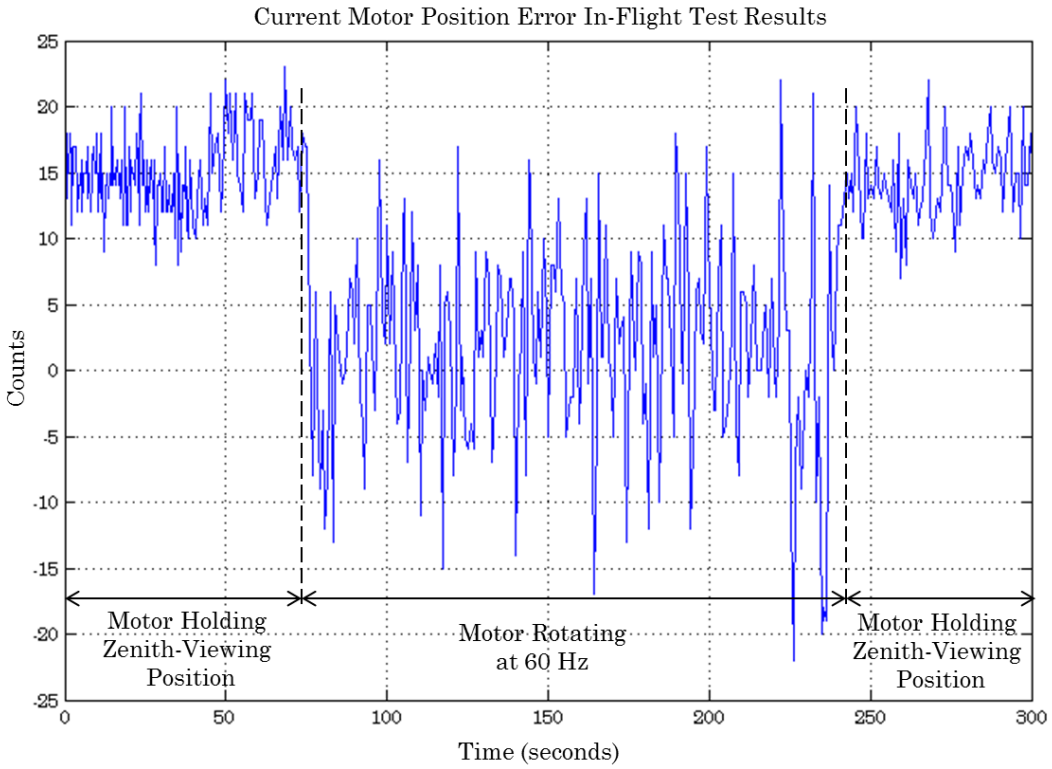


Figure 164: Current Motor Position Error In-Flight Test Results

### 8.4.1.3 Liquid Nitrogen Calibration Target

Similar to Section 8.2.2 an LN2 calibration target was used to characterize the instrument immediately before take-off and immediately after landing. This helps to track the how to instrument fluctuates during flight. For the Blue Mesa Reservoir flights the LN2 calibration target had not yet been finalized so the wings and the internal wall foil discussed in Section 8.2.2 were not present. The test performed a Y-factor measurement using the LN2 target as the cold load and the internal blackbody target as the hot load. To test the effectiveness of the internal blackbody target the LN2 target was measured before adding any LN2 and was considered a hot load. The setup for the test is shown in Figure 165 a) and b).

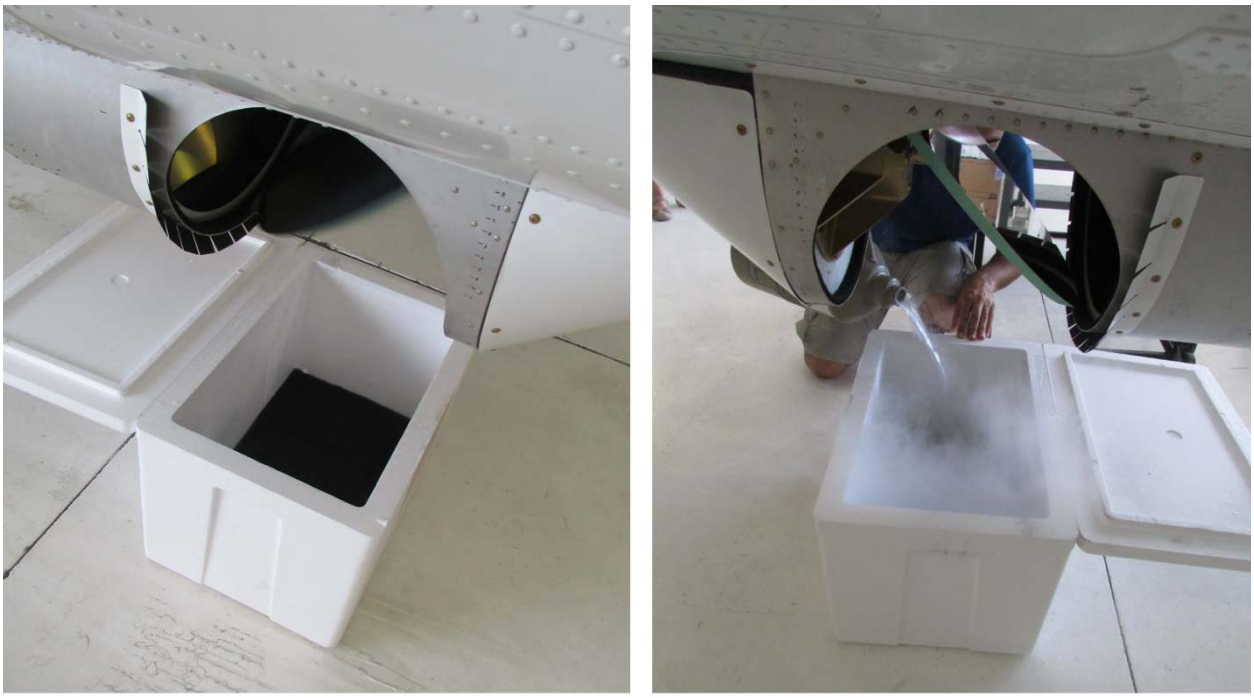

a) b)

Figure 165: a) Initial Version of Hot Calibration Target and b) Initial Version of Cold Calibration Target with LN2

Although the target was not in its' final configuration for the Blue Mesa Reservoir flight adjustments were made and it was completed before the Lake Powell flights were done.

### 8.4.2 Lake Powell

The purpose of the Lake Powell flights was to retrieve brightness temperature measurements over a large body of water that included land to water transitions. Lake Powell straddles the southern border of Utah and the northern border of Arizona with the majority of the water mass being located in Utah. It was chosen for these flights because it is about a 1 hour flight from the Grand Junction airport

and it is the second-largest artificial reservoir in the United States (Wikipedia, 2014). The flights over Lake Powell were done on July 10 and 11, 2014.

The results presented in Sections 8.4.2.3 through 8.4.2.5 show measured brightness temperatures for the corresponding radiometer channels.

#### 8.4.2.1 Lake Powell Flight Plan

The flight plan for Lake Powell was very similar to that of the Blue Mesa Reservoir discussed in Section 8.4.1.1 with the same requirements of maintaining pitch and roll deviations of less than ±10° while maintaining minimum flight speed. The critical paths for the Lake Powell flights are shown in Figure 166 with each critical path having a different color. This was done to easily distinguish the critical paths from each other while discussing flight plans with the pilots. Each path was repeated four times consecutively at approximately 3 km (10,000 feet) AMSL.

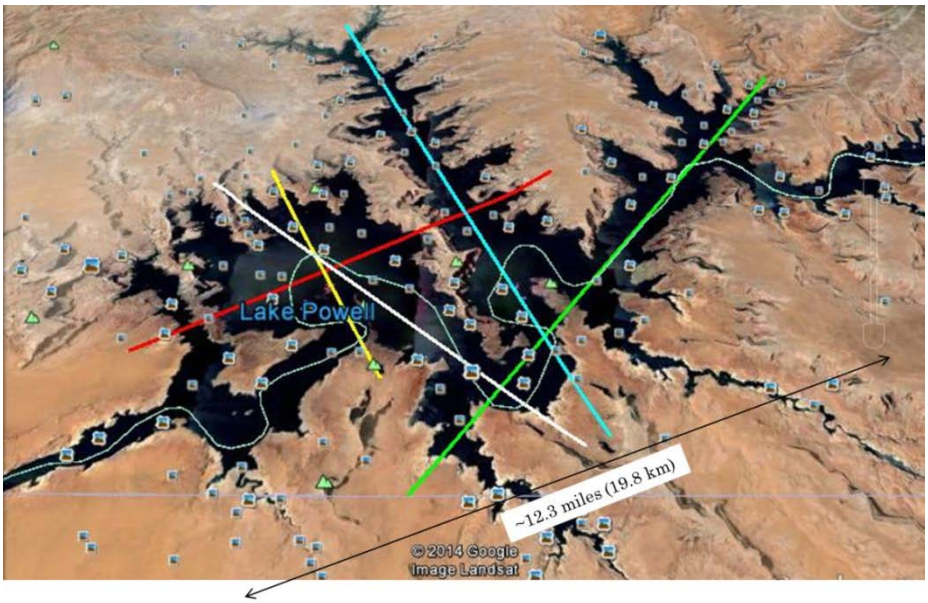


Figure 166: Lake Powell Flight Plan with Critical Paths Highlighted in Colors

The results presented in the following sections are for the part of the blue line shown in Figure 167.


Figure 167: Google Earth Image of Lake Powell Flyover for the Presented Results

#### 8.4.2.2 LN2 Calibration Target

The LN2 calibration target used for the Lake Powell flights is the same as the target described in Section 8.2.2. The target was used to perform Y-factor measurements immediately before take-off and immediately after landing. The setup configuration can be seen from two different perspectives in Figure 168 a) and b).

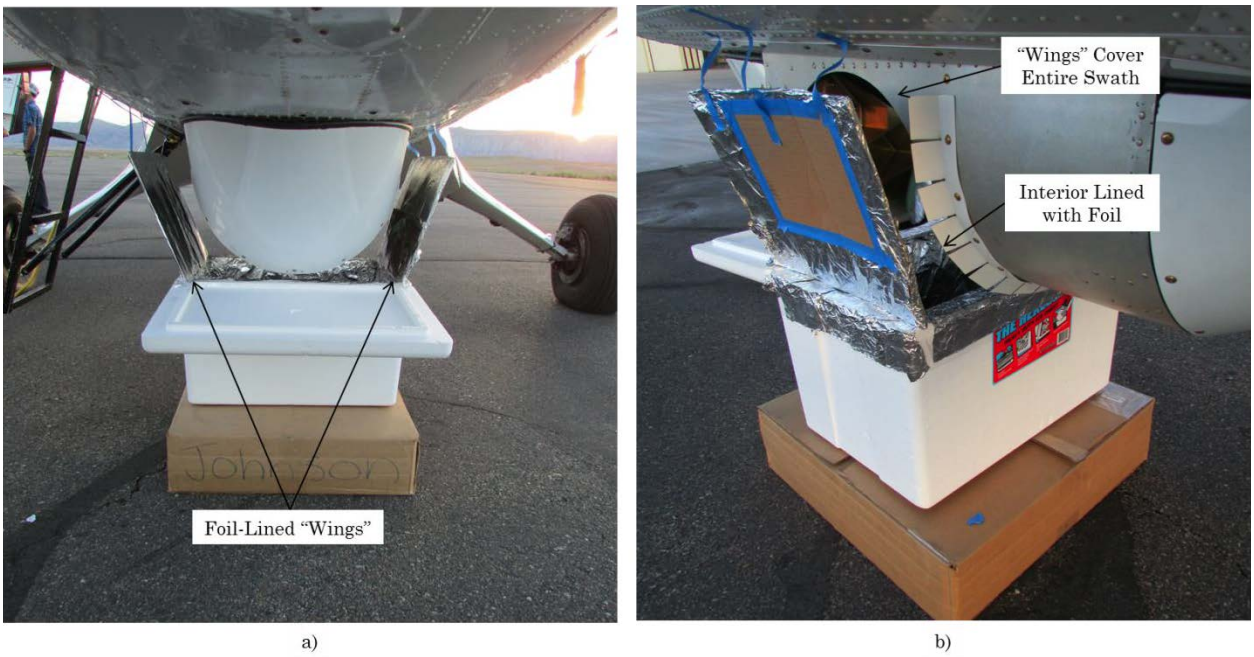


Figure 168: a) Front View of Improved Calibration Target and b) Side View of Improved Calibration Target

#### 8.4.2.3 Microwave Radiometers

The results in this section are measured microwave radiometer antenna temperatures taken over Lake Powell on July 11, 2014. The radiometers are calibrated using the LN2 target after landing as the cold load and the internal calibration target after landing for the hot load in a Y-factor calibration.

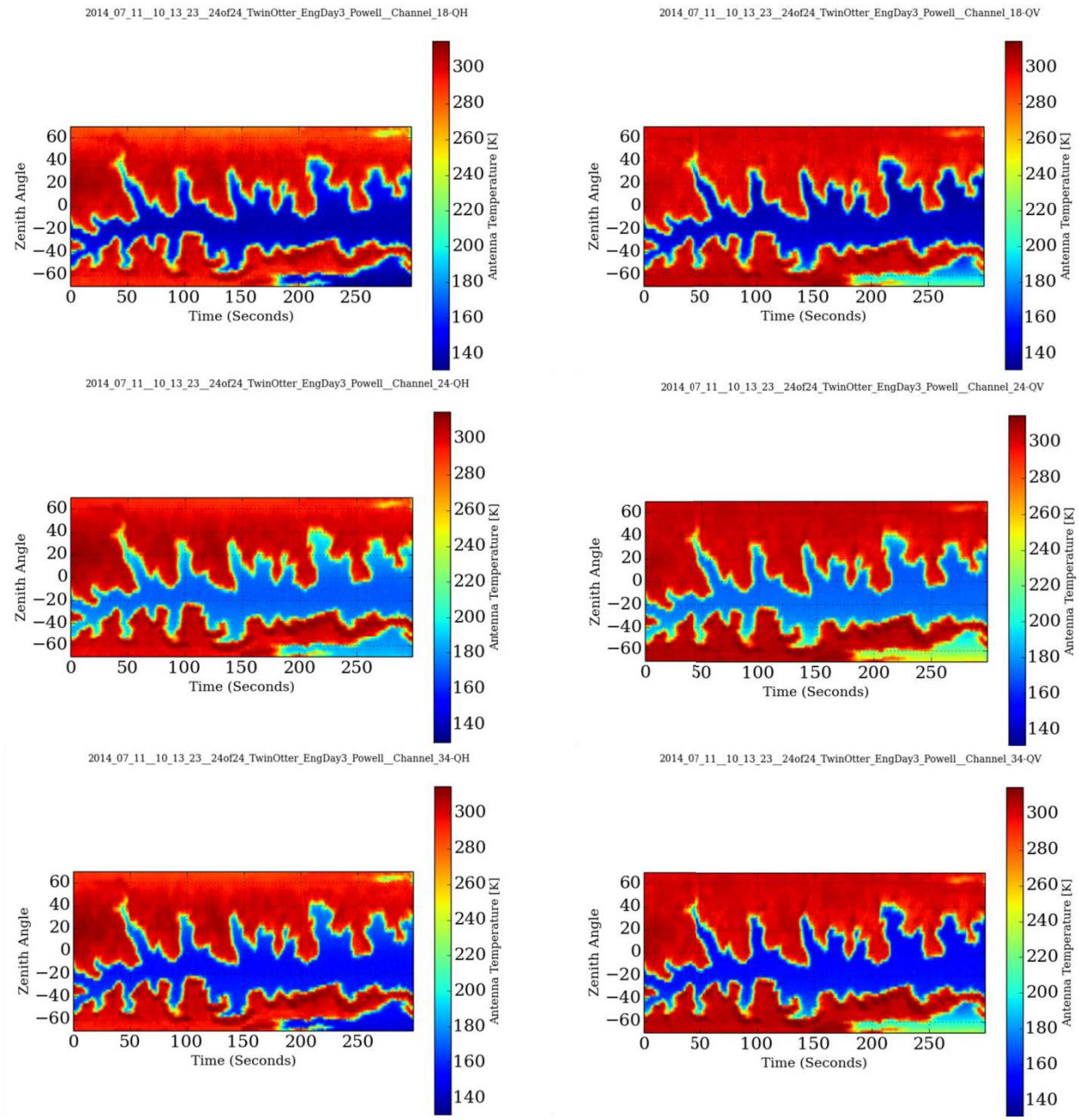


Figure 169: Microwave Channel Results

These results show that both polarizations of the microwave radiometers are sensitive to changes in brightness temperature in the observed scene. The microwave radiometers remained functional throughout all 15 hours of flight.

#### 8.4.2.4 Millimeter-Wave Window Radiometers

The results in this section are measured millimeter-wave window radiometer antenna temperatures taken over Lake Powell on July 11, 2014. The radiometers are calibrated using the LN2 target after landing as the cold load and the internal calibration target after landing for the hot load in a Y-factor calibration.

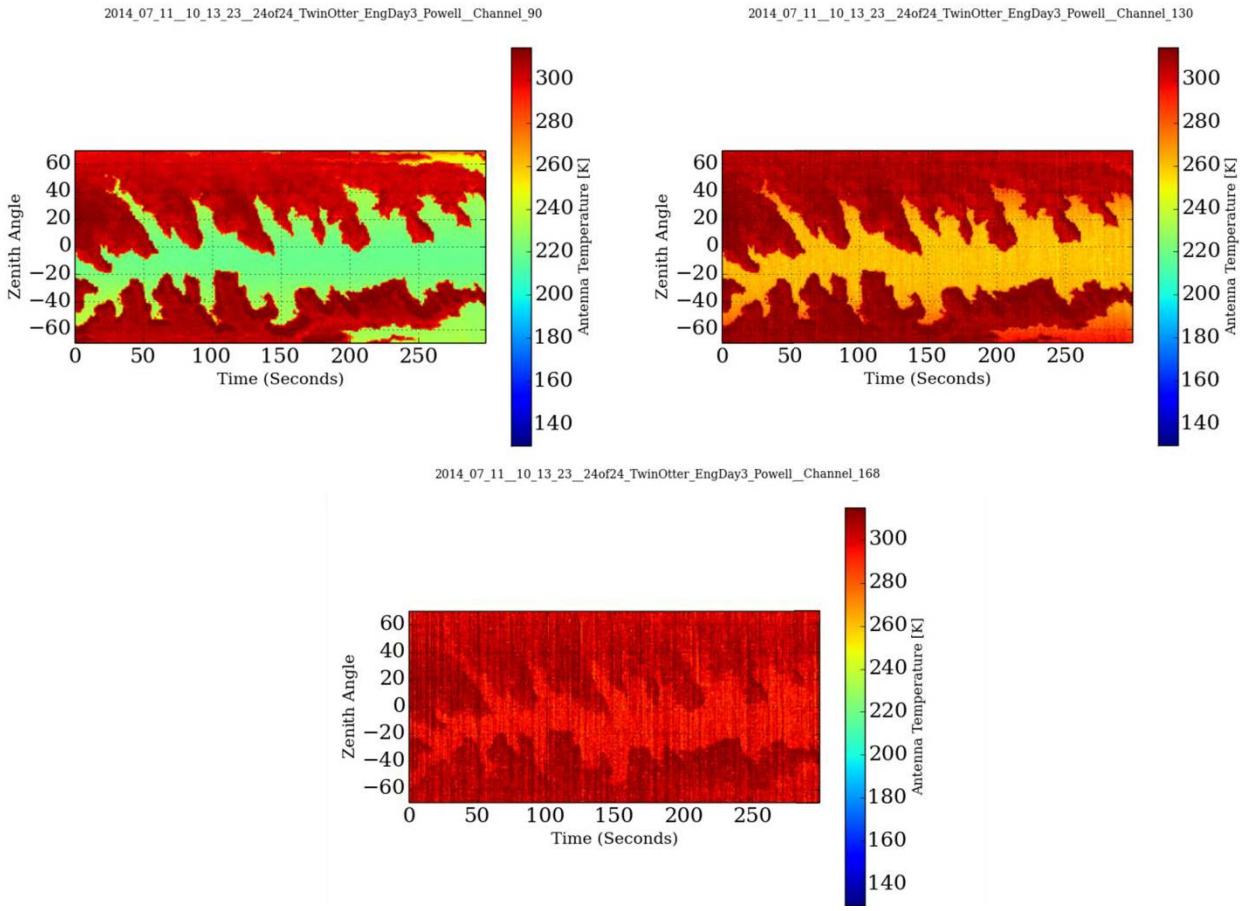


Figure 170: Millimeter-Wave Window Channel Results

These results show that the mm-wave windows channels show sensitivities corresponding to their measured receiver temperatures given in Section 6.4.1. This is expected as the receiver noise temperature is a key component in radiometric

resolution as shown in (II.34). The major contributor to noise in the 168 GHz module is gain instability as shown in Section 6.4.2. The instability of the 130 and 168 GHz receivers can be mitigated by using the Dicke switch to perform gain fluctuation cancellation as detailed in Section 2.5.

#### 8.4.2.5 Millimeter-Wave Sounding Radiometers

The results in this section are measured millimeter-wave sounding radiometer antenna temperatures taken over Lake Powell on July 11, 2014. The radiometers are calibrated using the LN2 target after landing as the cold load and the internal calibration target after landing for the hot load in a Y-factor calibration.

The temperature sounding channels, shown in Figure 171, were sensitive to the changes in brightness temperature of the measured scene and the coastline of Lake Powell can be seen in the data. There is no data for the +0 GHz offset channel and grainy data in the +5 GHz offset channel because an ABEB was malfunctioning at the time of the engineering flights. This problem was subsequently fixed and all eight oxygen sounder ABEB channels now function properly.

The water vapor sounding channels, shown in Figure 172, are almost all saturated. This is expected as a large amount of water vapor was present in the atmosphere and there is very high absorption at these frequencies. As the channels get further away from the absorption line, specifically the -7 and -8 GHz offsets, a faint outline of Lake Powell can be distinguished.

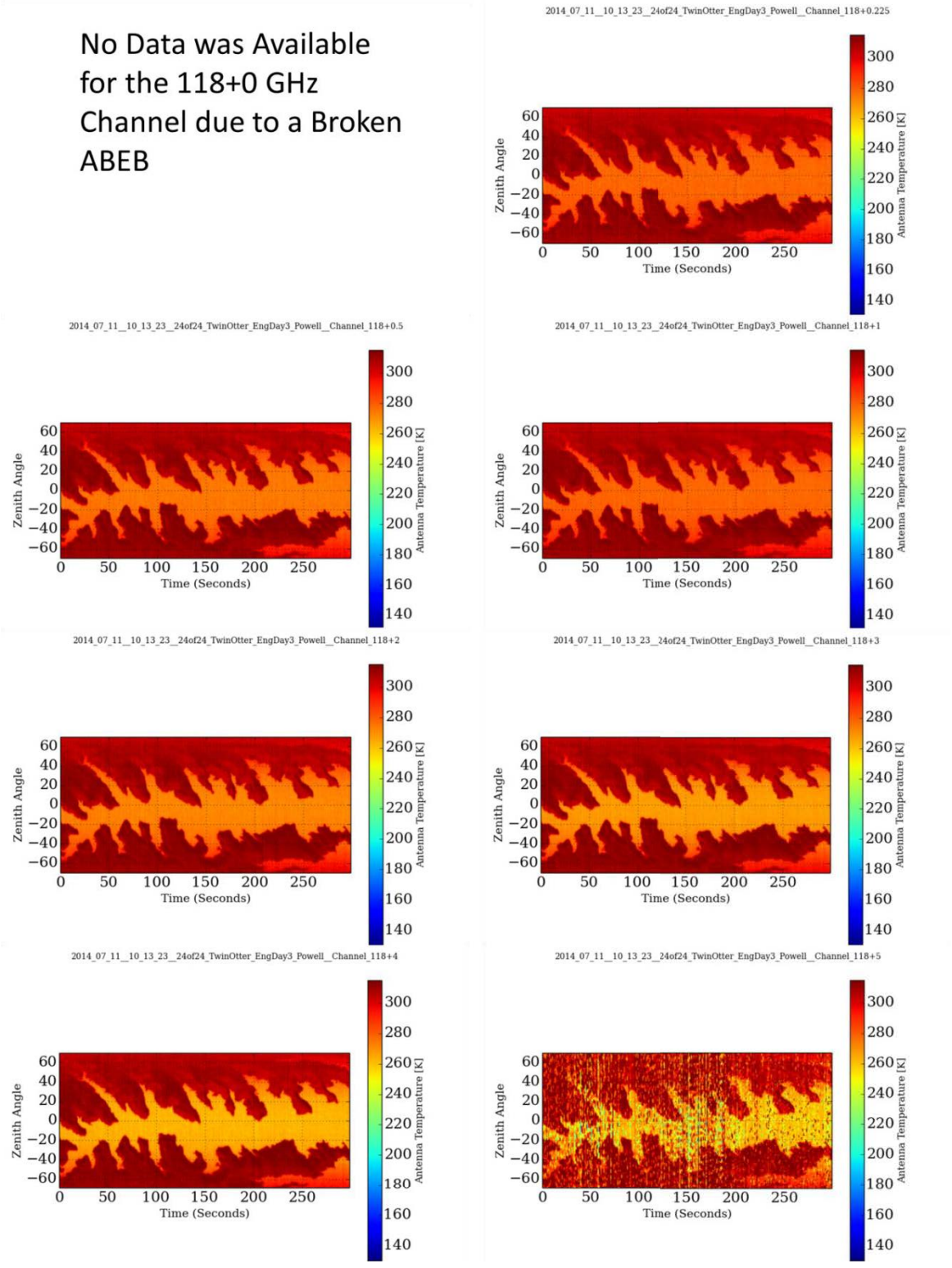


Figure 171: Temperature Sounding Results

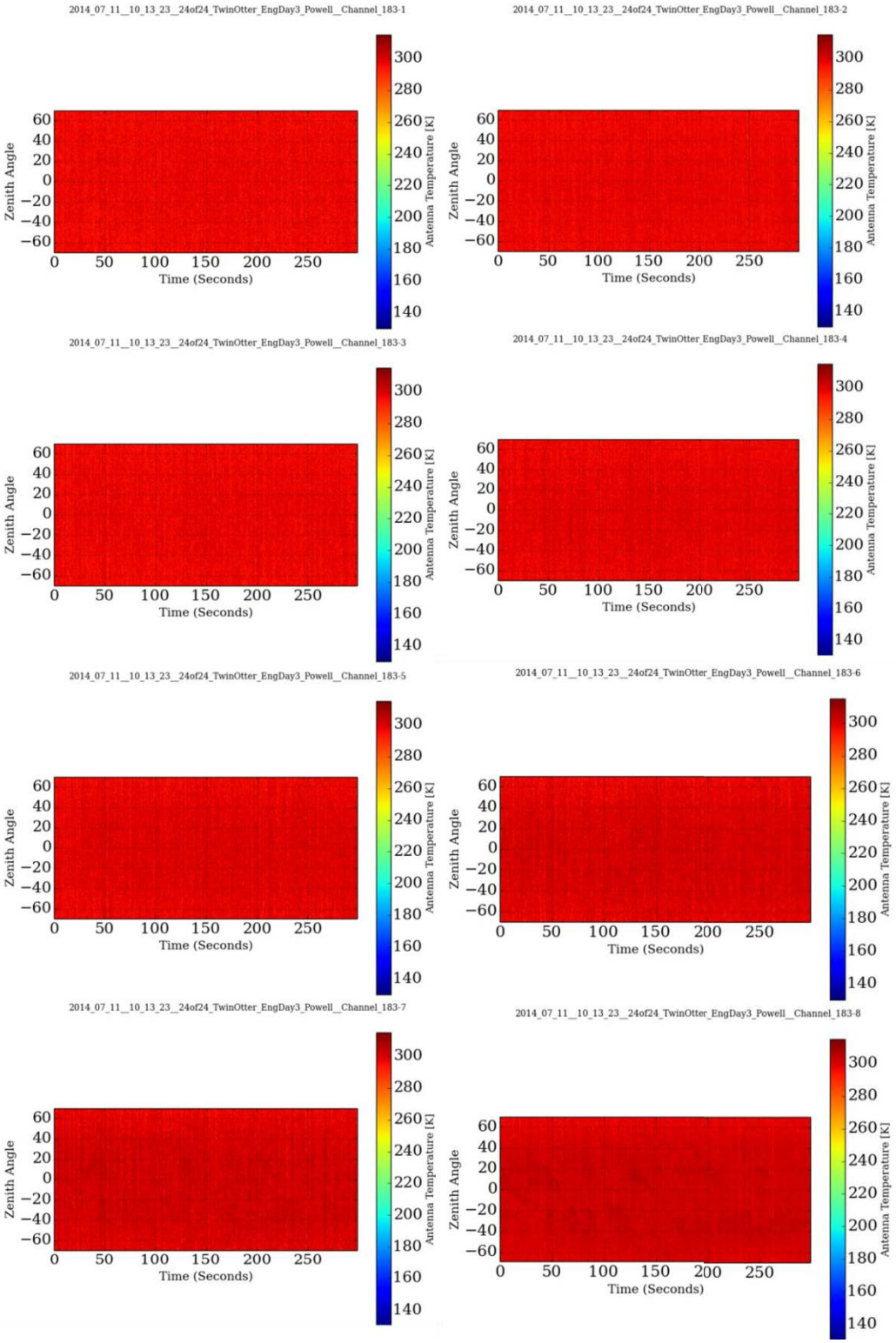


Figure 172: Water Vapor Sounding Channel Results

### 8.4.3 Microwave and Millimeter-Wave Window Resolution Comparison

The main purpose of this IIP-10 project was to demonstrate improved special resolution of measured wet-tropospheric path delay over the currently used microwave radiometers at 18.7, 23.8, and 34.0 GHz. To this end the mm-wave window radiometers at 90, 130, and 168 GHz have been developed and deployed. This section shows a comparison of the spatial resolution for these two frequency sets.

Figure 173 shows the retrieved brightness temperature for the microwave channels on the left side and the mm-wave window channels on the right side. A comparison of the two shows that the mm-wave window radiometers have far better spatial resolution for the retrieval of brightness temperatures than the microwave radiometers. This improved spatial resolution in brightness temperature retrieval directly corresponds to an increase in spatial resolution of wet-tropospheric path delay. The 130 and 168 GHz radiometers could have improved results with the reduction of system noise temperature thought to be caused by Dicke switch isolation and imbalance at their front ends.

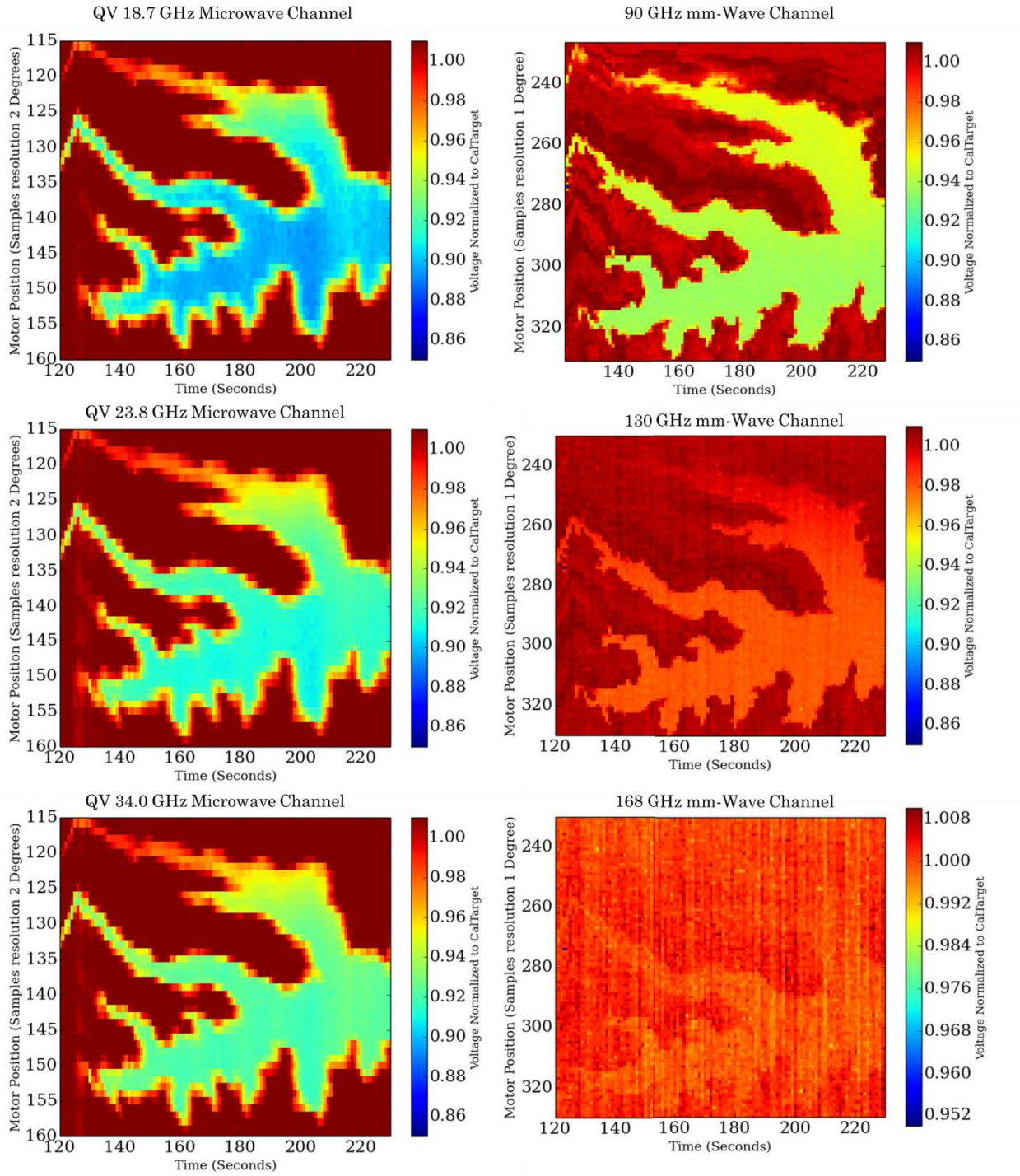


Figure 173: Comparison of Microwave and Millimeter-Wave Radiometer Measurements

### 8.4.4 Beam Offset Analysis

Because the microwave and mm-wave sounder feed horn antennas are offset from the paraboloid focal point as discussed in Section 3.4.5 the antenna beams do not leave the chassis aperture normal to the chassis. Instead, some offset is introduced which is discussed in detail in Section 3.4.5. This section illustrates the empirical results of these antenna offsets. Figure 174 shows the difference of the magnitudes of the spatial gradients normalized to antenna temperature between the 34.0 GHz microwave channel (red) and the 90 GHz (blue) mm-wave window channel. It can be seen that there is and offset in the location of the image between the two channels.

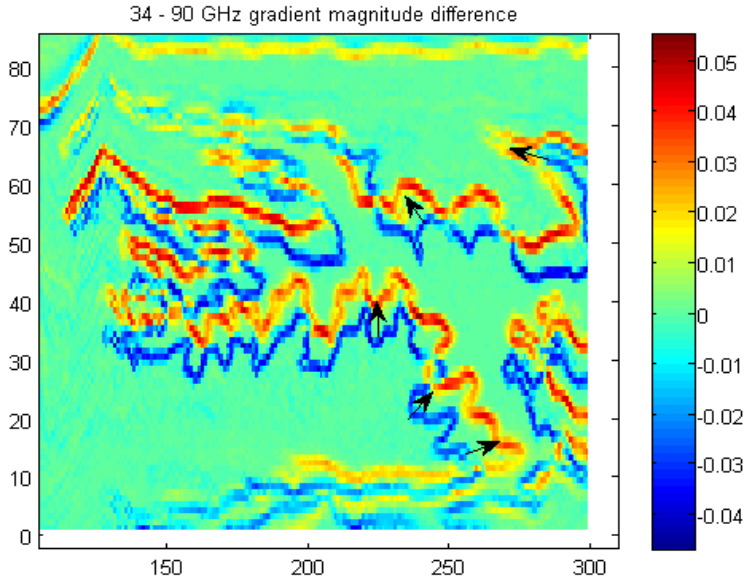


Figure 174: Difference of the Magnitudes of the Spatial Gradients between the 34.0 GHz Microwave Channel (red) and the 90 GHz (blue) Millimeter-Wave Window Channel

# Chapter IX. Summary, Conclusions, and Future Work

This thesis illustrates the design, integration, characterization, validation, and successful airborne demonstration of the 25-channel cross-track scanning high-frequency airborne microwave and millimeter-wave radiometer (HAMMR). The higher spatial resolution of the mm-wave window channels over that of the currently used microwave channels, as shown in the engineering flights, is expected to improve satellite-based retrieval of tropospheric wet path delay near coasts and over inland bodies of water. The theory, design process, and measured performance of all 25 radiometer channels and the supporting mechanical systems are presented. The work completed for this thesis contributed to the development, characterization, and initial airborne demonstration of the HAMMR system.

## 9.1 Thesis Summary

In Chapter I the scientific motivation for this project is summarized and the objectives of the Instrument Incubator Program that funded this project are explained.

Chapter II discusses the principles of atmospheric microwave radiometry including blackbody radiation, the radiative transfer equation, and atmospheric absorption models. The underlying principles of radiometer performance including noise and methods of calibration are explained as well as common radiometer architectures with detailed analysis of both direct detection and Dicke radiometers.

An overview of the HAMMR instrument is presented in Chapter III. This includes a description of how the sub-systems interact to achieve the system goals as well as the initial design, fabrication, integration, and verification of the instrument chassis, testing cart, and scanning motor assemblies. The design, fabrication integration and verification of the reflector sub-systems and feed horn placement is also expanded upon. A brief overview of the supporting sub-systems such as the power distribution, temperature sensing, GPS/IMU, and signal processing and digital back-end is also presented.

The internal blackbody calibration target is discussed in Chapter IV primarily focusing on the design and fabrication process. The results of the internal blackbody calibration target are also presented in this chapter.

Chapter V focuses on the architecture, integration, calibration and verification of both polarizations of the microwave radiometer channels at 18.7, 23.8, and 34.0 GHz. An overview of the system, including a block diagram and laboratory test results, are presented. A discussion on the internal calibration and stability of the instrument with respect to Allan variance is also included as well as a description of the effects of offsetting the microwave feed horn from the offset paraboloid reflector's focal point.

Chapter VI expands upon the architecture, integration, calibration and verification of the mm-wave window radiometer channels at 90, 130, and 168 GHz. An overview of the system including previous work, improvements made during this project, a

block diagram and laboratory test results are presented. A discussion on the internal calibration and stability of the instrument with respect to Allan variance is also included.

Chapter VII presents a summary of the mm-wave sounding radiometer channels at 118.75 and 183.31 GHz, including the system overview and architecture focusing on the difference between these channels and the mm-wave window and microwave channels. Results for laboratory tests on these channels are discussed and the 60 Hz noise seen in these channels is explained.

Chapter VIII focuses on the characterization and calibration of the fully integrated HAMMR system. This includes a description of how external calibration is accomplished, what a tipping curve measurement is, and tests done in the parking lot of the CSU Lory Student Center to characterize any scan bias due to the HAMMR chassis. The Twin Otter aircraft used for the flight tests is described and the results of the flight campaign are presented and discussed. The effect of offsetting the microwave and mm-wave sounding feed horn is also shown in the results.

## 9.2 Conclusions

Two key scientific objectives of NASA's Surface Water and Ocean Topography (SWOT) mission are to characterize the ocean's mesoscale and sub-mesoscale circulation with a spatial resolution of 15 km, monitor the height of inland bodies of water with areas larger than 250 $m^2$, measure flow rates of rivers at least 100 m

wide. To this extent, tropospheric wet-path delay needs to be accounted for to achieve 1 cm (baseline) to 3 cm (threshold) vertical resolution for sea surface height measurements.

Past and current satellite altimeter missions include nadir-viewing microwave radiometers from 18-34 GHz to retrieve tropospheric wet-path delay. These low-frequency microwave radiometers achieve retrievals with rms errors of less than 1 cm in the open ocean, up to about 40 km from the coasts. However, due to the large footprint of low-frequency microwave radiometers, land emissions contaminate the measurements in coastal areas, increasing the errors. To address this issue, we propose the addition of higher-frequency radiometers operating from 90-168 GHz to retrieve wet-path delay near the world's coastlines and potentially enabling retrievals over inland bodies of water.

The High-frequency Airborne Microwave and Millimeter-wave Radiometer (HAMMR) instrument was designed, built, tested and demonstrated on a Twin Otter aircraft as a collaborative effort between the Colorado State University (CSU) Microwave Systems Laboratory (MSL) and the Jet Propulsion Laboratory (JPL). HAMMR consists of three sets of radiometer channels, the newly-developed millimeter-wave window channels (90, 130 and 168 GHz), millimeter-wave sounding channels (near 118 and 183 GHz), and the low-frequency microwave channels (18.7, 23.8 and 34.0 GHz).

The HAMMR instrument successfully performed measurements on a Twin Otter aircraft based in Grand Junction, CO, from July 9-11, 2014. The first airborne demonstration of the high-frequency radiometers showed improved resolution compared to low-frequency microwave radiometers. In addition, the data set from the airborne demonstration is the first to combine all of these channels in a single measurement.

## 9.3 Lessons Learned

Throughout this project many lessons were learned concerning individual component design as well as overall system considerations. The major lessons learned for each part of the project are presented below.

### 9.3.1 HAMMR Chassis and Physical Layout

The design of the HAMMR chassis was done before the individual components for the sub-systems were chosen. This caused issues with the availability of space for subsequently designed sub-systems, problems with accessibility for mounting parts and maintenance, and thermal dissipation problems due to crowding. If time and budget had allowed, a much more efficient system could have been designed if the internal components had been specified before the chassis was finalized and fabricated.

Although the power distribution for the system works quite well and the ability to easily measure the current of each voltage for each subsystem is very beneficial.

The system could be improved by following more standard wiring practices that were learned after the assembly of HAMMR such as leaving service loops for each wire. If minimum wire gauges had been selected based off of expected current values for each cable the clutter in the system could have been reduced by not using unnecessarily large wires.

Another design error in the HAMMR chassis is the difficulty of installing and aligning the optical bench. If a system for this had been designed at the beginning of the project and subsequent sub-systems had been designed around this system the optical bench could have been easily installed and aligned. The last minute alteration of the mm-wave sounding channels ended up occupying much of the space left for the operator's hands when installing the optical bench making the process of installation and aligned extremely difficult.

### 9.3.2 Millimeter-Wave Window Channels

The mm-wave window channels were designed and fabricated without a plan to attach them to the optical bench. This forced a last minute design to be done for the mounting brackets that did not account for space limitations or ease of access, resulting in a difficult to disassemble system and a modification of the already installed internal blackbody calibration target. If mounting hardware had been built into the MCMs, the module could have been easily attached to the optical bench and could have remained easy to access for removal and maintenance. The box that thermally insulates the mm-wave window MCMs and all three feed horn

antennas was also severely limited in size due to this problem. This resulted in a very long design process for the box that could have been avoided.

### 9.3.3 Millimeter-Wave Sounding Channels

Due to time and budget constraints the mm-wave sounding channels were not fabricated to their design specifications. This resulted in two modifications that affected the rest of the system.

The first modification was that the 100 MHz clock for the sounder ASICs could not be integrated into the receivers, this forced an external clock and power splitter to be used to provide this clock signal. Because the optical bench was already quite crowded there was very little room for these components and they were placed where room had been left for tools to dismount, mount, and align the optical bench, leaving only 1.78 cm (0.7") of space between the mounting screws and the nearest component on each side. Prior to this design change there was greater than 7.62 cm (3") of clearance on each side.

The second modification was that the band definition filters, diode detectors, and video amplifiers were not integrated into the receivers. This means that the output of each sounder channel is a 1 mV approximately -26 dBm signal with 1 GHz of bandwidth. Because the power level for these signals was so low, 60 Hz noise from the linear power supply transformers was coupled into the coaxial output at a level of about 100 mV totally obscuring the measured results as discussed in Section 7.4.

The effect of the first modification is an extra 20-30 minutes and added difficulty when mounting or dismounting the optical bench. The effect of the second modification was 10 weeks of working overtime trying to solve the noise problem as well as spending approximately $1000 purchasing components to mitigate this issue. If the sounders had been built to specification a large amount of time and money could have been saved on this project by avoiding disassembling the entire instrument and debugging for 10 weeks which could have been spent finalizing the instrument and data processing.

## 9.4 Future Work

After the successful completion of the initial engineering flights in July 2014, HAMMR will be flown on a Twin Otter over the coast of Southern California in the early fall of 2014 for validation flights focusing primarily on data retrieval. In the time between the engineering and validation flights the frequency offset in the 118.75 GHz oxygen sounding channels can be further investigated and fixed and the chassis aperture may be modified to compensate for the beam offset in the microwave channels. After completion of the validation flights the instrument could be further optimized with the award of new grants. Ultimately, the HAMMR technology will hopefully be co-located with satellite altimeters to correct for tropospheric wet-path delay near coastlines and over inland bodies of water.

# Bibliography


Albers, D. (Fall 2012). *Design, Fabrication, and Demonstration of Low-Mass, Low-Power, Small-Volume, Direct Detection Millimeter-Wave Radiometers at 92 and 130 GHz.* Electrical and Computer Engineering. Fort Collins, CO USA: M.S. Thesis, Colorado State University.

Amphenol Connex. (n.d.). *SMC Str Jk, Solder Cup, 50 Ohm, Blkhd*. Retrieved July 2, 2014, from http://www.amphenolconnex.com/152127.html

Baumgardner, D., Newton, R., Kramer, M., Mayer, J., Beyer, A., Wendisch, M., et al. (2014). The Cloud Particle Spectrometer with Polarization Detection (CPSPD): A Next Generation Open-Path Cloud Probe for Distinguishing Liquid Cloud Droplets from Ice Crystals. *The 16th International Conference on Clouds and Precipitation.* Leipzig, Germany.

D V Land, A. P. (2007, March). The use of the Allan deviation for the measurement of the noise and drift performance of microwave radiometers. *Measurement Science and Technology, 18*(7), 1917-1928.

D. Allan, N. A. (1997). *The Science of Timekeeping.* Application Note, Hewlett-Packard Company.

Digi-Key. (2014). *Thermistors - NTC - KS502J2*. Retrieved June 25, 2014, from http://www.digikey.com/product-detail/en/KS502J2/615-1073-ND/2651614

Eclipse Microwave. (2014, August). Zero Bias Schottky Diode Detector. Retrieved from http://www.eclipsemicrowave.com/Prod_ZeroBiasSchottky.asp

Emerson & Cuming. (2013). Retrieved from Emerson & Cuming's Laird Technologies Web site: http://www.eccosorb.com/

F. Ticconi, L. P. (2011). Models for Scattering from Rough Surfaces. In P. V. Zhurbenko, *Electromagnetic Waves* (p. 510). InTech.

F. Ulaby, R. K. (1982). *Microwave Remote Sensing: Active and Passive* (Vol I ed.). (D. S. Simonett, Ed.) Boston, MA: Artech House.

Ghuman, P. (2010). *IIP ROSES 2010 Solicitation.* Retrieved May 28, 2014, from http://esto.nasa.gov/files/solicitations/IIP_10/ROSES2010_IIP_A35.pdf

Hadel, V. (2014). *Development of Internally-Calibrated Direct Detection Millimeter-Wave Radiometers to Improve Remote Sensing of Wet-Tropospheric Path Delay.* Colorado State University, Electrical and Computer Engineering. Fort Collins, CO USA: M.S. Thesis, Colorado State University.

Iturbide-Sanchez, F. (2007). *DESIGN, FABRICATION AND DEPLOYMENT OF A MINIATURIZED SPECTROMETER RADIOMETER BASED ON MMIC TECHNOLOGY FOR TROPOSPHERIC WATER VAPOR PROFILING.* PhD Dissertation, University of Massachusetts Amherst.

Janssen, M. (1993). *Atmospheric Remote Sensing by Microwave Radiometry.* New York, NY: John Wiley & Sons, Inc.

Jet Propulsion Laboratory. (n.d.). *Ocean Surface Topography from Space*. Retrieved July 8, 2014, from https://sealevel.jpl.nasa.gov/

Johnson, T., & Hadel, T. (2012). *Radiometer-on-a-Chip*. Fort Collins, CO: Colorado State University, Department of Electrical and Computer Engineering.

Kangaslahti, P., A., T., Lambrigsten, B., & Pukala, D. (2007). MIMRAM — Miniature MMIC low mass/power Radiometers for Geostationary Thinned Aperture Radiometer. *NASA Science Technology Conference*. College Park, MD.

Khayatian, B. (2011). *Airborne Systems, An Overview of Previous Work*. Pasadena, CA: JPL .

Kuester, C. H. (1994, Nov). A low-frequency model for wedge or pyramid absorber arrays-II: computed and measured results. *IEEE Transactions on Electromagnetic Compatibility, 36*(4), 307-313.

Lee, A. (Spring 2012). *Developoment and Fabrication of Internally-Calibrated, MMIC-Based Millimeter-Wave Radiometers at 92 GHz and 166 GHz.* Colorado State University, Electrical and Computer Engineering. Fort Collins, CO USA: M.S. Thesis, Colorado State University.

Measurement Specialties. (2014). 44906 GSFC Space Qualified Thermistor. Retrieved from http://www.meas-spec.com/: http://www.meas-spec.com/downloads/44906.pdf

Mediawave PC, Inc. (n.d.). *MW-5300: Fanless Embedded Computer*. Retrieved June 26, 2014, from http://www.mediawavepc.com/e_MW-5300.htm

Microwave Communications Laboratories, Inc. (2010). *90 Degree Hybrid Coupler - Stripline*. Retrieved June 27, 2014, from http://mcli.com/CatalogueRetrieve.aspx?ProductID=1126960&A=SearchResult&SearchID=8076474&ObjectID=1126960&ObjectType=27

Millitech. (n.d.). *Active Multiplier Chain*. Retrieved July 1, 2014, from http://www.millitech.com/pdfs/specsheets/IS000037-AMC.pdf

Mini Circuits. (n.d.). *Coaxial Power Splitter/Combiner*. Retrieved July 2014, 2, from http://www.minicircuits.com/pdfs/ZFSCJ-2-1.pdf

Mini Circuits. (n.d.). *Low Power Coaxial Amplifier*. Retrieved July 3, 2014, from http://www.minicircuits.com/pdfs/ZFL-1000.pdf

Miteq. (n.d.). *Mechanically-Tuned Dielectric Resonantor Oscillators*. Retrieved July 1, 2014, from https://miteq.com/docs/MITEQ-DROH16000.PDF

NASA ESTO. (2014, July). Retrieved from NASA ESTO Technology Readiness Levels: http://esto.nasa.gov/technologists_trl.html

National Aeronautics and Space Administration (NASA) Earth Science Technology Office (ESTO). (2014). *The Instrument Incubator Program (IIP)*. Retrieved May 23, 2014, from http://esto.nasa.gov/obs_technologies_iip.html

National Aeronautics and Space Administration. (2010, May 14). *Advanced Microwave Radiometer*. Retrieved June 26, 2014, from http://www.nasa.gov/mission_pages/ostm/overview/index.html#.U6xpPvmzGWU

Nelson, S. (Fall 2013). *Design, Fabrication, and Testing of a Data Acquisition and Control System for an internally-Calibrated Wide-Band Microwave Airborne Radiometer*. M.S. Thesis, Colorado State University, Fort Collins, Colorado.

Pozar, D. M. (2012). *Microwave Engineering* (4 ed.). Danvers, MA: John Wiley & Sons, Inc.

Quick Silver Controls, Inc. (2011, May 11). *Datasheet:QCI-DS009*. Retrieved June 26, 2014, from William Tell

Quicksilver Controls Inc. (2014). Datasheet:QCI-DS009. Retrieved from http://www.quicksilvercontrols.com/SP/DS/QCI-DS009_QCI-A34.pdf

Quicksilver Controls, Inc. (2014, July). Retrieved from QuickControl: http://www.quicksilvercontrols.com/QuickControl.html

Rahmat-Samii, Y. (1998). "Beam Efficieny of Reflector Antennas: The Simple Formula". *IEEE Antennas and Propogation Magazine, 40*(5).

Randa, J., Lahtinen, J., Camps, A., Gasiewski, A. J., Hallikainen, M., Le Vine, D. M., et al. (Aug. 2008). *Recommended Terminology for Microwave Radiometry*. Washington D.C.: National Institute of Standards and Technology.

Reising, S. C., Bosch-Lluis, X., Nelson, S., Hadel, T., Johnson, T., Kangaslahti, P., et al. (2013). *Development of an Internally-Calibrated Wide-Band Airborne Microwave Radiometer to Provide High-Resolution Wet-Tropospheric Path Delay Measurements for SWOT.* Colorado State Univeristy, Electrical and Computer Engineering, Fort Collins, CO.

Reising, S. C., Kangaslahti, Brown, S. T., Dawson, D. E., Albers, D., Lee, A., et al. (2011). Development of Low-Mass, Low-Power, High-Frequency Microwave Radiometers with Internal Calibration to Provide High-Resolution Wet-Tropospheric Path Delay Measurements for the SWOT Mission. *Earth Science Technology Forum*. Pasadena, CA.

Reising, S., Bosch-Lluis, X., Nelson, S., Hadel, T., Johnson, T., Kangaslahti, P., et al. (2013). *SWOT IIP-10 Year 2 Annual Review: Development of an Internally-Calibrated Wide-Band Airborne Microwave Radiometer to Provide High-Resolution Wet-Tropospheric Path Delay Measurements for SWOT.* Fort Collins, CO: Colorado State University.

Rosenkranz, P. (Jul.-Aug. 1998). Water Vapor Microwave Continuum Absorption: A Comparison of Measurements and Models. *Radio Sci., 33*(4), 919-928.

Sahoo, S. (private communication). *Radiometric Information Content for Water Vapor and Temperature.*

SBG Systems. (n.d.). *IG-500N: GPS aided miniature INS*. Retrieved June 25, 2014, from http://www.sbg-systems.com/products/ig500n-miniature-ins-gps

Skou, N., & Le Vine, D. (2006). *Microwave Radiometer Systems.* Norwood, MA: Artech House.

SPG Systems. (n.d.). *IG-500N: GPS aided miniature INS*. Retrieved June 25, 2014, from http://www.sbg-systems.com/products/ig500n-miniature-ins-gps

Superlogics. (2010). *8017: 8 Channel Analog Input, 16-Bit, Data Acquisition Module (RS-485 DAQ).* Retrieved June 25, 2014, from http://www.superlogics.com/option.asp?cat=807&prod=786#

Ulaby, F., Moore, R., & Fung, A. (1981). *Microwave Remote Sensing: Active and Passive, Vol. I - Microwave Remote Sensing Fundamentals and Radiometry.* Reading, MA: Addison-Wesley.

Vernotte, P. F. (2014, August). Retrieved from IFCS/EFTF Joint Conference: http://www.ifcs-eftf2011.org/sites/ifcs-eftf2011.org/files/editor-files/Slides_Vernotte.pdf

von Engeln, A., & Buhler, S. (2002). Temperature profile determination from microwave oxygen emissions in limb sounding geometry. *Journal of Geophysical Research: Atmospheres, 107*(D19).

Voronin, B. A., & Voronina, S. S. (2002). Contribution of Weak Water Vapor Absorption Lines to Extinction of Narrow-Band Laser Radiation in Atmopheric Microwindows. *Atmos. Ocean. Optics, 15*(4), 321-324.

Wenzel Associates, Inc. (n.d.). *501-04516D*. Retrieved July 1, 2014, from http://www.wenzel.com/wp-content/parts/501-04516.pdf

Wiedner, M. C. (2002). *Noise Characterization and Allan Variances of Water Vapor Monitors*. Memo, Harvard Smithsonian Astrophysical Ovservatory Submillimeter Array, Cambridge.

Wikipedia. (2014, July). Retrieved from Blue Mesa Reservoir: http://en.wikipedia.org/wiki/Blue_Mesa_Reservoir

Wikipedia. (2014, July). Retrieved from Lake Powell: http://en.wikipedia.org/wiki/Lake_Powell

Wi-Sys Communications Inc. (2014). Retrieved from http://datasheet.octopart.com/WS3910-3M-SMA-PCTEL-datasheet-11987595.pdf

# Appendix I

| |
|---|
| 0.25A X 3 |
| 0.315A X 2 |
| 0.5A X 3 |
| 1A X 2 |
| 1.6A X 2 |
| 3A X 2 |
| 4A X 2 |

**AC**

| | |
|---|---|
| White | Neutral |
| Black | Live |
| Red/Gre | Ground |

**DC**

| **2-Wire** | |
|---|---|
| Red/White | + Live |
| Black | Return |
| **3-Wire** | |
| Red | + Live |
| Black | Return |
| White | - Live |

Figure 175: Color Code Legend for Fuse Ratings and HAMMR Wiring

| **+7 V** | | **-5 V** | |
|---|---|---|---|
| Current (mA) | Sub-System | Current (mA) | Sub-System |
| 600-640 | AMRs | 30-45 | AMRs |
| 600-640 | | 30-45 | |
| 3 x 60 =170-200 | Window | 3 x 6 =18-25 | Window |
| 420-500 | 183 Sounder (OMT) | 1 | Sounder |
| 410-490 | 118 Sounder | 1 | |

Figure 176: Expected Current Values for the +7 and -5 V Distribution Blocks

| +11.5 V | | -11.5 V | |
|---|---|---|---|
| Current (mA) | Sub-System | Current (mA) | Sub-System |
| 19-22 | AMRs | 19-22 | AMRs |
| 19-22 | | 19-22 | |
| 7 x 175 = 1190-1300 | ABEB | 7 x 160 = 1085-1180 | ABEB |
| 2 x 635 = 1100-1300 | Freq Mult | 3 x 11.5 =30-45 | Window |
| 3 x 11.5 =30-45 | Window | | |

Figure 177: Expected Current Values for the ±12 V Distribution Blocks

| +15 V | | +16 V | |
|---|---|---|---|
| Current (mA) | Sub-System | Current (mA) | Sub-System |
| 0-80 | AMRs + Window NSs | 0.6 | FPGA |
| 0-80 | | | |
| 2 x 50 + 65 = 150-175 | DROs + OP Amp | | |
| Start = 600-900 SS = 500-600 | Thermistors + SND CLK | | |

Figure 178: Expected Current Values for the +15 and +16 V Distribution Blocks

# Appendix II

Table 19: List of Screws Used in HAMMR Instrument

| Component | Type | Size | Length | # Used | Misc |
|---|---|---|---|---|---|
| ± 12 and 7 V Acopian PSUs | Machine CS=82° | 8-32 | 1/2" | 4 | Locking |
| ABEB Chassis | SHCS | 10-32 | 3/16" | 8 | Locking |
| AC Power Distribution | Machine CS=82° | 8-32 | 3/8" | 4 | Locking w/nuts |
| Acopian PSUs Small | Machine CS=82° | 4-40 | 3/8" | 16 | Locking |
| AMR Back Bracket | SHCS | 4-40 | 1/4" | 2 | Locking |
| AMR Block Mounting | SHCS | 1/4-28 | 1/2" | 23 | Locking w/nuts |
| AMR Front Bracket | SHCS | 10-32 | 3/8" | 2 | Locking |
| AMR Horn Mount Brackets | SHCS | 8-32 | 3/8" | 3 | Locking |
| AMR Receiver Mounting | SHCS | 8-32 | 1" | 24 | |
| Buffer Board Chassis | SHCS | 10-32 | 3/8" | 4 | Locking |
| Computer Mount | SHCS | 10-32 | 3/16" | 4 | Locking |
| FPGA Platform Poles | Machine CS=82° | 8-32 | 1/2" | 4 | Locking |
| HAMMR Lid | Machine | 8-32 | 1/2" | >25 | Mil Spec |
| Int Computer PSU Mount | Machine CS=82° | 8-32 | 1/2" | 2 | Locking w/nuts |
| Motor Controller | SHCS | 4-40 | 3/4" | 3 | Locking |
| Motor PSU | SHCS | M4 | 8 mm | 4 | Locking |
| Op Bench Brackets | SHCS | 8-32 | 3/8" | 16 | |
| Sounder Horn Mount | SHCS | 2-56 | 5/8" | 3 | Locking |
| Sounder Horn Mount Bracket | SHCS | 8-32 | 3/8" | 4 | Locking |
| Thermistor ADCs | SHCS | M3 | 30 mm | 8 | Locking w/nuts |
| Thermistor ADCs Mounts | SHCS | 10-32 | 3/16" | 8 | Locking |
| Tri-freq Horn Mount | SHCS | 2-56 | 5/8" | 6 | Locking |
| Tri-freq Horn Mount Bracket | SHCS | 8-32 | 3/8" | 4 | Locking |
| Upper Bench | Machine | 10-32 | 1/2" | >25 | Mil Spec |